Heterogeneous Copper-Based Catalysts for Low-Temperature Methanol Steam Reforming



William Vickery

St Cross College

University of Oxford

A thesis submitted for the degree of

Doctor of Philosophy - Inorganic Chemistry

Hilary 2022

Acknowledgements

Mum and Dad, this work could never have been completed without you and your support, you were there for me every step of the way; I love you buckets and buckets and I am immeasurably grateful for all that you have done for me.

Chris, you have been the best brother ever, thank you! I am also incredibly thankful for the whole family being behind me. Especially to Nan for giving both grammar advice and banana bread! I love you all!

Christina, you have been a light on in the dark. Without the joy, fun, caring and strength you have brought into my life, my time in Oxford would have been nowhere near as cherished. Here's to many more adventures, I love you!

Of course Wills, Hamish, Ollie and Jake all deserve acknowledgement for their support; thank you all for the games and friendship, it means a lot!

Tuğçe, you have been the best mentor I could have asked for, your dedication, scientific integrity and work ethic are all extremely impressive and admirable. This research project couldn't have been completed without your insight and contributions but, arguably more importantly, you have been a great friend and I wish you all the best in your future career!

I'd like to thank Konstantin and Jamie from the bottom of my heart, without your collaboration and hard work the extent of this research could not have been so far reaching within the field. I will try and get all of the papers finished I promise!

A big thank you to all my lab mates past and present! And a special shout-out to Chris, Bruce, Baron and Jianwei for the extra assistance and discussions.

Last but not least, Professor S. C. E. Tsang, I am very grateful for the opportunity you provided me with and for all the expert advice and facilitation; thank you very much!

Abstract

This thesis concerns the development of a new class of methanol steam reforming (MSR) catalyst precursors. The work aims to facilitate advances in on-board, MSR-powered proton exchange membrane fuel cell technology by producing catalysts with high H_2 production rates and optimal H_2:CO selectivity.

CuZn-based layered double hydroxides (LDHs) were synthesised and exfoliated using a novel, simple and scalable aqueous miscible organic solvent method to yield catalyst precursors with high surface areas and copper dispersions. This is the first time such methods were used in the preparation of MSR catalysts; a CuZnAl-LDH precursor achieved a BET surface area and copper dispersion percentage of 252 $m^2.g^{-1}$ and 53.9 %, respectively.

It was found that an optimal content of Ce doped into the catalysts suppressed CO production. Many of the catalysts in this work produced a higher H_2:CO mol ratio than the previous best recorded ratio in literature, 3000 mol_{H_2}:mol_{CO}, under conditions that favoured higher reverse water gas shift activity; specifically, 27 % less water content and a 70 % lower weight hourly space velocity (WHSV). Notably, a CuZnGaCe catalyst from this work produced 4721 mol_{H_2}:mol_{CO}, with an activity of 14.4 $\mu mol_{H_2}.s^{-1}.g_{cat}$, at 180 °C using a 1.1:1 mol ratio of water/methanol reactants and a 2.03 h^{-1} WHSV.

Additionally, this work investigated the previously unsolved structure of lanthanide-doped LDHs with a wide variety of techniques including high resolution-EDX, Ce L_3 edge XAS and DFT analysis; this allowed the structure to be proposed. XAS was also used to analyse catalyst samples from different stages of water gas shift reactions to gather insight on how the catalysts improved selectivity.

Contents

1 Introduction **1**

1.1 Hydrogen as a potential energy carrier 1

1.1.1 Challenges with establishing a hydrogen economy 1

1.1.2 The case for MSR-PEMFCs 3

1.2 Goals of this work 6

2 Fundamental concepts **7**

2.1 Energy and reactions 7

2.1.1 Electronegativity and polarisability 8

2.1.2 Lattice energy 9

2.2 Unit cells and Miller indices 10

2.3 Coprecipitation 13

2.4 Adsorption 14

2.5 Heterogeneous catalysis 15

2.5.1 Rate-determining step 15

2.5.2 Catalysis and equilibria 17

2.5.3 Nanoparticles 18

2.5.4 Catalyst deactivation 21

2.5.5 Metal-support interactions 23

2.6 Reducible oxides 24

2.7 Methanol steam reforming 26

2.7.1 Side reactions 27

3 Literature Review **30**

3.1 MSR conditions used in literature 31

3.2 MSR catalysts 35

3.3 Cu-based MSR catalysts in literature 39

3.4 Proposed Cu-catalysed MSR mechanisms 43

3.5 Side reactions in MSR literature . . . 52
3.6 The oxidation states of Cu and Zn . . . 55
3.6.1 Potential role of Cu^+ . . . 56
3.6.2 Potential role of Zn^0 . . . 58
3.7 AMO-LDHs as catalyst precursors . . . 62
3.7.1 Properties of LDHs . . . 64

4 Research Plan **72**

5 Experimental **75**
5.1 Synthesis of AMO-LDHs . . . 75
5.1.1 AMO method theory and other considerations . . . 75
5.1.2 Synthesis of CuZn-based AMO-LDHs . . . 77
5.2 Calcination, reduction and catalyst storage . . . 78
5.3 PXRD . . . 79
5.3.1 X-Ray diffraction theory . . . 79
5.3.2 PXRD methodology . . . 80
5.4 TGA . . . 81
5.4.1 TGA methodology . . . 81
5.5 TPR . . . 81
5.5.1 TPR methodology . . . 81
5.6 BET surface area analysis . . . 82
5.6.1 BET surface area theory . . . 82
5.6.2 BET surface area analysis methodology . . . 82
5.7 D_{Cu} % analysis . . . 82
5.7.1 N_2O/H_2 titration theory . . . 82
5.7.2 N_2O/H_2 titration methodology . . . 83
5.8 EPR . . . 83
5.8.1 EPR theory . . . 83
5.8.2 EPR methodology . . . 84
5.9 TEM analysis . . . 84
5.9.1 TEM theory . . . 84
5.9.2 TEM methodology . . . 84
5.10 X-ray photoelectron spectroscopy . . . 85
5.10.1 XPS theory . . . 85
5.10.2 XPS method . . . 88
5.11 XAS . . . 88

5.11.1 XAS theory . . . 88
5.11.2 XAS spectra collection . . . 89
5.11.3 XAS modelling . . . 90
5.12 DRIFTS . . . 91
5.12.1 DRIFTS methodology . . . 92
5.13 ICP-MS . . . 92
5.14 EDX . . . 93
5.15 Catalytic testing . . . 93
5.15.1 MSR catalytic testing method . . . 95

6 Dilution of the active metal species 96
6.1 The usage of Mg in steam reforming catalysis . . . 96
6.2 The goal with Mg dilution . . . 98
6.3 The CuZnMgAl AMO-LDH series . . . 100
6.3.1 Thermogravimetric analysis of the Mg LDH series . . . 102
6.3.2 PXRD analysis of the Mg LDH series . . . 108
6.3.3 Calcination of the Mg series . . . 117
6.3.4 TPR analysis of the Mg LDO series . . . 121
6.3.5 BET analysis of the Mg LDH/LDO series . . . 122
6.3.6 N_2O/H_2 titration of the Mg LDO series . . . 125
6.3.7 MSR catalytic activity of the Mg reduced series . . . 127
6.4 Mg chapter summary . . . 136

7 Modifying the primary LDH M^{3+} ions 137
7.1 The goal of M^{3+} ion experimentation . . . 137
7.2 The usage of Ga and Al in steam reforming catalysis . . . 138
7.3 The CuZnGa and CuZnAl AMO-LDH series . . . 141
7.3.1 PXRD analysis of the Ga and Al LDH series . . . 143
7.3.2 Calcination and Reduction of the Ga and Al series . . . 154
7.3.3 TPR analysis of the Ga and Al LDO series . . . 158
7.3.4 BET analysis of the Ga and Al LDO series . . . 162
7.3.5 N_2O/H_2 titration of the Al and Ga LDO series . . . 164
7.3.6 MSR catalytic activity of the Al and Ga reduced series . . . 167
7.4 AlGa chapter summary . . . 179

8 Doping CuZnGa AMO-LDHs with Cerium 181
8.1 The usage of Ce in catalysis . . . 181

8.2 The goal of doping MSR catalyst LDH-precursors with Ce 186
8.3 The CuZnGaCe AMO-LDH series 187
8.4 Analysis of the Ce-doped LDH structure 189
8.4.1 PXRD analysis of the Ce LDH series 189
8.4.2 TEM analysis of the Ce LDH series 199
8.4.3 EDX analysis of the Ce LDH series 204
8.4.4 XPS analysis of the Ce LDH series 205
8.4.5 XAS analysis and DFT modelling of Ce-doped LDHs 212
8.5 Analysis of the calcined and reduced Ce series 222
8.5.1 PXRD analysis of the Ce LDO/reduced series 222
8.5.2 TEM analysis of the Ce LDO series 224
8.5.3 BET analysis of the Ce LDO series 227
8.5.4 N_2O/H_2 titration of the Ce LDO series 233
8.5.5 XAS analysis of reacted catalysts 235
8.5.6 MSR catalytic activity of the Ce reduced series 240
8.5.7 Other lanthanide dopants 244
8.6 Ce chapter summary 247

9 Conclusion **250**

10 Appendix **253**
10.1 TPR analysis of the Ce LDO series 253
10.2 DRIFTS analysis of the Ce reduced series 256
10.3 EPR analysis of the Al and Ga LDO series 263
10.4 EPR analysis of the Ce LDO series 267

Bibliography **269**

List of Figures

1.1 A simplified overview of how the current use of fossil fuels generates greenhouse gases. It also demonstrates how potential sustainable energy and hydrogen use(from water electrolysis) can provide a carbon-neutral replacement infrastructure. This figure does not include the CO_2 emissions related to using methanol as a hydrogen carrier. Figure used with permission from: A. M. Oliveira, R. R. Beswick, Y. Yan, *Current Opinion in Chemical Engineering*, 2021, **33**, 100701. ©2021 Elsevier Ltd. 2

1.2 A proposed system for fuelling a ship with electrolysed water and captured CO_2 via methanol reforming. Figure used with permission from: E. Malmgren, S. Brynolf, E. Fridell, M. Grahn, K. Andersson, *Sustainable Energy & Fuels*, 2021, **5**, 2753-2770.©2021 Royal Society of Chemistry. 4

1.3 A simplified schematic of a PEMFC. It depicts how hydrogen electrochemically reacts at the anode, how electrons and protons are conducted separately and the resultant, water-generating reaction at the cathode. Figure used with permission from: S. J. Peighambardousta, S. Rowshanzamirab, M. Amjadia, *International Journal of Hydrogen Energy*, 2010, **35**, 9349-9384. ©2010 Elsevier Ltd. 5

2.1 Pauling electronegativity of the periodic table. Figure used with permission from: *https://sciencenotes.org/list-of-electronegativity-values-of-the-elements/* (Accessed:13/12/2021).©sciencenotes.org. 8

2.2 An example metal oxide lattice is displayed in the centre oval, where A,B = different metals and O = oxygen. The light blue arrows point to various scenarios in which defects can form within metal oxides or between two phases of different metal oxides. Figure used with permission from: W. Li, J. Shi, K. H. Zhang, J. L. MacManus-Driscoll, *Materials Horizons*, 2020, **7**, 2832-2859.©2020 Royal Society of Chemistry. 10
2.3 The Born-Haber cycle of NaCl; ΔH_L corresponds to lattice enthalpy and ΔH_f corresponds to the standard enthalpy of formation. Figure used with permission from: R. S. Treptow, *Journal of chemical education*, 1997, **74**, 919.©1997 American Chemical Society. 11
2.4 The 14 Bravais lattices; the coloured dots represent atoms or monoatomic ions. Figure used with permission from: E. Ameh, *The international journal of advanced manufacturing technology*, 2019, **105**, 3289-3302. (The figure was based off the work: D. Askeland, P. Fulay, W. Wright, *The Science and Engineering of Materials*, 6^{th} Edition, 2011.) 12
2.5 Nine different examples of Miller indices. Figure used with permission from: M. Wahab, *Numerical Problems in Crystallography*, Springer, 2021, pp. 137– 178.©2021 Springer Nature Ltd. 13
2.6 An exothermic reaction (green line) and how a catalyst can affect the activation energy and reaction pathway (red dotted line). In this simple example, the catalyst stabilised the transition state and introduced a new transition state. Figure made using paint.NET® and Inkscape®. 16
2.7 Gold metal nanoparticles supported on titanium dioxide, one nanoparticle can be seen to be 4.96 nm thick, equivalent to the diameters of $\approx$ 12 gold atoms in a plane (assuming room temperature and a face-centered cubic structure). The image was taken by a high-resolution transmission electron microsope. Figure used with permission from: M. Abd Elmoula, E. Panaitescu, M. Phan, D. Yin, C. Richter, L. H. Lewis, L. Menon, *Journal of Materials Chemistry*, 2009, **19**, 4483-4487.©2009 Royal Society of Chemistry. 19

2.8 a) How the relative melting temperature (T_m/T_0) of In, Pb, Bi and Sn nanoparticles changes with nanoparticle size. b) How melting temperature (K) for Au nanoparticles changes with nanoparticle size. c) How melting temperature (K) for Cu nanoparticles changes with nanoparticle size. Figures used with permission from: a) C. Chen, J.-G. Lee, K. Arakawa, H. Mori, *Applied Physics Letters*, 2011, **99**, 013108.©2011 American Institute of Physics. b) J. Zhu, Q. Fu, Y. Xue, Z. Cui, *Journal of Materials Science*, 2016, **51**, 4462-4469.©2016 Springer Nature Ltd. c) H. H. Kart, H. Yildirim, S. O. Kart, T. Çağin, *Materials Chemistry and Physics*, 2014, **147**, 204-212.©2014 Elsevier Ltd. . . . 23

2.9 Examples of metal-support interactions and methods of tuning heterogeneous cataysts' surfaces. Figure used with permission from: T. W. van Deelen, C. H. Mejía, K. P. de Jong, *Nature Catalysis*, 2019, **2**, 955-970.©2019 Springer Nature Ltd. 25

2.10 How the performance of a MSR catalytic system (H_2/CO molar fractions and methanol conversion) thermodynamically changes with S/C (steam:carbon or H_2O:CH_3OH) ratio and temperature. Figure used with permission from: S. Xing, C. Zhao, S. Ban, Y. Liu, H. Wang, *International Journal of Hydrogen Energy*, 2020, **45**, 7015-7024.©2020 Elsevier Ltd. 28

2.11 a) Observed experimental data for a $CuZnGaO_x$ catalyst under MSR conditions with a varying temperature and a 2:1 water:methanol ratio (the numbers next to the red triangles represent CO concentration in ppm). b) Thermodynamic calculations for the exact same experiment and conditions. Figure used with permission from: K. M. K. Yu, W. Tong, A. West, K. Cheung, T. Li, G. Smith, Y. Guo and S. C. E. Tsang, *Nat.Commun.*, 2012, **3**, 1-7.©Springer Nature Ltd. 29

3.1 An example diagram of a standard, laboratory-scale MSR reactor. A) Carrier gas. B) H_2O:CH_3OH solution. C) Carrier gas mass flow controller. D) Liquid pump E) Computer programme connected to gas mass flow controller. F) Furnace. G) Thermocouple for the furnace. H) Catalyst. I) Quartz wool either side of the catalyst, packing it. J) Furnace temperature controller. K) Glass condenser. L) Dry ice bath for the glass condenser. M) Gas chromatograph's thermal conductivity detector. N) Gas chromatograph's flame ionisation detector. O) Software for gas chromatograph. Figure used with permission from: K. M. K. Yu, W. Tong, A. West, K. Cheung, T. Li, G. Smith, Y. Guo, S. C. E. Tsang, *Nature Communications*, 2012, **3**, 1-7.©2012 Springer Nature Ltd. 32
3.2 How the water:methanol ratio affects the CO production of two different MSR systems. Figure used with permission from: S. Patel, K. K. Pant, *Journal of Power Sources*, 2006, **159**, 139-143.©2006 Elsevier Ltd. 42
3.3 a) The potential energy of surface MSR species over Cu (1 1 1). The formation of HCHO* + OH* + 3H* is also favoured by Pd (1 1 1), however b) shows that the favoured pathway for Pd (1 1 1) proceeds to form CO*. Figure used with permission from: X.-K. Gu, W.-X. Li, *The Journal of Physical Chemistry C*, 2010, **114**, 21539-21547.©2010 American Chemical Society. 45
3.4 Common species observed in literature MSR reactions. Figure used with permission from: S. T. Yong, C. W. Ooi, S. P. Chai and X. S. Wu, *Int. J. Hydrog. Energy*, 2013, **38**, 9541-9552.©2013 Elsevier Ltd. 48
3.5 Proposed MSR mechanism over Cu/ZnO. Figure used with permission from: W. Tong, K. Cheung, A. West, K.-M. Yu and S. C. E. Tsang, *Phys. Chem. Chem. Phys.*, 2013, **15**, 7240-7248.©2013 Royal Society of Chemistry. 51
3.6 Proposed MSR mechanisms, involving two different active sites, for Cu-based and non-Cu metallic heterogeneous catalysts; includes a methyl formate intermediate pathway. Figure used with permission from: B. Frank, F. C. Jentoft, H. Soerijanto, J. Kröhnert, R. Schlögl, R. Schomäcker, *Journal of Catalysis*, 2007, **246**, 177–192.©2007 Elsevier Ltd. 51

3.7 Proposed MSR mechanism at a Cu^0-CeO_2 interface. Figure used with permission from: Y. Men, H. Gnaser, R. Zapf, V. Hessel, C. Ziegler, *Catalysis Communications*, 2004, **5**, 671–675.©2004 Elsevier Ltd. . . . 52
3.8 Proposed WGS mechanism over Cu/ZnO. Figure used with permission from: W. Tong, K. Cheung, A. West, K.-M. Yu and S. C. E. Tsang, *Phys. Chem. Chem. Phys.*, 2013, **15**, 7240-7248.©2013 Royal Society of Chemistry. 55
3.9 Proposed WGS mechanism over inert SiO_2 and either Cu^0 or Cu^+. Figure used with permission from: Z. Bian, W. Zhong, Y. Yu, B. Jiang, S. Kawi, *International Journal of Hydrogen Energy*, 2020, **45**, 27078–27088.©2020 Elsevier Ltd. 57
3.10 a) A simplified schematic of how the inclusion of Ga^{3+} and the formation of spinel oxide and a staggered type II heterojunction can cause excited electrons to favour aggregation in the lower-energy conduction band i.e. in ZnO. b) The potential energy of differently-sized Cu, Zn and CuZn nanoparticles. Figures used with permission from: a) M. M.-J. Li, Z. Zeng, F. Liao, X. Hong, S. C. E. Tsang, *Journal of Catalysis*, 2016, **343**, 157-167.©2016 Elsevier Ltd. b) M. M.-J. Li, J. Zheng, J. Qu, F. Liao, E. Raine, W. C. H. Kuo, S. S. Su, P. Po, Y. Yuan, S. C. E. Tsang, *Scientific Reports*, 2016, **6**.©2016 Springer Nature Ltd. . 59
3.11 a) CO_2 hydrogenation activity of a CuZn-based catalyst with time. b) The in-situ XPS Zn $2p_{3/2}$ peak analysis for the same reaction. Figure used with permission from: S. Kattel, P. J. Ramírez, J. G. Chen, J. A. Rodriguez, P. Liu, *Science*, 2017, **355**, 1296–1299.©2017 American Association for the Advancement of Science. 61
3.12 Optimal models of LDHs intercalated by carbonate anions, with varying M^{2+}:M^{2+} ratios. It should be noted that hydroxyl groups are always orientated towards the interlayer regions/galleries. Figure used with permission from: G. Fan, F. Li, D. G. Evans, X. Duan, *Chemical Society Reviews*, 2014, **43**, 7040–7066.©2014 Royal Society of Chemistry. 63
3.13 a) 3R LDH polytype and b) 2H LDH polytype unit cells along the *c* axis. c) (1 1 0) projection of a LDH layer. Figure used with permission from: E. S. Zhitova, S. V. Krivovichev, I. Pekov, H. C. Greenwell, *Mineralogical Magazine*, 2019, **83**, 269–280.©2018 Cambridge University Press. 66

3.14 Zn-LDH models of $3R_1$ and $3R_2$ polytypes. A, B and C represent LDH layers with differently-aligned vertical OH^- groups; $3R_1$ and $3R_2$ are eclipsed and staggered, respectively. A lower case b represents the plane of Zn cations. Figure used with permission from: S. Radha, S. Prasanna, P. V. Kamath, *Crystal growth & design*, 2011, **11**, 2287–2293.©2011 American Chemical Society. 68

3.15 Left) Simulation of 2H and $3R_1$ LDH polytypes' PXRD patterns. Right) Experimental PXRD of MgAl-LDHs at a) 70 °C (predominantly $3R_1$) and at b) 180 °C (predominantly $3R_2$). Figures used with permission from: Left) A. Faour, C. Mousty, V. Prevot, B. Devouard, A. De Roy, P. Bordet, E. Elkaim, C. Taviot-Gueho, *The Journal of Physical Chemistry C*, 2012, **116**, 15646– 15659.©2012 American Chemical Society. Right) S. P. Newman, W. Jones, P. O'Connor, D. N. Stamires, *Journal of Materials Chemistry*, 2002, **12**, 153–155.©2002 Royal Society of Chemistry. 69

5.1 Molecular dynamics simulations of LDH interlayer spaces. a) Simulated partial density of LDH interlayer gallery model; including densities of H_2O, LDH layer and carbonate anions. WAT = water and CRBN = carbonate anion. b) The simulated LDH interlayer spacing, *d*, as a function of AMO method solvent. WAT = water, ACT = acetone, iP = isopropanol, TBut = tert-butanol, THF = tetrahydrofuran. The shapes represent different solvent:water molecule ratios used in the models: Circle = 100:1000, Triangle = 200:600 and Square = 300:300 (For water models these shapes represent: Circle = 0:800, Triangle = 0:1000 and Square = 0:1400). Figures used with permission from: V. Erastova, M. T. Degiacomi, D. O'Hare and H. C. Greenwell, *RSC Adv.*, 2017, **7**, 5076 .©2017 Royal Society of Chemistry. 76

5.2 Exploded schematic of common TEM components. Figure used with permission from: B. Inkson, *Materials characterization using nondestructive evaluation (NDE) methods*, Elsevier, 2016, pp. 17–43.©2016 Elsevier Ltd. 85

5.3 Diagram of an experimental XPS set-up, figure used with permission from: H. Seyama, M. Souma, B.K.G. Theng, *Developments in Clay Science*, 2013, **5**, 161-176.©2013 Elsevier Ltd. 87

5.4 Simplified schematic of the final iteration MSR catalytic flow reactor. Figure made using paint.NET® and Inkscape®. 95

6.1 The periodic table showing the Herfindahl-Hirschman Index generated from the 2011 U.S. Geological Survey. Figure used with permission from: M. W. Gaultois, T. D. Sparks, C. K. H. Borg, R. Seshadri, W. D. Bonificio, D. R. Clarke, *Chemistry of Materials*, 2013, **25**, 2911-2920. ©2021 American Chemical Society. 97
6.2 TGA of the Mg-based AMO-LDH series, measured with a 10 °C.min^{-1} heating rate. 103
6.3 The derivative mass, dm/dT, of the Mg-based AMO-LDH series. The graph was calculated using data from the TGA, Figure 6.2, and smoothed with a LOESS regression. The solid line at 330 °C represents the calcination temperature used before MSR catalytic activity testing. . . . 104
6.4 PXRD patterns of the Mg-based AMO-LDH series. 108
6.5 The a parameters of the Mg-based AMO-LDH series. Calculated from the PXRD data (Figure 6.4). The red line represents a linear fit where: y = 3.079 - $(5.132 \times 10^{-4})x$ and the R^2 value = 0.981. 110
6.6 The c parameters of the Mg-based AMO-LDH series. Calculated from the PXRD data (Figure 6.4). The red line represents a linear fit where: y = 22.85 + $0.006x$ and the R^2 value = 0.72. 111
6.7 The mean crystallite thickness of each AMO-LDH from the Mg-based series. Calculated from the PXRD data (Figure 6.4) using the standardised integration method used across this thesis. The red line represents a cubic fit where: y = 52.0 - $1.40x$ + $0.03x^2$ - $1.86x^3$ and the R^2 value = 0.864. 114
6.8 The mean no. of LDH layers per crystallite of each AMO-LDH from the Mg-based series. Calculated from the PXRD data (Figure 6.4). The red line represents a cubic fit where: y = 7.17 - $0.20x$ + $0.004x^2$ - $(2.27\times10^{-5})x^3$ and the R^2 value = 0.78. 116
6.9 The mean plate diameter of each AMO-LDH from the Mg-based series. Calculated from the PXRD data (Figure 6.4) using the standardised integration method used across this thesis. The red line represents a linear fit (ignoring the 52.5Mg-LDH data point) where: y = 93.3 - $0.23x$ and the R^2 value = 0.54. 117
6.10 The PXRD patterns of the calcined Mg-based AMO-LDO series. . . . 119

6.11 The TPR analysis of the calcined Mg-based AMO-LDO series; measured with a 10 °C.min^{-1} heating rate. 122
6.12 The BET surface areas of: Green) the Mg-based AMO-LDH series and Black) part of the Mg-based calcined (LDO) series; the error = ± 1.0 m^2.g^{-1}. The red line represents a cubic fit of the LDH where: y = 223.7 + 6.44x - 0.08x^2 - 2.89x^3 and the R^2 value = 0.61. The blue line represents a quadratic fit of the LDO where: y = 230.0 + 6.47x - 0.08x^2 and the R^2 value = 0.96. 123
6.13 The D_{Cu} % of the calcined Mg-based AMO-LDH series; measured via N_2O/H_2 titration. The red line represents a linear fit (ignoring the 0Mg-LDO data point) where: y = 25.5 + 0.691x and the R^2 value = 0.958. 126
6.14 The MSR catalytic test results of the reduced Mg-based series; the hydrogen production rate and CO production rate units are $\mu mol_{H_2}.s^{-1}.g_{cat}^{-1}$ and $nmol_{CO}.s^{-1}.g_{cat}^{-1}$, respectively. Tested at 180 °C for 5 hours, with with 75 mg of catalyst, a N_2 gas flow of 10 mL.min^{-1} and a 0.075 mL.min^{-1} liquid flow of water:methanol solution (1.1:1 mol ratio). WHSV = 5.41 h^{-1}. 128
6.15 The hydrogen production rate ($\mu mol_{H_2}.s^{-1}.g_{cat}^{-1}$) of the reduced Mg-based series shown against time in the x axis (Time = 0, coincides with the start of reactant flow). Tested at 180 °C for 5 hours, with 75 mg of catalyst, a N_2 gas flow of 10 mL.min^{-1} and a 0.075 mL.min^{-1} liquid flow of water:methanol solution (1.1:1 mol ratio). WHSV = 5.41 h^{-1}. 130
6.16 The maximum hydrogen production rate ($\mu mol_{H_2}.s^{-1}.g_{cat}^{-1}$) observed for each reduced Mg-based catalyst, shown against the (Hydrogen production rate at 300 mins / The peak hydrogen production rate) ratio. Tested at 180 °C for 5 hours, with 75 mg of catalyst, a N_2 gas flow of 10 mL.min^{-1} and a 0.075 mL.min^{-1} liquid flow of water:methanol solution (1.1:1 mol ratio). WHSV = 5.41 h^{-1}. 131

6.17 A rearranged format of the MSR catalytic test results of the reduced Mg-based series, seen in Figure 6.14; the hydrogen production rate and CO production rate units are $\mu mol_{H_2}.s^{-1}.g_{cat}^{-1}$ and $nmol_{CO}.s^{-1}.g_{cat}^{-1}$, respectively. Tested at 180 °C for 5 hours, with with 75 mg of catalyst, a N_2 gas flow of 10 $mL.min^{-1}$ and a 0.075 $mL.min^{-1}$ liquid flow of water:methanol solution (1.1:1 mol ratio). WHSV = 5.41 h^{-1}. Error bars (x/y) are shown inverted within the data point symbols. 134
6.18 The H_2:CO mol ratio produced by the reduced Mg-based series during MSR (as a function of their hydrogen production); the hydrogen production rate's units are $\mu mol_{H_2}.s^{-1}.g_{cat}^{-1}$. Tested at 180 °C for 5 hours, with 75 mg of catalyst, a N_2 gas flow of 10 $mL.min^{-1}$ and a 0.075 $mL.min^{-1}$ liquid flow of water:methanol solution (1.1:1 mol ratio). WHSV = 5.41 h^{-1}. Error bars (x/y) are shown inverted within the data point symbols. 135

7.1 PXRD patterns of the Al- and Ga-based AMO-LDH series. 144
7.2 PXRD patterns of the Al- and Ga-based AMO-LDH series between 8 ° and 30 ° 2θ; showing the (0 0 3) and (0 0 6) peaks. 145
7.3 PXRD patterns of the Al- and Ga-based AMO-LDH series between 58 ° and 62 ° 2θ; showing the (1 1 0) and (1 1 3) peaks. 145
7.4 The a parameters of the Al- and Ga-based AMO-LDH series. Calculated from the PXRD data (Figure 7.1). 146
7.5 The c parameters of the Al- and Ga-based AMO-LDH series. Calculated from the PXRD data (Figure 7.1). 148
7.6 The mean crystallite thickness of each AMO-LDH from the Al- and Ga-based series. Calculated from the PXRD data (Figure 7.1) using the standardised Scherrer and integration methods used across this thesis. 150
7.7 The mean no. of LDH layers per crystallite of each AMO-LDH from the Al- and Ga-based series. Calculated from the PXRD data (Figure 7.1). 151
7.8 The mean plate diameter of each AMO-LDH from the Al- and Ga-based series. Calculated from the PXRD data (Figure 7.1) using the standardised Scherrer and integration methods used across this thesis. 152
7.9 The PXRD patterns of the calcined Al- and Ga-based AMO-LDO series. 155
7.10 The PXRD patterns of the reduced Al- and Ga-based series. 156

7.11 The average particle diameter of Cu^0 of each reduced sample from the Al- and Ga-based series. Calculated from the PXRD data (Figure 7.10). The Cu^0 is assumed to be FCC and the calculation error is ± 3 Å. 157
7.12 The TPR analysis of the calcined Al- and Ga-based AMO-LDO series; measured with a 10 °C.min^{-1} heating rate. 159
7.13 The BET surface areas of the calcined Al- and Ga-based series (LDOs); the error = ± 1.0 m^2.g^{-1}. 163
7.14 The D_{Cu} % of the calcined Al- and Ga-based AMO-LDO series; measured via N_2O/H_2 titration. 166
7.15 The MSR catalytic test results of the reduced Al- and Ga-based series; the hydrogen production rate and CO production rate units are $\mu mol_{H_2}.s^{-1}.g_{cat}^{-1}$ and $nmol_{CO}.s^{-1}.g_{cat}^{-1}$, respectively. Tested at 180 °C for 5 hours with 200 mg of catalyst, a N_2 gas flow of 10 mL.min^{-1} and a 0.1 mL.min^{-1} liquid flow of water:methanol solution (1.1:1 mol ratio). WHSV = 2.70 h^{-1}. Error bars (x/y) are shown inverted within the data point symbols. 168
7.16 The H_2:CO mol ratio produced by the reduced Al- and Ga-based series during MSR (as a function of their hydrogen production); the hydrogen production rate's units are $\mu mol_{H_2}.s^{-1}.g_{cat}^{-1}$. Tested at 180 °C for 5 hours, with 200 mg of catalyst, a N_2 gas flow of 10 mL.min^{-1} and a 0.1 mL.min^{-1} liquid flow of water:methanol solution (1.1:1 mol ratio). WHSV = 2.70 h^{-1}. Error bars (x/y) are shown inverted within the data point symbols. 169
7.17 The hydrogen production rate ($\mu mol_{H_2}.s^{-1}.g_{cat}^{-1}$) of the reduced Al- and Ga-based series shown against time in the x axis (Time = 0, coincides with the start of reactant flow). Tested at 180 °C for 5 hours, with 200 mg of catalyst, a N_2 gas flow of 10 mL.min^{-1} and a 0.1 mL.min^{-1} liquid flow of water:methanol solution (1.1:1 mol ratio). WHSV = 2.70 h^{-1}. 173
7.18 The maximum hydrogen production rate ($\mu mol_{H_2}.s^{-1}.g_{cat}^{-1}$) observed for each reduced Al- and Ga-based catalyst, shown against the (Hydrogen production rate at 300 mins / The peak hydrogen production rate) ratio. Tested at 180 °C for 5 hours, with 200 mg of catalyst, a N_2 gas flow of 10 mL.min^{-1} and a 0.1 mL.min^{-1} liquid flow of water:methanol solution (1.1:1 mol ratio). WHSV = 2.70 h^{-1}. 174

8.1 PXRD patterns of the Ce-based AMO-LDH series. 190
8.2 PXRD patterns of the Ce-based AMO-LDH series between 8 ° and 30 ° 2θ; showing the (0 0 3) and (0 0 6) peaks. 190
8.3 PXRD patterns of the Ce-based AMO-LDH series between 58 ° and 62 ° 2θ; showing the (1 1 0) and (1 1 3) peaks. 191
8.4 The a parameters of the Ce-based AMO-LDH series. Calculated from the PXRD data (Figure 8.1). The red line represents a linear fit where: y = 3.11 - $(1.18\times10^{-4})x$ and the R^2 value = 0.076. 193
8.5 The c parameters of the Ce-based AMO-LDH series. Calculated from the PXRD data (Figure 8.1). The red line represents a cubic fit where: y = 22.74 + 0.062x - 0.006x^2 + $(1.15\times10^{-5})x^3$ and the R^2 value = 0.67. 194
8.6 The mean crystallite thickness of each AMO-LDH from the Ce-based series. Calculated from the PXRD data (Figure 8.1) using the standardised Scherrer and integration methods used across this thesis. The red line represents a sigmoidal fit where: y = 246 - $\frac{1986}{1+(\frac{x}{0.065})^{1.5}}$ and the R^2 value = 0.92. 195
8.7 The mean no. of LDH layers per crystallite of each AMO-LDH from the Ce-based series. Calculated from the PXRD data (Figure 8.1). The red line represents a sigmoidal fit where: y = 32.8 - $\frac{170}{1+(\frac{x}{0.074})^{1.4}}$ and the R^2 value = 0.90. 196
8.8 The mean plate diameter of each AMO-LDH from the Ce-based series. Calculated from the PXRD data (Figure 8.1) using the standardised Scherrer and integration methods used across this thesis. The red line represents a linear fit where: y = 157 + 1.23x and the R^2 value = 0.87. 197
8.9 Dark-field TEM images of 35Zn20Ga-LDH. 200
8.10 Dark-field TEM images of 19.25Ga0.75Ce-LDH. 202
8.11 Dark-field TEM images of 12.5Ga7.5Ce-LDH. 203
8.12 EDX imaging analysis of 35Zn20Ga-LDH. 204
8.13 EDX imaging analysis of 19.25Ga0.75Ce-LDH. 204
8.14 EDX imaging analysis of 12.5Ga7.5Ce-LDH. 205
8.15 XPS spectra of 35Zn20Ga-LDH. Top) Zn B.E. Middle) Cu B.E. Bottom) Ga B.E. 208
8.16 XPS spectra of 19.25Ga0.75Ce-LDH. Top) Zn B.E. Middle) Cu B.E. Bottom) Ga B.E. 209
8.17 XPS spectra of 12.5Ga7.5Ce-LDH. Top) Zn B.E. Middle) Cu B.E. Bottom) Ga B.E. 210

8.18 XPS spectrum of Ce binding energies for 12.5Ga7.5Ce-LDH. 211
8.19 Left) Experimental Ce L_3 edge XANES spectra of 12.5Ga7.5Ce-LDH and CeO_2. Right) The Gaussian fitting of the 12.5Ga7.5Ce-LDH XANES spectrum using the literature-known $a/b/c/d$ Ce^{x+} transitions. 213
8.20 Blue line) Experimental Fourier-transformed $|\chi(R)|$ (above) and filtered back-Fourier Transformed $R_e|\chi(R)|$ (below, which is used to remove effects from higher coordination shells) EXAFS spectra of 12.5Ga7.5Ce-LDH. The red line represents simulated EXAFS spectra for the following models: a) 'monolayer' $Ce^{4+}O_2$ b) 6-coordinate Ce^{3+} substituted in LDH lattice position c) 8-coordinate Ce^{4+} substituted in defective layered lattice position. 215
8.21 a/b) Different angles of the bulk $Ce^{4+}O_2$ model (no LDH layer). c/d) Different angles of the 6-coordinate Ce^{3+} substitution model. e/f) Different angles of the 8-coordinate Ce^{4+} substitution model. g/h) Different angles of an adsorbed $Ce_3^{4+}O_x$ model. Models viewed with VESTA software (K. Momma and F. Izumi, "VESTA 3 for three-dimensional visualization of crystal, volumetric and morphology data, *J. Appl. Crystallogr.*, 2011, **44**, 1272-1276). 220
8.22 XANES spectra of the simulated 8-coordinated Ce^{4+}- and 6-coordinated Ce^{3+}-substituted models compared to experimental results. The 'mixed 6/8-CN model' XANES spectra was simulated for a mixture of 20 mol % of the 6-coordinated Ce^{3+}- and 80 mol % of the 8-coordinated Ce^{4+}-substituted models (reflecting the experimental oxidation state mixture estimated via XPS and Gaussian XANES fitting analysis). . 221
8.23 The PXRD patterns of the calcined Ce-based AMO-LDO series. . . . 223
8.24 The PXRD patterns of the reduced Ce-based series. 223
8.25 a) Light-field TEM image of 35Zn20Ga-LDO. b/c/d) Dark-field TEM images of 35Zn20Ga-LDO. 225
8.26 Dark-field TEM images of 19.25Ga0.75Ce-LDO. 226
8.27 The BET surface areas of the calcined Ce-based series (LDOs); the error = $\pm$ 1.0 $m^2.g^{-1}$. The red line represents a linear fit (ignoring the 19.5Ga0.5Ce-LDO data point) where: y = 100.9 + 1.62x and the R^2 value = 0.60. 228
8.28 BJH desorption pore volume and pore diameter for the Ce-based LDO series (data from Figure 8.27). 229

8.29 The total BJH pore volume and modal pore diameter for the Ce-based LDO series (data from Figure 8.27). 230
8.30 Hysteresis loops for the Ce-based LDO series in the upper relative pressure regime. x axis = relative pressure (P/P_0), y axis = amount adsorbed ($cm^3.g^{-1}$). Data from Figure 8.27. 231
8.31 Hysteresis loops for the Ce-based LDO series across all relative pressure regimes. x axis = relative pressure (P/P_0), y axis = amount adsorbed ($cm^3.g^{-1}$). Data from Figure 8.27. 232
8.32 The D_{Cu} % of the calcined Ce-based AMO-LDH series; measured via N_2O/H_2 titration. The red line represents a sigmoidal fit where: y = 26.0 - $\frac{20.7}{1+(\frac{x}{0.07})^{0.93}}$ and the R^2 value = 0.53. 234
8.33 The experimental Cu K XAS analysis of the reduced/WGS-reacted catalysts and Cu foil. 240
8.34 The MSR catalytic test results of the reduced Ce-based series; the hydrogen production rate and CO production rate units are $\mu mol_{H_2}.s^{-1}.g_{cat}^{-1}$ and $nmol_{CO}.s^{-1}.g_{cat}^{-1}$, respectively. Tested at 180 °C for 5 hours with 200 mg of catalyst, a N_2 gas flow of 10 $mL.min^{-1}$ and a 0.075 $mL.min^{-1}$ liquid flow of water:methanol solution (1.1:1 mol ratio). WHSV = 2.03 h^{-1}. Error bars (x/y) are shown inverted within the data point symbols. 242
8.35 The H_2:CO mol ratio produced by the reduced Ce-based series during MSR (as a function of their hydrogen production); the hydrogen production rate's units are $\mu mol_{H_2}.s^{-1}.g_{cat}^{-1}$. Tested at 180 °C for 5 hours, with 200 mg of catalyst, a N_2 gas flow of 10 $mL.min^{-1}$ and a 0.075 $mL.min^{-1}$ liquid flow of water:methanol solution (1.1:1 mol ratio). WHSV = 2.03 h^{-1}. Error bars (x/y) are shown inverted within the data point symbols. 243
8.36 The maximum hydrogen production rate ($\mu mol_{H_2}.s^{-1}.g_{cat}^{-1}$) observed for each reduced Ce-based catalyst, shown against the (Hydrogen production rate at 300 mins / The peak hydrogen production rate) ratio. Tested at 180 °C for 5 hours, with 200 mg of catalyst, a N_2 gas flow of 10 $mL.min^{-1}$ and a 0.075 $mL.min^{-1}$ liquid flow of water:methanol solution (1.1:1 mol ratio). WHSV = 2.03 h^{-1}. 245
8.37 PXRD patterns of the Ln-based AMO-LDH series. 246

8.38 The MSR catalytic test results of the reduced lanthanide-doped, LDH-derived series; the hydrogen production rate and CO production rate units are $\mu mol_{H_2}.s^{-1}.g_{cat}^{-1}$ and $nmol_{CO}.s^{-1}.g_{cat}^{-1}$, respectively. Tested at 180 °C for 5 hours with 200 mg of catalyst, a N_2 gas flow of 10 $mL.min^{-1}$ and a 0.075 $mL.min^{-1}$ liquid flow of water:methanol solution (1.1:1 mol ratio). WHSV = 2.03 h^{-1}. Error bars (x/y) are shown inverted within the data point symbols. 247

8.39 a) Propylene oxidation activity of lanthanide oxides; y = overall yield and R_0 = initial reaction rate. b) n-butane oxidation activity of lanthanide oxides; filled circle = n-butane conversion, empty circle = CO_2 yield, empty square = CO yield, filled triangle = hydrocarbon yield, filled diamond = n-butenes. Figure used with permission from: M. P. Rosynek, *Catalysis Reviews*, 1977, **16**, 111-154.©1977 Informa UK Ltd. 248

10.1 The TPR analysis of the calcined Ce-based AMO-LDO series; measured with a 10 °C.min^{-1} heating rate. 254

10.2 Baseline-corrected DRIFTS spectra for various LDH-derived catalysts at 180 °C. Each sample was saturated with a flow of $^{12/13}CH_3OH/N_2$ (g) before measurement. Time = 0 s coincides with the replacement of the $^{x}CH_3OH/N_2$ (g) flow with a $^{1/2}H_2O/N_2$ (g) flow. 257

10.3 A representation of Figure 10.2 where the peaks of various IR absorptions are highlighted. 259

10.4 Baseline-corrected DRIFTS spectra for various LDH-derived catalysts at 25 °C. Each sample was saturated with a flow of 400 ppm CO/N_2 (g) before measurement. Time = 0 s coincides with the replacement of the CO/N_2 (g) flow with a H_2O/N_2 (g) flow. 260

10.5 A representation of Figure 10.4 over the 2050 - 2250 Hz range; depicting CO adsorption modes. 261

10.6 Experimental X-band EPR spectra, measured at 77 K, for a monomeric Cu complex, with organic ligands, under different conditions: a) Pure crystalline powder. b) Dissolved in chloroform. c) Dissolved in dimethylformamide, in this scenario the Cu centres do not interact with each other; therefore, there is well resolved hyperfine splitting. Figure used with permission from: P. Subramanian, E. Suresh, D. Srinivas, *Inorganic chemistry*, 2000, **39**, 2053 – 2060.©2000 American Chemical Society. 265

10.7 Electron paramagnetic resonance analysis of the Al- and Ga-LDO series 266
10.8 Electron paramagnetic resonance analysis of the Ce-LDO series . . . 268
10.9 Electron paramagnetic resonance analysis of the Ln-LDO series . . . 268

Abbreviations

AMO - Aqueous miscible organic solvent (method)
B.E. - Binding Energy
BET - Brunauer Emmett Teller
BJH - Barrett Joyner Halenda
D_{Cu} % - Copper dispersion percentage
DFT- Density-functional theory
DME - Dimethyl ether
DRIFTS - Diffuse reflectance infra-red Fourier transform spectroscopy
EMSI - Electronic metal-support interaction
FCC- Face centred cubic
FT- Fourier transform
FTIR - Fourier transform infra-red spectroscopy
FWHM - Full width half maximum
HAADF - High-angle annular dark-field
ICP-MS - Inductively coupled plasma mass spectrometry
IR - Infra-red
LDH - Layered double hydroxide
LDO- Layered double oxide
MD - Methanol decomposition
MeOH - Methanol
MOF - Metal organic framework
MSI - Metal-support interaction
MSR - Methanol steam reforming
-OH - Hydroxide group
PEMFC - Proton exchange membrane fuel cell
PXRD - Powder X-Ray diffraction
RDS - Rate-determining step
RWGS - Reverse water gas shift
SMSI - Strong metal-support interaction
STEM - Scanning transmission electron microscopy
TPD - Temperature programmed desorption
TPR - Temperature programmed reduction
WGS - Water gas shift
WHSV - Weight hourly space velocity

Chapter 1

Introduction

1.1 Hydrogen as a potential energy carrier

1.1.1 Challenges with establishing a hydrogen economy

Hydrogen fuel cells facilitate an electrochemical reaction between oxygen (O_2) and hydrogen (H_2) to produce an electrical current; the only waste product is water (H_2O). [1] Such fuel cells, and a resultant 'hydrogen economy', are often touted as a replacement for fossil fuel energy carriers because carbon dioxide (CO_2) is not a direct product of the fuel cell reaction; Figure 1.1 is a simplified depiction of how a hydrogen economy would fit into a wider sustainable economy. [2] Whilst CO_2 is a greenhouse gas and its production from the burning of fossil fuels, such as petrol and diesel, is one of the main driving forces of the anthropogenic enhanced greenhouse effect; a lot of research is still required before a sustainable and 'carbon-neutral' hydrogen economy is a conceivable alternative. [3]

There are notable issues with using hydrogen as a commercial 'fuel' or an energy carrier. Currently it is energetically and/or spatially inefficient to transport gaseous or liquid hydrogen in tanks attached to a vehicle ('on-board use'), moreover ≈ 80 % of all hydrogen in 2021 was produced from natural gas (CH_4) or coal; for the remaining 20 % hydrogen is a side product e.g. in the production of gasoline. [4]

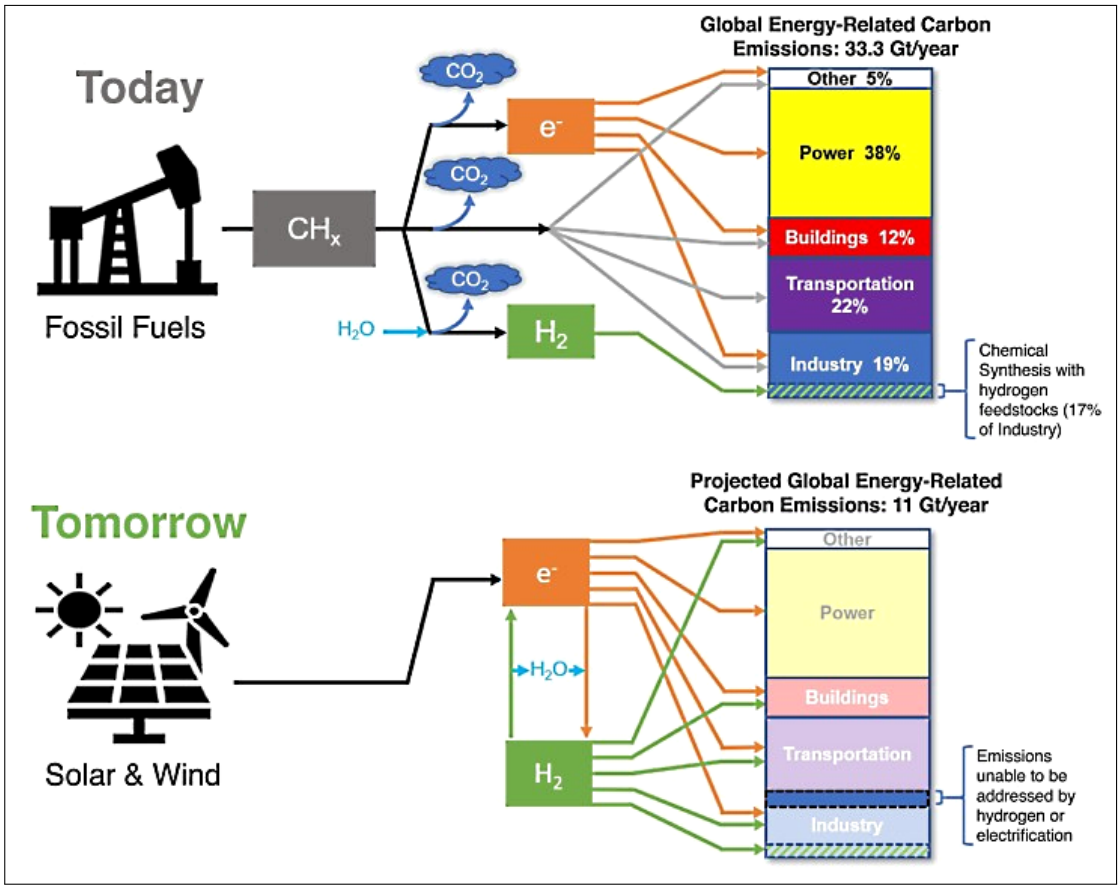


Figure 1.1: A simplified overview of how the current use of fossil fuels generates greenhouse gases. It also demonstrates how potential sustainable energy and hydrogen use(from water electrolysis) can provide a carbon-neutral replacement infrastructure. This figure does not include the CO_2 emissions related to using methanol as a hydrogen carrier. Figure used with permission from: A. M. Oliveira, R. R. Beswick, Y. Yan, *Current Opinion in Chemical Engineering*, 2021, **33**, 100701. ©2021 Elsevier Ltd.

Novel high-pressure tanks can store hydrogen gas at 450 bar making them a reasonable size for mobile vehicle applications however they still only achieve 4 % weight of hydrogen and the pressure drop on accessing the fuel presents considerable risks. [5] Liquefying hydrogen requires an amount of energy equal to 20 % of the energy available from using the fuel; evaporation also loses a further 2 % of that energy daily. [6] This renders both on-board liquid and gaseous hydrogen storage as problems in the commercial performance of hydrogen-powered vehicles; however, such research fields have potential.

1.1.2 The case for MSR-PEMFCs

Certain materials, known as catalysts, are needed to react hydrocarbons with another species to produce hydrogen gas; such a reaction is known as 'reforming'. The reforming or gasification of hydrocarbons to produce H_2 would allow liquid (at room temperature and pressure) hydrocarbon fuel, that is compatible with current refuelling infrastructure, to be used as a 'hydrogen carrier' for on-board hydrogen production, mitigating the upfront cost that is associated with establishing new infrastructure. [7] However such processes produce CO_2 as a major product; nullifying the main purpose of using hydrogen fuel cells as a sustainable option. The extraction of the hydrocarbon precursors from biomass waste has the potential to offset the carbon footprint of the process. Alternatively, ammonia, NH_3, can be used as a hydrogen carrier in a hydrogen economy cycle that has the potential to avoid hydrocarbons whilst benefiting from much milder temperatures and pressures for liquefaction compared to pure hydrogen gas; however, to make such a cycle renewable and sustainable both the Haber-Bosch process and water electrolysis would need much milder conditions and higher yields, respectively (both areas are subject to ongoing research but are not covered in this work). [8–10]

Of the potential hydrocarbon precursors, methanol routinely provides relatively high hydrogen and low soot yields during reforming processes for hydrogen production; this originates from methanol's inherent high H:C ratio (4:1). [7, 11] The reforming temperature for methanol is also significantly lower compared to those of other hydrocarbons, due to the lack of C-C bonds that increase the reforming activation energy for other hydrocarbons. [12] Kamarudin et al. have researched the production of methanol from biomass waste via pyrolysis; the work suffered from low methanol yields and more recently, in a review, Gautum et al. cite feedstock logistics and economic-viability as large issues for methanol production from biomass. [13, 14]

Biomass-derived methanol is arguably further away from being commercial than on-board hydrogen storage but there are opportunities in this field as interest in the replacement of traditional oil refineries, with 'biorefineries', is growing; such research aims to convert waste into key chemicals efficiently utilising novel catalysts and processes. [15] More significantly, in recent studies a ship propulsion system has been proposed that synthesises methanol from the electrolysis of sea water and captured carbon dioxide, this methanol is then reformed to provide on-board hydrogen for a fuel cell; the resultant carbon dioxide from reforming is captured and re-used for the initial electrolysis (see Figure 1.2). [16] Therefore, the exploration of methanol as a hydrogen carrier may have some potential and is worthwhile.

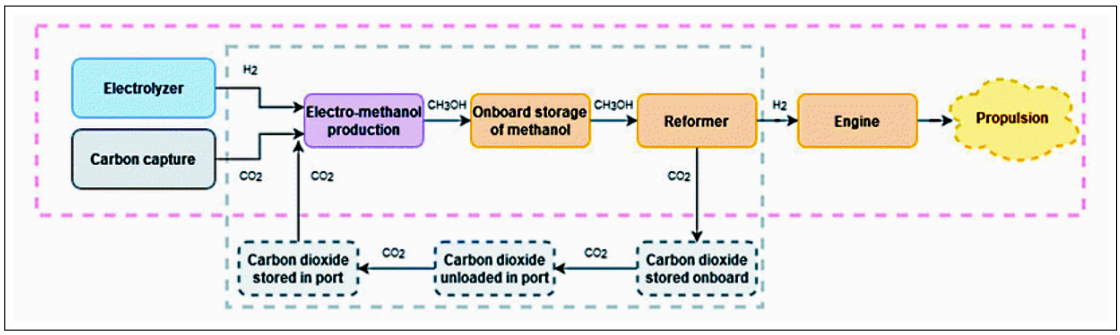


Figure 1.2: A proposed system for fuelling a ship with electrolysed water and captured CO_2 via methanol reforming. Figure used with permission from: E. Malmgren, S. Brynolf, E. Fridell, M. Grahn, K. Andersson, *Sustainable Energy & Fuels*, 2021, **5**, 2753-2770.©2021 Royal Society of Chemistry.

There are multiple reforming methods but methanol steam reforming (MSR) inherently produces the least carbon monoxide (CO) via side reactions due to the presence of water (see Section 2.7.1); MSR in literature has been performed at temperatures as low as 150 °C. [11,12,17] Low temperatures and CO outlet concentrations make MSR an attractive process for powering proton exchange membrane fuel cells (PEMFCs) aboard small vehicles. The operation of such cells involves splitting H_2 into protons, H^+, that are then transported across a hydrated membrane to the cathode where they react with O_2 to form water; an overview is shown in Figure 1.3. [18]

PEMFCs typically operate at < 80 °C because the polymer electrolyte membrane has to be hydrated (below water's boiling point) and to not exceed the membranes' glass transition temperatures (where they would lose their structure/functionality). [19] Hydrocarbon reforming often occurs at > 200 °C, so this temperature has to be minimised if MSR is to be efficiently used in conjunction with a PEMFC. An additional problem is that > 10 ppm of CO in a H_2 gas feed is enough to severely diminish a PEMFC's activity because the platinum electrode strongly adsorbs CO; which would block sites for the reaction of H_2. [20–22]

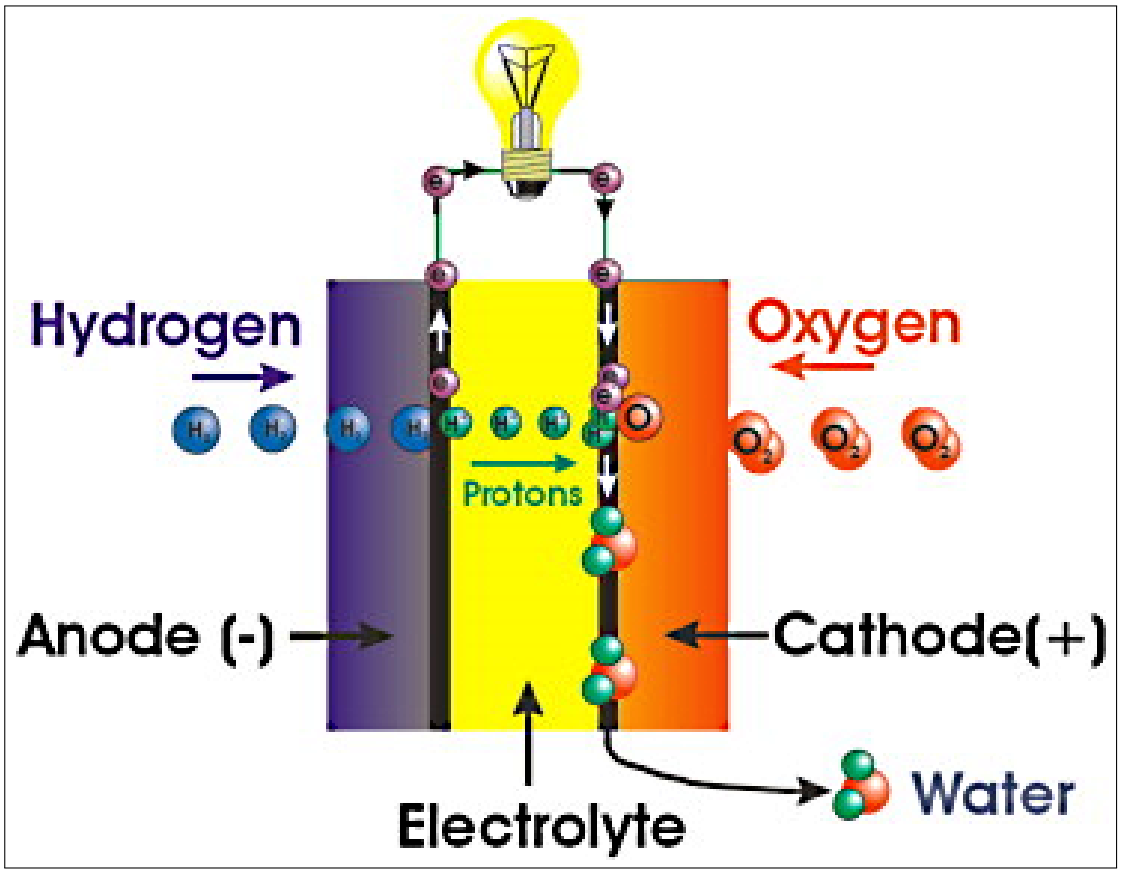


Figure 1.3: A simplified schematic of a PEMFC. It depicts how hydrogen electrochemically reacts at the anode, how electrons and protons are conducted separately and the resultant, water-generating reaction at the cathode. Figure used with permission from: S. J. Peighambardousta, S. Rowshanzamirab, M. Amjadia, *International Journal of Hydrogen Energy*, 2010, **35**, 9349-9384. ©2010 Elsevier Ltd.

1.2 Goals of this work

Issues with biomass-derived methanol production aside, the main issues with using MSR to fuel PEMFCs are often: i) the catalyst operating temperature far exceeds that of a PEMFC, meaning additional heating would be required in a MSR-PEMFC system beyond the operating temperature of the PEMFC (energetically inefficient); ii) the CO concentration is many orders higher than 10 ppm and therefore post-MSR CO oxidation catalysts would be required (reducing efficiency in terms of materials and energy); or iii) at lower temperatures, the activity is too low to power even a handheld device. The goal of this work was to develop MSR catalysts that could maximise the H_2 production and H_2:CO ratio, whilst minimising the required reforming temperature.

In this work a metric, the H_2:CO ratio, was used to standardise and compare MSR catalysts from across different research papers (that were reported using different units); subsequently, important catalyst traits were reviewed and identified. Using this data as a guide, various novel catalyst series were planned and synthesised; finally, the performance of these materials was tested, analysed and critiqued.

Chapter 2

Fundamental concepts

This chapter briefly explains scientific concepts that will be important throughout this work. Readers familiar with methanol steam reforming catalysis and materials chemistry can proceed to Chapter 3.

2.1 Energy and reactions

Whether a chemical reaction or process can occur under specific conditions (happen spontaneously) is determined by the Gibbs free energy change, ΔG, which is calculated as: $\Delta G = \Delta H - T.\Delta S$; where T = temperature (in Kelvin only), change in enthalpy = ΔH, and change in entropy = ΔS. [23] When $\Delta G < 0$ the process happens spontaneously; therefore, both entropy and enthalpy need to be considered when trying to explain reactions.

The overall energy change of a reaction may be net favourable and have $\Delta G < 0$ but the initial energy cost of breaking the original bonds is known as the 'activation energy'. [24] This energy needs to be provided for the reaction to occur and often has to be provided via thermal energy from the environment; therefore, the 'rate' of a chemical reaction increases with an increase in temperature and decreases with an increase in the required activation energy. [24] Activation energies coincide with peaks in potential energy caused by unstable, transient chemical structures, known

as transition states; such species can never be isolated.

2.1.1 Electronegativity and polarisability

Electronegativity is a parameter that can be experimentally measured, according to various conventions, but is always used to quantify the 'power' a given atom has to attract an electron. [25] This allows for the relative comparison of different elements without having to individually consider all the multiple factors that dictate interatomic electrostatic interactions. Typically electronegativity decreases from right to left and top to bottom across the periodic table, see Figure 2.1; the Pauling scale is a commonly used electronegativity scale. [26]

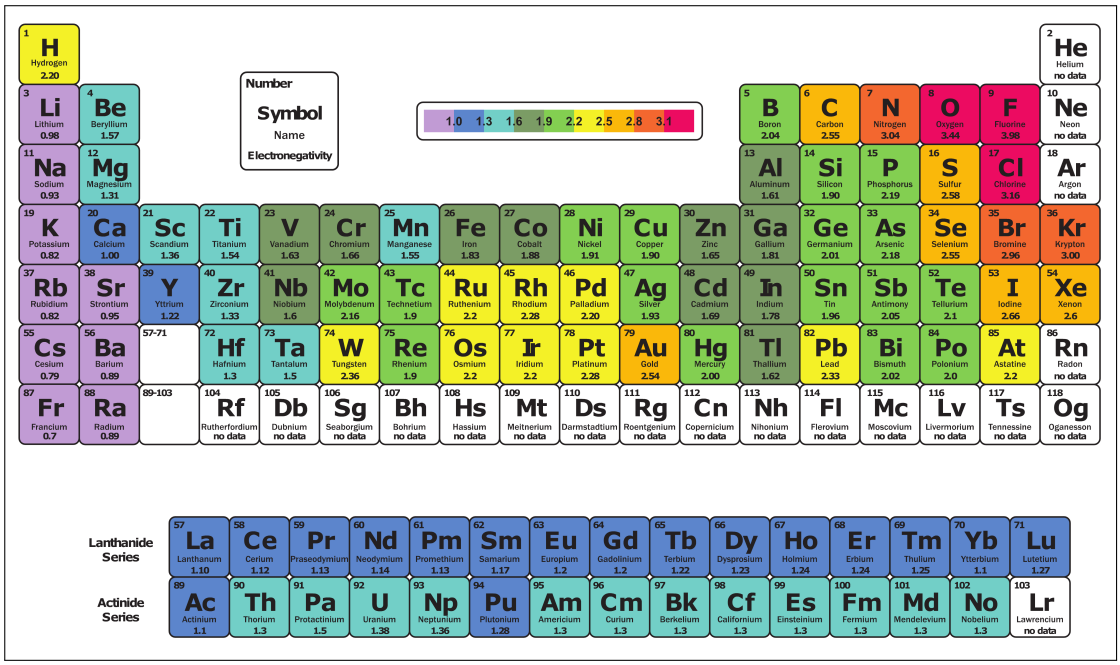


Figure 2.1: Pauling electronegativity of the periodic table. Figure used with permission from: *https://sciencenotes.org/list-of-electronegativity-values-of-the-elements/* (Accessed:13/12/2021).©sciencenotes.org.

Polarising power and polarisability are opposite quantitative parameters; like electronegativity, they are used to describe a combination of effects. The higher the polarisability of an atom/ion, the easier it is for an external charge (or dipole) to distort its electrons and orbitals; this causes a dipole to form in the distorted

ion/atom. [27, 28] Therefore, polarising power is a measure of an ion's ability to distort the electrons of another atom/ion (or 'induce' a dipole).

2.1.2 Lattice energy

Atoms can form lattices which are distinct repeating 3D structures that can form very large networks of bonds. [29] Pure metal atoms form simple close-packed lattices with metallic bonding orbitals that delocalise electrons over all of the atoms. [29] Oxidised metals can form various types of metal oxide: an example lattice is shown in Figure 2.2; the metal-oxygen (M-O) bonds can form various different angles and shapes. [30] Lattices are repeating structures but in reality 'defects' can disrupt these patterns; examples of defects are also shown in Figure 2.2. [30]

Enthalpies, entropies and Gibbs free energy changes can be associated with all types of chemical reactions and changes in bonding/interactions. Lattice enthalpy and lattice energy are the change in enthalpy or potential energy, respectively, of the following process: $MX(s) \longrightarrow M^{+}(g) + X^{-}(g)$; which involves the dissociation of a metal (M) cation and anion (X) solid lattice into the component gaseous ions. [31] Lattice enthalpies and energies are often very similar in terms of the energy per mol of lattice ($kJ.mol^{-1}$) and are often used interchangeably (even though strictly they should not be). [31] These values are always positive because a large amount of bonds and favourable electrostatic interactions have to be broken to break the lattice; moreover, lattice enthalpies or energies are good descriptors of a lattice's thermal stability and average bond strength.

Lattice enthalpy differs from 'enthalpies of formation' but the two enthalpies can be linked by Born-Haber diagrams (see Figure 2.3). [32] Born-Haber cycles can be used to calculate various enthalpies associated with a reaction depending on what enthalpies can be isolated and experimentally calculated. To link formation and lattice enthalpy, various ionisation and electron affinity enthalpies are required. [31]

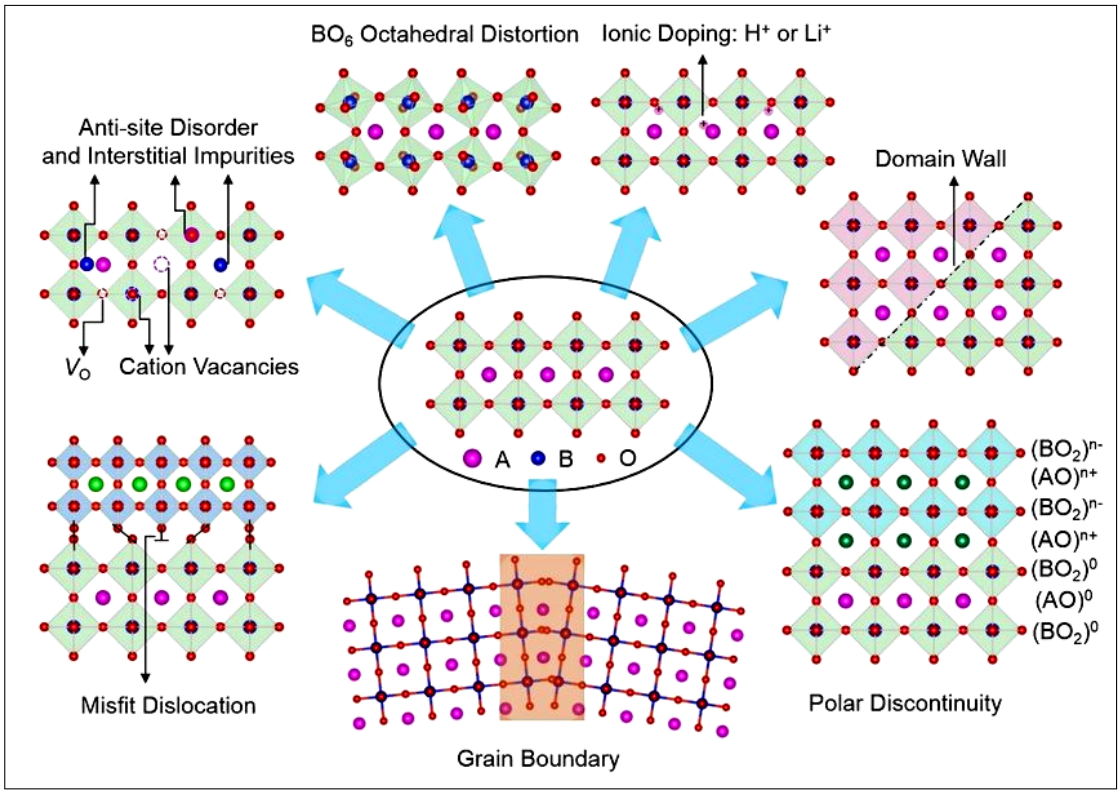


Figure 2.2: An example metal oxide lattice is displayed in the centre oval, where A,B = different metals and O = oxygen. The light blue arrows point to various scenarios in which defects can form within metal oxides or between two phases of different metal oxides. Figure used with permission from: W. Li, J. Shi, K. H. Zhang, J. L. MacManus-Driscoll, *Materials Horizons*, 2020, **7**, 2832-2859.©2020 Royal Society of Chemistry.

2.2 Unit cells and Miller indices

The simplest repeatable group of ions/atoms in a lattice that can be related by translation is referred to as a 'unit cell'; subsequently the dimensions and angles in a unit cell can dictate the behaviour and chemical reactivity of the larger lattice. [33] Unit cells are 3D and have the dimensions a, b and c (instead of x, y and z); unit cells usually adopt one of 14 'Bravais lattice' types, see Figure 2.4. [34, 35]

Within unit cells there can be repeatable planes formed by atoms or species of a given type, this has implications in analysis such as X-ray diffraction (see Section 5.3.1). Such 'Miller indices' planes are denoted with (h k l) which assigns where

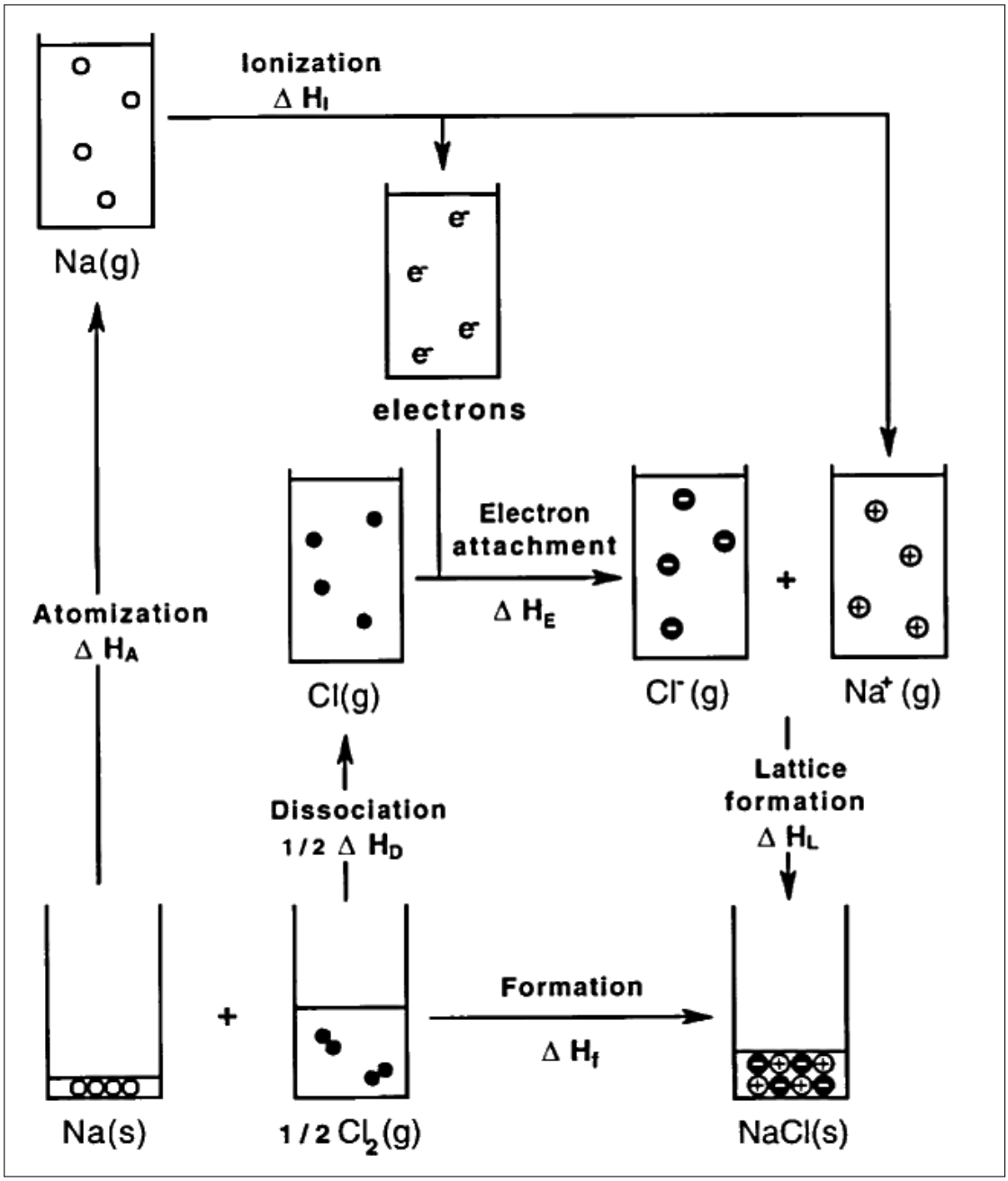


Figure 2.3: The Born-Haber cycle of NaCl; ΔH_L corresponds to lattice enthalpy and ΔH_f corresponds to the standard enthalpy of formation. Figure used with permission from: R. S. Treptow, *Journal of chemical education*, 1997, **74**, 919.©1997 American Chemical Society.

each unit cell axis is intersected by the plane with a reciprocal number. [33] For example, the a axis is intersected by a repeating plane at its halfway point, the b axis is intersected into thirds, whilst the c is perpendicular to the plane in question,

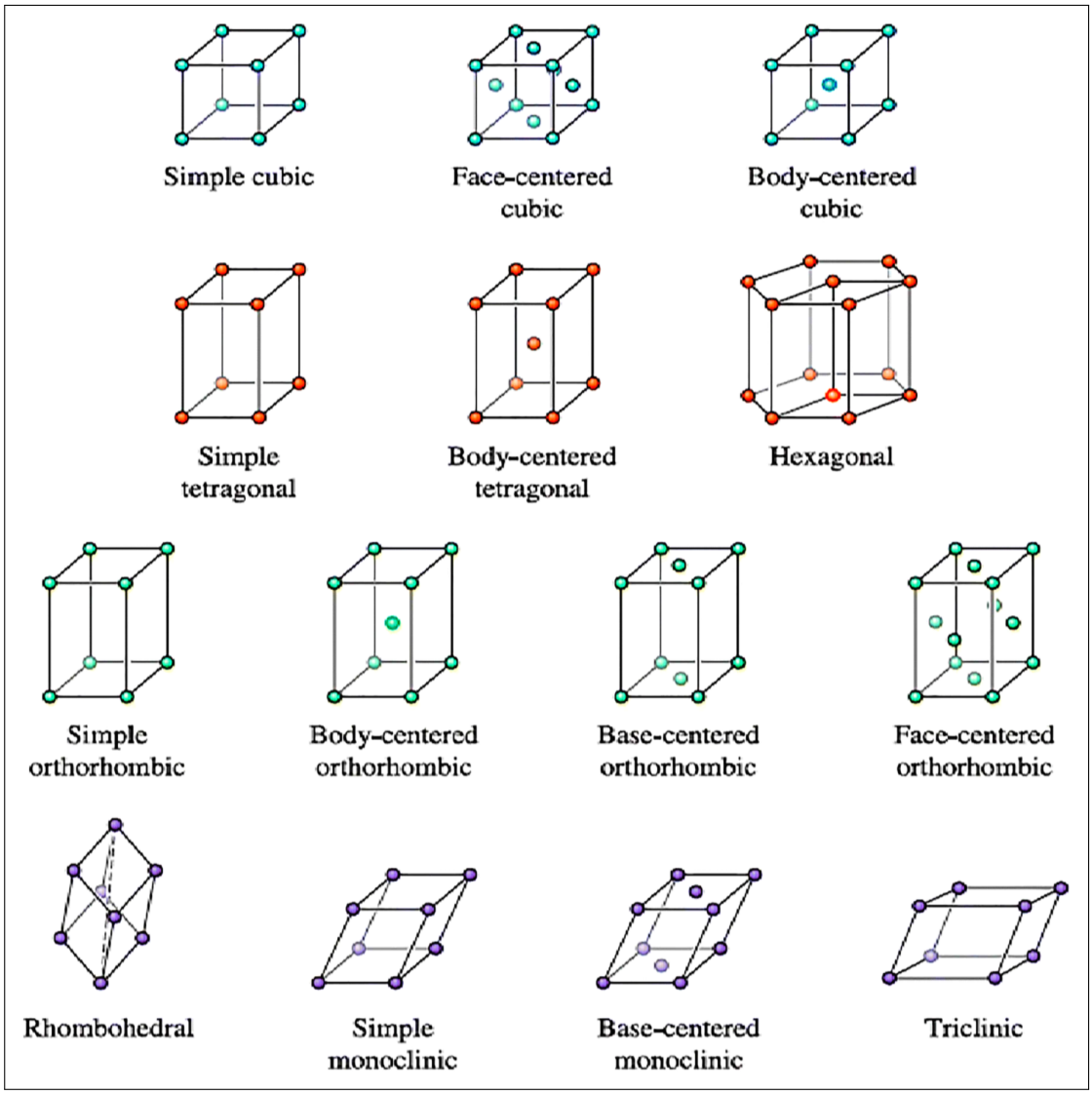


Figure 2.4: The 14 Bravais lattices; the coloured dots represent atoms or monoatomic ions. Figure used with permission from: E. Ameh, *The international journal of advanced manufacturing technology*, 2019, **105**, 3289-3302. (The figure was based off the work: D. Askeland, P. Fulay, W. Wright, *The Science and Engineering of Materials*, 6^{th} Edition, 2011.)

assuming the unit cell dimensions are all equal (a, b, $c = 1$), the plane is labelled as follows: $(h\ k\ l) = (\frac{a}{2}, \frac{b}{3}, \frac{c}{\infty}) = (2\ 3\ 0)$. Figure 2.5 depicts examples of such planes and their Miller indices. [36]

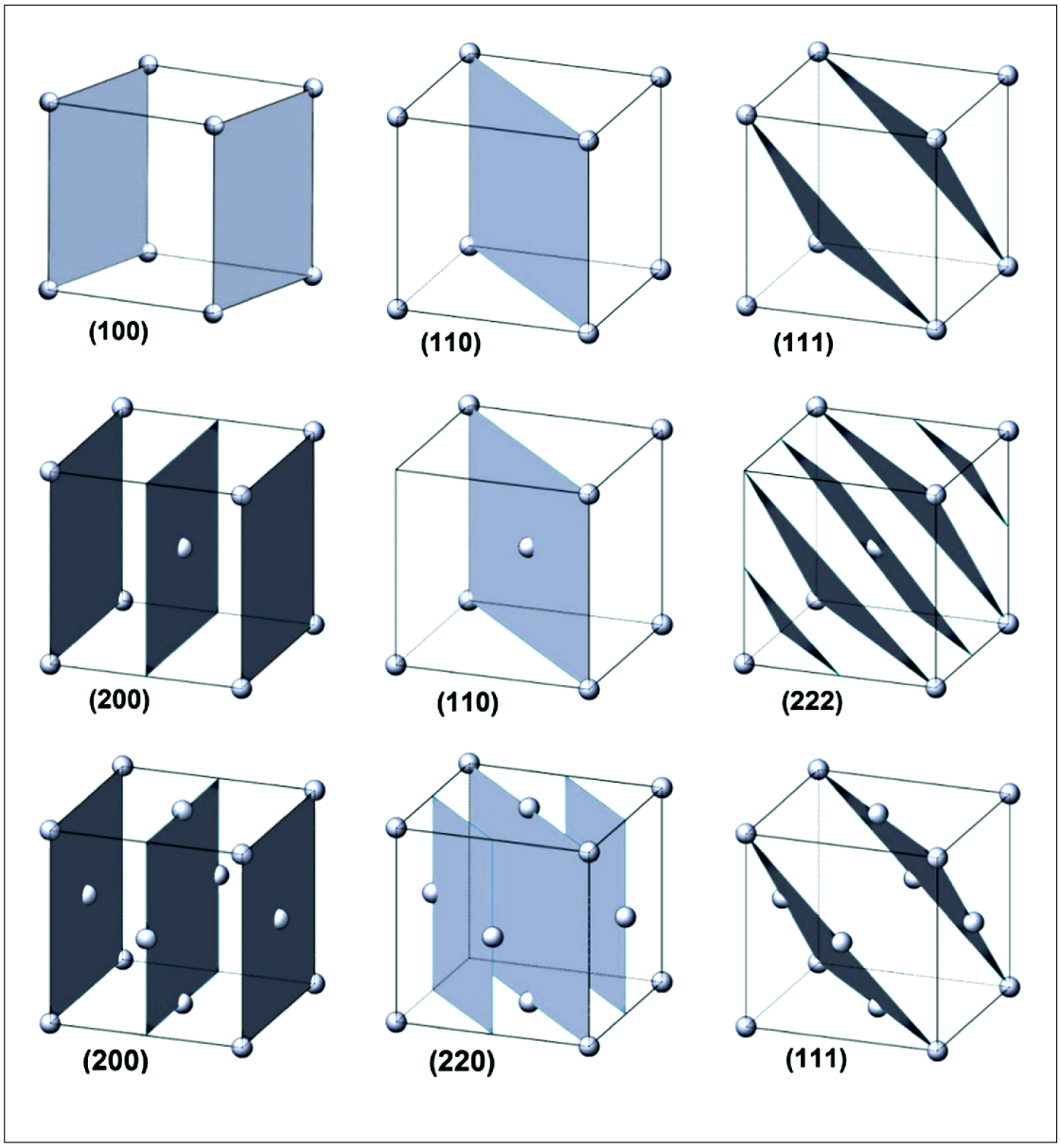


Figure 2.5: Nine different examples of Miller indices. Figure used with permission from: M. Wahab, *Numerical Problems in Crystallography*, Springer, 2021, pp. 137–178.©2021 Springer Nature Ltd.

2.3 Coprecipitation

Solids can be dissolved in liquids e.g. an ionic species like NaCl (s), table salt, can dissolve in water (the ions 'dissociate'), which would be written as: $NaCl(s) \longrightarrow Na^{+}(aq) + Cl^{-}(aq)$ (where aq stands for aqueous, or dissolved in water). When an

ionic compound dissolves, all the ionic bonds break and new electrostatic attractive forces form between dipoles from the liquid molecules and the charged dissociated ions; as always there are enthalpic and entropic considerations for whether a species is soluble in a certain liquid or solvent. [37]

Precipitation reactions occur between two chemical species that are both dissolved in the same liquid solvent, one of the products of the reaction is insoluble in the solution and therefore 'precipitates' out of the solvent as a solid. [38] Coprecipitation is where multiple reactants are used to cause the precipitation of a product that usually has a relatively complex lattice and contains various elements, cations and anions. This technique is useful in the preparation of catalysts (see Section 2.5), which make use of various metallic elements to improve chemical reactions in various ways, without being used up.

2.4 Adsorption

Solid catalysts prepared by coprecipitation can interact with other chemical reactions that happen in the liquid or gas phase, due to a phenomenon known as adsorption. Adsorption is when a molecule or species 'sticks' to a solid surface.

'Physisorption' is when adsorption is caused by intermolecular forces (such as dipole-dipole interactions and van der Waals forces) and can occur at low temperatures because no bonds need to be broken to allow the interaction to take place. [39] 'Chemisorption' is where a bond forms between the surface and the adsorbing molecule (adsorbate); this requires bonds and electron sharing interactions in the adsorbate and/or the surface to break i.e. chemisorption occurs at higher temperatures than physisorption due to the increased activation energy cost (see Section 2.1). [39]

Despite the difference in the ΔH (interaction strength) of the different adsorption types, if the thermal energy of the system is enough to provide the activation energy

for adsorption it is enough to provide the activation energy for desorption as well; therefore, the rate of desorption is temperature dependent. [39] More on adsorption analysis and assumptions is discussed in Section 5.6.1.

2.5 Heterogeneous catalysis

Reactions can involve several steps of various bonds being formed and broken, each step has an associated activation energy and transition state chemical structure. Catalysts speed up chemical reactions and allow them to occur at lower temperatures without the catalyst being consumed, they can also change the selectivity preference of the potential products; this is called 'catalysis'. [40] They do this by reacting with the starting reagents over several steps, the catalyst is not used up because in the final step of the 'catalytic cycle' the catalyst is one of the products of reaction; it is regenerated. Catalysts speed up the reaction and alter the preferred product because they can lower certain activation energies by energetically-stabilising transition states; this is often done via electron withdrawing or donating effects. Sometimes catalysts can introduce new reaction pathways by introducing transition states with geometries and bonds that would not be possible in the absence of the catalyst.

Specifically, heterogeneous catalysis refers to situations where the catalyst is a different state of matter to the reactants. In this work solid catalysts are used to catalyse gas-phase reactions; this is made possible by adsorption. [39]

The rate of a catalysed reaction or the catalysed production of a specific product is called the catalyst's 'activity' and the parameter can be used to compare catalysts; it is usually given as mols of reactant converted or product produced, per time, per mass or mol of catalyst.

2.5.1 Rate-determining step

In Section 2.1 activation energy and reaction rates were briefly introduced; the

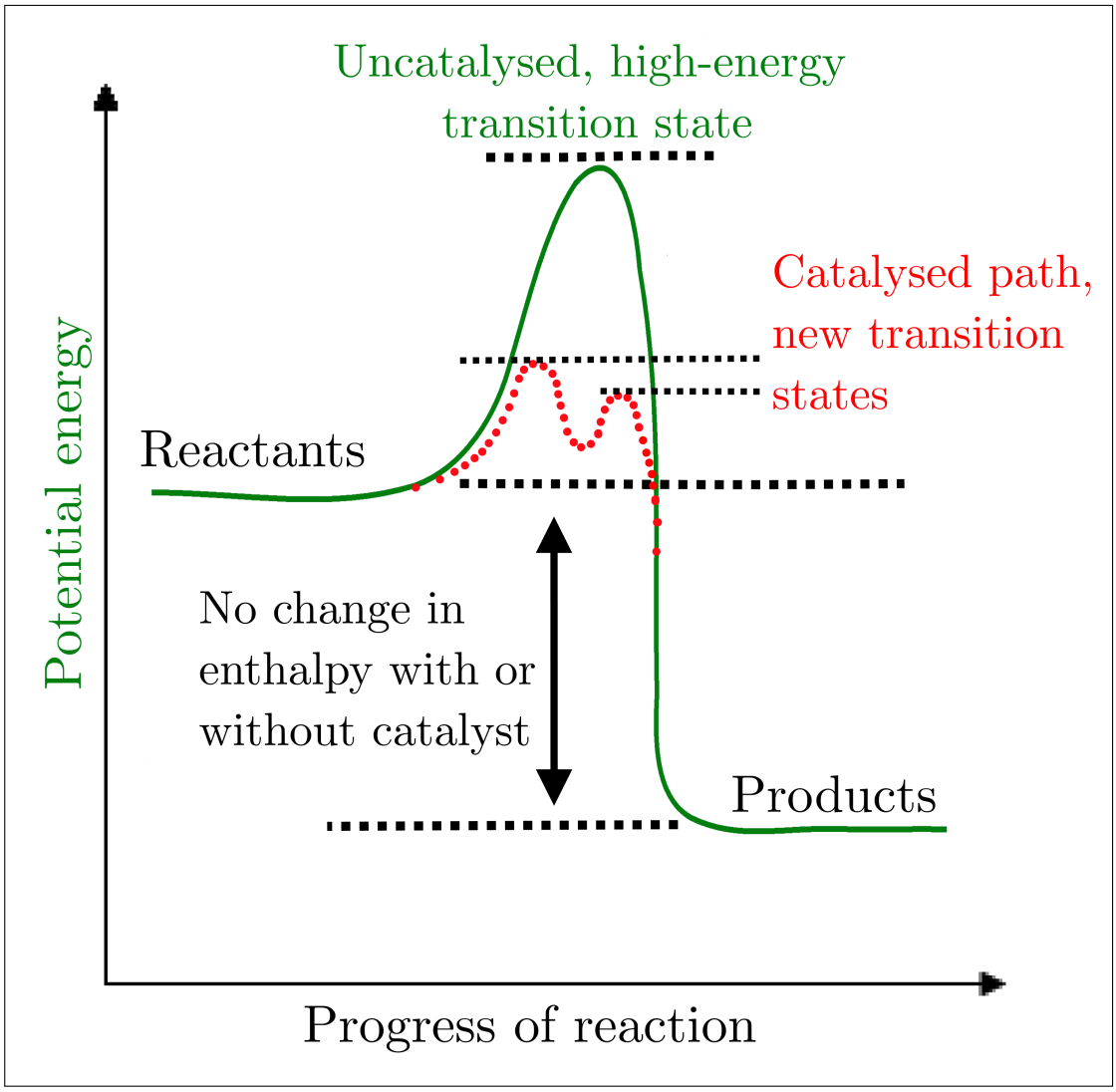


Figure 2.6: An exothermic reaction (green line) and how a catalyst can affect the activation energy and reaction pathway (red dotted line). In this simple example, the catalyst stabilised the transition state and introduced a new transition state. Figure made using paint.NET® and Inkscape®.

dependence of the rate of reaction on temperature and activation energies were discussed. Over the course of a reaction, multiple activation energies may be required to proceed to the next step(s); however, if the highest activation energy can be achieved due to external energy from the system (such as thermal energy), then all of the activation energies can be achieved. [24] This means that the rate of a reaction is only dependent upon one activation energy, the highest one, and the associated reaction

step is known as the 'rate-determining step' (RDS). [24]

A catalyst has to stabilise the RDS transition state to increase the speed of a chemical reaction or introduce alternative transition state(s) that are lower in energy than the RDS transition state. Often assumptions are used where the rate of reaction is only dependent on the RDS and no other step rates, however not all reactions have a RDS and this assumption breaks down; exceptions occur when multiple reaction steps have very similar activation energies.

2.5.2 Catalysis and equilibria

Equilibrium occurs when a chemical reaction and the exact reverse reaction are occurring at equal rates (it is represented as a $\rightleftharpoons$ arrow in chemical equations); the concentrations of all involved reactants/products do not have to be equal. [41] The initial rate in which equilibrium is reached depends on the rates of reaction and, therefore, the temperature, RDS and activation energies.

Le Chatelier's principle states: "when an external change is made to a system in dynamic equilibrium, the system responds to minimise the effect of the change". [41] Therefore, if one reaction increases in rate, the other reaction will increase in rate to minimise the change in the reactant concentrations and a point of equilibrium will be reached where the forward reaction rate equals the backwards reaction rate. [41] A 'shift' in equilibrium position is said to occur when the ratio between the relative concentrations of the two sides of the reaction changes in favour of one of the reaction directions. Due to Le Chatelier's principle, the equilibrium position is dictated by the enthalpy of each direction, entropy of each direction, the conditions of the reaction system and the presence of other chemical species.

Equilibrium reactions occur via the same transition states in both directions, therefore catalysts theoretically increase rates for both directions and the rates remain

equal. 'Microreversibility' is a principle that states: "under equilibrium conditions, any molecular process and the reverse of that process will be taking place, on average, at the same rate". [42] This is true for simple equilibria but this principle can be broken during some catalytic reactions e.g. in the water gas shift reaction (see Section 2.7.1). [43] The microreversibility principle assumes the catalyst is exactly the same for forward and backward steps; exceptions to the rule usually occur because the local surface of a heterogeneous catalyst can change with reactant concentrations, especially when multiple different chemical processes can happen on the catalyst surface. [43,44]

Often a constant relative flow of reactant gases are passed over a stationary heterogeneous catalyst, which constantly replaces the gases in the heated reactor environment and adsorbed to the catalyst; this does not allow an equilibrium to be reached in the catalysed reactions. The slower the flow of reactants, the longer each given molecule spends in the reactor (an increased 'residence time'); allowing the reaction rates to shift closer towards those at the equilibrium point. [45] Therefore, in heterogeneous catalysis many factors have to be considered to optimise the selectivity and rate of the catalysed reaction, including: flow rates of the reactants, pressure of the system, volume of the system, surface area of the catalyst, theoretical equilibrium points and the possible configurations of the catalyst surface under varying conditions.

2.5.3 Nanoparticles

'Nanomaterials' are made of nanoparticles that have at least one dimension that is between 1 - 100 nm long. [46] Nanoparticles of pure metals or alloys are often synthesised for use as heterogeneous catalysts and are the focus of this section. Metal nanoparticles can be synthesised both in solution or in the vapour phase via various techniques but in these cases the conditions must be carefully controlled because the particle's size is very sensitive to conditions such as temperature, pH and other reactant concentrations; this is due to their stability. [46] Some nanoparticles can be

suspended in solution but in solid heterogeneous catalysts the nanoparticles exist 'on top of' another phase, known as the support. [46] Supported nanoparticles are shown in Figure 2.7. [47]

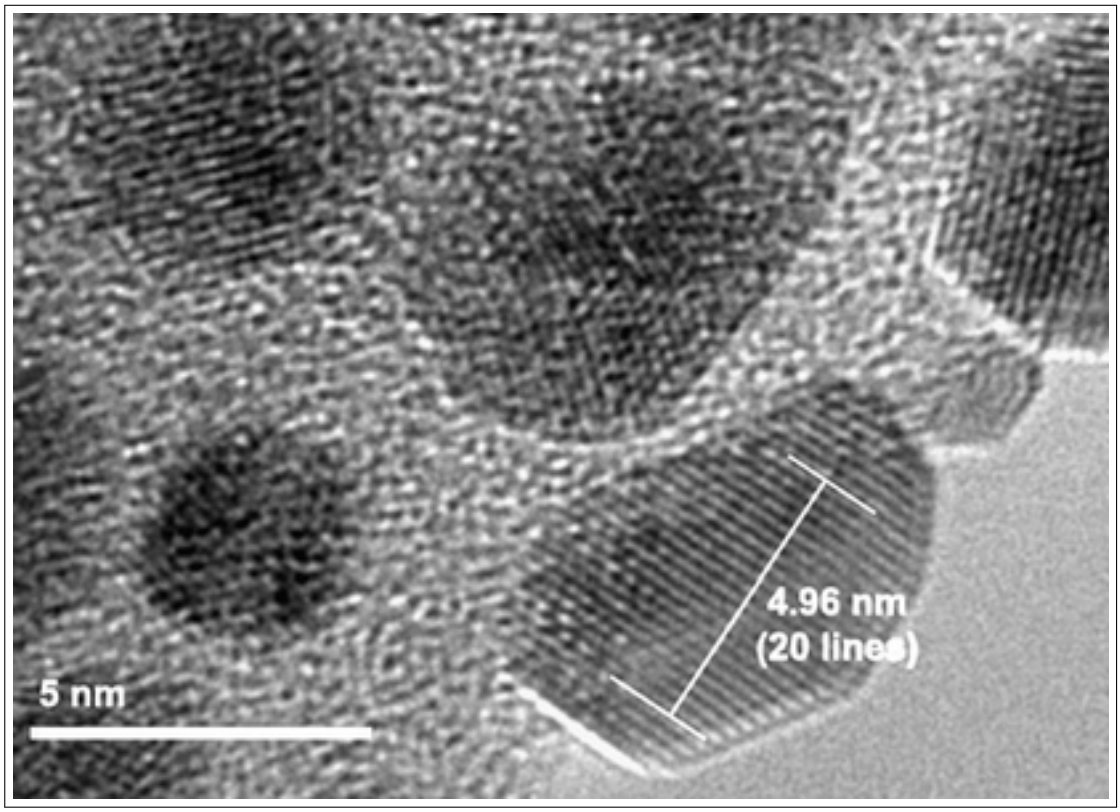


Figure 2.7: Gold metal nanoparticles supported on titanium dioxide, one nanoparticle can be seen to be 4.96 nm thick, equivalent to the diameters of ≈ 12 gold atoms in a plane (assuming room temperature and a face-centered cubic structure). The image was taken by a high-resolution transmission electron microsope. Figure used with permission from: M. Abd Elmoula, E. Panaitescu, M. Phan, D. Yin, C. Richter, L. H. Lewis, L. Menon, *Journal of Materials Chemistry*, 2009, **19**, 4483-4487.©2009 Royal Society of Chemistry.

In this work, coprecipitation is used to synthesise a metal oxide containing various different metal cations; then a low-temperature reduction process is used to react one of the constituent metals with H_2 so only that type of metal is reduced and leaves the lattice to form pure metallic nanoparticles. Metallic nanoparticles are bound together with metallic bonding as with large particles of metal; however, nano and large metal particles have very different reactivity due their surface areas and

coordination environments.

An ion or atom is coordinatively 'saturated' when it has formed its optimal number of bonds i.e. the electron density in its orbitals is arranged in the lowest potential energy configuration. Of course, this can be different depending on the ion's charge, nucleus size and outer, energetically-accessible (or valence) orbital size. [29,48] In a solid lattice some ions/atoms are on the surface whilst the others are said to be in the interior or 'bulk' of the material. Species in the bulk can form bonds in every direction and are often coordinatively saturated because the formation of a strong, optimal bonding network likely drove their initial formation with a large negative ΔH value. Compared to bulk lattice positions, surface atoms/ions have less neighbouring atoms/ions and, therefore, cannot form as many bonds causing them to be coordinatively unsaturated; the fewer bonds a surface atom has with its neighbours, the less stable it is (or it is said to have higher surface energy). [49] This is still applicable for metallic bonding cases because the ions' orbitals need to overlap to delocalise the bonding electrons; in surface atoms they cannot use all orientations of their orbitals as efficiently to accept and donate this electron density (this is equivalent to less 'bonds' forming). [50, 51]

Surface atoms have outward facing orbitals that can interact or accept electron density with minimal activation energy requirements, in terms of the amount of metallic bonds needing to be broken before new bonds can be formed. No matter the size of the metal particle, there will always be surface atoms but for a particle to form there needs to be an overall negative ΔG of formation due to the bonds formed in the bulk; the smaller the metal particle, the less negative its ΔH of formation (per mol, kJ.mol^{-1}). To summarise, surface atoms are coordinatively unsaturated, meaning they can form bonds with other species without the need to break any of their current bonds (or at least completely) to their solid lattice neighbours; this causes

metal surfaces to have high reactivity due to their reactions having lowered required activation energies.

Smaller particles of metal will have a higher reactivity, per mol of metal, than larger particles of the same metal phase for the same reaction; this is because the surface:bulk atom ratio in the smaller particle is higher. When a particle has corners and edges it is 'faceted', these corners and edges have even lower coordination numbers than the other surface atoms and are, therefore, more reactive. [39]

In heterogeneous catalysis, reactants adsorb and react on metal particle surfaces at certain positions called 'active sites'; therefore, catalysts with smaller metal nanoparticles, higher measured surface areas and higher surface:bulk metal ratios (higher metal 'dispersion') will have a higher activity because more reactions can occur per second per metal active site. [39] Metal (M) dispersion, $\mathrm{D}_M = \frac{Surface\ M\ mol}{Total\ M\ mol}$.

2.5.4 Catalyst deactivation

When a metal nanoparticle is acting as a catalyst it can lose activity in a number of ways. Various reaction conditions can alter the particle by oxidising or reacting with the metal in a way that does not regenerate the catalyst. Some adsorbates can bind so strongly to a surface, it can be effectively permanent depending on the conditions; this is known as 'poisoning'. Reactions can deposit a range of hydrocarbons, called 'coke', on the surface that adsorb to the surface but do not react; in both these scenarios less catalytic active sites are available and the catalysed reaction's rate drops. All three situations reduce catalyst activity, deactivating them, and can be dependent on a specific set of conditions or reactions. [52] The aggregation of nanoparticles, involving their movement across the support surface caused by thermal energy, is common in nanoparticle-catalysed reactions at elevated temperatures; however, some catalysts are specifically designed to resist this.

Thermally-induced metal surface area loss is known as 'sintering'. [53] The increased temperature allows attractive forces between the nanoparticle and support to be overcome; atoms or entire particles can move across the support surface, these types of sintering are known as atomic migration (Ostwald ripening) and crystallite migration, respectively. [54] The temperature at which sintering begins to occur can be related to the metallic bonding strength in the metal nanoparticle, which can be linked to that metal's melting temperature. The Hüttig and Tamman temperatures are a third and a half, respectively, of a given metal's melting temperature. [54] The Hüttig temperature estimates the temperature at which atomic migration begins to occur and the Tamman temperature estimates the beginning of crystallite migration. [54] These can act as estimates but properties like the particle/surface shapes and the metal-surface attractive interactions also have a large effect on sintering. The smaller the nanoparticle, the weaker its metallic bonding per atom because a higher percentage of atoms are on the surface and not in the bulk; this leads to a decrease in the effective melting temperature of the metal nanoparticle, and subsequently a decrease in the temperatures at which sintering begins. For nanoparticles that are roughly < 10 nm in diameter this can be significant; nanoparticles of In, Pb, Bi, Sn and alloys of them are seen to have a ≈ 10 - 40 % decrease in their melting temperature when the nanoparticle size decreases from ≈ 10 to 3 nm (Figure 2.8). [55] Figure 2.8 also shows similar situations for Au and Cu nanoparticles. [56, 57]

The overall trend is that sintering will increase with temperature and the time spent at that elevated temperature. The increased temperature provides the activation energy for sintering whilst the thermodynamic driving force for sintering can be considered as the negative ΔH change associated with more surface metal atoms forming metallic bonds and becoming part of the bulk. Sintering can deactivate a catalyst because the decrease in surface area can dramatically diminish the number of potential catalytic active sites. Sintering can also 'smooth' faceted particles to

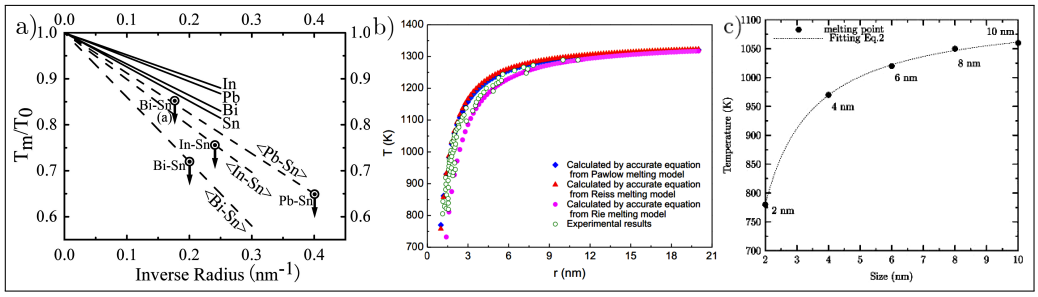


Figure 2.8: a) How the relative melting temperature (T_m/T_0) of In, Pb, Bi and Sn nanoparticles changes with nanoparticle size. b) How melting temperature (K) for Au nanoparticles changes with nanoparticle size. c) How melting temperature (K) for Cu nanoparticles changes with nanoparticle size. Figures used with permission from: a) C. Chen, J.-G. Lee, K. Arakawa, H. Mori, *Applied Physics Letters*, 2011, **99**, 013108.©2011 American Institute of Physics. b) J. Zhu, Q. Fu, Y. Xue, Z. Cui, *Journal of Materials Science*, 2016, **51**, 4462-4469.©2016 Springer Nature Ltd. c) H. H. Kart, H. Yildirim, S. O. Kart, T. Çağin, *Materials Chemistry and Physics*, 2014, **147**, 204-212.©2014 Elsevier Ltd.

stabilise the corner and edge atoms (lowering their surface energy) but sometimes such atoms provide the active sites; therefore, catalysts often have to be designed to avoid sintering. [58]

Oxygen vacancies (empty oxygen lattice positions at the surface) and oxygen adatoms (which are additional O^{2-} anions that are 'adsorbed' to the support) can interact with nanoparticles increasing the energy required to move across the surface, and therefore sinter. [59] Porous (including mesoporous) and layered support materials can physically separate particles to limit sintering. [58, 60]

2.5.5 Metal-support interactions

Increasing the attractive force between the support and metal nanoparticle increases resistance to sintering. [53] The strength of the M-O bonds the metal (M) nanoparticle makes with the support's O atoms (or strength of adhesion) correlates with increasing density of surface O, increasing metal nanoparticle oxophilicity and decreasing oxophilicty of the oxide. [61] 'Oxophilicity' is representative of an element's tendenacy to bond with oxygen. Dai et al. correlate it to the formation enthalpy of

that element's most stable oxide, per mol of the metal. [53] In scientific literature interactions between nanoparticles and their supports have been described with a wide range of additional effects, including: electrostatic forces; van der Waals interactions; and nanoparticle adsorption to defects, or areas of high surface energy, on the support. [62, 63]

The term 'strong metal-support interactions' (SMSI) has been previously used to describe interactions where the support forms a thin layer over the top of the metal nanoparticles; the mechanism of SMSI is much debated in literature but it has links to reduction of the support occuring at certain interfacial sites and a ΔH driving force from the overlayer reducing the surface energy of the system. [64, 65] More recently, the term 'electronic metal-support interactions' (EMSI) has described how bonding, orbital and electrostatic effects can tune the 'interface' on the surface between the metal nanoparticle and support to have unique catalytic activity. [65] van Deelen et al. describe metal-support interactions (MSI) more broadly because nearly any chemical property of the metal or support oxide can effect the other, their interface and the catalytic activity; Figure 2.9 displays the MSIs proposed by van Deelen et al. and effects that can be specifically targeted during the synthesis of supported metal nanoparticles. [58]

2.6 Reducible oxides

A metal oxide can be reduced, this involves the loss of oxygen, the formation of 'oxygen vacancies' and a reduction in the oxidation state of a lattice metal ion. [66,67] An oxygen vacancy is an empty lattice position that is on the surface that was occupied by an oxygen; ions adjacent to the oxygen vacancy become coordinatively unsaturated. Thermodynamically, low partial pressures of oxygen and high temperatures favour oxygen vacancy formation. [66] These conditions vary for reducing different metal oxides and a 'reducible' oxide is not quantitatively defined; however,

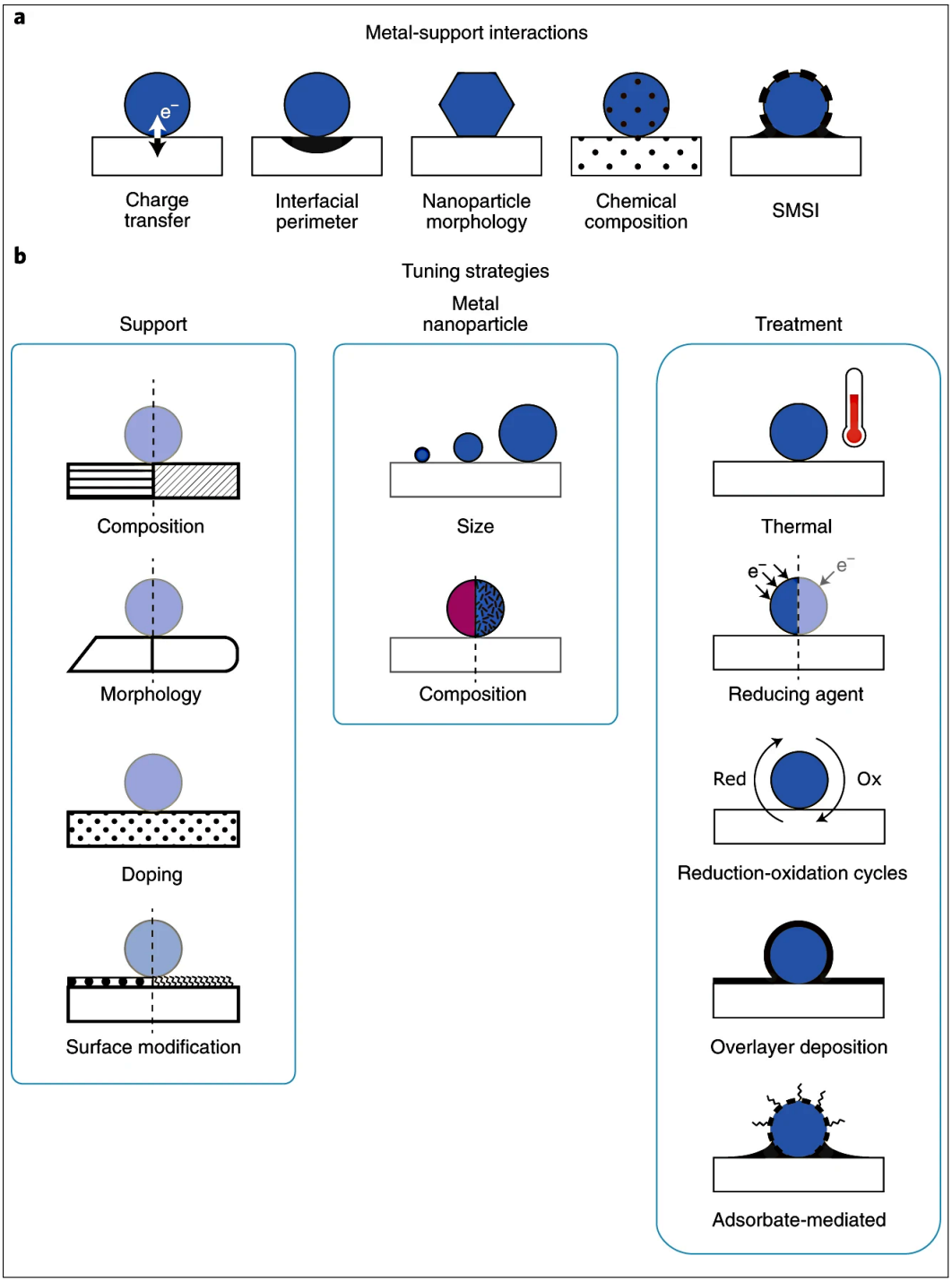


Figure 2.9: Examples of metal-support interactions and methods of tuning heterogeneous catayst's surfaces. Figure used with permission from: T. W. van Deelen, C. H. Mejía, K. P. de Jong, *Nature Catalysis*, 2019, **2**, 955-970.©2019 Springer Nature Ltd.

reducible oxides are reducible at relatively high oxygen partial pressures and low temperatures. [66] This can often allow a reducible oxide to act as an oxygen provider

or acceptor for catalytic cycles. [66] M-O bond strength, metal oxidation state stability and steric repulsion within oxides are determining factors in the reducibility of an oxide; these can be affected by dopants in lattices. [66, 67] The energy of vacancy formation inversely correlates with the ionic radius or polarisability of the dopant. [66] Oxygen vacancies expose metal cations and therefore electronegative species will strongly chemisorb to them; in fact, oxygen vacancies are theorised to play a role in many literature catalysts' performances. [66] Metal nanoparticles can donate electron density to reducible oxides at the metal-support interface to reduce the oxide and form an oxygen vacancy. [66]

2.7 Methanol steam reforming

The reaction of gaseous methanol and steam to produce carbon dioxide and hydrogen:

$$CH_3OH(g) + H_2O(g) \longrightarrow 3\,H_2(g) + CO_2(g)$$

The reaction is endothermic and its associated enthalpy, Δ H, is +49.7 kJ.mol^{-1}. [68] The change in entropy of the reaction is positive because there are double the mols of gas in the products than in the reactants. Overall the reaction is favoured at higher temperatures and if only thermodynamics are considered theoretically will spontaneously occur with 100 % methanol conversion between 100 and 450 °C (see Figure 2.10 below). [17, 69, 70] However, the activation energy kinetically limits the reaction.

Song et al. computationally estimated the rate of this reaction is 0 at 300 °C without a catalyst due to extremely high activation energies. [71] Lee et al. compiled various activation energies of catalysed MSR reactions and they are in the range of $\approx$ 75 - 120 kJ.mol^{-1}; Tong et al. catalysed MSR at 150 °C. [22, 72] This large difference occurs because catalysts provide a surface for the dissociative adsorption

of the reactants, in other words, in the same step as the initial methanol and water bonds break, new bonds can be formed via chemisorption to the surface. Whereas, in an uncatalysed reaction the activation energy is so high because bonds are only broken and it would leave gaseous, extremely-unstable, unsolvated anions.

2.7.1 Side reactions

In conditions where MSR is catalytically performed the water gas shift (WGS) equilibrium and methanol decomposition (MD) reaction will likely occur.

The WGS equilibrium has the following equation:

$$CO(g) + H_2O(g) \rightleftharpoons H_2(g) + CO_2(g)$$

WGS refers to the forward reaction (production of hydrogen) and the reverse water gas shift (RWGS) produces CO; this CO production is what causes issues when considering MSR systems as potential hydrogen carriers for fuel cell use.

RWGS is endothermic, $\Delta H = +41.2$ kJ.mol^{-1}, so at higher temperatures the equilibrium will shift to try and lower the temperature, in doing so it will favour the RWGS and the equilibrium concentration of CO will be higher. [68]

Methanol decomposition is also an unwanted side reaction because it produces CO, its equation is as follows:

$$CH_3OH(g) \longrightarrow 2\,H_2(g) + CO(g)$$

MD is endothermic, Δ H = +90.2 kJ.mol^{-1}; as with MSR the entropy change is positive because there are more mols of gas in the products than in the reactants. [68] Fortunately MD often has higher activation energies than MSR, WGS and RWGS and can be kinetically limited at lower reforming temperatures; but high temperatures and certain catalysts can cause MD to become a problem.

For the same reasons as MSR, the WGS, RWGS and MD reactions need to be catalysed on an active surface due to activation energy costs. [71] Xing et al. used com-

putational analysis to calculate the thermodynamics of a non-catalysed MSR reaction, taking into account other possible side reactions that could lead to formaldehyde or methane formation (these are typically high temperature reactions). [69] The results of Xing et al. are shown in Figure 2.10. [69] Computationally-calculated thermodynamic equilbria for MSR, WGS and MD are are also shown in Figure 2.11; the Figure provides a good example of how MSR and WGS are kinetically, not thermodynamically, limited as it shows that the calculated equilibrium values are not achieved experimentally at lower temperatures. [17]

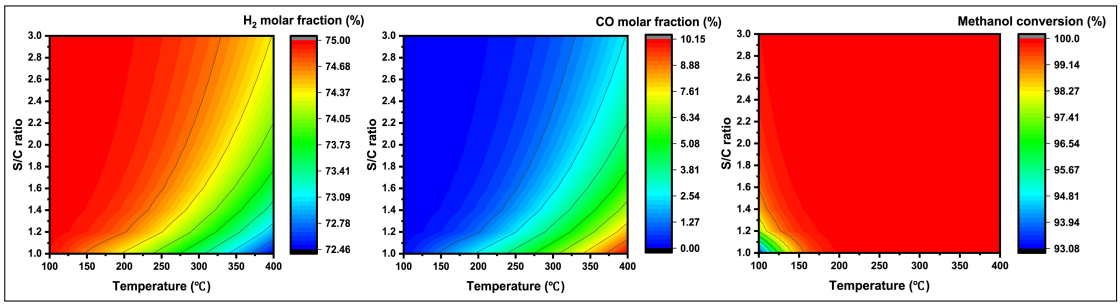


Figure 2.10: How the performance of a MSR catalytic system (H_2/CO molar fractions and methanol conversion) thermodynamically changes with S/C (steam:carbon or H_2O:CH_3OH) ratio and temperature. Figure used with permission from: S. Xing, C. Zhao, S. Ban, Y. Liu, H. Wang, *International Journal of Hydrogen Energy*, 2020, **45**, 7015-7024.©2020 Elsevier Ltd.

Figure 2.10 shows increasing the water to methanol concentration in the reactants can decrease CO concentrations in the products; however, this can have negative side effects. Such side effects are discussed in the next chapter, the literature review will also explore catalysed MSR, its side reactions and try and identify effective catalysts for achieving the goals of the work. An ideal catalyst would catalyse MSR but not the WGS equilibrium or MD to maximise the H_2:CO ratio.

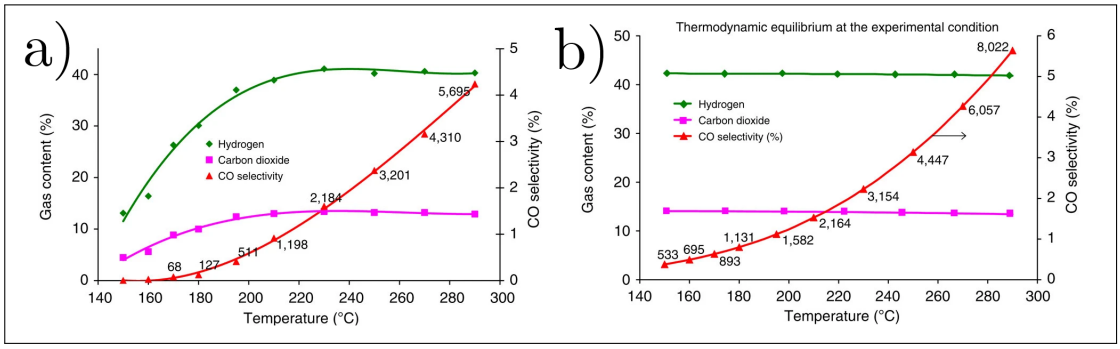


Figure 2.11: a) Observed experimental data for a $CuZnGaO_x$ catalyst under MSR conditions with a varying temperature and a 2:1 water:methanol ratio (the numbers next to the red triangles represent CO concentration in ppm). b) Thermodynamic calculations for the exact same experiment and conditions. Figure used with permission from: K. M. K. Yu, W. Tong, A. West, K. Cheung, T. Li, G. Smith, Y. Guo and S. C. E. Tsang, *Nat.Commun.*, 2012, **3**, 1-7.©Springer Nature Ltd.

Chapter 3

Literature Review

Several large chemical companies have previously produced catalysts intended for hydrocarbon reforming or low-pressure CO_2 hydrogenation; these often had Cu:Zn:Al molar ratios of ≈ 40-80:10-30:5-10. [73, 74] Lee et al. tested a 'commercial' MSR catalyst that had a molar ratio of Cu:Zn:Mg:Al of 64:24:10:2 and found the reaction rate to depend upon methanol and hydrogen partial pressures. [22] The catalyst produced 1 mol % CO; enough to severely poison a PEMFC. [22]

Sá et al. gathered data from 61 copper-based MSR catalysts (from 21 publications), this data showed only reaction temperatures > 240 °C achieve methanol conversions in excess of 80 % but this does not prove such conversions cannot be achieved at lower temperature; none of the catalysts tested below 240 °C had recorded BET surface areas above 30 $m^2.g^{-1}$. [75] Often these catalysts are prepared via coprecipitation or wet impregnation before being heat-treated (calcined) and then reduced with H_2 to yield metal nanoparticles supported on mixed metal oxides (MMOs).

This literature review aims to discern what properties cause an MSR catalyst to suppress CO formation whilst maintaining a high H_2 production.

3.1 MSR conditions used in literature

Primarily the research-scale reactor systems reviewed in this section comprise similar components. In order these are: a methanol/water liquid pump, a heated condenser (to get the reactants into the gas phase), an inert carrier gas, a catalyst between inert packing material in a furnace, a condenser and, finally, a gas chromatograph to quantify the product feed. An example reactor set-up is shown in Figure 3.1. [17] A gas chromatograph can analyse a discrete volume of the product feed in regular time intervals if known quantities of gas are calibrated at the pressure of the MSR conditions i.e. the amount of H_2, CO, CO_2, CH_4 and CH_3OCH_3 can be quantified.

Excess water (compared to methanol) can be used under MSR conditions to reduce the CO concentration in the products; this occurs because the WGS equilibrium position thermodynamically shifts, in line with Le Chatelier's principle, to favour the forward WGS reaction. This will increase the relative WGS rate compared to RWGS until equilibrium is reached, however, if the residence time is low enough, equilibrium will never be reached because an atmosphere with excess water is continuously being added to the catalyst system by the reactant flow; maintaining that the WGS rate is faster than the RWGS rate. However, this tactic would not be beneficial for a MSR-PEMFC system because having excessive water would decrease the overall energy efficiency by increasing the energy used by an evaporator to get the water into the gas phase; additionally, there would be a larger wt % of water in the product feed going to the PEMFC inlet that would need to be removed. [12, 19, 76]

When analysing literature catalysts it is important to take into account the temperature, water content, reaction time and reactant flow rate of the MSR catalytic system because these can affect the selectivity for MSR, MD and RWGS i.e. some catalysts may be lauded as highly selective MSR catalysts whilst it is the tempera-

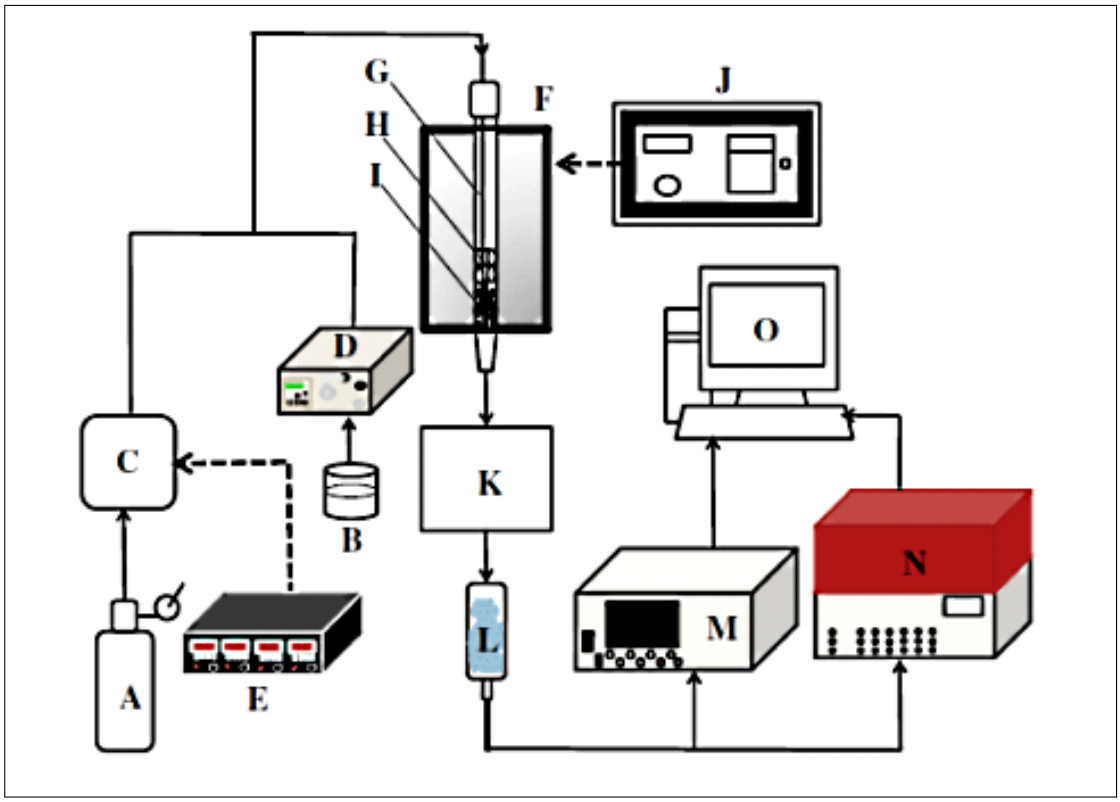


Figure 3.1: An example diagram of a standard, laboratory-scale MSR reactor. A) Carrier gas. B) H_2O:CH_3OH solution. C) Carrier gas mass flow controller. D) Liquid pump E) Computer programme connected to gas mass flow controller. F) Furnace. G) Thermocouple for the furnace. H) Catalyst. I) Quartz wool either side of the catalyst, packing it. J) Furnace temperature controller. K) Glass condenser. L) Dry ice bath for the glass condenser. M) Gas chromatograph's thermal conductivity detector. N) Gas chromatograph's flame ionisation detector. O) Software for gas chromatograph. Figure used with permission from: K. M. K. Yu, W. Tong, A. West, K. Cheung, T. Li, G. Smith, Y. Guo, S. C. E. Tsang, *Nature Communications*, 2012, **3**, 1-7.©2012 Springer Nature Ltd.

ture or water content suppressing the CO content. Tables 3.1 and 3.2 both display experimental data of various MSR catalysts; unfortunately often papers do not report an in-depth analysis of their experimental conditions. This includes a wide variety in what is reported, for example reaction flow is sometimes reported in terms of liquid flow ($mL.min^{-1}$), gas hourly space velocity (volume of reactant gas per reactant volume per time) or weight hourly space velocity (mass of reactant gas flow per mass of catalyst per time); often these cannot be compared across different papers because

the data that are required to standardise the rate of flow are missing, usually the reactor volume. For this reason, only temperature and water:methanol ratios are reported in the tables 3.1 and 3.2.

Herein, some of the better catalysts were reviewed in more detail; their reaction times and reactant flows were investigated because this gives information on how sintering/stability and residence time affect the MSR performance, respectively. From both tables it can be seen that the average water:methanol mol ratio in the reactants is $\approx$ 1.1 - 1.2. [19, 20, 76] Additionally, most papers used an unmodified thermal conductivity detector (TCD) to measure their CO content, this can mean that no CO is detected even when it is orders of magnitude above the 10 ppm limit that would poison PEMFCs; exceptions include papers that used FID-methanizers to convert CO to CH_4 for an increased signal sensitivity and also Mateos-Pedrero et al. because CO was detected with a sensitivity of $\pm$ 0.2 ppm using an IR detector. [20, 77]

Table 3.1: In the top section, Ni-, Co-, Pd-, Pt-, Ir- and Ru-based MSR catalysts from literature are displayed. In the bottom section, literature for Cu catalysts is introduced. The catalysts are sorted by H_2:CO ratio, then temperature, then H_2 productivity.

Reference	Catalyst	Temperature (°C)	Reactant H_2O:MeOH (mol ratio)	H_2 Productivity* ($\mu mol_{H_2}.s^{-1}.g_{cat}$)	CH_3OH Conversion (mol %)	CO selectivity (mol %)	Product H_2:CO* (mol ratio)
[78]	Ir/ZnO	220	1	-	2.6	79.0	< 1
[79]	10 wt % Co/ZnO	220	1	-	13.1	86.7	< 1
[79]	10 wt % Ni/ZnO	220	1	-	19.1	97.0	< 1
[80]	1 wt % Pd/Al_2O_3	200	1	1.9	-	98.6	< 1
[79]	10 wt % Pt/Ga_2O_3	220	1	-	5.4	24.5	9
[81]	NiAl-(LDH)MMO	340	1.2	42.7	16.1	-	11
[82]	$Ni/CuAl_2O_3$	275	-	-	86.9	-	18
[79]	10 wt % Pd/Ga_2O_3	220	1	-	21.2	5.4	53
[79]	10 wt % Pt/ZnO	220	1	-	27.6	4.6	62
[80]	1 wt % Pd/ZnO	200	1	8.3	-	3.0	97
[83]	1 wt % $Pt/InCeO_x$	300	-	68.3	69.4	1.2	247
[79]	10 wt % Pd/ZnO	220	1	-	54.2	0.8	372
[84]	NiCu/ZnAl-(LDH)MMO	240	1.5	-	69	24.3	11
[84]	Pd/ZnAl-(LDH)MMO	240	1.5	-	22	5.2	58
[84]	RuCu/ZnAl-(LDH)MMO	240	1.5	-	95	2.0	89
[84]	Cu/ZnAl-(LDH)MMO	240	1.5	-	75	1.6	177

* = calculated in this work (unless exact H_2/CO compositions given), using data from the reference, the ideal gas equation and assuming CO (mol %) = $\frac{CO\ mol}{CO\ mol + CO_2\ mol\ (+\ hydrocarbon\ product\ mol)}$, as is reported in most literature reports. [76, 79, 84–86].

3.2 MSR catalysts

Noble metal or Ni MSR catalysts are often screened for high-temperature MSR catalytic activity because Cu nanoparticles begin to sinter at ≈ 300 °C (depending on their size); relative to other transition metals Cu has low cohesive energy and melting temperatures. [7, 12, 76] Additionally, steam from untreated water can introduce sulfur and chlorine contamination to a system which can further poison Cu catalysts; CuCl has a low melting temperature so can accelerate sintering and S can chemisorb strongly to Cu sites blocking them from reactants. [87]

Qi et al. synthesised various metal nanoparticles supported on NiAl oxide, for use as MSR catalysts, via the coprecipitation of layered double hydroxide precursors; the main objective was to achieve a higher thermal stability than the commercial copper-based catalysts. [88] Qi et al. used a molar ratio of 1.2 water to methanol and the reaction temperature was varied from 280 - 380 °C; Qi et al. found that adding Au, Rh and Ir to the catalyst favoured the methanation reaction: $4\,CH_3OH \longrightarrow 3\,CH_4 + 2\,H_2O + CO_2$. [89] Whilst methanol conversion reached 99.4 % for the NiAl-Au catalyst at 380 °C, for all catalysts and temperatures either the CO or CH_4 mol % selectivity was above 4 %; both far beyond the limits for a PEMFC. [88] As previously mentioned, CO production is a major problem when using MSR to provide H_2 for a PEMFC; additionally, methane is a more potent greenhouse gas than CO_2 and its production severely reduces the potential hydrogen production i.e. 4 mol of methanol would produce 3 mol of methane via methanation or 12 mol of hydrogen via MSR.

Oar-Arteta et al. proposed that often the most preferable reaction step for noble metal catalysts, such as Pt or Pd, is methanol decomposition (MD) to CO and then WGS produces CO_2 using this CO; such a proposal is discussed in Section 3.4. [90] Whereas, it is proposed Cu-based catalysts can perform a direct reforming mechanism that does not involve CO as an intermediate. [90]

Iwasa et al. published several MSR papers focusing on Pd-, Ir-, Ni- and Pt-based catalysts, some of which can be seen in Table 3.1. [78–80] All catalysts were tested in a conventional flow reactor with a reactant water:methanol ratio of 1; all catalysts gave a carbon monoxide production level that would be unacceptable for use in conjunction with PEMFCs. However, the 10 wt % Pd nanoparticles supported on zinc oxide catalyst gave the highest H_2:CO mol ratio of the non-Cu catalysts, 372 mol_{H_2}:mol_{CO}. Without ZnO modification Pd supported on various metal oxides favoured methanol decomposition, once modified with ZnO MSR was favoured in a much higher selectivity. [91]

The proposed mechanisms of MSR are discussed in Section 3.4; however, it is important to note that formaldehyde is an intermediate in the MSR catalytic cycle to explain the performance of Ni, Pt and Pd MSR catalysts. [7] Rodriguez et al. used temperature programmed desorption (TPD), mass spectroscopy, X-Ray photoelectron spectroscopy (XPS) and molecular orbital calculations to find that if Zn was alloyed to Ni, Rh, Pt or Pd metal it would decrease the CO adsorption strength compared to the pure metal surface; this perturbation was largest for Pd. [92] Rodriguez et al. proposed Ni, Pt and Pd can act as d orbital electron donors and s/p orbital electron acceptors to form bimetallic bonds with Zn, the molecular orbital theory is very complex but the reported net effect is that this weakens the electron π^* back donation from the metal surface to CO, correlating with the lowered CO desorption temperatures in TPD. [92] Studies by Davis et al. (EELS), McCabe et al. (EELS) and Madix et al. (TPD) found that formaldehyde adsorbed via a η^2-(C-O)-adsorption mode to Pd, Pt and Ni respectively; Sexton et al. discovered that formaldehyde adsorbed via a η^1-(O)-adsorption mode to Cu (1 1 0) surfaces via both EELS and TPD analysis. [93–96] Iwasa et al. suggested that when Zn was alloyed to Pd, in the more MSR-selective Pd/ZnO catalyst, there was a large decrease in the electron back donation ability of the metal nanoparticle causing the favoured formaldehyde

adsorption mode to switch from η^2-(C-O) to η^1-(O). [91] It was proposed that the η^2-(C-O) adsorption mode of the formaldehyde intermediate causes a preference for C-C and C-H bond scission due to the occupation of the C-O π^* anti-bonding orbitals; explaining why methanol decomposition is the favoured pathway for pure Pd, Ni and Pt nanoparticles; whereas, Cu nanoparticles, with η^1-OCH_2 intermediates, are proposed to favour the MSR pathway because, theoretically, formaldehyde would desorb before it could decarbonylate. [91]

Kim et al. found that the addition of Ni to an LDH-derived, MMO-supported catalyst reduced the Cu dispersion and therefore the MSR activity. [19] In summary, Ni and noble metal MSR catalysts often have high CO and methane yields (see Table 3.1). [7,12,88,90,97] This indicates a Ni or noble metal-based catalyst would not be a suitable catalyst for use in conjunction with a PEMFC because it would quickly poison the fuel cell, via CO generation, or not provide a good rate of hydrogen production due to substantial methane production.

At the bottom of Table 3.1, below the horizontal line, there are four catalysts from a study by Lin et al.; in the study Cu was used as an active MSR metal alongside Ni, Ru and Pd. [84] The CuZnAl catalyst provided the lowest CO production whilst remaining active, it was discovered that Cu^0-support oxide interface provided the active sites for the dehydrogenation of adsorbed methoxy groups and that Ni/Pd metals reduced the amount of interface by lowering the dispersion of Cu. [84] Both Lin et al. and Iwasa et al. have suggested that the η^1-(O)-adsorption mode of formaldehyde is important for low CO production; therefore, Cu-based MSR catalysts should be investigated as potential low-CO MSR catalysts.

Table 3.2: Cu-based MSR catalysts from literature. Sorted by H_2:CO ratio, then temperature, then H_2 productivity.

Reference	Catalyst	Temperature (°C)	Reactant H_2O:MeOH (mol ratio)	H_2 Productivity* ($\mu mol_{H_2}.s^{-1}.g_{cat}$)	CH_3OH Conversion (mol %)	CO selectivity (mol %)	Product H_2:CO* (mol ratio)
[98]	Cu/ZnO_x-MMO	250	0.25	485	33	58	4
[98]	Cu/ZnO_x-MMO	250	0.25	318	20	21	11
[19]	Cu/Al-(LDH)MMO (400 °C calcination)	200	1.1	20.7	10	$0 < x < 2$	N/A
[99]	$Cu/ZnO_x/Al_2O_3$	300	1.3	185	100	1.2	247
[76]	10 wt % Cu/Al_2O_3	300	1.2	-	99.9	0.92	323
[85]	$Cu/CeZnAlO_x$-MMO	240	1.2	19.3	92	0.9	330
[100]	Cu/MnO_x-MMO	213	2	-	77.0	0.2	370
[101]	$Cu/ZnZrAlO_x$	260	1.4	244	97	0.8	372
[102]	Cu/CeO_2/MOF	270	1.5	148	-	0.5	597
[86]	Cu/ZnAl-(LDH) (330 °C calcination)	260	1	60	63.1	0.5	597
[103]	Cu/ZnZr/MCM41	281	2	-	81.1	0.5	600
[104]	Cu/CeO_2-MMO	220	1	37.3	27.6	0.4	747
[105]	Cu-Ce/$ZnAlO_x$	250	1.2	-	100	0.39	766
[106]	$Cu/ZnAlO_x$-(LDH)MMO	250	1.3	-	99.1	0.06	1250
[104]	Cu/ZnO-MMO	220	1	22.0	16.4	0.2	1500
[104]	$Cu/ZnAlO_x$-MMO	220	1	19.8	14.7	0.2	1500
[77]	$Cu/ZrAlO_x$	220	1.5	128	-	0.1	3000
[107]	Cu/Zn@FSM-16	230	1.88	-	59.5	0†	N/A
[108]	$Cu/ZnAlO_x$-MMO	200	1.2	48.2	47.4	0†	N/A
[20]	$Cu/ZnGaO_x$-MMO	150	2	2.9	22.5	0‡	N/A

* = calculated in this work (unless exact H_2/CO compositions given), using data from the reference, the ideal gas equation and assuming CO (mol %) = $\frac{CO\ mol}{CO\ mol + CO_2\ mol\ (+\ hydrocarbon\ product\ mol)}$, as is reported in most literature reports. [76, 79, 84–86] † = CO detected using a TCD, not suitable for detecting low ppm concentrations. ‡ = CO detected using a FID fitted with a methanizer.

3.3 Cu-based MSR catalysts in literature

Günter et al. investigated Cu/ZnO-catalysed MSR with in-situ XRD and XAS analysis; it was found that Cu occupied the 0 oxidation state when the catalyst was active. [98] Many researchers correlated catalyst Cu^0 surface area to MSR activity. [19, 20, 103, 109, 110] Metallic Cu^0 has a lower lattice energy than other MSR-active metals, as evidenced by a correlated lower Hüttig temperature; subsequently, it has a lower required temperature for reduction compared to Ni or Co ($M^{2+} + 2e^- \longrightarrow M^0$) and therefore is suited to low-temperature MSR catalysis. [97]

Fornari et al. performed statistical calculations based on a "commercial" $Cu/ZnAlO_x$ catalyst and proposed the optimal weight percentages of Cu and Zn were 20.7 and 13.4 %, respectively; however, whilst such ratios may be economically cheaper for predominantly-Al MMOs it would not provide a metal mol ratio that allows layered double hydroxide precursor synthesis (a high surface area precursor, see Section 3.7). [111] Table 3.2 displays Cu catalysts from literature with the highest H_2 production rates and highest H_2:CO mol ratios; in this section their advantages and disadvantages will be discussed with regards to potential for a MSR-PEMFC system i.e. high temperatures, water excess and CO contents are unfavourable.

Lindstrom et al. prepared Cu^0 supported on ZnO which, in-turn, was impregnated on a high surface area Al_2O_3; this MSR catalyst had a very high surface area, 184 $m^2.g^{-1}$ and MSR activity, 185 $\mu mol_{H_2}.s^{-1}.g_{cat}$. [99] Despite the intermediate water excess, the reaction temperature was very high, 300 °C; this temperature explains the high MSR activity. However, when tested in 200 °C MSR conditions it gave a $\approx$ 0.5 % CO selectivity and it gave lower CO production than analogous CuZrAl and CuCrAl materials tested under the same conditions in the same study. [99] Lindstrom observed that Cu surface area and D_{Cu} % (copper dispersion) correlated with MSR activity and also that the temperature of the Cu temperature programmed reduction

(TPR) peak inversely correlated with MSR activity. [99] Smaller particles of Cu, with high D_{Cu} %, likely have to be stabilised by the support; therefore, it makes sense that the TPR analysis shows Cu^0 particles can be formed, via reduction, at lower temperatures i.e. because the support lowers the particles' potential energy making their formation more thermodynamically favourable. However, Lindstrom et al. do not propose a reason why a lower Cu reduction temperature would increase MSR activity.

Patel et al. impregnated Cu, Zn and Ce on the surface of a high surface area Al_2O_3 support, not dissimilar to the methodology used by Lindstrom et al. [99, 101] One of the subsequent reduced $Cu/ZnCeAlO_x$ catalysts gave the highest activity, 244 $\mu mol_{H_2}.s^{-1}.g_{cat}$, of any MSR catalyst that produced under 1 % mol of CO; this is especially noteworthy because 260 °C is a high temperature for MSR and thermodynamically favours a high RWGS rate. [101] However, the steam excess is reasonably high relative to other studies, the reactor set-up is not recorded and the calculation for the reactant residence time is not clear; when tested with a 1.1 water:methanol mol ratio the CO mol % was $\approx$ 3 %. [101] Patel et al. suggested the D_{Cu} % correlated with MSR activity and that the inclusion of CeO_2 helped minimise Cu sintering and coke formation. [101]

Chen et al. produced a novel Cu/CeO_2 catalyst supported on a high surface area metal organic framework (MOF); however CuO aggregated on the surface and had a surface area of 99 $m^2.g^{-1}$. [102] This is by no means a low surface area but it is less than that of the catalysts of Patel et al. and Lindstrom et al. [99, 101] After calcination and reduction, this Cu/CeO_2/MOF catalyst had an activity of 148 $\mu mol_{H_2}.s^{-1}.g_{cat}$; however, the temperature was high, 270 °C, as was the steam excess, 1.5. [102] Chen et al. proposed that CeO_2 increased the D_{Cu} % due to MSI, which in turn correlated with, not just the MSR activity, but also it inversely correlated with

CO content; supposedly due to a "reverse spillover" of oxygen from the ceria to Cu, which could be used to oxidise CO. [102]

Liu et al. synthesised a Cu/ZnO catalyst via coprecipitation, calcination and reduction, it produced 0.2 % mol of CO whilst catalysing MSR at 220 °C; although this CO concentration is still too high for a PEMFC, it is impressive as a 1:1 water:methanol reactant mix was used. [104] Liu et al. theorised a high D_{Cu} % was responsible for the MSR activity but did not mention CO selectivity in great detail; the report focused on the deactivation of the catalysts via coking. [104] Liu et al. also synthesised Cu/CeO_2 catalysts and proposed that MSIs caused the formation of Cu^+ which in turn increased the MSR activity; the role of Cu^+ is discussed in Section 3.6.1. [104]

Mateos-Pedrero et al. achieved the highest H_2:CO ratio in literature that had a measurable CO content, ≈ 3000 mol_{H_2}:mol_{CO}, in part due to their sensitive IR detector that could distinguish CO to $\pm$ 0.2 ppm; the catalyst used was Cu^0 supported on a ZrAl MMO. [77] The temperature was not one of the lowest in the field, 220 °C, but the H_2O:CH_3OH mol ratio was a bit excessive, 1.5, and likely heavily contributed to the low CO content. [77] For reference, in the study by Patel et al., a 1.5 H_2O:CH_3OH ratio gave a much lower CO content compared to a 1.1 H_2O:CH_3OH ratio for the same catalyst, see Figure 3.2. [101] The catalyst was prepared by using a wet impregnation method to deposit CuO on the ZrAl support, polyvinyl alcohol was used as a stabilising agent to increase the D_{Cu} % of the CuO particles formed. [77] The catalyst with the highest D_{Cu} %, 23.1 % (pre-MSR), had a specific Zr:Al ratio, Mateos-Pedrero et al. suggested this support ratio was best at stabilising Cu nanoparticles; it was the most active on average, however the reaction time is not specifically denoted. [77] Presumably both D_{Cu} % and sinter-resistance are important for maintaining high MSR activity.

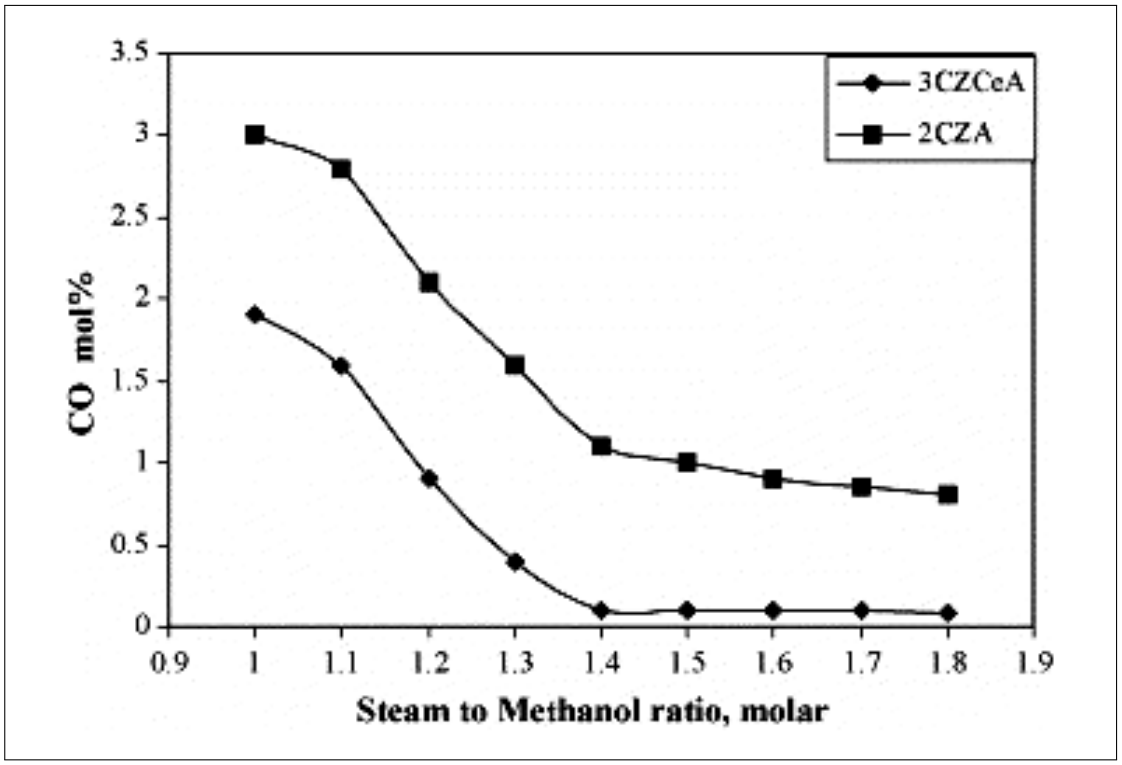


Figure 3.2: How the water:methanol ratio affects the CO production of two different MSR systems. Figure used with permission from: S. Patel, K. K. Pant, *Journal of Power Sources*, 2006, **159**, 139-143.©2006 Elsevier Ltd.

Both Jakdetchai et al. and Shishido et al. observed no CO content during Cu-catalysed MSR at $>$ 200 °C; however, only a standard TCD was used to record the CO content and the respective detector limits were not quoted, therefore it can be assumed there was unmeasured CO content. [107, 108] Of the two papers, the work by Shishido et al. was more promising due to a moderate 1.2 water:methanol ratio and relatively high hydrogen production rate, 48.2 $\mu\text{mol}_{H_2}.\text{s}^{-1}.\text{g}_{cat}$ at 200 °C. [108] The catalyst prepared by Shishido et al. was Cu^0 supported on a ZnAl MMO, much like 'commercial' and other literature catalysts; however urea was used to precipitate the precursor. [108] As with other literature reports, Shishido et al. noted the surface area and D_{Cu} % of a catalyst were important for MSR activity; they also noted the addition of Al helped stabilise the catalyst in the reaction stream more so than just ZnO. [108]

Tong et al. synthesised a $CuZnGaO_x$ MMO via coprecipitation and then calcined it and reduced it to produce a MSR catalyst; the CO content of the subsequent reaction was measured with a methanizer. [20] Such a detector used a Ni catalyst bed to completely hydrogenate CO and CO_2 to CH_4 directly before the FID to provide them with an oxidation signal in the flame; such detectors can detect CO to a limit of $\approx$ 5 ppm (the detection limit of the work in this thesis). Tong et al. measured no CO, unfortunately they used a water:methanol ratio of 2 which is extremely high compared to the average literature report (see Tables 3.1 and 3.2) and coupled this with the lowest MSR temperature in literature. [20] Whilst operation at such a low temperature could make it a prime candidate for use with PEMFCs; the MSR conditions also meant that the true CO selectivity inherent to the catalyst could not be seen. Ribeirinha et al. tested a very similar $CuZnGaO_x$ MMO-derived catalyst at 180 °C with a 1.5 H_2O:CH_3OH ratio and detected 600 ppm of CO at 80 % methanol conversion; however, this $Cu/ZnGaO_x$ catalyst had substantially higher MSR activity and a lower CO production than 'commercial' catalysts under the same conditions, in the same study. [112]

For the best MSR catalysts in the literature, most authors propose that several key factors have a large role on both MSR activity and CO selectivity, these include: D_{Cu} %, surface area, MSIs and/or nanoparticle stability. In the next sections the MSR and WGS surface mechanisms will be explored in an attempt to relate these properties to their catalytic effect.

3.4 Proposed Cu-catalysed MSR mechanisms

Historically, there have been several different proposed MSR mechanisms, early work with non-Cu catalysts and low H_2O content in the reactor feed introduced additional side reactions such as methanation and methyl formate formation, that complicated the picture. [7, 89] Early studies proposed MSR occured due to MD

reactions followed by forward WGS reactions to convert the CO; however, over the last two decades in-situ studies of Cu-based MSR catalysts and subsequent kinetic/thermodynamic modelling have shed light on the MSR mechanism. [12, 113] A 'direct' reforming mechanism was postulated to oppose the mixed MD/WGS scheme, this section reviews which mechanism is more likely to occur in Cu^0-catalysed MSR systems.

The first step in the majority of proposed MSR mechanisms in literature involves the dissociative adsorption of methanol to a Cu metal surface, Wachs et al. studied the adsorption of methanol to clean, Ar-sputtered Cu surfaces (with varying *hkl* indices) and found that this dissociative adsorption could be promoted if the surface was partially oxidised. [114] It was proposed that this was because the strength of an electron donating interaction from methanol's C-O or O lone pair to surface Cu would increase due to electrostatic forces if Cu possessed a partial $\delta+$ charge. [7] For an oxide-supported Cu nanoparticle such a partial charge could be induced at the metal-support interface due to Cu/O interactions; therefore, water decomposition, labile O adatoms and incomplete reduction have been proposed to increase methanol's interaction strength with Cu^0. [7, 115] Water was shown to decompose to H_2 and an adsorbed oxygen species on reduced, unsupported Cu^0 at 73 °C via in-situ mass spectroscopy. [116]

Several researchers have claimed through experimental or theoretical evidence that the dehydrogenation of the adsorbed methoxy group is the RDS of Cu-catalysed MSR. [22, 117–119] The product of this dehydrogenation has been described as adsorbed formaldehyde, dioxymethylene (as a result of a rapid formaldehyde oxidation) or formate; however, it was proposed dioxymethylene intermediates often are not observed due to their high reactivity. [7]

In Section 3.2, the adsorption mode of formaldehyde (formed from the dissocia-

tive adsorption and dehydrogenation of methanol) was found to be different for Cu and Ni/Pd catalysts; η^1-(O) for the former and η^2-(C-O) for the latter. Gu et al. confirmed this with the DFT modelling of MSR over both Pd^0 (1 1 1) and Cu^0 (1 1 1); subsequently this caused the different surfaces to favour different initial bond scissions. [119] The Pd^0 surface had a lower activation energy for the decomposition of formaldehyde to CO whereas the lowest activation energy pathway for the Cu^0 surface followed the formation of formate (see Figure 3.3). [119] Alongside the data from Table 3.1, it is apparent why Ni, Pd and/or Pt catalysts were often proposed to follow a MD/WGS mechanism under MSR conditions. The model by Gu et al. suggested the formation of formate could mean that MSR over a Cu-based catalyst is more complicated. [12, 119]

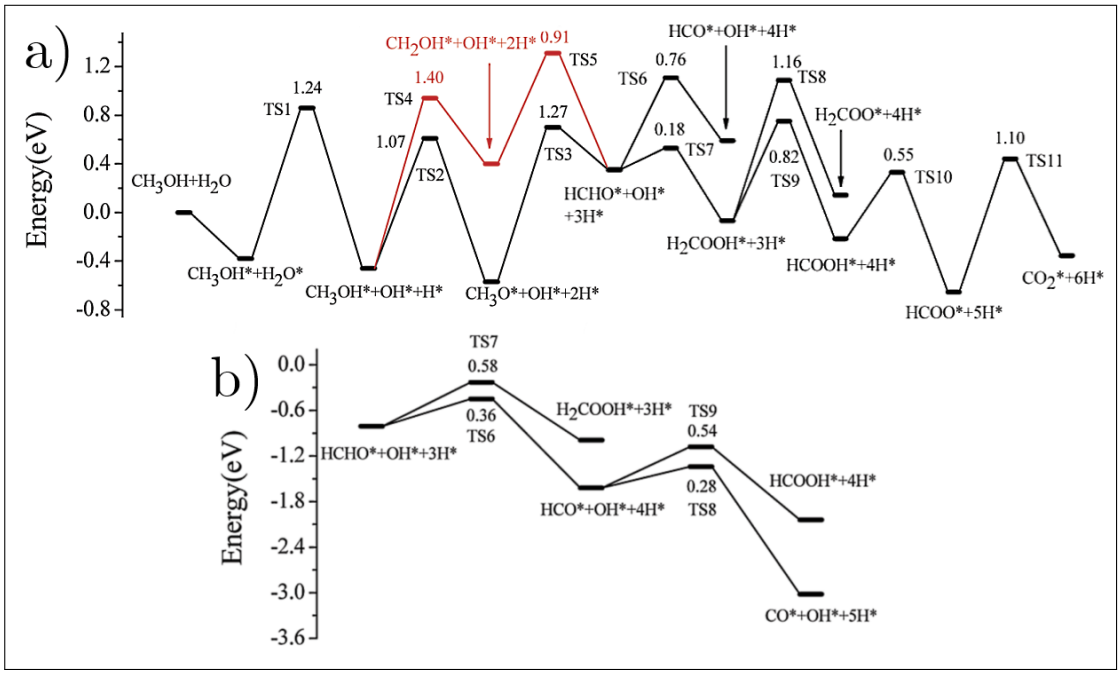


Figure 3.3: a) The potential energy of surface MSR species over Cu (1 1 1). The formation of HCHO* + OH* + 3H* is also favoured by Pd (1 1 1), however b) shows that the favoured pathway for Pd (1 1 1) proceeds to form CO*. Figure used with permission from: X.-K. Gu, W.-X. Li, *The Journal of Physical Chemistry C*, 2010, **114**, 21539-21547.©2010 American Chemical Society.

Peppley et al. kinetically modelled MSR, MD and WGS using data from MSR

experiments catalysed by MMO-derived $Cu/ZnO/Al_2O_3$; a direct MSR mechanism was proposed, as opposed to MD/WGS being responsible for the hydrogen production. [120] It was also suggested that MD had a different active site (likely clean fcc Cu^0) compared to the active site for WGS/MSR; additionally, η(-H) adsorbed species didn't compete for the same adsorption sites as η(-O) species. [120] Lee et al. found that the rate-determining step (RDS) for $Cu/ZnMgAlO_x$-catalysed MSR was the dehydrogenation of adsorbed methoxy groups, a simplified equation of such a process is as follows (where ad = adsorbed): CH_3O (ad) + O (ad) $\longrightarrow$ H (a) + OCH_2O (ad). [22] The adsorbed O species often comes from the support whilst the OCH_2O species is known as dioxymethylene, it can adsorb to the catalyst surface via both its oxygens (this intermediate is discussed below). Also in the investigation of commercial $Cu/ZnMgAlO_x$ catalysts, Lee et al. found that the adsorption of species, that weren't methanol or hydrogen, had a negligible impact on the MSR rate; indicating a direct MSR reaction mechanism. [22]

Takezawa et al. performed extensive MSR investigations into SiO_2-supported Cu/Ni/Pt/Pd catalysts. [121] Catalytic tests with formaldehyde and acetaldehyde steam reforming were also included; as in Section 3.2, Cu was found to have the highest selectivity for MSR at atmospheric pressure. [121] The Cu/SiO_2 catalyst favoured methyl formate production (94 % selectivity) when only methanol was introduced in the absence of water, whereas other metal catalysts only performed methanol decomposition to CO. [121] This likely can be explained by the different adsorption modes favoured over Cu^0 as opposed to other metals i.e. the η^1-(O) formaldehyde adsorption does not favour MD (see Section 3.2) and allows for nucleophilic attack from other methoxy species at the formaldehyde or formate carbon, resulting in an addition reaction and the formation of methyl formate.

Takezawa et al. found that the addition of CO did not affect the rate of formation

of H_2/CO_2 during MSR tests of Cu/SiO_2 with stoichiometric or excess water content; therefore, WGS did not have a substantial role in the main MSR mechanism. [121] In tests of formaldehyde steam reforming, Takezawa et al. found methanol, H_2 and CO_2 were the main products and that the formation of H_2 and CO_2 was many orders above that for MSR. [121] This indicated that formaldehyde was an intermediate of both CO_2 hydrogenation and MSR and that the observations were in agreement with other studies that had proposed methoxy dehydrogenation as the RDS of MSR. [22,117–119]

Thus far, the MSR mechanism has been theorised to involve the dissociative adsorption of methanol on Cu^0 followed by the dehydrogenation of adsorbed methoxy species to formaldehyde. The intermediates between formaldehyde and complete MSR conversion are discussed below.

Takezawa et al. did not attempt to identify the intermediates of steam reforming between formaldehyde and the products (H_2/CO_2). [121] Electron energy loss spectroscopy (EELS) and temperature programmed desorption (TPD), in conjunction with literature infra-red data, showed dioxymethylene could be stabilised on certain metal oxide surfaces after the oxidation/dehydrogenation of an adsorbed methoxy group. [122] Dioxymethylene was also identified as a product in the adsorption of formaldehyde on metal oxides below room temperature by in-situ FTIR; however, when the temperature was increased above room temperature the dioxymethylene was replaced with formates and methoxide groups due to 'disproportionation'. [123] Frank et al. observed Cu-based, MMO-supported catalysts' surfaces were dominated by methoxy and formate species during in-situ DRIFTS/MSR tests; however, they reported formaldehyde and dioxymethylene are likely transient species. [124] The MSR intermediates discussed in this section are displayed in Figure 3.4. [7]

Mazoli et al. proposed surface formaldehyde species could react together in a disproportionation reaction to form adsorbed formate and methoxy species, however

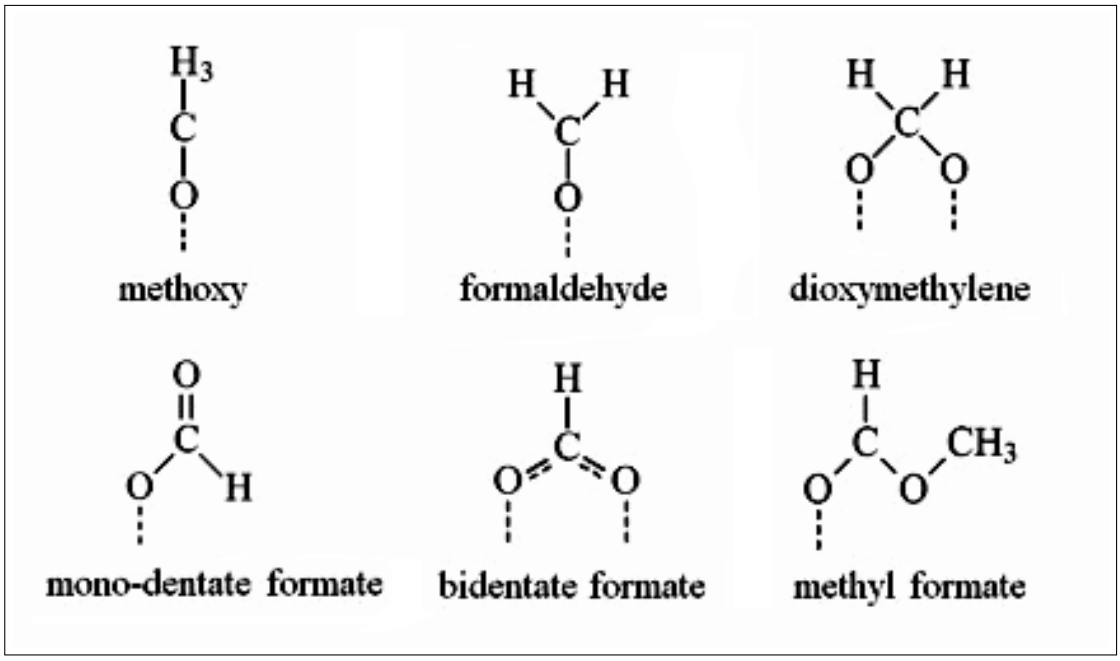


Figure 3.4: Common species observed in literature MSR reactions. Figure used with permission from: S. T. Yong, C. W. Ooi, S. P. Chai and X. S. Wu, *Int. J. Hydrog. Energy*, 2013, **38**, 9541-9552.©2013 Elsevier Ltd.

they studied 'MSR-like' conditions over copper surfaces without water excess and with the addition of O_2 (g). [125] Therefore, because such a reaction produces water it is unlikely to be favoured by Le Chatelier's principle in typical MSR conditions with a water excess; in fact Manzoli et al. seem to be outliers because, whilst researchers do observe formate species in Cu-catalysed MSR, it is generally attributed to the dehydrogenation of dioxymethylene. [7]

In literature, a study by Clarke et al. is often cited as evidence for formate formation proceeding via the dehydrogenation of formaldehyde and/or dioxymethylene; the study involved using Cu/SiO_2 for methanol TPD and FTIR studies. [126, 127] Clarke et al. did not include water as a reactant in their studies rather they investigated oxidised and reduced versions of the Cu/SiO_2 material; they assigned FTIR peaks to formaldehyde, dioxymethylene and both mono- and bi- dentate formate species. [127] However, the exact nature of the FTIR study is not clear regarding whether the

adsorbed methoxy-Cu system was closed or under a gas flow; additionally, methyl formate was not mentioned despite Takezawa et al. finding that Cu/SiO_2 produced mostly methyl formate in the absence of water. [121, 127]

Due to the nature of dioxymethylene being so transient it hasn't be experimentally observed for in-situ MSR. The above studies where dioxymethylene is isolated on metal oxides below room temperature, observations of mono- or bi- dentate formate in multiple studies and DFT calculations all suggest dioxymethylene is an intermediate in Cu-catalysed MSR; as opposed to the evidence for dioxymethylene proposed by Clarke et al. [122, 123, 127, 128]

Thus far it has been proposed that adsorbed methoxy reacts on the Cu catalyst surface to form η^1-(O) formaldehyde, which in turn favours a reaction pathway to that forms transient dioxymethylene.

Gomes et al. conducted computational DFT to specifically investigate the formation of formate on copper; both the reaction of formaldehyde with surface oxygen to form dioxymethylene and the subsequent decomposition of dioxymethylene to formate is found to be thermodynamically favourable compared to other alternative reactions for each step. [129] Zuo et al. used DFT calculations to study MSR, MD and methanol oxidation on Cu (1 1 1), they claim dioxymethylene is an intermediate in CO_2 hydrogenation; however for MSR they propose two intermediates exist between formaldehyde and formate: 1) hydroxymethoxy (CH_2OOH), which then has a C-H break to form 2) formic acid (CHOOH). [130] Yong et al. observed formate during in-situ FTIR MSR experiments and proposed the formation of adsorbed formate via dehydrogenation occurred faster on reduced Cu surfaces, rather than metal oxide surfaces, due to stronger hydrogen adsorption on the Cu surface. [131] Yong et al. also theorised the oxide was needed to provide the oxygen for the partial oxidation of formaldehyde to dioxymethylene. [131] Despite dioxymethylene supposedly favour-

ing the formation of monodentate formate according to Clarke et al., the species can then adopt the the more stable bidentate binding mode; Bo et al. performed a DFT specifically on the steam reforming of formaldehyde on Cu (1 0 0) surfaces and found that both dioxymethylene and formate species energetically prefer to use both their oxygens to bind to the surface. [127, 132] Lustemberg et al. used DFT combined with FTIR to study the bonding modes of formate on support CeO_2 and found that the mono- or bidentate formate concentration is dependent on the H_2O and H_2 concentrations in the system. [133]

Both mono- or bi- dentate formate dehydrogenates to H_2 and CO_2. [7, 132] Additionally, it was reported labile oxygen from support oxides can nucleophilically attack carbon atoms in methoxy or formaldehyde species to form dioxymethylene species; whilst formate formation over metal oxides was commonly reported. [7, 122]

Methyl formate production has been observed experimentally in some MSR, this could be associated with a lower water partial pressure because Takezawa et al. showed Cu-based catalysts could produce a high selectivity of methyl formate in the absence of water. [7, 121] DFT models confirmed this and proposed no further dehydration reactions occur due to methyl formate's low adsorption strength. [134]

Overall for Cu-catalysed MSR only low CO concentrations are observed at low temperatures due to RWGS, below 200 °C the WGS equilibrium can be heavily kinetically limited; unfortunately so is MSR, just to a lesser extent. [135–137] At higher temperatures MSR, MD and WGS will all increase in rate because they're exothermic. The direct MSR mechanism can be summarised by the following: methanol dissociatively adsorbs on the Cu^0, it is then dehydrogenated via formaldehyde, dioxymethylene and formate into CO_2 and H_2.

Methanol and H_2O are thought to adsorb on the Cu^0 particle face and oxide support, respectively. [17, 20, 120] Oxygen vacancies have been suggested adsorb and

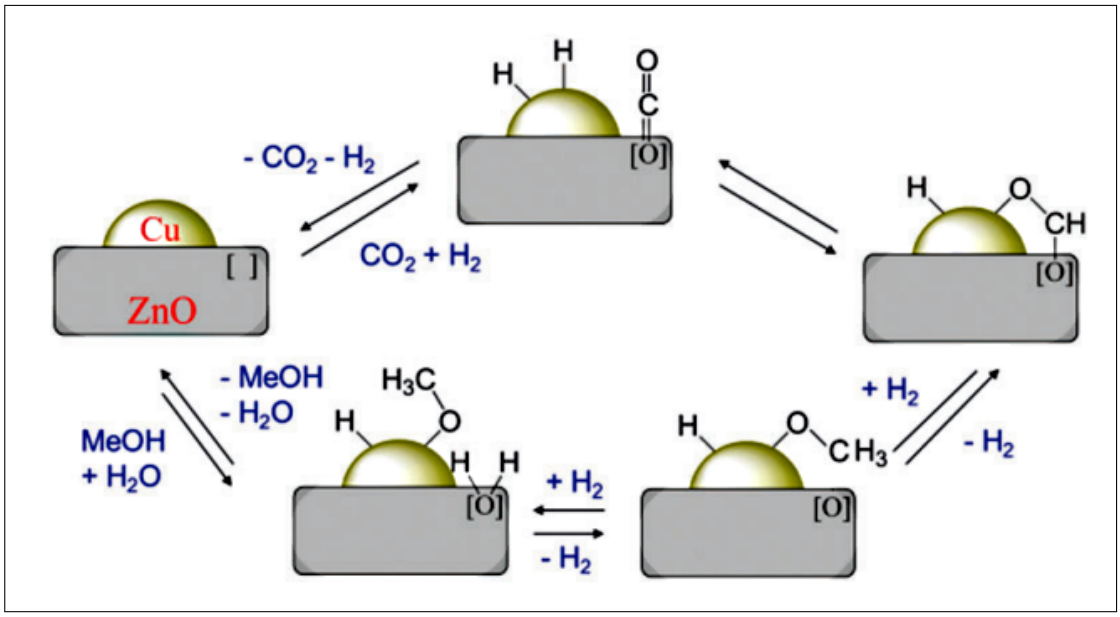


Figure 3.5: Proposed MSR mechanism over Cu/ZnO. Figure used with permission from: W. Tong, K. Cheung, A. West, K.-M. Yu and S. C. E. Tsang, *Phys. Chem. Chem. Phys.*, 2013, **15**, 7240-7248.©2013 Royal Society of Chemistry.

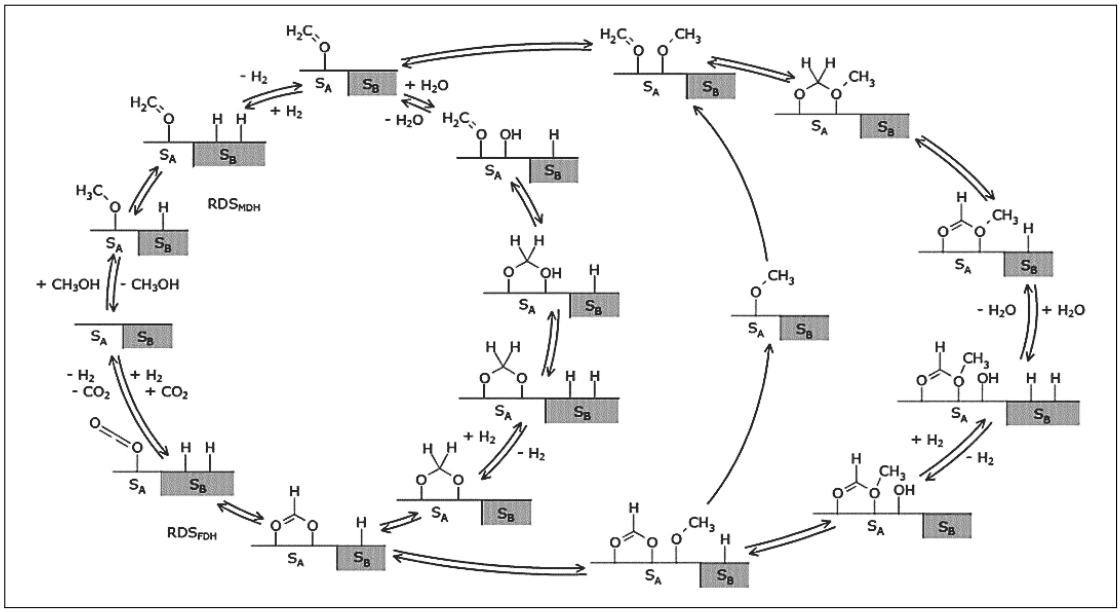


Figure 3.6: Proposed MSR mechanisms, involving two different active sites, for Cu-based and non-Cu metallic heterogeneous catalysts; includes a methyl formate intermediate pathway. Figure used with permission from: B. Frank, F. C. Jentoft, H. Soerijanto, J. Kröhnert, R. Schlögl, R. Schomäcker, *Journal of Catalysis*, 2007, **246**, 177–192.©2007 Elsevier Ltd.

activate water. [20, 138] Whilst adsorbed species can move across a surface with kinetic energy and across metal-support boundaries (spillover), it is probable the MSR reaction will take place at the metal-support interface, between where both reactants favour adsorption. This is reflected in literature because many studies found the MSR activity is dependent on D_{Cu} %, which correlates with the amount of Cu-metal interface sites. [20, 77, 99, 101, 102, 104, 108] It was also found by Tong et al. that neither the Cu^0 or MMO support phase was active in MSR alone, subsequently a MSR mechanism was proposed (see Figure 3.5); the mechanism by Tong et al. can be considered the best fit to the observations assembled in this literature review. [20] Older but similar MSR mechanisms can be seen in Figures 3.6 and 3.7. [124, 139]

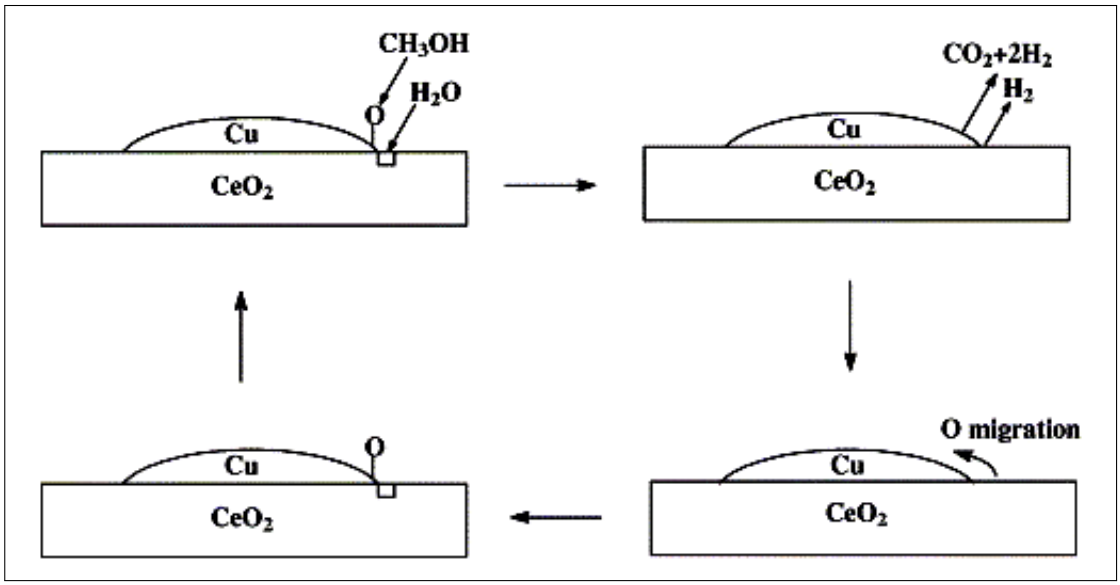


Figure 3.7: Proposed MSR mechanism at a Cu^0-CeO_2 interface. Figure used with permission from: Y. Men, H. Gnaser, R. Zapf, V. Hessel, C. Ziegler, *Catalysis Communications*, 2004, **5**, 671–675.©2004 Elsevier Ltd.

3.5 Side reactions in MSR literature

Under MSR conditions, the formation of dimethyl ether (DME) can occur if the only catalytic sites are Brønsted acidic sites and MD can occur at higher temperatures. [139] However, at temperatures below 230 °C with Cu-based MSR catalysts the WGS

equilibrium is often the only significant side reaction that occurs; this is because longer residence times are observed to increase CO production at the expense of CO_2. [20, 112, 140, 141]

Metal oxide surfaces, such as CeO_2, can act as active sites for the dissociation of water during WGS. [142] Defective metal oxide sites, such as oxygen vacancies, are the most active for water dissociation. [143] Wang et al. studied WGS over Cu/CeO_2 with in-situ DRIFTS, XRD and XAS, it was proposed CO was predominantly adsorbed on the Cu^0 but could react at any CeO_2 site to form an oxygen vacancy and CO_2, water would then react with with this vacancy producing H_2 and a reoxidised CeO_2 surface. [144] Wong et al. applied DFT calculations to find that Cu^0 can donate 3d electron density to the lowest energy unoccupied $2\pi^*$ antibonding CO orbital, providing the preferential CO adsorption. [145]

Raupp et al. investigated TiO_2 metal oxides in the absence of metal nanoparticles with TPD; it was found that CO only adsorbs very weakly to oxidised TiO_2, but this adsorption strength increases with the extent of reduction of the oxide. [146] Raupp et al. also observed that TiO_2 strongly adsorbed water and carbon dioxide. [146] Based on the findings of Raupp et al. it was suggested oxide surfaces could not dissociate H_2; however, adsorbed H species have been shown to readily spillover from metal to oxide surfaces (via the Grotthuss hopping mechanism) to form hydroxyl groups on the support; such a mechanism involves proton 'conduction' via adsorbed water. [146–150] Therefore, the theory proposed by Tong et al., that RWGS can happen on an oxide site not in the near vicinity of a metal nanoparticle (during MSR), is possible; this is further confirmed by observations that some bulk oxide surfaces (including ZnO) can catalyse WGS. [20, 151]

Chen et al. found that a higher D_{Cu} % and a higher concentration of oxygen vacancies also increased the forward WGS reaction rate when catalysed by Cu/ZrO_2

at atmospheric pressure; the RDS was found to be water dissociation. [152] Ziemba et al. discovered that the rate of WGS depends on the oxygen defect energy of formation, desorption energy of CO_2 and the activation energy for water dissociation. [153]

Water, CO and CO_2 compete for similar adsorption sites on metal oxide surfaces under MSR conditions, whereas the dissociative adsorption of H_2 preferentially occurs on metal nanoparticles. [120,143] The above studies imply WGS/RWGS can occur on nearly any oxide surface but CO or H spillover may need to be involved for high WGS or RWGS activity, respectively. In these above studies by Ziemba et al., Chen et al. and Wang et al. the WGS reaction was studied independently, predominantly focusing on the reaction of CO with H_2O, without the introduction of methanol, so no insight was offered into whether the MSR and WGS reactions compete for the same active sites. [142, 152, 153] Whilst Cu-based MSR studies often present varied H_2:CO ratios for different catalysts that do not align with expected thermodynamic calculations (see Tables 3.1 and 3.2), the relationship between MSR and WGS active sites has not been studied in-depth. Tong et al. proposed that the RWGS reaction can occur on oxygen vacancy sites on the metal oxide support that are isolated away from the Cu nanoparticle interface (see Figure 3.8) because the dissociated water cannot react with an adsorbed methoxy species, whilst water that dissociates at oxygen vacancies at the metal-support interface will favour a MSR mechanism; this theory is used to explain why D_{Cu} % was observed to inversely correlate with CO production. [20]

This proposal seems feasible because other literature reports found increasing D_{Cu} % can decrease the CO selectivity. [102] Purnama et al. theorise that smaller particles of Cu can decrease the CO concentration produced in MSR because smaller particles can lead to a less restrictive intraparticle diffusion limit and, therefore, an effectively shorter residence time. [154] Gao et al. propose oxygen vacancies at the metal-support interface can help stabilise formaldehyde or formate intermediates, in-

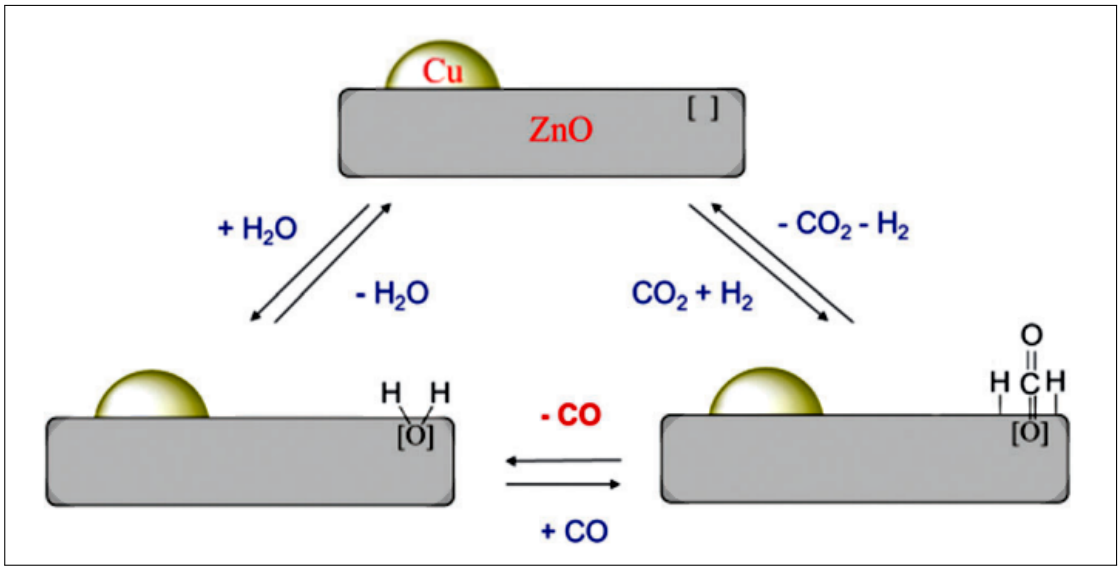


Figure 3.8: Proposed WGS mechanism over Cu/ZnO. Figure used with permission from: W. Tong, K. Cheung, A. West, K.-M. Yu and S. C. E. Tsang, *Phys. Chem. Chem. Phys.*, 2013, **15**, 7240-7248.©2013 Royal Society of Chemistry.

creasing selectivity for MSR reactions; it is also propsoed that Cu^+ formation is related to oxygen vacancy formation at the interface (see Section 3.6.1). [155]

3.6 The oxidation states of Cu and Zn

It has been established that the Cu^0-ZnO interface is important in MSR catalysis. Specifically a high Cu^0 surface area and amount of interface (D_{Cu} %) correlates with MSR activity. [20, 76, 106, 109] Whilst a high D_{Cu} % can increase MSR activity and minimise RWGS activity, this is likely due to a higher ratio of (MSR+RWGS interface):(RWGS oxide only) active sites. [20]

ZnO is one the most commonly used MSR catalyst supports in literature, it can provide oxygen vacancies for the catalytic mechanisms and it provides physical/textural support to increase the resistance of the Cu^0 nanoparticles against sintering. [12, 17, 74, 106, 109, 156, 157] Additionally ZnO has been observed to lower the TPR reduction temperature for the formation of Cu^0 by $\approx$ 100 °C, this was theorised to occur because the metal oxide, that cannot be reduced by H_2, can act as a H_2

reservoir under highly reducing conditions and provide H_2 via spillover to the Cu surface. [7, 158, 159] However, spillover likely only plays a small role in this lowered reduction temperature because the reduction temperature of a material can depend on many structural effects e.g. on the lattice energy of the precursor and the thermodynamic stability of the forming nanoparticle. Therefore, Burch et al. propose the primary role of ZnO is to support the Cu nanoparticles against sintering; which in turn makes the formation of the nanoparticles thermodynamically more favourable (as seen in TPR). [12, 74, 160–162]

Thus far, it has mostly been assumed that Cu is in the (0) oxidation state after the pre-reaction reduction process and the Zn in the metal oxide support is in the (+2) oxidation state; some literature studies have proposed Cu^+ and Zn^0 may play roles in MSR catalysis.

3.6.1 Potential role of Cu^+

It has been proposed that Cu^+ may form as a result of a redox reaction in which a CeO_2 surface is reduced to form an oxygen vacancy whilst Cu^0 is oxidised to Cu^+ (see Section 8.1). [17, 104, 163] This can be thought of as Cu^0 donating electron density to stabilise the 2+ charged oxygen vacancy (which had just lost O^{2-}); however, the picture can be complicated by other MSR adsorbing species, interface effects and the fact that mono-atomic O^{2-} ions need to react before the resultant molecule can desorb as a gas. Frost et al. has even proposed that Cu can reduce the high energy cost of oxygen vacancy formation on ZnO under highly reducing conditions by accepting electron density but this depends on the band energy levels of the different surfaces. [164] In simplified terms, the transition state of the RDS of oxygen vacancy formation can be theoretically stabilised by neighbouring Cu nanoparticles. Several literature MSR studies have detected Cu^+ in MSR catalysts via XAS. [20, 139, 165]

When Cu^+ is discussed in literature, most theories about its role revolve around

the $\delta+$ charge on the metal nanoparticle increasing the adsorption strength of methoxy or carbonyl groups electrostatically or its involvement in oxygen vacancy formation. [139] During in-situ FTIR studies of CuO and variably-treated CuZnAl catalysts, it has been deduced that CO only adsorbs to Cu^0 weakly; on the other hand Cu^+ can bind CO with a much stronger adsorption due to the increased strength of the σ bonding from the C lone pair to the Cu^+. [21,123,163] Bian et al. also used DRIFTS and mass spectrometry to investigate in-situ WGS over Cu/SiO_2, it was found that not only did Cu^+ bind CO stronger but also promoted its activation for the forward WGS reaction (see Figure 3.9). [166]

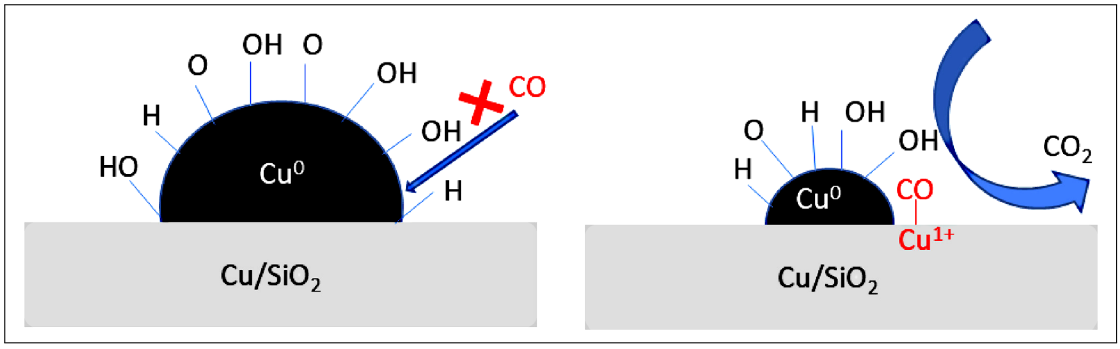


Figure 3.9: Proposed WGS mechanism over inert SiO_2 and either Cu^0 or Cu^+. Figure used with permission from: Z. Bian, W. Zhong, Y. Yu, B. Jiang, S. Kawi, *International Journal of Hydrogen Energy*, 2020, **45**, 27078–27088.©2020 Elsevier Ltd.

Günter et al. used in-situ XAS to follow the oxidation state of Cu in a Cu/ZnO-catalysed, MSR/O_2 reaction cycle, it was found that the reduced catalyst under MSR conditions was $>$ 99 % Cu^0; however, when O_2 was introduced to oxidise the catalyst, methyl formate production stopped and it took a re-reduction to 80 wt % Cu^0 before the CO and methyl formate production began again (this production hit a maximum at $>$ 99 % Cu^0). [98] Günter et al. also found that the oxidation or reduction of Cu between the (0) and (II) oxidation states proceeds via an intermediate Cu(I). [98]

As with other factors that catalyse WGS, the principle of microreversibilty states that the other direction RWGS should be equally catalysed; however, equilibrium is

not reached in flow reactors. It is unclear whether Cu^+ or oxygen vacancies could significantly increase the adsorption strength or residence time of CO, relative to the other three WGS reactant species, in a way that would suppress the CO production rate under MSR conditions.

3.6.2 Potential role of Zn^0

Several researchers observed Zn^0 using in-situ XAS techniques during MSR or CO_2 hydrogenation. [167–170] Hansen et al. used in-situ TEM to show that D_{Cu} %, Zn^0 content and the number of oxygen vacancies can all change under WGS-like conditions. [168] Textural support of ZnO, lewis acidic Zn sites, Zn-driven improvement of Cu dispersion, stabilisation of Cu^+ caused by a Ga_2O_3 support and metal oxide electronic promotion had all been previously reported effects in Cu-based catalysis literature; Li et al. proposed that 'heterojunctions' in the precursors could cause such effects via the formation of Zn^0 under reducing conditions. [169, 170]

Heterojunctions occur at boundaries between two different semiconductor phases, in type-II heterojunctions when electrons are excited they localise in the conduction band of the 'lower energy' material whilst the positive holes localise in the valence band of 'higher energy' material (see Figure 3.10.a). [169, 171] Often such transitions are excited by photons of electromagnetic radiation and were not thought to have significant thermally-excited lifetimes; however, recent DFT modelling has shown that non-negligible electron redistribution can occur due to thermal vibrations (termed 'pyroelectricity'). [172]

Liao et al. and Li et al. propose such thermally-excited transitions have a long enough lifetime to take part in chemical reactions and promote the reduction of one of the semi-conductor oxide phases (in the presence of hydrogen) to form metal nanoparticle alloys (FePd or CuZn); TRPL analysis showed the type-II heterojunction excitations had relatively extended lifetimes. [169, 171] Li et al. suggest the electron

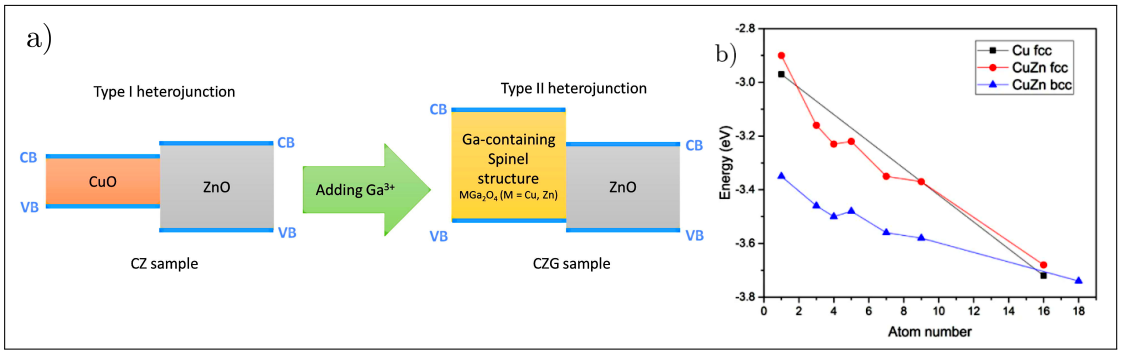


Figure 3.10: a) A simplified schematic of how the inclusion of Ga^{3+} and the formation of spinel oxide and a staggered type II heterojunction can cause excited electrons to favour aggregation in the lower-energy conduction band i.e. in ZnO. b) The potential energy of differently-sized Cu, Zn and CuZn nanoparticles. Figures used with permission from: a) M. M.-J. Li, Z. Zeng, F. Liao, X. Hong, S. C. E. Tsang, *Journal of Catalysis*, 2016, **343**, 157-167.©2016 Elsevier Ltd. b) M. M.-J. Li, J. Zheng, J. Qu, F. Liao, E. Raine, W. C. H. Kuo, S. S. Su, P. Po, Y. Yuan, S. C. E. Tsang, *Scientific Reports*, 2016, **6**.©2016 Springer Nature Ltd.

holes can be viewed as 'activated' oxygen species that react with adsorbed -H species, that spill over from the metal nanoparticle onto the semiconductor oxide at the interface, to form water; therefore, the electrons reduce the M^{x+} cations in the support oxide. [169] It was proposed the introduction of Ga^{3+} into Cu/ZnO materials could cause the formation of a type-II heterojunction and that the formation of Cu^0/Zn^0 alloys could increase CO_2 hydrogenation activity and selectivity by increasing the adsorption strength of H_xCO intermediates. [169] Additionally, β-brass bcc CuZn alloy catalysts (with high Zn^0 surface content) were shown to have exceptional resistance to sintering during catalytic accelerated deactivation tests, DFT models proposed this was because bcc CuZn alloys had lower surface energy than both fcc CuZn and fcc Cu particles (matching literature metallurgy data, see Figure 3.10.b); such an effect is not dissimilar to SMSI. [170] Li et al. found that bcc ZnCu alloys were preferentially formed with higher Zn^0 concentrations, which in turn was controlled via Ga^{3+} concentrations and calcination temperatures; the Zn^0:Zn^{2+} ratio reached a maximum at a Cu:Zn:Ga metal mol ratio of 43:52:5 and a calcination temperature of 330 °C. [170]

Conversely, Kattel et al. investigated various Cu/ZnO and CuZn materials after they had catalysed CO_2 hydrogenation reactions, without exposing the samples to air, and did not detect any Zn^0 or Zn LMM Auger features in an 'active' catalyst via XPS. [173,174] They suggest CuZn alloys are not stable under 20 atm of H_2 and that ZnO is the species that increases the activity (the CuZn alloy is not active in their Monte Carlo simulations); they provide O and C XPS evidence that further back up the claims and Zn^0 bound to formate is not observed post-reaction. [173,174] Kattel et al. propose that increases in stability/activity reported in previous works, supposedly caused by CuZn alloys, are likely better explained by highly disperse ZnO decorating Cu particles under reaction conditions. [173] Kattel et al. theorise Cu/ZnO is an active CO_2 hydrogenation catalyst due to the interface acting as the active site whilst ZnO stabilises Cu particles and acts as a hydrogen reservoir. [173, 174]

Methanol synthesis comparisons can be relevant to MSR discussions because Cu/ZnO-based catalysts are often used in CO_2 hydrogenation, which can be thought of as the reverse to MSR. It is possible the microreversibility principle could apply for a given catalyst but the conditions in a flow reactor would dictate the net reaction e.g. a high pressure flow of hydrogen and carbon dioxide will lead to methanol formation whereas an atmospheric pressure flow of water and methanol will lead to hydrogen formation. [12,17] However, microreversibility only applies for systems at equilibrium, which isn't often reached in flow reactor systems; therefore, optimal metal ratios in CuZnAl catalysts for methanol synthesis (CO_2 hydrogenation) and MSR reactions are different. [87]

Furthermore Kattel et al. only use XPS in the identification of the oxidation state of Zn and do not use a technique more sensitive to the topmost surface layer, such as high sensitivity low energy ion scattering. [170, 173] XPS analyses the top $\approx$ 20 atomic layers. [175] However, Kattel et al. did observe Zn^0 binding energy in XPS,

its transformation to Zn^{2+} coincided with an increase in methanol production (see Figure 3.11). [173]

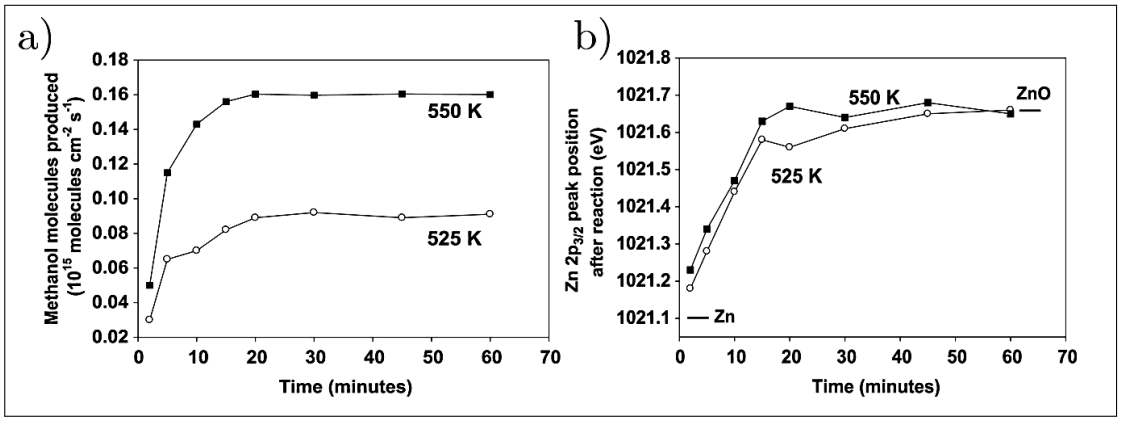


Figure 3.11: a) CO_2 hydrogenation activity of a CuZn-based catalyst with time. b) The in-situ XPS Zn $2p_{3/2}$ peak analysis for the same reaction. Figure used with permission from: S. Kattel, P. J. Ramírez, J. G. Chen, J. A. Rodriguez, P. Liu, *Science*, 2017, **355**, 1296–1299.©2017 American Association for the Advancement of Science.

It should be noted that Lunkenbein et al. observe a ZnO layer form over Cu^0 particles in CuZnAl materials exposed to reducing conditions via TEM and propose SMSI is responsible. [176] Therefore, it is not clear whether the Zn^0 formed under the pre-reaction reduction conditions by Kattel et al. is important in the generation of an active ZnO overlayer under catalytic conditions (SMSI). [173] The lack of M^{3+} cations and, therefore heterojunctions, in the work by Kattel et al. might be responsible for the difference in Zn^0 observations to Li et al.; additionally, the conditions widely differ between the two studies, different processes are catalysed and Kattel et al. do not investigate atmospheric pressure conditions. [169, 173]

There is a lack of literature regarding the use of thermally-excited heterojunctions in catalysis and it is unclear whether Zn^0 would be beneficial or disadvantageous to MSR catalysis; however, such effects would need to be discussed if Zn^0 was detected is MSR catalysis.

3.7 AMO-LDHs as catalyst precursors

Previously in this section, the properties of the best MSR catalysts have been discussed; one property that can have a positive effect upon both MSR selectivity and activity is D_{Cu} %.

Layered double hydroxides (LDHs) have inherently high elemental dispersions and can be used as precursors for materials with high D_{Cu} %. LDHs are anionic clay materials that are constituted by cations coordinated octahedrally by hydroxyl groups at vertexes, these octahedra are then arranged in a 2-D layer structure where the octahedra share edges; water and anions occupy interlayer spaces bonding with the layers (see Figure 3.12). [177–179] Often LDH layers are described as brucite- or hydrotalcite-like layers but can contain nearly any metal cation unlike the aforementioned specific minerals; the structure of these materials is discussed further in Section 3.7.1. [178] LDHs can be oxidised under elevated temperatures (calcined) into MMOs with high, uniform elemental dispersion (compared to MMOs prepared by different methodologies) that is maintained from the inherently high elemental dispersion of the precursor LDH; these LDH-derived MMOs often have high surface areas and thermal stability too. [19, 97, 106, 179, 180]

LDHs have been used as precursors for MSR catalysts previously in literature; Tables 3.1 and 3.2 are labelled with LDH to represent catalysts derived from LDHs. Often LDHs are calcined into MMOs, that are then reduced to form metal nanoparticles supported on a MMO (labelled as (LDH)MMO in the above Tables); however, low calcination temperatures, below $\approx$ 400 °C, can cause layered double oxides to form (see below in Section 3.7.1). LDHs that hadn't been calcined and reduced took 10 h to reach the activity of pre-reduced catalysts under MSR conditions. [106]

LDH layers can be exfoliated when the interlayer hydrogen bonding and ionic bonding networks are broken, exfoliated LDH layers give higher surface areas when

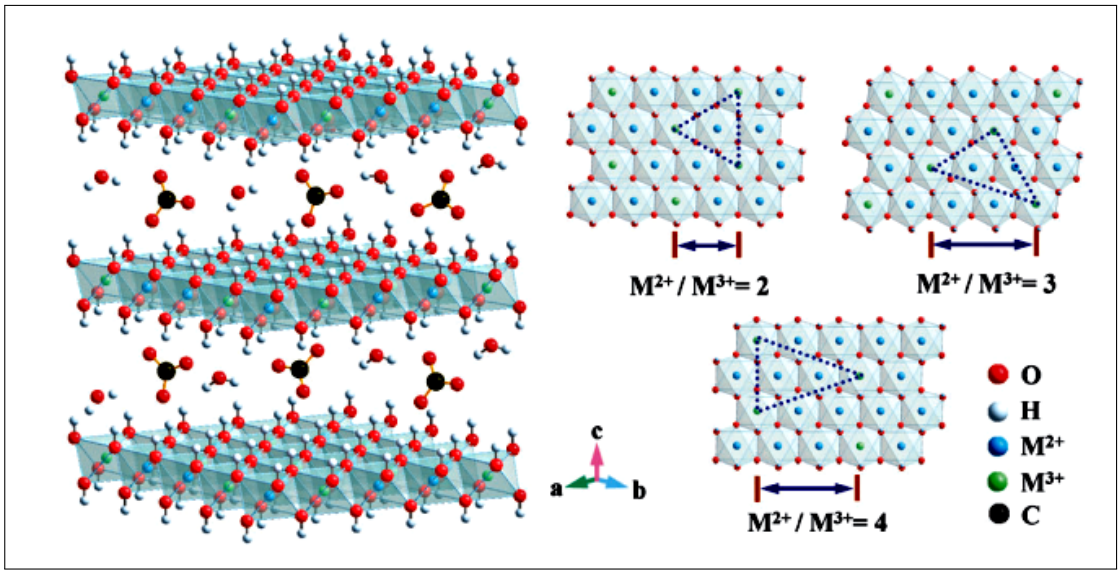


Figure 3.12: Optimal models of LDHs intercalated by carbonate anions, with varying M^{2+}:M^{2+} ratios. It should be noted that hydroxyl groups are always orientated towards the interlayer regions/galleries. Figure used with permission from: G. Fan, F. Li, D. G. Evans, X. Duan, *Chemical Society Reviews*, 2014, **43**, 7040–7066.©2014 Royal Society of Chemistry.

compared to conventional LDHs where the layers are aggregated due to hydrophilicity. [181] Unfortunately, previous methods of LDH layer exfoliation have used multi-step processes, inert atmospheres and toxic solvents, whilst suffering from low yields and a lack of scale-up potential. [181, 182] Recently Li et al. used a novel exfoliation technique to prepare a CuZn-based CO_2 hydrogenation catalyst with 46.0 D_{Cu} % and a 99.2 $m^2.g^{-1}$ Cu surface area, compared to an MMO with the same stoichiometric formula but a 19.6 D_{Cu} % and a 41.3 $m^2.g^{-1}$ Cu surface area. [180] For an additional reference, Turco et al. synthesised conventional, non-exfoliated CuZnAl-LDHs that had a 90 $m^2.g^{-1}$ total BET surface area (not just Cu surface) and a 8.5 D_{Cu} %. [163] This technique used by Li et al. was the aqueous miscible organic solvent treatment (AMO) method, it synthesised AMO-LDHs and it involved washing a wet cake of conventionally-prepared LDHs with a water-miscible solvent; the majority of the water was then filtered off and the LDH layers were stirred in the AMO solvent. [180–182] The AMO method is very quick, it takes approximately 1

day, and it is industrially scalable as the water-miscible solvent can be recovered easily, room temperature can be used and a number of cheap, abundant laboratory solvents can be utilised. [180–182] AMO-LDHs have acheived BET surface areas of $>$ 400 $m^2.g^{-1}$ compared to analogous conventional LDHs with $\approx$ 100 $m^2.g^{-1}$. [182] The main negative aspect of AMO-LDHs is that they typically have lower decomposition temperatures than conventional LDHs (see Section 3.7.1) but related problems can be avoided with low calcination, reduction and reaction temperatures (as are required for PEMFCs). [181]

The AMO-LDH precursor synthesised by Li et al. gave the highest D_{Cu} % of any MSR or CO_2 hydrogenation catalyst in literature and, as was mentioned before, it is known that CuZn-based MMOs can catalyse both MSR and CO_2 hydrogenation; therefore, the AMO method looks ideal for producing a novel, CuZn-based, high-D_{Cu} % MSR catalyst. [17, 113, 180] The AMO method was the basis from which the goals of this work were tackled, the theory behind how the AMO method exfoliates LDH layers is discussed in Section 5.1.1.

3.7.1 Properties of LDHs

LDHs have the following formula: $[M^{2+}_{1-x}M^{3+}_{x}(OH)_2]^{x+}(A^{n-})_{\frac{x}{n}} \bullet mH_2O$; x is equal to the molar ratio of M^{3+}/total metal and is generally in range of 0.2 - 0.4, whilst m is equal to the mol of water and can equal between $\approx$ 0 - 10. [178, 179, 181] AMO-LDHs have the same formula but also have an additional '$\bullet\, c$(AMO solvent)' component to the formula as well, where c = 0 - 10. [181] Metal cations with an ionic radii of $\approx$ 0.086 - 0.103 nm can occupy LDH cation lattice positions; however, metal cations with an oxidation state of $>$ 3 are often theorised to form non-LDH phases. [178]

Within the LDH layers M-OH bonds dominate the lattice energy whilst hydrogen bonding networks in the interlayer 'gallery' and electrostatic interactions between the layers are caused by interlayer water and anions, respectively. [179] Many different

anions can occupy this space depending on the synthesis method, often when metal nitrates are used for coprecipitation the majority anion will be NO_3^-; whereas, if the coprecipitation is conducted under non-inert, atmospheric conditions, CO_3^{2-} often becomes the dominant anion. [178, 183] Sasai et al. found that carbonate anions in LDH interlayer galleries do not undergo efficient anion exchange reactions, like other anions, because CO_3^{2-} forms an extremely thermodynamically-favourable hydrogen bonding network with interlayer water. [183]

It is theorised that the nature of the LDH lattice does not favour the aggregation of the same type of cations when various metallic precursors are introduced simultaneously unlike in the synthesis of some MMOs, which can have sections (or 'lakes') of different oxide phases. [179] This is the reason for LDHs' inherent elemental dispersion, and this dispersion can be topotactically maintained through reduction processes often leading to small metal particles that experience strong SMSI effects from the support i.e. high D_{Cu} % values. [179] However, the synthesis of LDHs is very sensitive to reaction conditions, especially pH, and as such very specific methodologies are required for their formation (see Section 5.1.2). Different elements' Pourbaix diagrams give just a small insight into the variation that can occur when only one synthesis parameter is changed for one element (because a potential is not applied in LDH synthesis); assuming no applied electric potential, there are 4, 2, 5 or 4 different phases that can form for Al, Ce, Cu or Zn cations alone in solution between 1 - 14 pH, respectively. [184] The pHs for different structural preference are different for each element, so when 3 or 4 metals are coprecipitated simultaneously there is the option for many different phase combinations i.e. different pHs, different flow rates/ratios/concentrations of metal precursors and different temperatures can lead to different thermodynamically-favoured precipitation reactions and crystallite sizes.

Conventional LDHs and AMO-LDHs have no differences in their PXRD patterns

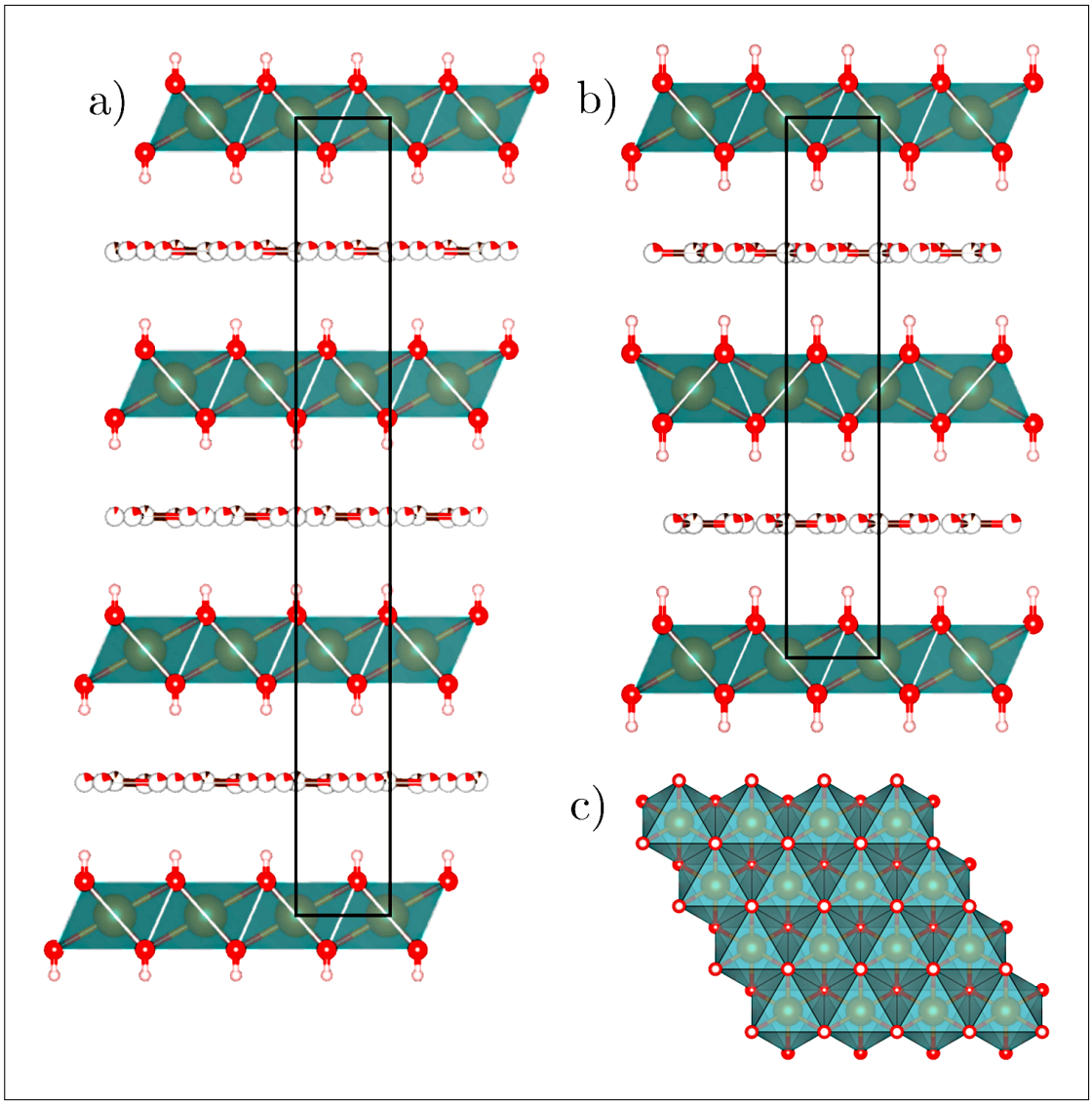


Figure 3.13: a) 3R LDH polytype and b) 2H LDH polytype unit cells along the *c* axis. c) (1 1 0) projection of a LDH layer. Figure used with permission from: E. S. Zhitova, S. V. Krivovichev, I. Pekov, H. C. Greenwell, *Mineralogical Magazine*, 2019, **83**, 269–280.©2018 Cambridge University Press.

or IR spectra. [181] There are different polytypes of LDHs that have different layer stacking geometry, for example $2H_1$ (2 layers hexagonally-stacked) and $3R_1/3R_2$ (3 layers rhombehedrally-stacked); this can result in different space groups, $P6_3/m$ and R3m respectively, models of these spacegroups are shown in Figure 3.13. [178, 185] The $3R_1$ polytype has a stacking sequence of: (AC CB BA AC...), whilst $3R_2$ has a stacking sequence of: (AC BA CB AC...), shown in Figure 3.14. [186] The major Cu

K-α PXRD peaks associated with the 3R-LDH phase (when a hexagonal 'unit' cell is used for calculations) include: (0 0 3) at ≈ 12 °, (0 0 6) at ≈ 24 °, (0 0 9) at ≈ 35 °, (0 1 2) at ≈ 36 °, (0 1 5) at ≈ 39 °, (0 1 8) at ≈ 47 °, (1 1 0) at ≈ 60 ° and (1 1 3) at ≈ 61 °. [181, 187] However, Cu K-α PXRD peaks with smaller intensities can also be seen for 3R-LDHs: (1 0 4) at ≈ 37 °, (1 0 7) at ≈ 43.5 °, (0 0 12) at ≈ 48 °, (1 0 10) at ≈ 52.5 °, (0 1 11) at ≈ 56 °, (1 0 13) at ≈ 63.5 ° and (1 1 6) at ≈ 64.5 °. [188–193] $3R_2$-LDH phases give very similar PXRD patterns to $3R_1$-LDHs, except the (0 1 2)/(0 1 5)/(0 1 8) are associated with and much stronger for $3R_1$-LDHs and (1 0 1)/(1 0 4)/(1 0 7) are associated with and much stronger for $3R_2$-LDHs. [194] Additionally, when a $3R_2$ polytype is formed from $3R_1$ the (0 0 6) peak shifts to ≈ 25 °, and new non-indexed peak appears at ≈ 19°. [195]

3R-LDHs and 2H-LDHs produce different Cu K-α PXRD peaks, see Figure 3.15. [196] The PXRD peaks associated with the $P6_3/m$ 2H LDH phase include: (0 0 2) at ≈ 11.6 °, (1 0 0) at ≈ 20.1 °, (1 0 1) at ≈ 21.0 °, (0 0 4) at 23.3 °, (1 1 0) at ≈ 35.2 °, (1 1 1) at ≈ 35.7 °, (1 1 2) at ≈ 37.2 °, (1 1 3) at ≈ 39.6 °, (1 1 4) at ≈ 42.7 °, (1 1 5) at ≈ 46.4 °, (1 1 6) at ≈ 50.7°, (1 1 8) at ≈ 60.5 °, (3 0 0) at ≈ 63.1 ° and (2 0 8) at ≈ 64.5 °. [197] It is not uncommon to observe all 2H and $3R_{1/2}$ polytypes in one LDH PXRD sample when carbonate anions are in the interlayer gallery. [196] The differences between the 2H, $3R_1$ and $3R_2$ LDH polytypes' PXRD patterns are visualised in Figure 3.15. [194, 196]

For MgAl-LDHs under LDH-synthesis conditions at ≈ 110 °C, the observed polytype can change from solely $3R_1$, which is more thermodynamically stable at lower temperatures, to $3R_2$ which is more stable at elevated temperatures; this change was only observed when the LDH was dispersed in solvent and not in the solid phase. [195] Budhysutanto et al. also noted that the transformation between LDH polytypes was kinetically faster when carbonate anions were not present in the interlayer region;

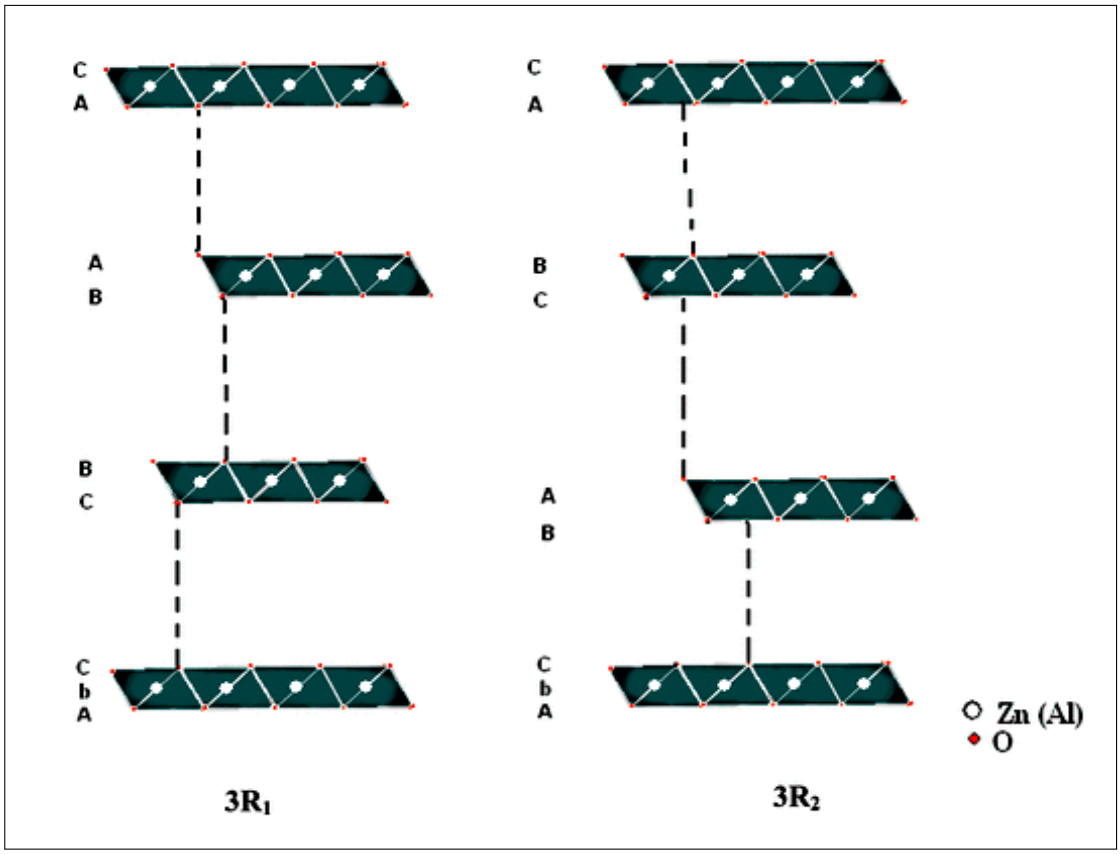


Figure 3.14: Zn-LDH models of $3R_1$ and $3R_2$ polytypes. A, B and C represent LDH layers with differently-aligned vertical OH^- groups; $3R_1$ and $3R_2$ are eclipsed and staggered, respectively. A lower case b represents the plane of Zn cations. Figure used with permission from: S. Radha, S. Prasanna, P. V. Kamath, *Crystal growth & design*, 2011, **11**, 2287–2293.©2011 American Chemical Society.

reflecting the observations of Sasai et al. that stated carbonate anions form very strong bonding networks in the LDH interlayer gallery compared to other potential anions. [183, 195]

Liu et al. studied LDHs with a DFT study and found that smaller anions that are more compactly-orientated and a higher LDH layer charge led to a smaller interlayer distance; this is reflected in the unit cell dimensions, that can be calculated from PXRD data (see Section 5.3.1). [198] Whereas, the M^{2+}:M^{3+} lattice ratio had a relatively large effect on the interlayer distance, it had a much smaller effect on the dimensions within the layered lattice. [198]

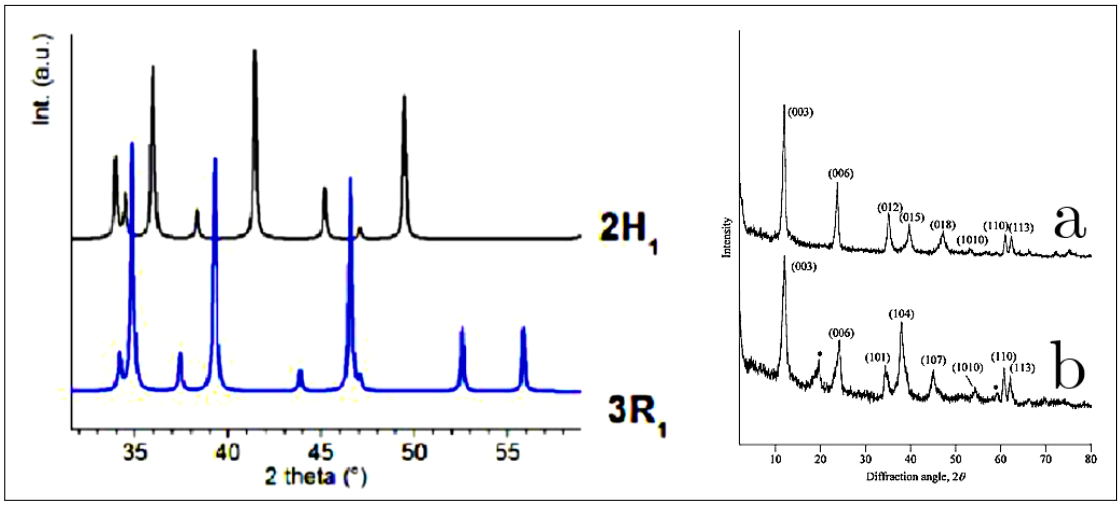


Figure 3.15: Left) Simulation of 2H and $3R_1$ LDH polytypes' PXRD patterns. Right) Experimental PXRD of MgAl-LDHs at a) 70 °C (predominantly $3R_1$) and at b) 180 °C (predominantly $3R_2$). Figures used with permission from: Left) A. Faour, C. Mousty, V. Prevot, B. Devouard, A. De Roy, P. Bordet, E. Elkaim, C. Taviot-Gueho, *The Journal of Physical Chemistry C*, 2012, **116**, 15646– 15659.©2012 American Chemical Society. Right) S. P. Newman, W. Jones, P. O'Connor, D. N. Stamires, *Journal of Materials Chemistry*, 2002, **12**, 153–155.©2002 Royal Society of Chemistry.

Thermal transitions of LDHs are considered 'topotactic'; this term means that the products of a solid state transformation have their orientation/crystal structure determined by their precursor, the original material/lattice. [199] LDHs undergo topotactic changes under consistent oxidising and thermal conditions because the LDH precursor possesses a high order and uniform elemental distribution. [179] Even when calcined at very high temperatures that provide a lot of thermal energy to favour entropy-driven changes, such as 700 °C, the LDH-derived MMOs still retain high elemental dispersion relative to calcined MMOs synthesised via other routes. [178, 180]

Conventional LDHs have three thermal transitions as follows: i) < 150 °C, the loss of interlayer, physisorbed water and solvents ii) 200 - 400 °C, the replacement of OH^- groups with O^{2-} in the lattice (dehydroxylation) and loss of interlayer anions, such as carbonate (decarbonation) iii) > 450 °C, decomposition to MMOs. [106, 177, 178, 181] These temperatures will vary depending on the ratios of metals that constitute

them, as this will change the nature of the bonding and electrostatic interactions and, therefore, the lattice energy; for example, Hobbs et al. observe these transitions at different temperatures for NiFe- and MgAl-LDHs via TEM. As mentioned AMO-LDHs are less thermodynamically stable than conventional LDHs, so these transitions may occur at relatively lower temperatures. [181]

Dehydroxylation of LDHs where the hexagonal layered morphology is topotactically-retained leads to the formation of layered double oxides (LDOs). [177] Decomposition of LDHs can increase the BET surface area of the materials, however, thermal treatment above 400 °C for some LDHs (such as CuZnAl LDHs) can lead to a decrease in the surface area due to the loss of layered morphology. [163] Hobbs et al. observe the losses of certain PXRD peaks, and therefore LDH (h k l) phases, at certain temperatures e.g. for NiFe-LDHs, the (1 0 1) peak is lost during the dehydration of the interlayer spaces and the (0 0 3) broadens with temperature but is retained up until 450 °C, when hexagonal crystallinity is completely lost and the sample becomes an amorphous MMO. [200] It was found that whilst slower calcination heating rates preserved a higher degree of crystallinity in LDH-derived materials, it lowered the surface areas of the resultant calcined materials; therefore, it appeared that a slightly defective layered structure gives a higher surface area than a wholly crystalline or decomposed structure. [163]

It should also be noted, that once calcined, LDOs should be kept under conditions with minimal humidity to avoid unexplained differences when comparing the properties of different LDOs. This is because a 'memory effect' is well documented for LDHs, due to the nature of their topotactic transitions, water from the atmosphere can re-hydroxylate the sample re-form LDH interlayer regions. [178]

The only instance of a LDH-derived MSR catalyst, that was synthesised using a calcination temperature theoretically low enough to cause the formation of a Cu

nanoparticles supported on a LDO, was performed by Kuhl et al. [86] The catalyst used by Kuhl et al. is displayed in Table 3.2, it was found that the use of high calcination temperatures led to MMOs but a calcination temperature of 330 °C led to a very amorphous PXRD where the phase was not discernible; the term 'layered double' was not discussed beyond the naming convention of the precursors and the formation of near-amorphous oxide structures was attributed to the 330 °C calcination temperature. [86] The catalyst had a relatively impressive H_2:CO production ratio, 597 mol_{H_2}:mol_{CO}, considering the MSR conditions used were at 260 °C and did not have an excess water content. [86]

Chapter 4

Research Plan

This work looks to prepare optimal catalysts for a MSR process that produces H_2 for a PEMFC, without the need for an additional catalyst to remove the CO by-product. This requires a catalyst that can operate at relatively low MSR temperatures whilst having a high H_2 production rate and a high H_2:CO selectivity ratio. The literature review in Chapter 3 has demonstrated that Cu-based catalysts are good catalysts for low temperature MSR and that increasing their surface area, thermal stability and D_{Cu} % can increase the H_2 production rate. The most important of which appeared to be D_{Cu} % because it was theorised that the main pathway for synthesising CO under low-temperature MSR conditions is RWGS, which can occur on both the Cu-support interface and metal oxide vacancy sites, whereas MSR can only occur at the interface. [20] Therefore, maximising D_{Cu} % should theoretically maximise the ratio of (MSR+RWGS):(only RWGS) active site ratio, and subsequently improve the H_2:CO production ratio.

Currently the deployment of Cu-based MSR catalysts to power on-board PEMFC vehicles is not economically feasible. For reference a 'Toyota Mirai 2017®' hydrogen fuel cell powered car requires $\approx$ 1 $kg_{H_2}.h^{-1}$ which is equivalent to $\approx$ 137,000 $\mu mol_{H_2}.s^{-1}$. [201] The highest H_2 production rate of a Cu-based catalyst in the low-temperature MSR regime (defined as $<$ 200 °C in a kinetic study of CuAl catalysts

by Idem et al.) produces 48.2 $\mu mol_{H_2}.g_{cat}^{-1}s^{-1}$. [108, 202] This means an on-board PEMFC vehicle would require roughly 2 kg of current Cu-based literature catalysts to operate and that is without factoring in the catalyst stability. Additionally, the best observed H_2:CO ratio, $\approx$ 3000 mol_{H_2}:mol_{CO}, observed by a Cu-based MSR catalyst would still produce a high enough CO concentration ($>$ 10 ppm) to significantly poison a PEMFC. [20–22, 77] However, there is much room to improve upon these catalysts, the catalyst synthesised by Shishido et al., that had the best low-temperature MSR activity, had a BET surface area of $\approx$ 108 $m^2.g^{-1}$ and the catalyst with the highest H_2:CO ratio, synthesised by Mateos-Pedrero et al., had a 23.1 % D_{Cu} %. [77, 108] A new class of AMO-LDHs materials have been found to potentially achieve BET surface areas of up to $\approx$ 400 $m^2.g^{-1}$; Li et al. synthesised a CuZnGa catalyst, using an AMO-LDH as a precursor, that achieved a D_{Cu} % of 46.0 %. [108, 180]

AMO-LDHs offer a lot of potential as MSR catalyst precursors because they provide great elemental dispersion, can incorporate a wide variety of elements and are cheap to synthesise.

Specifically, this research aims to achieve its goals by synthesising Cu nanoparticles supported on layered double oxides. Such materials would potentially achieve very high Cu dispersions as seen by Li et al. and also have an increased surface area due to a partial decomposition of the LDH structure but not a complete decomposition to MMO. [180] Avoiding complete decomposition and retaining a layered morphology should theoretically maximise the BET surface area whilst physically limiting Cu nanoparticle sintering with the mesoporous/layered morphology of LDOs (see Section 2.5.4). [58, 60, 163] The experimental Chapters 6, 7 and 8 explore how the presence of different constituent M^{2+}/M^{3+} cations in CuZn-based LDH precursors improve MSR activity via potential textural support, MSIs, oxygen vacancy formation, redox reactions and many other effects. Each chapter focuses on the addition of a dif-

ferent element or elements and contains a preface summarising why the given element was of interest. Additionally, this work aims to explain why these catalytic performance improvements occur and a wide range of techniques were applied to achieve this (see next in Chapter 5); including the computational modelling of previously-unsolved lanthanide-doped LDHs' structure.

Before this work, no AMO-LDH-derived MSR catalysts had been reported in literature and only the use of one potentially-LDO-based MSR catalyst was reported (but its layered morphology was not explored); these research plans were novel when they were established.

Chapter 5

Experimental

5.1 Synthesis of AMO-LDHs

5.1.1 AMO method theory and other considerations

As outlined in Section 3.7.1 LDHs have a structure of stacked, positively-charged layers, in between the layers is a 'gallery' of water hydrogen bonding networks and anions. Figure 5.1.a demonstrates the distribution of these species in relation to each other via a modelled LDH interlayer gallery. [182] The molecular dynamics simulations of Erastova et al. show water molecules form three 'hydration shells' at the LDH surface because the orientation of the surface hydroxyl groups and carbonate anions cause the water to adopt the most sterically and electrostatically favourable positions; however beyond this, water adopts a bulk-like distribution at the centre of the interlayer gallery. [182]

When water-miscible solvents are introduced to LDHs dispersed in water they can enter the water hydration shells and interact with the LDH surface. [182] The principle of the AMO-LDH method is that AMO solvents hydrogen bond with the LDH hydroxyl groups and then block the formation of an extended water hydrogen bonding network from the surface to the water in the interlayer space. [182] This weakens the interlayer attraction and exfoliates layers when LDHs have the majority

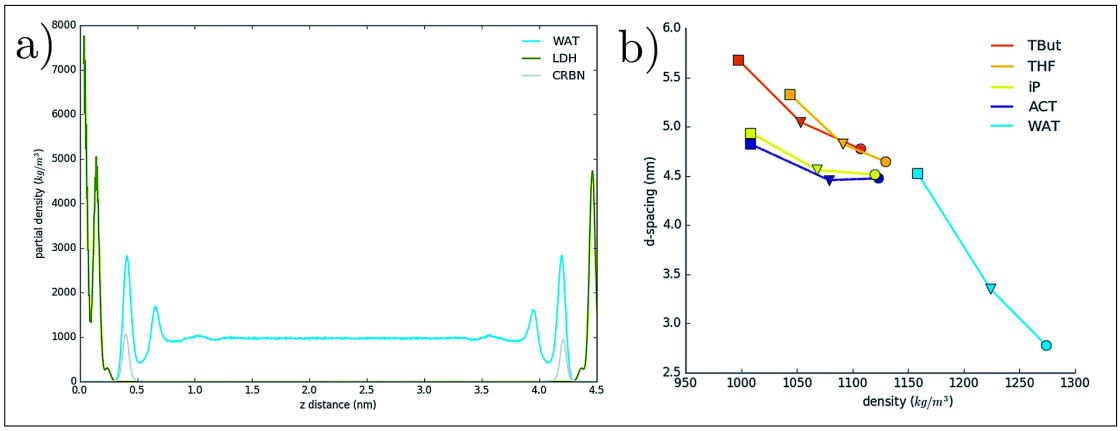


Figure 5.1: Molecular dynamics simulations of LDH interlayer spaces. a) Simulated partial density of LDH interlayer gallery model; including densities of H_2O, LDH layer and carbonate anions. WAT = water and CRBN = carbonate anion. b) The simulated LDH interlayer spacing, *d*, as a function of AMO method solvent. WAT = water, ACT = acetone, iP = isopropanol, TBut = tert-butanol, THF = tetrahydrofuran. The shapes represent different solvent:water molecule ratios used in the models: Circle = 100:1000, Triangle = 200:600 and Square = 300:300 (For water models these shapes represent: Circle = 0:800, Triangle = 0:1000 and Square = 0:1400). Figures used with permission from: V. Erastova, M. T. Degiacomi, D. O'Hare and H. C. Greenwell, *RSC Adv.*, 2017, **7**, 5076 .©2017 Royal Society of Chemistry.

of the interlayer water replaced with the AMO solvent by filtration and stirring cycles. The effectiveness of an AMO solvent for exfoliating LDH layers is determined by: i) their hydrophilicity and an ability to mix into the hydration shells and reach the LDH surface ii) the strength of the hydrogen bond they can form with the surface hydroxyl iii) the steric bulk of their alkyl chains and how effectively this disrupts hydrogen bonding in the hydration shells. Figure 5.1.b displays simulations of how various amounts of different AMO solvents can exfoliate LDH layers i.e. reduce their density and increase the intelayer distance, *d*. [182]

For this work, acetone was chosen as the AMO solvent of choice because it caused the third greatest decrease in interlaying H-bonding of the 9 common solvents simulated by Erastova et al. [182] Additionally, it is abundant, non-toxic, cheap and, importantly, highly volatile. It was theorised it would only require mild vacuum and temperature conditions for its removal following the synthesis of AMO-LDHs.

This allowed the acetone to be removed at room temperature after synthesis as a precaution, avoiding any potential thermal sintering/decomposition effects of the relatively unstable AMO-LDH lattices but allowing the materials to be stored in a dry desiccator.

Using Cu^{2+} in LDH synthesis has previously caused malachite phases to form; Turco et al. had to introduce the Cu reactant dropwise during coprecipitation to allow pure LDH structures to form. [97, 163] However, above a Cu metal mol ratio of 0.15, some polyphasic materials formed; this was attributed to Jahn-Teller Cu distortions and the urea LDH synthesis method generating ammonia that "depleted" the Cu content via the formation $[Cu(NH_3)_x(H_2O)_x]$ complexes. [163] Therefore, this work adopted a non-urea coprecipitation method that added the metal precursors slowly via syringe pump.

5.1.2 Synthesis of CuZn-based AMO-LDHs

0.015 mol of metal nitrate hydrates, in the chosen Cu:Mg:Zn:Ga:Al:Ce mol % ratio, and 32 mL of deionised H_2O were added to a 60 mL syringe. 32 mL of pH 10.2 Na_2CO_3 (aq) was added to a 3-neck round bottom flask. The nitrate solution was added to the round bottom flask at 0.84 $mL.min^{-1}$ via syringe pump, the mixture was stirred at 700 rpm at room temperature by a magnetic stirrer bar; the pH was kept constant at pH 10.2 $\pm$ 0.2 by adding 1 M NaOH (aq) via a variable flow rate peristaltic pump. The mixture was left to stir at 700 rpm and room temperature for 18 hours. The mixture was filtered under vacuum and the precipitate was washed with 400 mL of deionised H_2O and then 200 mL of acetone; $\approx$ 5 mL of acetone wash was left on top of the precipitate to keep it as a wet cake. The wet cake was then added to 200 mL of acetone and stirred at 700 rpm for 2 hours at room temperature. The resulting mixture was then filtered under vacuum and the precipitate was washed with 200 mL of acetone. The precipitate was then dried under 20 mbar of dynamic

vacuum at room temperature for 16 hours to yield the LDH precursor.

Two batches for each AMO-LDH material mentioned in this thesis were synthesised due to the high number of different analytical techniques used; the respective 'first batches' were primarily used up for catalytic testing, PXRD and reduced-PXRD. In exception to this, only one batch of each non-Ce, lanthanide-doped AMO-LDH was synthesised and for some materials a third batch was synthesised exclusively for further XAS analysis.

5.2 Calcination, reduction and catalyst storage

LDHs were calcined under 50 mL.min^{-1} of air with the following temperature programme: Ramp 10 °C.min^{-1} to 80 °C, dwell 1 h, ramp 10 °C.min^{-1} to 150 °C, dwell 1 h, ramp 10 °C.min^{-1} to 330 °C, dwell 3 h.

Calcined samples were placed in a quartz boat in a closed flow reactor/furnace system; the system was purged with N_2 (g) for 30 minutes before the sample was reduced with 30 mL.min^{-1} of 3 % H_2/N_2 (g) following temperature programme: Ramp 10 °C.min^{-1} to 290 °C, dwell 2 h.

Both LDH and calcined samples were stored under 10 mbar of static atmosphere in a vacuum desiccator with a desiccant. This was to minimise the extent of the LDH memory effect and aggregation of the previously-exfoliated LDH layers by atmospheric water. Reduced samples were transferred to and stored in a glove box without exposure to atmospheric conditions (entire sealed furnace tubes were transferred into the glove box); this allowed sealed samples of reduced samples to be prepared in the glove box for various other experimental techniques such as PXRD and XAS.

5.3 PXRD

5.3.1 X-Ray diffraction theory

Incident X-rays can be diffracted by powdered materials, powder X-ray diffraction analysis uses a detector to determine the angle of the diffracted X-rays relative to the sample. Bragg's Law equates the distance (d) between two planes of atoms in a crystal to the diffraction angle. Therefore, this angle can be used to assign the different Miller indices ($h\ k\ l$) planes of atoms that exist in a crystal because such planes have different d spacing. The intensity of the X-ray absorption at a given angle is related to the amount of that crystal plane in the sample. Additionally, the Scherrer equation can use the broadness of a PXRD peak, its full width at half maximum intensity (FWHM), to estimate the dimension of the responsible crystallite perpendicular to the relative ($h\ k\ l$) plane. Additionally, Bragg's law can be combined with 'plane spacing' equations to estimate unit cell dimensions. The Scherrer equation, the plane spacing equation for a hexagonal unit cell and Bragg's Law are shown below: [203, 204]

$$\text{Bragg's Law: } \lambda = 2d\sin(\theta)$$

$$\text{Hexagonal plane spacing equation: } \frac{1}{d_{hkl}^2} = \left(\frac{4}{3} \times \frac{h^2 + hk + k^2}{a^2}\right) + \frac{l^2}{c^2}$$

$$\text{Scherrer equation: D} = \frac{R\lambda}{\beta(cos\theta)}$$

Where λ = wavelength of incident X-ray radiation (0.15406 nm in this work), d = interplanar spacing, θ = glancing angle, hkl = miller indices, a/c = hexagonal unit cell parmaters, D = crystallite thickness, R = Scherrer constant (0.9 in this work), and β = PXRD peak FWHM. [203, 204]

In Section 3.7.1, it was established hexagonal LDH layers could be stacked in two major polytypes, 2H ($P6_3/m$) and 3R (R3m), which stacked LDH layers in a hexagonal or rhombohedral fashion, respectively. Both $P6_3/m$ and R3m LDHs' unit cells are modelled in literature with hexagonal 'unit' cells, but containing 2 and 3 LDH

layers respectively i.e. the unit cells' angles $\alpha/\beta = 90$ ° and $\gamma = 120$ °, whilst the unit cell dimensions are $a = b \neq c$. [190, 191, 197] This has resulted in PXRD calculations for hexagonal unit cells being used for LDHs throughout literature. [177, 187, 203, 205] It is important to remember that the hexagonal 'unit' cells, used for R3m LDH PXRD calculations, may not be the smallest repeating unit for that structure but they allow plane spacing equations to be conducted. This is because the rhombohedral spacing equation would not be valid for calculating the interlayer distance because it assumes the interlayer distance was fixed with respect to the M-OH bond lengths within the lattice, which is not the case; for example, studies have proven that varying M^{2+}:M^{3+} content in the hydroxide layers or temperature can change the interlayer spacing and, therefore, the c parameter. [177, 182, 206] This technique, of not using the smallest repeating cell, does not change the real average M-OH or interlayer distance. Overall, it is important to remember that 3R-LDH polytypes' PXRD data is displayed using a hexagonal unit cell and, therefore, the PXRD peaks are labelled with (h k l) planes from that hexagonal unit cell; however, the calculated c parameter is equivalent to 3 interlayer d-spacings.

5.3.2 PXRD methodology

The powder X-Ray diffraction (PXRD) patterns for LDHs and LDOs were recorded using a X'Pert PRO PANalytic X-ray diffractometer; 40 kV and 40mA powered Cu Kα X-Rays. Samples were packed onto flat glass holders and scanned in 2θ steps of 0.0167 ° at a rate of 1.2 s per step; each measurement covered a 2θ range of 5 – 72 °.

A standardised semi-automated method of integrating the LDH PXRD patterns was implemented, and the resultant data was analysed using the Bragg's Law/plane spacing equation/Scherrer equation, assuming the LDH samples had hexagonal 'unit' cells.

The PXRD analysis for the reduced catalyst samples was performed using a

Bruker AXS D8 Advance Eco diffractometer and custom air-tight metal/plastic holders. 40 kV and 25mA Cu Kα X-Rays were used to scan a 2θ range of 30 - 80 °, in 2θ steps of 0.019 ° at a rate of 1 s per step. The Cu^0 particles were assumed to be cubic. A standardised method of integrating the reduced PXRD patterns was implemented.

5.4 TGA

Thermogravimetric analysis (TGA) can identify the thermal stability of materials. When a thermally-induced process changes the mols of different species in the solid sample, this is detected during a continuous weighing of the sample.

5.4.1 TGA methodology

TGA was conducted with a SDT Q600 thermal analysis machine. A sample was loaded into an tared alumina pan of known mass and the pan was attached to a weighing scale. The reaction conditions were sealed, the sample was subjected to a consistent flow of 100 mL min^1 dry air and the sample was heated to 800 °C at a rate of 10 °C.min^{-1}.

5.5 TPR

Temperature programmed reduction (TPR) exposes materials to a continuous stream of reducing hydrogen gas whilst ramping the temperature. When a species achieves the required thermal activation energy and begins to react with the hydrogen, the drop in outlet hydrogen is detected using a TCD. This allows species with different reduction temperatures within a sample to be determined.

5.5.1 TPR methodology

TPR experiments were carried out using a Quantachrome ChemBET Pulsar TPR/TPD chemisorption instrument. For each measurement, $\approx$ 30 mg of LDO sam-

ple was loaded into a quartz u-tube, the system was purged with nitrogen gas at 100 °C before it was returned to 40 °C and 20 mL.min-1 5 % H_2/N_2 (g) was introduced; the sample was then heated to 600 °C at 10 °C.min^{-1}. A TCD measured the flow of hydrogen gas leaving the sample tube.

5.6 BET surface area analysis

5.6.1 BET surface area theory

Brunauer–Emmett–Teller (BET) surface area analysis involves completely degassing a solid sample at elevated temperatures, before exposing it to a cycle of gradual nitrogen gas exposure and vacuum whilst the system is cooled by liquid nitrogen. The sample is constantly weighed so the amount of adsorbing and desorbing nitrogen gas is quantified, as well as the associated rates. This allows for the determination of the material's surface area in $m^2.g^{-1}$ and additionally gives insight into the structure of the material because different pore sizes cause varying adsorption and desorption rates.

5.6.2 BET surface area analysis methodology

The BET surface areas of the calcined LDO samples were obtained using a micromeritics TriStarII PLUS; at the Surface Analysis Facility at the University of Oxford. The samples were placed in purpose-built glass vessels of known mass and degassed at 110 °C under vacuum overnight, then N_2 was adsorbed and desorbed from the samples at -196 °C; the total mass of sample and vessel was monitored throughout.

5.7 D_{Cu} % analysis

5.7.1 N_2O/H_2 titration theory

N_2O gas is well known to take part in the following reaction with copper: 2Cu

(s) + N_2O (g) $\longrightarrow$ Cu_2O (s) + N_2 (g). Reduced copper samples can be exposed to discrete injections of known quantities of N_2O gas and a TCD can be used to detect the outlet gas. The number of injections needs to be counted. For an injection cycle, if no N_2O is detected then it has all been reduced to nitrogen gas. But once the same amount of N_2O is subsequently detected for several injections, and corresponds to the known injection amount, the experiment can be stopped. Then using the known amount of N_2O (per the unreacted peak), the mols of reacted N_2O from the other injections can be calculated; therefore, the amount of surface Cu^0 mol can also be calculated. This value of surface Cu can be used in conjunction with ICP-MS data (see Section 5.13) to calculate the dispersion of Cu (D_{Cu} %), which is the ratio of surface Cu to total Cu.

5.7.2 N_2O/H_2 titration methodology

The Cu dispersion percentages of the samples were measured using a Quantachrome ChemBET Pulsar TPR/TPD chemisorption instrument. Each LDO sample, $\approx$ 20 mg, was loaded into a u-tube and reduced in-situ (using the standard reduction methodology, Section 5.2). Next, the temperature was lowered to 60 °C and N_2O (g) was introduced at 20 mL.min^{-1} for 90 min. Then the temperature was increased to 300 °C at 10 °C.min^{-1}, and 20 mL.min^{-1} of N_2 (g) was introduced. 95 µL of H_2 (g) was injected periodically, unreacted H_2 was detected by TCD; H_2 injections were stopped when the TCD peak representing unreacted H_2 plateaued.

5.8 EPR

5.8.1 EPR theory

In a magnetic field. the spin, m_s, of an unpaired electron can be changed by the absorption or emission of energy; this energy is dependent upon the environment of the electron (its position relative to other magnetic moments) and the applied

magnetic field strength. Continuous wave electron paramagnetic resonance (EPR) analysis changes the applied magnetic field strength whilst maintaining a constant incident energy. Energy absorption peaks can be assigned to a particular electron environment because the magnetic field and incident energy are known.

5.8.2 EPR methodology

Continuous wave EPR analysis was performed using a Bruker EMX EPR spectrometer set at 9.4 GHz (X-band). All X-Band spectra were collected over a magnetic field range of 2800 - 4000 Gauss, at a temperature of 291 K; 10 scans were collected for the analysis of each sample. These experiments were performed at the CAESR, University of Oxford.

5.9 TEM analysis

5.9.1 TEM theory

Visual images can be generated when a camera captures and processes beams of visible light photons that are reflected into the camera's lens by surrounding objects. Transition electron microscopy (TEM) applies a similar concept but for beams of electrons that are incident on a very thin material; the detector measures how many electrons pass through the sample rather than how much is reflected (see Figure 5.2). [207]. This data is then used to generate an image that can visualise nanoparticles (with a resolution of up to 0.1 nm). [168]

5.9.2 TEM methodology

Scanning transmission electron microscopy, with high-angle annular dark-field detection (HAADF-STEM), was performed on an aberration-corrected JEOL ARM200F microscope to obtain images of the samples. TEM samples were prepared by sonicating $\approx$ 5 mg of the material in 2 mL acetone for 15 minutes, before dropwise addition

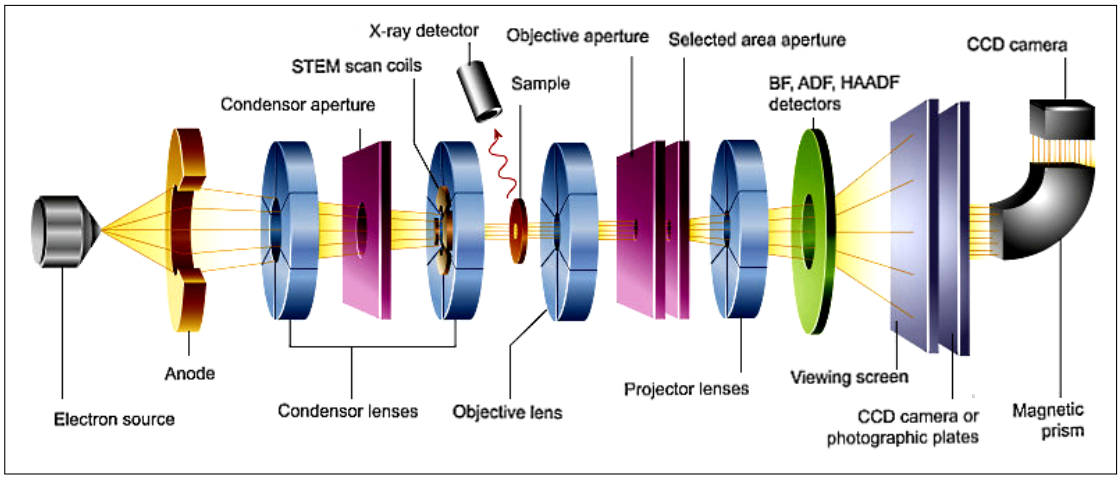


Figure 5.2: Exploded schematic of common TEM components. Figure used with permission from: B. Inkson, *Materials characterization using nondestructive evaluation (NDE) methods*, Elsevier, 2016, pp. 17–43.©2016 Elsevier Ltd.

of the solution onto the holey carbon coated copper 400 mesh grid. The copper grids were then dried overnight under vacuum at room temperature prior to imaging. The microscope was operated at 200 kV and the HAADF detector semi-angles ranged from 75 – 270 mrad; the probe array size was 512 x 512 and the dwell time per pixel was set at 0.3 s per pixel. These experiments were performed at the EM facility at the University of Oxford.

Lightfield TEM analysis was performed by Dr. Valeria Castelletto using JEOL-JEM 2100 at the Harwell Research Complex, UK. Samples for this analysis were prepared by sonicating ≈ 5 mg of the material in 1 mL ethanol for 15 minutes, before dropwise addition of the solution onto the holey carbon coated copper 400 mesh grid. The copper grids were then dried overnight under vacuum at room temperature prior to imaging.

5.10 X-ray photoelectron spectroscopy

5.10.1 XPS theory

XPS analysis involves irradiating a sample with a constant high-energy X-Ray

source to ionise the core electrons of its constituent elements. The analysis is performed under an ultra-high vacuum so the released, ionised electrons do not interact with any gaseous species, this allows the kinetic energy of the electrons to be determined by a detector. This kinetic energy can be used to calculate the ionisation energy, $E_k = h\nu$ - E_i; where E_k is the kinetic energy of the photoelectron (which is shown as the photoelectron energy, e_p, in Figure 5.3), $h\nu$ is the energy of the incident ionising X-Ray and E_i is the ionisation energy required. [208, 209] Each element has a characteristic binding/kinetic energy associated with an ionised electron for each specific orbital. Different oxidation states of a given element cause different characteristic ionisation energies and, therefore, XPS spectra can be used to uncover some information about the present oxidation states. XPS analyses the top few nm of a sample due to the photoelectron escape depth; therefore, to only analyse the topmost atomic layer a lower energy technique is required such as high-sensitive low-energy ion scattering. [170]

However, experimentally electrons from a given element's orbital do not give one B.E. peak. There are quantum microstates that electrons can occupy within orbitals, these arise due to electrons experiencing spin-orbit coupling and, therefore, these electrons have different total angular momentum and occupy different discrete energy levels. [210] The quantum number of total angular momentum is represented by j and is equal to a sum of the orbital angular momentum (l) and the electron spin quantum number (which can be $+\frac{1}{2}$ or $-\frac{1}{2}$). [210] Because there are two discrete electron spin quantum numbers, any orbital with $l > 1$ (any non-s orbital) has two discrete j energy levels; where the two angular momenta are either in the same direction (less energetically stable) or in the opposite direction (more energetically stable). Due to their different stability/energy levels, the quantum microstate with the lower j value appears to have a higher B.E. in XPS. [211] However, the quantum microstate with the higher j value will have a larger XPS signal area. This is because the two different

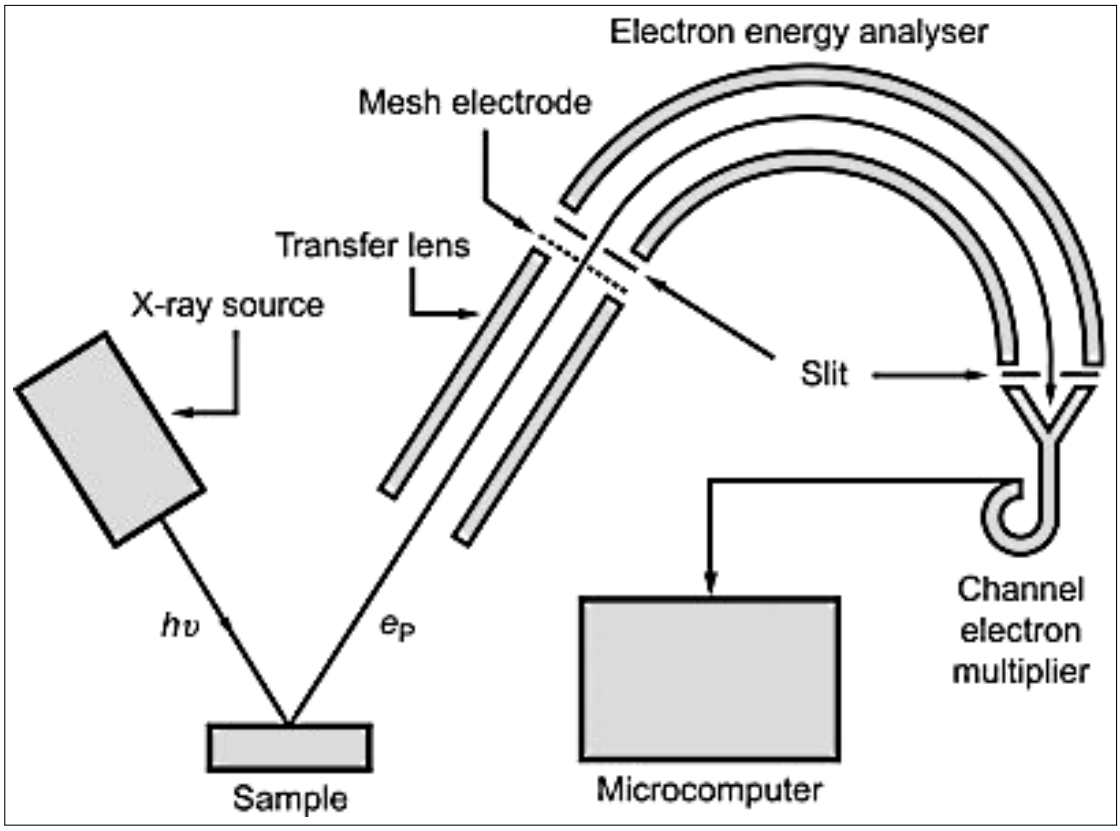


Figure 5.3: Diagram of an experimental XPS set-up, figure used with permission from: H. Seyama, M. Souma, B.K.G. Theng, *Developments in Clay Science*, 2013, **5**, 161-176.©2013 Elsevier Ltd.

j levels have a different number of degenerate energy levels based on the number of 3D 'real space' or 'z-projection' permutations they have. [211]

In summary, when analysing XPS spectra, the ionisation of electrons from a given element's p orbital give a doublet peak with a signal ratio of 1:2 and for an electron from a specific element's d orbital a doublet peak, with a 2:3 ratio, appears; the peak with a lower B.E., within a doublet, will always have the higher peak area. [211] It is also important to note that when any Ce^{4+} sample is initially exposed to X-ray radiation, the reduction to Ce^{3+} can partially be facilitated; therefore, this introduces a systematic error where all Ce^{3+} estimations are slightly too high. [212]

5.10.2 XPS method

X-ray photoelectron spectroscopy (XPS) measurements were conducted using a Thermo scientific NEXSA XPS system with a monochromatic Al Kα X-ray source (1486.6 eV); at EPSRC National Facility for X-Ray Photoelectron Spectroscopy, Harwell. It was operated at an anode voltage of 12 kV and a pass energy of 50 eV at about 10×10^{10} mbar vacuum. The X-ray spot diameter was 400 m, the scanning step size was 0.1 eV; the signal accumulation of 10 cycles was performed. A low-energy electron flood gun was used to deliver the electrons to the sample surface. The data was analysed using CasaXPS. The only parameter constraints enacted were on the peak intensities and positions of j-coupled states; to reflect the degeneracies of the states and their spin-orbit coupling energy.

5.11 XAS

5.11.1 XAS theory

Synchrotron X-ray sources can irradiate samples with a varying wavelength of X-ray radiation to excite core electrons. [208] As was discussed in Section 5.10.1, binding energies of electrons are very specific to the environment and element, in X-ray absorption spectroscopy (XAS) the ionisation energy of the target core electron is known as the 'edge' and the incident X-ray energy is increased slowly from just below the edge to above the edge over time.

XAS spectra have 3 important regimes for a given edge, these include: i) the pre-edge where core electrons are excited but not ionised. ii) the X-ray absorption near-edge structure (XANES) between the ionisation energy and 10 eV above it. Variation and distortions in oxidation numbers and coordination environments cause characteristic spectra to form. iii) $>$ 50 eV above the ionisation energy the extended X-ray absorption fine structure (EXAFS) regime can be observed. With high incident X-

ray radiation the ejected photoelectrons can be backscattered by neighbouring atoms. EXAFS analysis can give information on local coordination environments, including bond distances to nearby atoms even for amorphous samples. [208]

XANES and EXAFS analysis can be performed for one XAS spectrum but often multiple repetitions are conducted and merged to reduce the possible error. Gaussian fittings of XANES spectra using known binding peak energies from literature can be used to estimate the oxidation state of the atom responsible for the edge. Density functional theory computational (DFT) and super-computer modelling can be used to simulate XAS spectra for known structures and novel proposed models; these simulated spectra can then be used to recreate the experimental XAS spectra. This technique can be used iteratively to find the model(s) that statistically fit the experimental XAS spectra the best; thereby, deciphering the likely coordination number, bond lengths and oxidation number. Such models can be used to support experimental observations if the theoretical structure is probable and the statical fitting parameters are in agreement with the observed experimental data.

5.11.2 XAS spectra collection

Cu K and Ce L_3 edge EXAFS data was collected for LDHs at the BL07A beamline, National Synchrotron Radiation Research Centre, Taiwan. The Cu K and Ce L_3 absorption edges were measured using a Lytle fluorescence detector and a Si (111) double crystal monochromator was used to scan the photon energy. Two sets of scans for each ex-situ sample were collected for reproducibility. Metallic foils were used as calibrating references.

Cu/Zn K and Ce L_3 edge XAS data was collected using the B18 and I20 beamlines at Diamond Light Source synchrotron, UK, under the supervision of Dr. Diego Gianolio and Dr. Fred Mosselmans respectively. > 2 scans were collected for each sample's edge and they were merged using ARTEMIS software. Metallic foils were

used as calibrating references; whilst Cu, Zn and Ce oxides were measured as additional references. The spectra were measured in a protocol that minimised X-ray induced sample damage in partial fluorescence yield mode.

5.11.3 XAS modelling

Modelling was performed by Konstantin Lebedev, University of Oxford, 2021. XANES spectra were analysed using Demeter ATHENA and ARTEMIS. Firstly, a fitted, linear pre-edge background was subtracted from XANES spectra and the post-edge background was also processed. Then the edge height was normalised using an arctangent function. The maximum of the first derivative of the edge was used to determine the energy threshold. For some samples the XANES spectra were quantitatively fitted using Gaussian function(s).

Fourier transform (FT) functions were applied to experimental EXAFS spectra using ARTEMIS software.

Density-functional theory (DFT) calculations with an effective core potential and full-electron relativistic approach were performed using VASP software and a projector-augmented wave pseudopotential. [213] A generalized gradient approximation, Perdew—Burke—Ernzerhof form and a cutoff energy (450 eV) were adopted for the plane wave basis set. [214] The ionic convergence limit was set to 0.02 eV.Å^1, while the electronic convergence limit was set to 1×10^{-5} eV. The DFT-D3 scheme of dispersion correction used by Grimme et al. was adopted to describe van der Waals interactions in the systems. [215] To avoid interactions between the periodic units, a vacuum space of 15 Å was set. Supercells consisting of 2×2 cells were used for geometrical optimization and the electronic structure calculation. A Monkhorst—Pack grid of size of $6 \times 6 \times 1$ was used to sample the surface Brillouin zone. Crystal structure database .cif files were used for simulating XAS spectra for known structures. [216]

EXAFS and XANES spectra for DFT models were simulated using ATHENA and ARTEMIS software and method; assuming the muffin-tin approximation. The method was appropriate for the simulation of small, non-symmetrical structures but not for estimating core energy levels. These simulated spectra were R-space fitted to experimental spectra taking into account single-shell scattering contributions for the first three shells of atomic neighbours. The simulation of the EXAFS signals involved contributions from the first, second, and third coordination shells (the third shell contribution was very small but not non-negligible). Extra single-scattering contributions did not improve the quality of the fit. Multiple scattering effects were found to be minimal therefore only single-scattering effects were deemed important for the calculations. The adjustments of spectra were performed in the k and R ranges for each fitting of the sample, where R is the distance to the neighbouring atom; for the Ce L_3 edge this was $3 < k < 6.5$ Å^1 and $1.2 < R < 5$ Å. For the fitting procedure, the coordination number was fixed according to the coordination number from the DFT optimized structure, the distance (R) and the Debye-Waller factor (σ^2) were allowed to vary.

Linear combination fitting (LCF) was performed using ATHENA software. LCF analysis involved reconstructing EXAFS spectra using different combinations of model spectra and allowed the percentage of each model to be determined along with a respective R value.

5.12 DRIFTS

Diffuse reflectance infra-red Fourier transform spectroscopy (DRIFTS) applies infra-red radiation to a powdered sample, this reflects the radiation in many directions; all of this reflected radiation is detected and, therefore, the radiation absorbed by specific bonds can be determined and quantified. In this work, DRIFTS was used to investigate how common MSR/WGS reactants and products adsorbed to the surface

of the powdered catalysts; for example, gaseous and different adsorption modes of CO all absorb different frequencies of IR radiation. DRIFTS was performed in-situ so the amount of adsorbed species could be analysed relative to the reaction time.

5.12.1 DRIFTS methodology

$\approx$ 40 mg of calcined sample was loaded into the measurement chamber within a Nicolet-iS50 FTIR machine with a MCT/A detector. All gas lines and the reaction chamber were purged with N_2 (g) before the temperature of the reaction chamber was elevated to 290 °C and the standard reduction technique was performed (see Section 5.2). All gas lines and the reaction chamber were purged with N_2 (g) before the temperature was then set to 180 °C or 25 °C (depending on the experiment) and background measurements were collected. 10 mL.min^{-1} of one gaseous species at atmospheric pressure was introduced individually to the measurement chamber, simultaneously FTIR absorption spectra collection was initiated. When the relative FTIR absorption peaks of that species plateaued, the system was purged with N_2 (g) (or another gaseous species) whilst spectra collection was still performed. Various combinations of gases and purging gases were used e.g. WGS investigations replaced CO gas with water vapour (at 25 °C) whilst MSR investigations replaced methanol vapour with water vapour (at 180 °C). Both N_2 (g) and 400 ppm CO/N_2 (g) lines were available. N_2 (g) gas lines were also attached to sealed bubblers of $^{12}CH_3OH$, H_2O, D_2O or $^{13}CH_3OH$; therefore, the analogous vapours with N_2 carrier gas were used in DRIFTS experiments.

5.13 ICP-MS

Inductively coupled plasma mass spectrometry (ICP-MS) ionises a sample into mono-atomic and/or small polyatomic ions; a detector can then quantify ions relative to their mass. Because different metals have different atomic mass, ICP-MS can

accurately determine the weight % of different metals in a sample.

ICP-MS was performed using an Agilent 7800 ICP-MS instrument, before each measurement the system was calibrated with the standards of target elements; these experiments were carried out at the Research Centre of Atatürk University, Turkey. The LDH samples underwent microwave-assisted acid digestion and then were diluted with MilliQ water; an aliquot of the resultant sample solution was fed into ICP-MS instrument for quantitative analysis.

5.14 EDX

High resolution energy dispersive X-ray spectroscopy (super-EDX) irradiates a sample with an electron beam, exciting the sample's electrons, when the electrons return to the ground state they emit a characteristic X-ray which is detected and used to position its origin. As established in Section 5.10.1, different elements have different electron binding energies so this can be used to identify the elements in the sample. Like TEM, EDX analysis uses the signals from the detector to construct an image, or 'map', of a surface; however, unlike TEM, the image can be colour-coded to represent the location of different elements (both techniques are often used in tandem).

EDX analysis was performed by Dr. Winson Kuo, Texas A & M University Materials Characterization Facility, USA. It was conducted with an aberration-corrected scanning transmission electron microscope (S/TEM, Thermo Fisher Titan Themis Z 300) operated at 300 kV with a convergence semiangle of 23.6 mrad.

5.15 Catalytic testing

The MSR reactor system used in this work is displayed in Figure 5.4. The system operates under atmospheric pressure with a N_2 carrier gas, any unreacted

liquid is condensed out of the product flow because it would cause problems in the gas chromatograph's columns. A gas chromatograph (GC) contains loops of known volume, these can switch at a set reaction time to send several aliquots of gaseous sample to each of the GS's detectors. The known volume of sample travels through columns with an introduced carrier gas flow, columns separate out gaseous species based on their size, adsorption tendency, polarity or other chemical property. When the sample reaches a detector, each gaseous species has a different elution time because of the column system; therefore, each species can be identified. This requires known concentrations of the expected gaseous samples to be calibrated beforehand; then when an experiment with unknown quantities is performed, the gaseous species can be identified and quantified based on their elution time and signal peak area, respectively.

A thermal conductivity detector (TCD) can quantify the amount of a gaseous species by how its thermal conductivity varies from a simultaneous stream of reference gas. In this work, a TCD is used with a nitrogen reference gas; this allowed for the detection of H_2 (g). A flame ionisation detector (FID) oxidises samples in a flame to give a signal; however, CO_2 and CO are already oxidised so do not give a signal. In this work a methaniser is used in conjunction with the FID, this involves placing a heated Ni catalyst tube directly before the FID, but after the columns, to reduce CO and CO_2 to CH_4 (g). This causes strong methane peaks to occur at CO and CO_2 elution times; these peaks are very sensitve to concentration and as low as 5 ppm of CO was detectable based on calibrations using specialist mixes of 400 ppm CO/N_2 (g). Very broad, weak peaks of both methanol and water vapour were detected using a third detector (He-TCD); additionally, for some Al-based catalysts small amounts of dimethyl ether could be detected in MSR reactions using the FID (primarily for alumina hollow fibre catalysts, not reported within due to their poor activity).

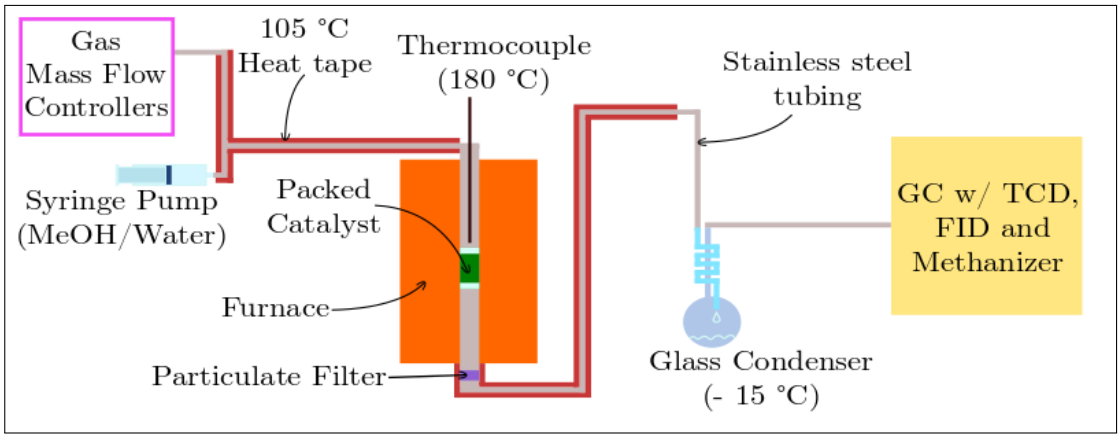


Figure 5.4: Simplified schematic of the final iteration MSR catalytic flow reactor. Figure made using paint.NET® and Inkscape®.

5.15.1 MSR catalytic testing method

≈ 200 mg of calcined sample was loaded between quartz wool inside the stainless-steel reactor set-up (see Figure 5.4) and it was reduced in-situ (this was 75 mg for the Mg series). The standard reduction procedure for the calcined samples was performed after the system was purged with N_2 (g) (see Section 5.2). The system was flushed with N_2 (g) whilst the reactor temperature stabilised at 180 °C. The condenser was placed in a dry ice/ethylene glycol bath (Maintained at ≈ -15 °C ± 5 °C). The carrier N_2 (g) was set at 10 mL.min^{-1} and 0.1 mL.min^{-1} of a liquid H_2O:CH_3OH mix (molar ratio = 1.1) was introduced via syringe pump; the gas chromatograph (GC) sequence program was started at the same time as the syringe pump. The syringe pump was run for 5 h (≈ 28 GC sequences). The Mg- and Ce-containing catalysts were tested using a 0.075 mL.min^{-1} flow of H_2O:CH_3OH.

Chapter 6

Dilution of the active metal species

6.1 The usage of Mg in steam reforming catalysis

At the time of writing, the value of metallic Mg, Zn and Cu is 1.70, 2.41 and 7.36 £/kg, respectively. [217–219] Additionally, Mg is more abundant on Earth and has a higher reserve than both Cu and Zn; Figure 6.1 summarises the availability of elements using three parameters that are derived from the 2011 U.S. Geological Survey; the Herfindahl-Hirschman Index estimates their availabilities based on geopolitical influences etc. [220]

Whilst Cu is substantially cheaper than the scarcer precious metals (for instance Pt metal is currently 28,670 £/kg), there would still be significant savings on an industrial scale if Mg could partially replace Cu and Zn in a catalyst, provided its performance could be maintained. [221] The dilution of an active metal by a cheaper substitute has been shown to not only be viable, but in some cases to increase catalysts' activity and selectivity; Luska et al. found that replacing Ru with Fe in bimetallic nanoparticles provided catalysts with high hydrogenation selectivity. [222] Examples from literature, that are closer in nature to this work, include studies that investigate the incorporation of Mg into NiCu ethanol steam reforming catalysts. Vizcaíno et al. prepared catalysts using NiMgAl LDHs and found that the addition of

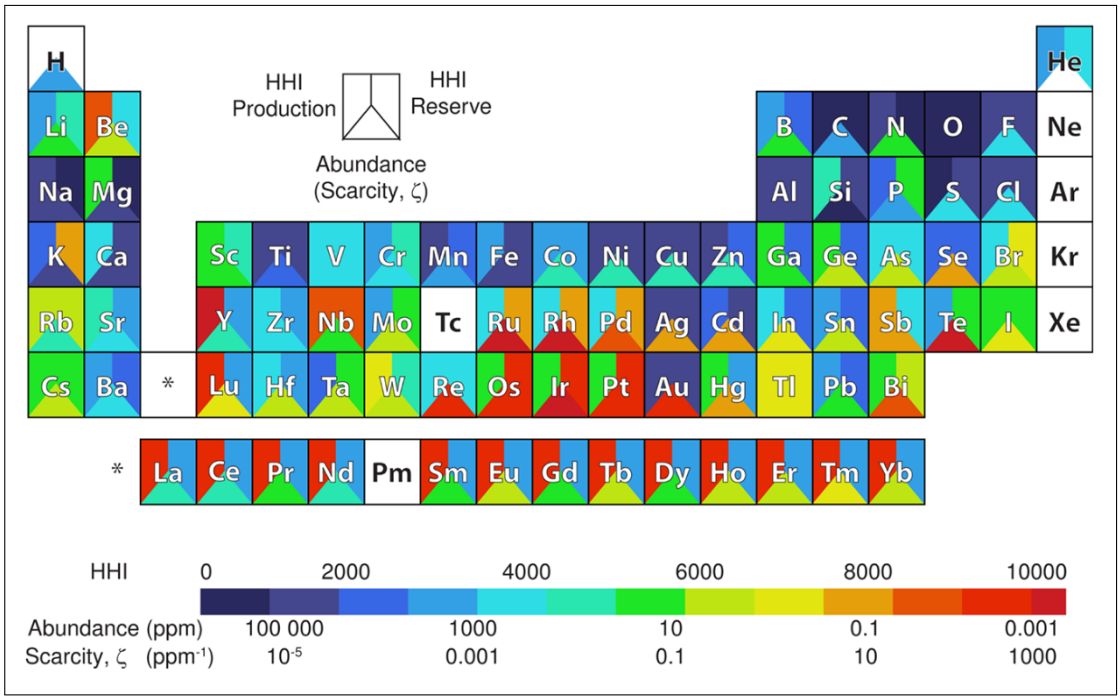


Figure 6.1: The periodic table showing the Herfindahl-Hirschman Index generated from the 2011 U.S. Geological Survey. Figure used with permission from: M. W. Gaultois, T. D. Sparks, C. K. H. Borg, R. Seshadri, W. D. Bonificio, D. R. Clarke, *Chemistry of Materials*, 2013, **25**, 2911-2920. ©2021 American Chemical Society.

Mg suppressed the ethanol to ethylene reaction pathway and increased the steam reforming activity; this effect was theorised to be caused by Mg neutralising acid sites. [223] Carrero et al. found that Mg increased the dispersion of Cu and Ni on SiO_2-supported catalysts and suggested that it was the main reason for the increase in ethanol steam reforming activity; however, when the Mg content was increased to 20 wt%, both the Cu/Ni dispersion and activity decreased. [224]

Mg has been utilised in MSR catalysts in literature as well; Yang et al. found that MgO eliminated Lewis acidic alumina sites that would have caused a side reaction (DME formation). [225] Penkova et al. also observed an inverse correlation between Mg content and acidic sites by analysing $NiSnMgAlO_x$ MSR catalysts in a pyridine absorption FT-IR study. [226] Hou et al. impregnated MgO onto the surface of Cu spinel oxide and found a low MgO content (of 1.7 %) improved MSR catalytic

performance whilst higher loadings of MgO (as high as 9.5 %) were detrimental to activity. [227] In the work by Hou et al. it was found that the copper particle size of the used catalysts and the BET surface area of the fresh catalysts both inversely correlated with Mg content. [227] The average MSR activity ($mol_{MeOH}.mol_{Cu}^{-1}.h^{-1}$) of the fresh catalysts and BET surface area of the used catalysts both appear to follow a volcano-like trend (with the low Mg catalysts having the highest values). [227] It was also theorised high Mg content loadings were having a negative coverage effect upon activity via blocking active Cu sites with increased levels of carbon deposition from the increased amounts of free Mg carbonate species. This was evidenced when the carbon deposition was removed with heat treatment, the regenerated catalyst's initial activity greatly increased. [227]

In a second study, Hou et al. investigated a one-pot synthesis technique, $Cu(OH)_2$, $MgCO_3$ and γ-AlO(OH) were milled together and then calcined at 900 °C; again the catalysts had differing Mg content and the most active and stable MSR catalyst had a medium Mg content (10 %) compared to the rest of series. [228] Unlike the previous three cited studies on Mg MSR catalysts prepared via post impregnation of supports, Hou et al. found the Mg content used in the one pot synthesis was correlated with the BET surface area of the products. [228] Additionally, it was observed that increased Mg content caused the copper particles to become less reducible; this was in contrast to the correlation between Mg concentration and D_{Cu} % and the reducibility of Cu observed by Yang et al. [225,228] These literature reports imply that the structure and location of Mg^{2+} on the surface or in the support, determined by the synthesis method, can lead to differing and competing effects; nonetheless, it seems advantageous to MSR catalytic performance to include Mg in the catalyst.

6.2 The goal with Mg dilution

In addition to the documented uses of Mg in MSR, Chen et al. reported MgAl

AMO-LDHs with BET surface areas of up to $365 m^2 g^{-1}$. [205] All these combined reasons made Mg a good candidate as the diluent for diluting the Cu in AMO-LDH-derived catalysts, where achieving a high surface area catalyst was important. CuMg-LDHs were already known to exist in literature, Li et al. used them as precursors for a WGS catalyst. [229] Similarly to the Mg-based steam reforming catalyst studies above, Li et al. noted Mg increased the D_{Cu} % and, therefore, the activity; the CuMgAl- and CuZnAl-LDHs had D_{Cu} % values of 41.0 and 29.4 % respectively. [229] However, it should be noted that the Cu wt %, determined by ICP-MS, was 24.9 and 34.5 % for the CuMgAl- and CuZnAl-LDHs, respectively. Therefore, the effect may come from a solely larger physical separation between Cu^{2+} cations throughout the LDH structure causing higher D_{Cu} % upon reduction. [229]

In this chapter, a series of catalysts derived from CuZnMgAl AMO-LDHs were investigated; the precursor AMO-LDHs follow the formula: $[(Cu_{4/7}\,Zn_{3/7})_{(0.7-x)}\,Mg_x\,Al_{0.3}\,(OH)_2]^{0.3+}\,(CO_3^{2-})_{0.15} \bullet yH_2O \bullet zCH_3COCH_3$ (where y and $z < 10$ according to Chen et al.). [181] Whether Mg or Zn was more efficient at dispersing Cu in the LDH and subsequent LDO structure was not initially considered as it was theorised many competing factors would change with Zn/Mg content. Regardless, Zn should still be included alongside Mg as it has important synergistic roles in the MSR catalysis (see Section 3.6). As long as the dilution of a cheaper element (replacement of Cu and Zn with Mg) resulted in a maintained MSR activity compared to a non-diluted catalyst this segment of the project would be considered beneficial for economic reasons. Mg is cheap, abundant and it reportedly has the potential to act as a Cu dispersant and surface area enhancer; so it was expected to be a useful diluting cation in AMO-LDHs but it was theorised that the activity of the materials during MSR would likely correlate to the amount of accessible interface between Cu^0 and a ZnO-containing support (see Section 3.4).

6.3 The CuZnMgAl AMO-LDH series

The synthesised series (see Table 6.1) fulfilled the empirical formula of an LDH, with a M^{3+} content of 30 mol % of total metal mols (or metal mol %). The Cu:Zn ratio was kept constant at 4:3 to stop changes in the active CuZn interface affecting trends in the series; the aim was to correlate such trends with the Mg content, which was increased in even divisions up the series. The set Cu:Zn and M^{2+}:M^{3+} ratios were originally chosen to loosely mimic optimal LDH-derived catalysts in various pieces of MSR and CO_2 hydrogenation literature, in pursuit of producing active catalysts. [20, 86, 137, 180]

All samples are labelled as follows: '-LDH' = as-prepared AMO layered double hydroxide; '-LDO' = calcined/LDO sample; and '-r' = reduced sample. Each CuZnMgAl-derived sample is also denoted with its constituent Mg content expressed as the metal mol % of Mg nitrate hydrate (of the total metal nitrate) used in synthesis.

For this chapter, it is important to note that the ICP-MS and TGA raw data and some of the PXRD and BET raw data for the CuZnMgAl AMO-LDH materials were collected as part of an collaboration and has already been displayed in a Masters thesis: J. Earl and S. C. E. Tsang, 2018, *(CuZn)(Mg)Al Layered Double Hydroxides in the Heterogeneous Catalysis of CO_2 Hydrogenation*, part II thesis, University of Oxford. All interpretations, calculations and figures of this raw data were revised, finished and redone for this work.

The experimentally-measured metal content of the as-synthesised LDHs correlates to the amounts of metal nitrates used in the co-precipitation as expected (See Table 6.2). ICP-MS measures the wt % of all elemental species so despite C, O, N and H not being shown in the table they will offset the values; this offset is theoretically consistent from sample to sample because the metal lattice sites and total mols of metal should be similar. Such measurements are also weighted relative to the molar

Table 6.1: The theoretical constituent metal mol ratios used during the synthesis of the CuZnMgAl AMO-LDH series.

Sample	Cu mol % (of total metal mols)	Zn mol % (of total metal mols)	Mg mol % (of total metal mols)	Al mol % (of total metal mols)
0Mg-LDH	40	30	0	30
8.75Mg-LDH	35	26.25	8.75	30
17.5Mg-LDH	30	22.5	17.5	30
26.25Mg-LDH	25	18.75	26.25	30
35Mg-LDH	20	15	35	30
43.75Mg-LDH	15	11.25	43.75	30
52.5Mg-LDH	10	7.5	52.5	30
61.25Mg-LDH	5	3.75	61.25	30
70Mg-LDH	0	0	70	30

mass, predictably Mg gives a lower numerical value for wt % compared to the mol % used during synthesis. Cu and Zn both have an individual atomic mass more than double that of Mg or Al which results in the two former elements having a larger change in the wt %, relative to the change in mol %, across the series. Therefore, C, O, N and H, from lattice -OH and interlayer counter anions, likely account for 50.42 % in 0Mg-LDH (due to the presence of Cu and Zn) and 70.55 % in 70Mg-LDH (where the metallic species are relatively lighter).

Table 6.2: The ICP-MS analysis results of the CuZnMgAl AMO-LDH series.

Sample	Cu (wt %)	Zn (wt %)	Mg (wt %)	Al (wt %)
0Mg-LDH	25.25	17.59	0.00	6.74
8.75Mg-LDH	23.07	16.00	1.77	6.99
17.5Mg-LDH	20.05	14.54	3.64	6.97
26.25Mg-LDH	18.69	12.54	6.84	7.22
35Mg-LDH	15.57	10.39	7.82	8.41
43.75Mg-LDH	10.17	7.07	11.78	8.42
52.5Mg-LDH	7.13	4.87	14.37	8.88
61.25Mg-LDH	3.76	2.62	16.38	9.83
70Mg-LDH	0.00	0.00	19.62	9.83

Assuming the series follows the exact formula, $[(Cu_{4/7}\ Zn_{3/7})_{(0.7-x)}\ Mg_x\ Al_{0.3}$

$(OH)_2]^{0.3+}$ $(CO_3^{2-})_{0.15}$ • yH_2O; then the water/acetone wt % can be calculated using the ICP-MS data. The metal content was measured, therefore the OH^- and CO_3^- amount was derived by balancing charges; under the above assumptions the remaining wt % is water or acetone. The ICP-MS water/acetone wt % results are shown in Table 6.3, in Section 6.3.1, where they are compared to the TGA results.

ICP-MS analysis confirms the inclusion of the metal cations in the materials is consistent with the amounts of metal nitrates used in the co-precipitation synthesis, with only a couple small outliers in the Al wt % trend.

6.3.1 Thermogravimetric analysis of the Mg LDH series

In literature LDHs have shown clear thermal transitions during TGA experiments. Specifically, Wright et al. and Chen et al. have shown, for MgAl-CO_3 AMO-LDHs, the loss of interlayer water/acetone and dehydroxylation occur around 50-200 and 200-400 °C, respectively. [177, 181] The same structural changes can be seen in the Mg series studied in this work. How the samples lose mass as the temperature is increased, as can be seen in Figure 6.2.

The separate transitions are more clearly visible when looking at the gradient of Figure 6.2, which is related to how much mass is lost per °C increase; this gradient is known as the 'derivative mass' and is plotted against temperature in Figure 6.3.

Figure 6.3 shows all samples have two major peaks each representing the transitions mentioned above. The lower temperature peak represents the loss of interlayer species; for the higher Mg content samples this peak can be seen to split slightly indicating both acetone and water can be lost from the sample at different temperatures as expected due to the difference in their volatility. The second higher temperature peak has a maximum around ≈ 190 °C for 0Mg-LDH, this maximum shifts up the series to almost ≈ 400 °C for the 61.25Mg-LDH sample. For the higher CuZn-content

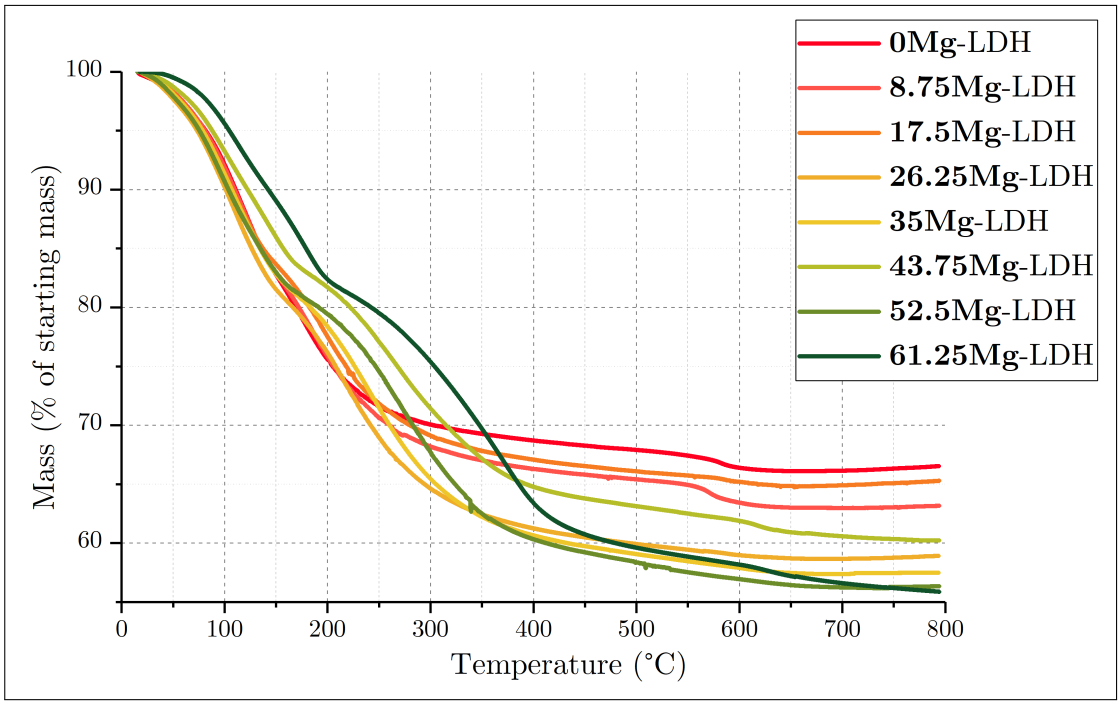


Figure 6.2: TGA of the Mg-based AMO-LDH series, measured with a 10 °C.min^{-1} heating rate.

samples the two transitions appear to have significant overlap.

The dm/dT peaks of Figure 6.3 can be integrated to estimate the percentage contribution of both the dehydroxylation/anion removal and interlayer solvent loss steps make towards the overall mass lost below 500 °C in Figure 6.2; this allowed the combined acetone and water wt % values of the LDHs to be calculated (see Table 6.3). Figure 6.3 shows that the 330 °C calcination temperature used for 0Mg- to 35Mg-LDH may have been to high for preferential partial decomposition to a LDO morphology i.e. there may be more MMO formation in less thermally-stable samples with lower Mg content (this is explored further in Section 6.3.5).

Table 6.3 shows the values of interlayer solvent wt % are slightly different when comparing the ICP-MS and TGA results. For both techniques it is hard to discern the human error affecting the accuracy as each sample was only tested once for each technique. Additionally, there is no consistent trend in either or between the results.

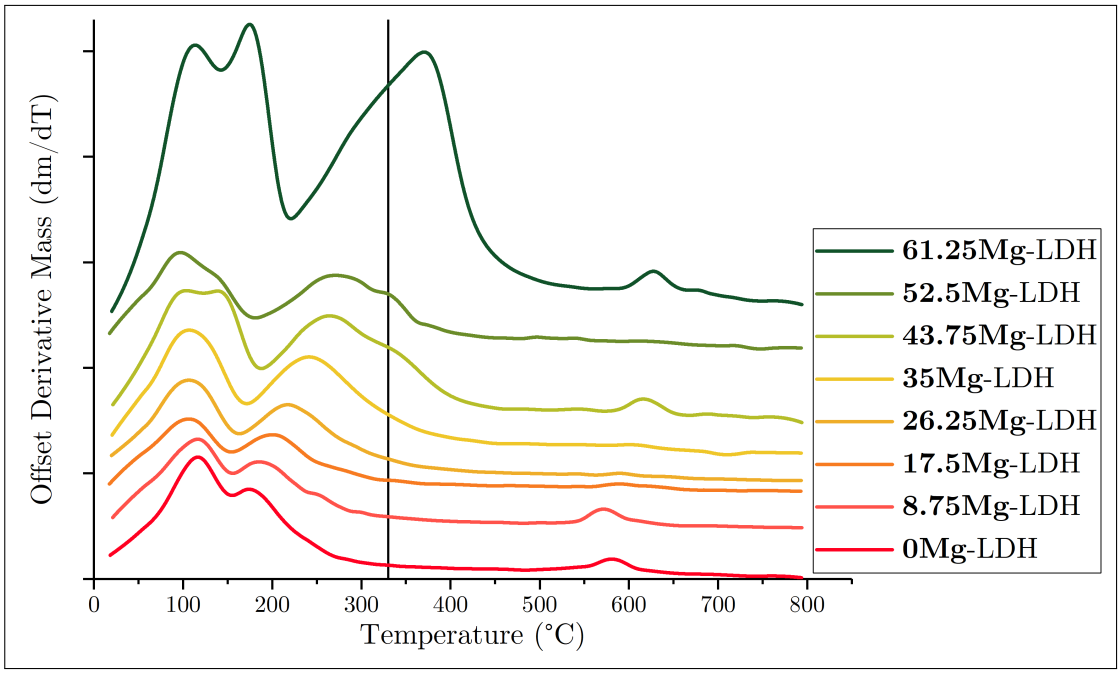


Figure 6.3: The derivative mass, dm/dT, of the Mg-based AMO-LDH series. The graph was calculated using data from the TGA, Figure 6.2, and smoothed with a LOESS regression. The solid line at 330 °C represents the calcination temperature used before MSR catalytic activity testing.

The average trend in water content (determined via ICP-MS) of the Mg-LDH series appears to roughly correlate with an increasing amount of Mg; however, there are too many anomalies for such a small series to claim a true correlation. Many assumptions were made in the calculations of the ICP-MS-derived water content; the inclusion of other anions, for instance NO_3^-, and varying degrees of non-LDH structure formation likely make the calculated value inaccurate.

Increased water content could see the LDH layers lose some exfoliation as hydrogen bonding networks reform, this could decrease the surface area of the derived catalysts, impacting the MSR activity negatively. Unfortunately, these results have unknown accuracy and are isolated without a reference; a study could be conducted to determine change in the water content of the LDHs over time. Such a study would allow the reliability be analysed due to the increase in data points but it would also

Table 6.3: The combined water and acetone content of the Mg-LDH series measured from the TGA results and calculated from the ICP results.

Sample	ICP H_2O+CH_3OH content (wt %)	TGA H_2O+CH_3OH content (wt %)
0Mg-LDH	11.8	18.8
8.75Mg-LDH	12.4	18.6
17.5Mg-LDH	14.9	18.3
26.25Mg-LDH	11.5	21.0
35Mg-LDH	13.2	19.4
43.75Mg-LDH	17.0	17.8
52.5Mg-LDH	17.2	20.3
61.25Mg-LDH	17.8	20.3
70Mg-LDH	19.8	-

be time intensive. For the purposes of this catalytic study, the materials were kept under conditions that were as dry as possible to minimise the effects of 'water re-adsorption' (LDH memory effect). The Mg LDH and LDO samples were kept in an electric regenerating desiccator, at atmospheric pressure, during initial TGA and ICP study but were later moved to a 20 mbar vacuum desiccator when the Ga/Ce AMO-LDH MSR catalyst work began.

The LDH dehydroxylation decomposition transition that occurs between 150-450 °C, shown in Figure 6.3 shifts to higher temperatures with increasing Mg content likely due to the increase in stability of average M^{x+}-OH^- bond. Thermodynamically speaking, the dehyrdroxylation process would only occur once the Gibbs free energy change, ΔG ($= \Delta H - T.\Delta S$), is negative. The enthalpy, ΔH, of dehydroxylation will be less negative the stronger the M^{x+}-OH^- bonds and the weaker M^{x+}-O^{2-} bonds are; the standard enthalpy of formation values are shown in Table 6.4. When the hydroxide formation enthalpy is subtracted from the oxide formation enthalpy it provides a good estimate of the ΔH for dehydroxylation of M^{x+}-OH_x; this is +323, +291 and +294 kJ.mol^{-1} for Mg^{+2}, Zn^{+2} and Cu^{+2} respectively.

As $Mg(OH)_2$ has the most positive estimated enthalpy of dehydroxylation it

Table 6.4: The standard enthalpy of formation and standard molar entropy for oxides and hydroxides; from various literature sources.

Material	Standard enthalpy of formation $\Delta_f H^{\ominus}$ (kJ.mol^{-1})	Standard molar entropy $\Delta S^{\ominus}$ J.mol^{-1}.K^{-1}
MgO [230]	-602	27
ZnO [231]	-351	44
CuO [230]	-156	43
$Mg(OH)_2$ [232]	-925	64
$Zn(OH)_2$	-642 [232]	78 [233]
$Cu(OH)_2$ [233]	-450	108

stands to reason that LDHs with higher Mg content will need a higher temperature to cause the Gibbs free energy of dehydroxylation to become negative; making the process spontaneous at that temperature. This is assuming the entropy, ΔS, change of dehydroxylation is positive. It was also assumed the entropy, ΔS, of dehydroxylation should be consistent across the various metal ratios as the lattice change will be very similar and all within the solid phase.

The standard molar entropies of the individual M^{x+}-OH_x species from literature (see Table 6.4) are around that of $Mg_{0.74}Al_{0.26}$-CO_3-LDH, which was revealed experimentally to be +86 J.mol^{-1}.K^{-1}. [234] On inspection of Table 6.4 the entropies of the individual metal oxides are lower than that of the analogous hydroxides i.e this estimation alone would break the assumption of positive entropy. However, the assumption that the overall entropy change is positive is rational because the interlayer CO_3^{2-} and NO_3^- would be lost as gases, which have a much higher standard molar entropy than the solid phases left behind. It can be noted that MgO has less standard molar entropy than both CuO and ZnO, which could contribute slightly to the Gibbs free energy explanation of why the LDHs, with higher Mg content, require a higher temperature for dehydroxylation.

Another problem with estimating the Gibbs free energy as above is that the standard enthalpy of formation for the M^{x+}-OH_x species does not include the con-

sideration of the enthalpy of losing interlayer anions. Allada et al. experimentally determined the standard enthalpy of formation of $Mg_{0.67}Al_{0.33}$- and $Zn_{0.67}Al_{0.33}$-LDHs determined as -1285 and -993 kJ.mol^{-1}, respectively i.e. slightly more exothermic than that of the individual metal hydroxides in Table 6.4. [235] Allada et al. also determined the enthalpy of the LDH formation starting from the relevant oxides as -59 and -45 kJ.mol^{-1} for the $Mg_{0.67}Al_{0.33}$- and $Zn_{0.67}Al_{0.33}$-LDHs, respectively; this specifically includes the thermodynamics of including the interlayer carbonate in the LDH formation from gaseous carbon dioxide. [235] This calculated enthalpy of formation from the oxide is similar to the reverse of the 'enthalpy of dehydroxylation'. This confirms that the enthalpy of dehydroxylation will be slightly endothermic and, as with the above estimations, it will be more positive for MgAl-LDHs compared to ZnAl-LDHs. [235] It could be theorised the trend of Mg content correlating with the temperature peak (of the LDH dehydroxylation/interlayer anion removal thermal transition) is dictated thermodynamically; the enthalpy of transition is more endothermic when more Mg is incorporated into the LDH due to the strength of the Mg-O bonds. However, kinetic arguments could also be used.

The enthalpy values displayed in Table 6.4 also allude to the $M^{\delta+}$-$(O)^{\delta-}$ bond strength being ordered as follows: Mg > Zn > Cu i.e. the stronger the forming bond, the more exothermic the bond formation process. The reverse of this trend correlates to the Pauli electronegativity of the metals: Mg < Zn < Cu. [236] Mg^{2+} is a harder ion than Cu^{2+} and Zn^{2+}, therefore the efficiency and strength of the orbital overlap between Mg^{2+} and an anionic O species, makes it the strongest and most 'ionic' bond of the three. This means that a higher average activation energy will be required to break the M^{x+}-OH^- bonds in LDHs with higher Mg content. In turn this means higher temperature conditions will be required to start the dehydroxylation process; this factor could also explain the shift of the transition seen in Figure 6.3.

TGA shows that an increase in Mg^{2+} content, at the expense of Cu^{2+}, increases the stability of LDH materials against thermal decomposition via increasing their lattice energy. Additionally, TGA suggests the 330 °C calcination temperature may have been too high for the partial decomposition of LDHs, with low Mg content, to LDOs.

6.3.2 PXRD analysis of the Mg LDH series

All synthesised materials in the $[(Cu_{4/7}\,Zn_{3/7})_{(0.7-x)}\,Mg_x\,Al_{0.3}\,(OH)_2]^{0.3+}\,(CO_3^-)_{0.3}$ series show the expected LDH PXRD pattern (see Figure 6.4). The following LDH planes give a visible diffraction in PXRD using Cu K-α X-ray radiation: (0 0 3) at ≈ 12 °, (0 0 6) at ≈ 24 °, (0 0 9) at ≈ 35 °, (0 1 2) at ≈ 36 °, (0 1 5) at ≈ 39 °, (0 1 8) at ≈ 47 °, (1 1 0) at ≈ 60 ° and (1 1 3) at ≈ 61 °. [181,187,191] Based on PXRD analysis the Mg-based AMO-LDH series contains almost exclusively the $3R_1$-LDH polytype (see Section 3.7.1).

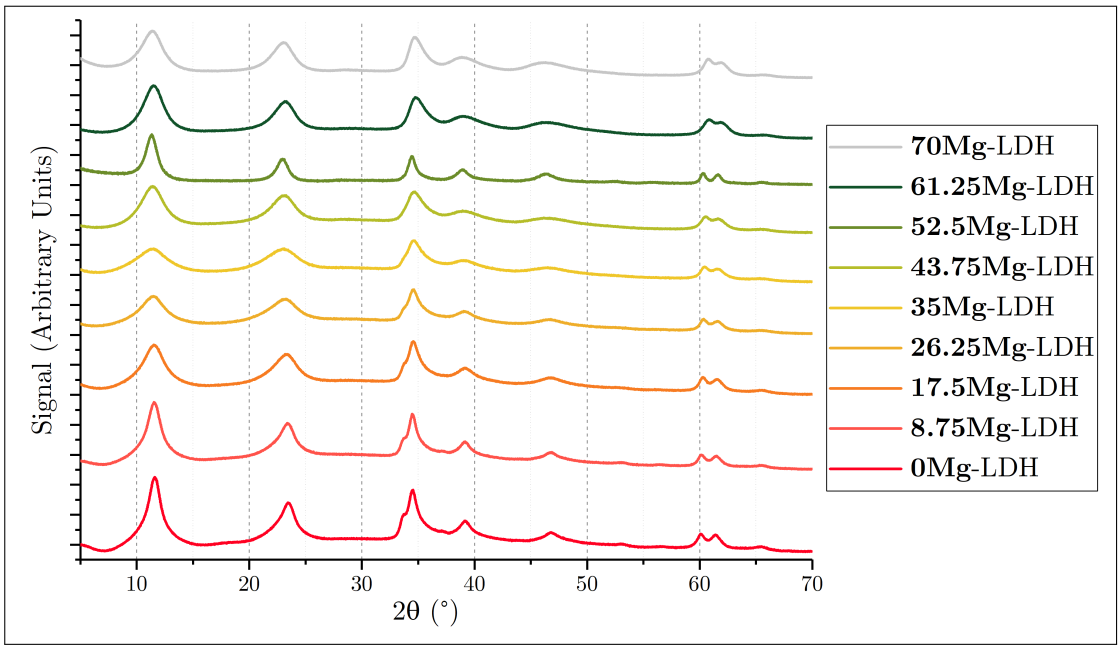


Figure 6.4: PXRD patterns of the Mg-based AMO-LDH series.

No other phase formed a particle large enough to be detectable in PXRD. This

information, alongside the correlation between the ICP-MS results and the syntheses' metal nitrate ratios, indicates all materials in the series have a high purity of LDH phase. Figure 6.4 does show some broadening of the PXRD peaks, this is due to the various average LDH crystallite sizes in the samples.

Measuring the 2θ and full width at half maximum (FWHM) of the diffraction peaks allows Bragg's Law and the Scherrer equation to be solved for information about the material's unit cell and lattice (see Section 5.3.1). Due to the assumed hexagonal LDH cell used for PXRD analysis, the calculated a and c parameters are correlated to the average ion size in the lattice and the distance between the LDH $\delta+$ brucite-like sheets, respectively. The diameter of crystallites, formed from stacked LDH layers, and their thickness can also be derived from the calculations; the latter gives an indication of how many LDH layers are stacked in one crystallite. How the layers stack depends on their morphology, which can be 'plate-like' or the layers can be stacked in formations that resemble flowers. [205]

The data, in Figures 6.5, 6.6, 6.7 and 6.9, was calculated using a standardised integration method. The error bars include the zero error of the X-Ray diffractometer and the human error involved with integrating and calculating the parameters. The human error was considered by looking at the minimum and maximum values previously calculated in this work's original non-standardised methodologies.

The a parameter inversely correlates with increasing Mg content as expected (See Figure 6.5). Mg^{2+} forms stronger, and therefore shorter, bonds with the lattice hydroxide than Cu^{2+} and Zn^{2+} due to its smaller orbital size (see Section 6.3.1); shorter bonds will reduce certain dimensions of unit cell, and therefore the a parameter.

The c parameter correlates with the Mg content up until 52.5Mg-LDH, after that the c parameter drops off. For LDHs the c parameter relates to the distance between the hydroxide layers and also the thickness of the individual layers. [187]

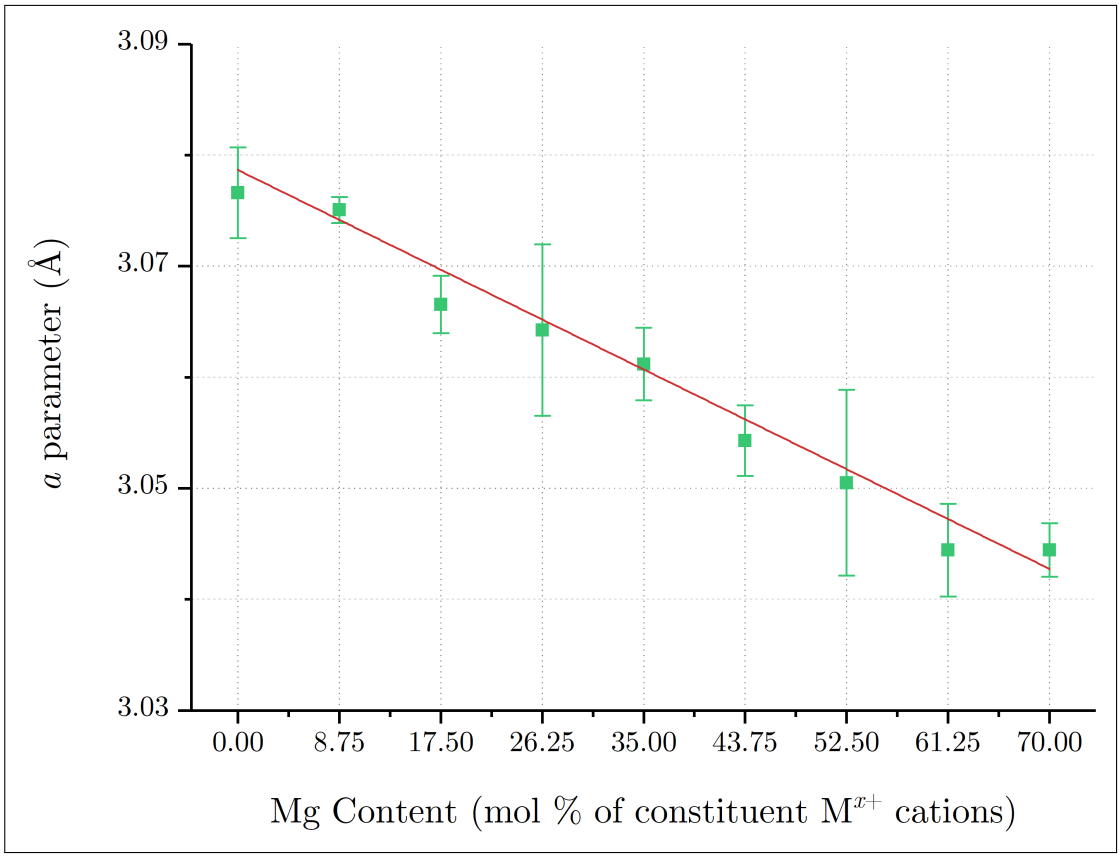


Figure 6.5: The a parameters of the Mg-based AMO-LDH series. Calculated from the PXRD data (Figure 6.4). The red line represents a linear fit where: y = 3.079 - $(5.132 \times 10^{-4})x$ and the R^2 value = 0.981.

Mg^{2+}, Cu^{2+} and Zn^{2+} all have similar ionic radii but as mentioned above the Mg-OH bonds in the lattice will be shorter than those of Cu- and Zn-OH. [237] Therefore, increasing Mg content would theoretically contract the thickness of the individual layers, thus a competing effect is needed to explain the observed c parameter trend. Gao et al. synthesised an LDH series where Al^{3+} is replaced gradually by Y^{3+} and they observed an increase in the c parameter with increasing Y^{3+} content; it was theorised that increasing the amount of the larger, less polarising Y^{3+} ion meant the coloumbic attractive forces between the positive LDH layer and the interlayer anions were weaker. [187] This cannot explain the trend in this work as Mg^{2+} is less electronegative and more polarising (it has a lower 'polarisibility') than the Cu^{2+} and

Zn^{2+} it is replacing; the mean electronic polarisibilities for Mg^{2+}, Zn^{2+} and Cu^{2+} are $\approx$ 0.6-0.8, 1.7, 2.2-2.3 Å^3, respectively. [28]

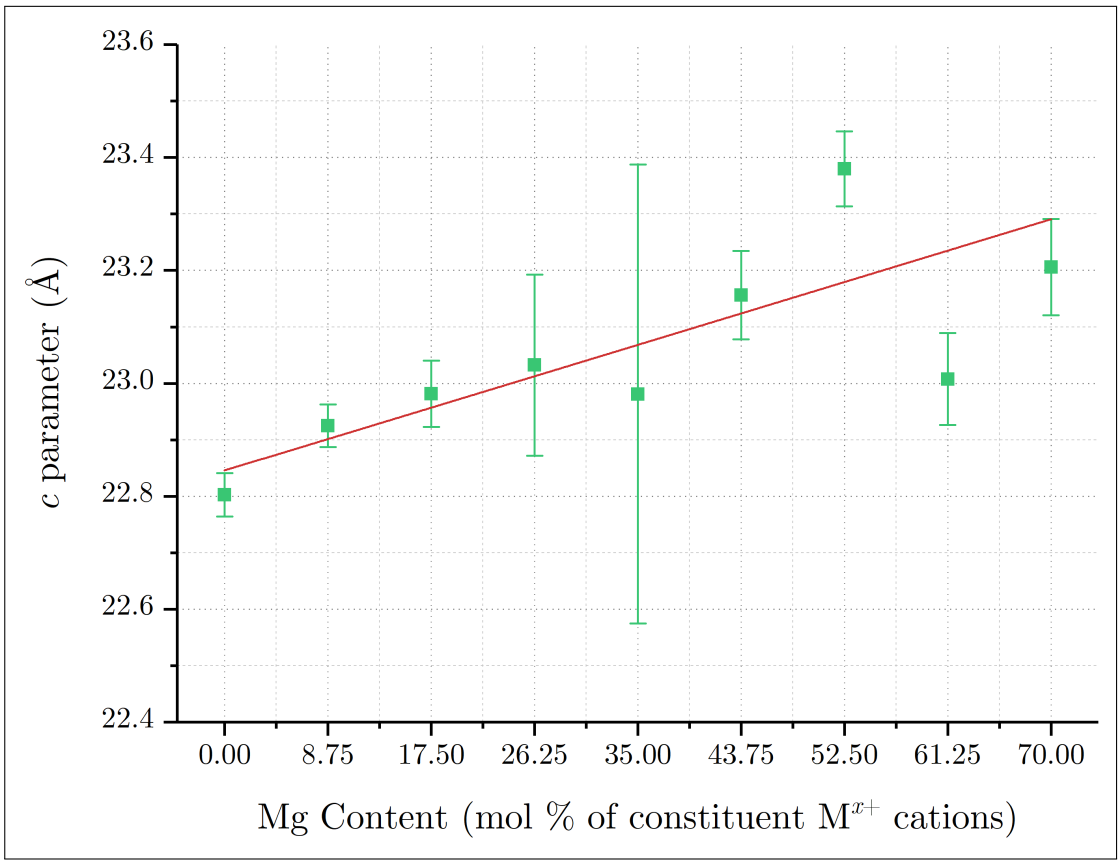


Figure 6.6: The c parameters of the Mg-based AMO-LDH series. Calculated from the PXRD data (Figure 6.4). The red line represents a linear fit where: y = 22.85 + 0.006x and the R^2 value = 0.72.

The correlation between the c parameter and Mg content, shown in Figure 6.6, is weak and not completely linear; especially at high Mg content, this indicates there may be competing effects. Unlike in the study by Gao et al., in this work acetone is used to exfoliate the LDH layers and in doing so theoretically increase the c parameter for AMO-LDHs relative to non-exfoliated LDHs. [187] This occurs because the acetone's polar C=O bond is weakly attracted to the δ^+ LDH layer and then the acetone's non-polar -CH_3 groups disrupt the interlayer water hydrogen bonding network; reducing interlayer attraction, causing the LDH layers to exfoliate. [182] As shown by Shannon et al. Mg^{2+} has more 'polarising power' (a lower polarisibil-

ity) than Cu^{2+} and Zn^{2+} (the quantitative values are shown above). [28] Meaning Mg^{2+} theoretically has a greater ability to distort the electron fields in the LDH layer and polarise the -OH groups; making the $H^{\delta+}$ species more positive. This would cause the hydrogen bonding, between the surface -OH groups and the interlayer water/acetone, to increase in strength. During synthesis water was vacuum filtered off the LDH wet cake precipitate, and acetone is introduced multiple times during the filtration to replace it to prevent the sample drying. The sample is then stirred in acetone for 2 hours. During this stirring step and assuming negligible effects from interlayer water, the sample with the strongest hydroxyl-acetone hydrogen bonds will theoretically have the highest concentration of acetone adsorbed to the LDH layers at equilibrium. This is theorised because the thermodynamically-unfavourable steric interactions between acetone molecules in close proximity will be offset by the stronger hydroxyl-acetone bonds, which are thermodynamically-favourable. The greater the concentration of acetone bound to the LDH surface, the weaker the interlayer attractive forces become; causing a greater degree of exfoliation and, therefore, a higher *c* parameter.

It is proposed that the increase in hydroxyl-acetone bond strength, as a result of the Mg^{2+}-based polarisation of the lattice OH, dominates the *c* parameter regime up until 52.5Mg-LDH; shown in Figure 6.6. When the Mg content is increased further, contractions of the layer thickness and increased electronic attraction between interlayer anions and layers, with more polarising power, start to have a visible effect on the *c* parameter. It is likely the surface area of the as-prepared LDHs will be affected in a similar manner to *c* parameter by the above interlayer interactions, see Section 6.3.5.

In LDH materials, the brucite-like layers stack to form the crystallites; therefore the thickness of those crystallites, in the same axis as the *c* parameter, is determined

by the number of layers per crystallite, the strength of interlayer attractive forces and exfoliation technique. The crystallite thickness of the CuZnMgAl-LDHs, as a function of their Mg content, can be seen in Figure 6.7; the trend is akin to the inverse of a volcano plot. Initially, as Mg content increases, the crystallite thickness decreases to 26.9 Å for 35Mg-LDH, which is close to its c parameter; meaning there is an average 3.5 LDH layers per crystallite (see Figure 6.8) and, therefore, extensive exfoliation. The c parameter corresponds to one dimension of the assumed hexagonal cell and for $3R_1$-LDH polytypes the unit cell contains 3 LDH layers. [238] The crystallite thickness then increases again with increasing Mg content, suggesting a mix of competing factors determine the trend; likely effects similar to the ones that determine the c parameter and BET surface area. The thickness of the individual layers likely has a less weighted effect and the degree of exfoliation, a more highly weighted effect, when compared to their effect on the c parameter; this is because the c parameter is calculated for 3 stacked layers (specifically 2 full and 2 half LDH layers). Fully exfoliated or misaligned layers may not be close enough together to give a measurable plane X-ray diffraction; therefore the extent of exfoliation's impact on the c parameter is likely limited, and smaller relative to the effect it has on crystallite thickness. Which is an average function of all LDH layers across all crystallites (not just the average between pairs of stacked layers), the measurement of the crystallite thickness is not limited by the degree of exfoliation.

Figure 6.7 suggests that for the crystallite thickness trend, up until 35Mg-LDH, the degree of exfoliation is the dominant effect. The change in crystallite thickness is a significant percentage change, demonstrating exfoliation has a larger percentage impact on the crystallite thickness compared to the c parameter. 35Mg-LDH has an average crystallite thickness 51.8 % of that of 8.75Mg-LDH; whereas, there is only a 2.0 % increase in c parameter from 8.75Mg-LDH to 52.5Mg-LDH (see Figure 6.6). The interlayer attractive forces become the determining effect at a lower Mg content

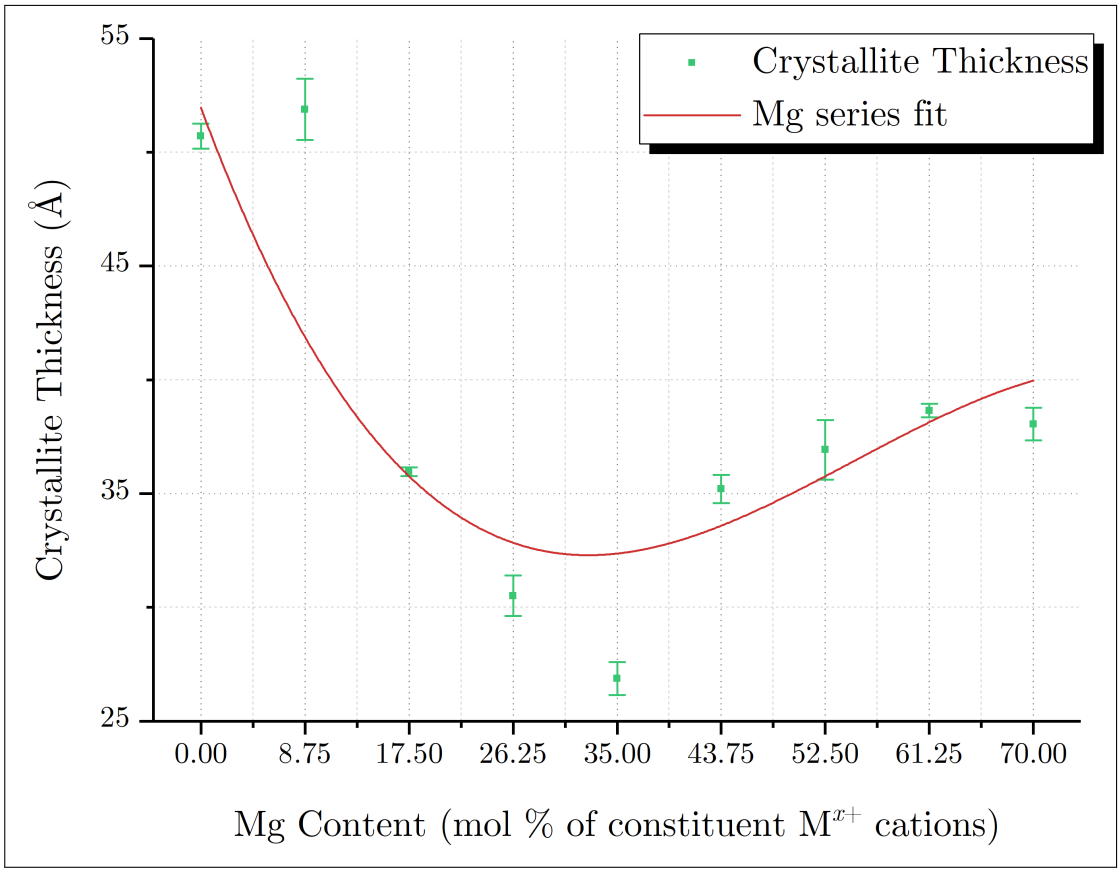


Figure 6.7: The mean crystallite thickness of each AMO-LDH from the Mg-based series. Calculated from the PXRD data (Figure 6.4) using the standardised integration method used across this thesis. The red line represents a cubic fit where: y = 52.0 - $1.40x$ + $0.03x^2$ - $1.86x^3$ and the R^2 value = 0.864.

in crystallite thickness trend and at a higher Mg content in the *c* parameter trend. Both interlayer attractive forces and the polarisation power of the layers directly affect/contribute to the degree of exfoliation. Therefore, the 'earlier' change in regime (at a lower Mg content) could be due to a new factor that affects only the crystallite thickness and not the *c* parameter. This factor could be a mixture of the partial exfoliation and irregular *ab*-plane re-stacking of the crystallites; in a way that they only overlap partially in the *a* and *b* dimensions. Such non-aligned stacking would likely not affect the *c* parameter measured between two or three stacked layers but would increase the average crystallite thickness.

The stacking and exfoliation of plates would also be affected by the morphologies of the LDH material. The degree of non-aligned *ab* plane stacking will vary with morphology of the LDH i.e. platelets will be more aligned in that plane compared to LDH layers in a flower morphology. In this work, the experimental procedure was followed for the synthesis of AMO-LDHs in flower morphology as opposed to platelet morphology; the morphology for this works' non-Mg AMO-LDHs is analysed in Section 8.4.2. Chen et al. demonstrated that LDHs with a platelet morphology experience a lesser degree of exfoliation than analogous flower-morphology LDHs when exposed to the same amount of acetone; they theorise this is because it is harder for acetone to get into the layers' hydration shells when there is a higher degree of *ab* stacking. [205] Therefore, the above proposed theory of irregular *ab*-plane stacking could likely be the factor that causes the volcano trends of the *c* parameter and crystallite thickness to be offset from each other, regarding the Mg content. Unfortunately, TEM analysis of the Mg-based AMO-LDH series was not performed for this work so it is unclear whether they adopt plate or flower morphologies.

The number of LDH layers per crystallite follows an extremely similar trend to that of the crystallite thickness, see Figure 6.8. Therefore, the effects that determine the crystallite thickness also determine the number of LDH layers per crystallite. This is because the *c* parameter range across the series is 0.58 Å; whereas the range in crystallite thickness, 25 Å, is much more dominant.

There is no obvious trend in the 'plate' diameter of the Mg-based AMO-LDH crystallites, see Figure 6.9. This may be, in part, due to the large errors involved in the parameter's calculation. Even with similar selected baselines, manual integrations of the overlapping (1 1 0) and (1 1 3) PXRD peaks could give quite different values to the standardised, semi-automated integration method. Additionally, Chen et al. showed that flow rates of reagents and aging times during synthesis could have large

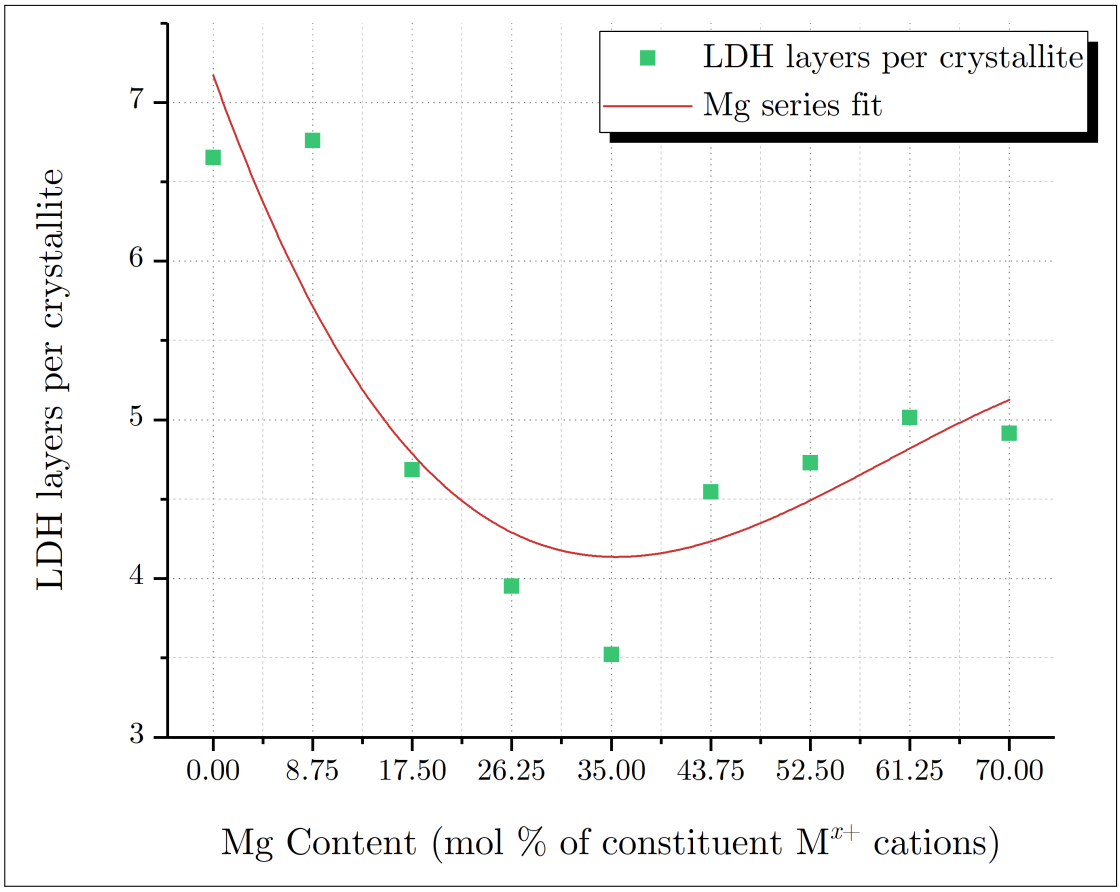


Figure 6.8: The mean no. of LDH layers per crystallite of each AMO-LDH from the Mg-based series. Calculated from the PXRD data (Figure 6.4). The red line represents a cubic fit where: y = 7.17 - 0.20x + 0.004x^2 - (2.27×10^{-5})x^3 and the R^2 value = 0.78.

effects on the morphology and average crystallite diameter. [205] No TEM analysis was performed for this series of Mg-based materials; however, as the synthesis of them was very close to the procedure used by Chen et al., it is theorised the morphology of the LDH series is made up of ≈ 80-120 Å flowers. [205]

Overall, PXRD demonstrated that all CuZnMgAl AMO-LDHs adopt the $3R_1$ polytype during synthesis. It can be observed that increasing Mg content decreases the a unit cell parameter due to its smaller cationic radii. However, the crystallite thickness in the plane of LDH layer stacking follows an inverse volcano trend relative to Mg content, where 35Mg-LDH has the smallest crystallite thickness at almost

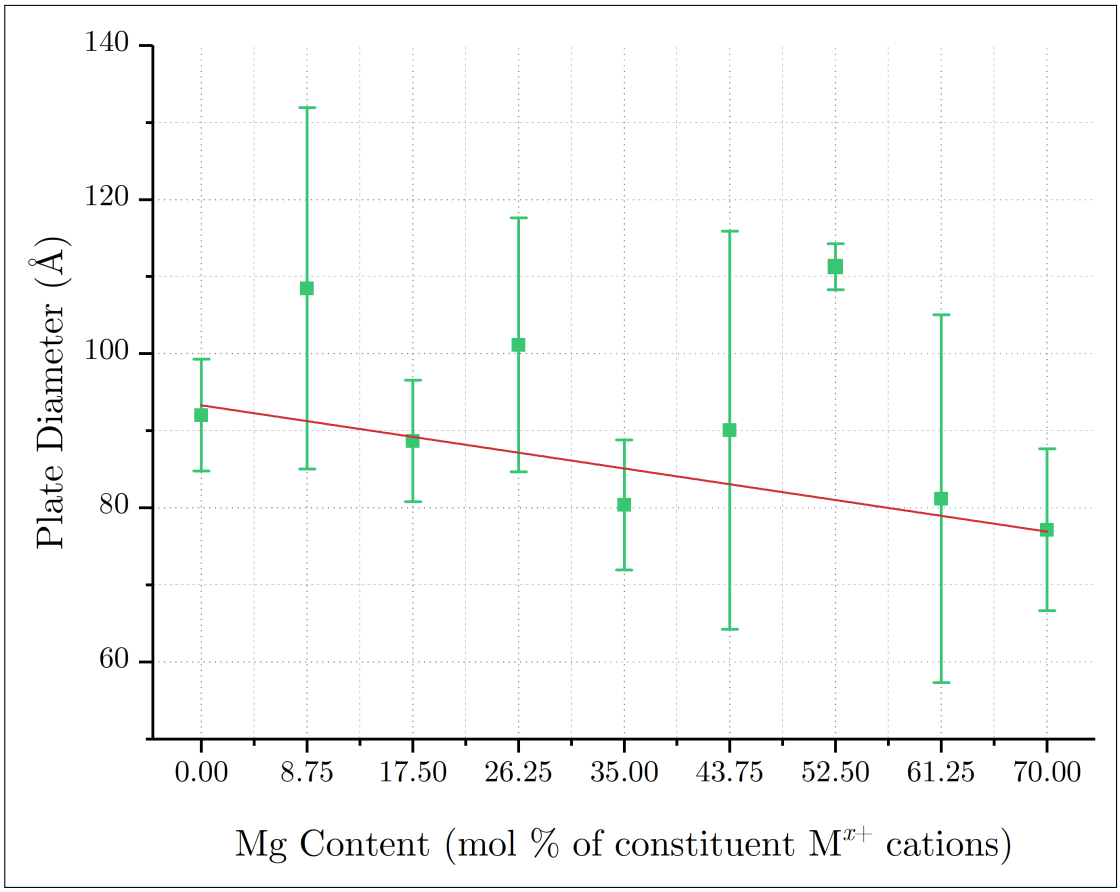


Figure 6.9: The mean plate diameter of each AMO-LDH from the Mg-based series. Calculated from the PXRD data (Figure 6.4) using the standardised integration method used across this thesis. The red line represents a linear fit (ignoring the 52.5Mg-LDH data point) where: y = 93.3 - 0.23x and the R^2 value = 0.54.

three layers thick. The trend in crystallite thickness is proposed to be caused by Mg content correlating with the interlayer attractive forces and each LDH layer's average polarising power (which increases the extent of exfoliation via favouring higher interlayer acetone concentrations during synthesis); these have opposite/competing effects upon the crystallite thickness.

6.3.3 Calcination of the Mg series

In literature, partially decomposing conventional LDHs to LDOs was shown to increase the materials' surface areas; therefore, thermal calcinations were performed in this work to try and achieve higher surface areas to benefit the catalytic activ-

ity. [76, 177] The calcined LDH samples in this work are labelled as 'LDOs' because literature shows that when LDHs are calcined, at temperatures just above those which are required for dehydroxylation, they become oxides but maintain some of the layered structure and precursor morphology. Wright et al. reported non-exfoliated MgAl-LDHs lost (0 0 3) PXRD diffraction and hydroxyl FTIR absorption peaks at $\approx$ 300 and 350 °C, respectively; implying a thermal transition from crystalline LDHs to more amorphous LDOs. [177] Also in work on non-exfoliated MgAl-LDHs, Hobbs et al. observed the loss of LDH layer periodicity above 250 °C due to dehydroxylation; they also noted the MgAL-LDHs became amorphous at higher temperatures compared to NiFe-LDHs. [206] Hobbs et al. continued to observe 'LDH morphology' for the MgAl-LDHs up until 450 °C despite the samples becoming amorphous and more porous; additionally, even the NiFe-LDHs, which were more susceptible to thermal degradation at lower temperatures than the MgAl-LDHs, maintained octahedral hexagonal morphology at 450 °C. [206] Sjåstad et al. observed only octahedral Al peaks, using ^{31}Al NMR analysis, for non-exfoliated MgAl-LDHs treated at 150 °C; however, they began to observe tetrahedral Al at 275 °C indicating a breakdown of the octahedral hydroxide structure. [239]

In the thermogravimatric analysis performed in this work (see Section 6.3.1), the varying empirical formula of the LDHs played a role in the temperature required for their dehydroxylation; similarly to how Hobbs et al. observed differences in the thermal transitions between MgAl- and NiFe- LDHs. Figure 6.10 shows the PXRD patterns of the Mg-'LDO' series, after the LDH samples had been calcined at 330 °C. In Figure 6.3, displaying TGA results, a x axis marker is visible at 330 °C, some LDH samples with high Mg content have thermal dehydroxylation processes that occur at temperatures higher than the marker; therefore, some Mg-based AMO-LDHs may not have been fully calcined. However, during TGA analysis a heating rate of 10 °C.min^{-1} was used, whereas during calcination the temperature was held at 330 °C

for 3 hours; allowing more dehydroxylation time for each sample. Figure 6.10 shows the calcined samples give PXRD patterns with only an amorphous background but some higher Mg content samples have a few very broad peaks. Samples with lower Mg content may have been decomposed to a larger extent during calcination, this was investigated further with BET surface area analysis (see Section 6.3.3).

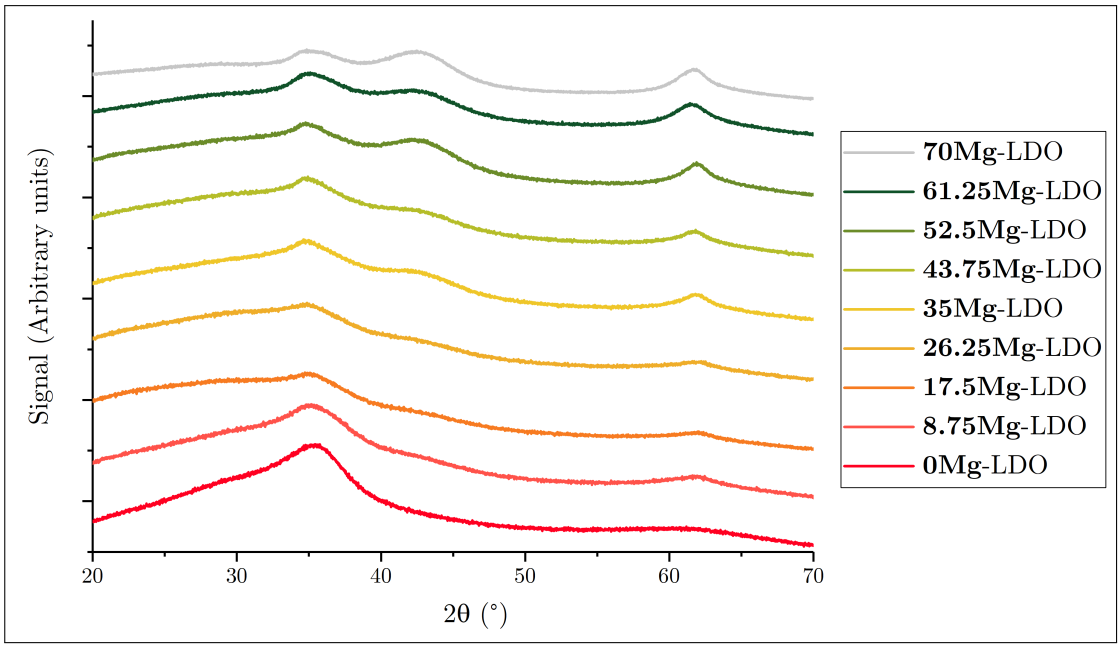


Figure 6.10: The PXRD patterns of the calcined Mg-based AMO-LDO series.

As seen in Figure 6.10, for all samples the major peak of the amorphous background is ≈ 35 °, around where the (0 0 9) LDH peak occured due to X-Ray scattering within the brucite-like layer in the c axis. This could be a coincidence but as previously mentioned above, in the reference to the work by Hobbs et al., and in Section 3.7.1, LDOs can be formed from the calcination of LDHs. Therefore, some layered morphology likely exists after calcination at 330 °C; however, any diffraction pattern of (0 0 9) is severely broadened due to the assumed partial decomposition and loss of stacking order/crystallinity. Unfortunately, no TEM analysis was done in this work for the Mg-based AMO-LDH series to compliment this theory. For the 35Mg-LDO and higher Mg content samples, very broad amorphous peaks can be seen at 41 and

61 °, from possibly remaining crystalline (0 1 8) and (1 1 0) planes; all 3 visible peaks sharpening with increasing Mg content. This is likely due to incomplete dehyroxylation of the LDH layers, it is unclear whether longer calcination times would take the process to completion or if some hydroxyl groups, in local sections of pure MgAl-LDH, have an activation energy of dehydroxylation that is too high. Conversely, the PXRD peaks at 41 and 61 ° could be caused by MgO that formed during calcination. [240] Whilst the formation of MMO phase often occurs around 450 °C for conventional LDHs, AMO-LDHs are less thermally stable so it is possible there could be partial decomposition to MMOs during a 330 °C calcination (see Section 3.7.1); Chen et al. observed that MgAl-based AMO-LDHs could begin to decompose to MMOs at 340 °C via TGA. [181] However, the TGA in this work implies that increased decomposition to MMOs would be favoured by low Mg content samples (see Figure 6.3); overall, the unknown calcined PXRD peaks could not be assigned.

The Mg-based AMO-LDH samples have a cyan colour due to the presence of octahedral Cu^{2+}, the colour's saturation correlates with the concentration of the Cu content; 70Mg-LDH is white, 61.25Mg-LDH has the palest blue colour, 0Mg-LDH is the 'bluest' etc. Upon calcination the samples turn to a darker shade of cyan, for the samples with higher Cu content it is almost pine green. This is likely because distorted square planar CuO is black in colour; when the cyan and black colours mix, due to the dehydroxylation and partial degradation of the octahedral Cu^{2+} crystallite structure, a darker cyan/green is visible. LDOs have a memory effect by which they can adsorb water and CO_2 from the air to convert back to their LDH form. [239] The calcined samples in this work were kept in an electric dessicator and then a static 10 mbar vacuum dessicator; therefore, no colour change or reversion back to LDH form was observed in the PXRD experiments.

6.3.4 TPR analysis of the Mg LDO series

The reducibility of the Cu^{2+} in the LDHs of the Mg series was determined via TPR, see Figure 6.11; the peaks observed are most likely due to the hydrogen consumption of reducing Cu^{2+} to Cu^0. This is because the standard Gibbs free energies of crystallite formation (per metal mol) for CuO, ZnO, MgO and Al_2O_3 are -129.7, -320.5, -569.3 and -791.4 $kJ.mol^{-1}_{metal}$ respectively. [241] The opposite process to oxide formation involves the breaking of the structure and $M^{\delta+}$-$O^{\delta-}$ bonds down to the constituent element standard states i.e. metals will be in the 0 oxidation state. This reverse process is similar to reduction, therefore CuO likely has the least positive Gibbs free energy of the reduction; meaning the temperatures required for reducing the constituent metals follows the trend Cu < Zn < Mg < Al.

It is possible a small amount of Zn^{2+} was reduced to Zn^0 at a temperature close to that of Cu because it has been reported by Li et al. that CuZn alloys can form when $CuO/ZnO/Ga_2O_3$ is reduced at 250 °C; due to a theorised 'electronic heterojunction' between ZnO and a Ga-based spinel oxide [169]. Whereas, Zabilskiy et al. report no evidence of Zn^0 even when CuO/ZnO, on a Na, Ca, Mg, Al, Si-based zeolite support, is exposed to highly reducing conditions at 260 °C. [242] It is likely such CuZn alloys are reoxidised to Cu/ZnO under reaction conditions when exposed to H_2O or CO_2 but potential Zn^0 would still affect the TPR results as no oxidising species are present. [173,174,242] The possible presence of Zn^0 and how it could affect the TPR data is investigated in Section 8.5.5.

The initial assumption, here in Section 6.3.4, is that the reduction of Cu^{2+} dominates the peaks seen in Figure 6.11; due to the lack of a 'reducible oxide' (see definition in Section 2.6) or evidence of spinel oxide in the PXRD patterns of the calcined Mg-LDOs. Following this assumption, the reducibility of the Cu^{2+} decreases with increasing Mg content; this observation ties in with the Gibbs free energy of crys-

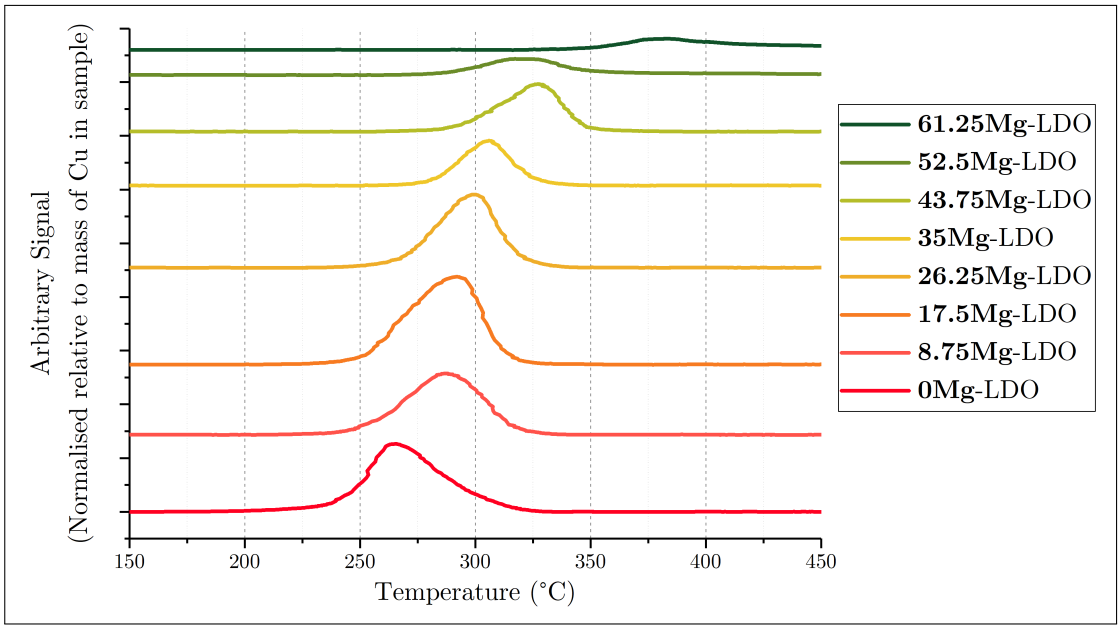


Figure 6.11: The TPR analysis of the calcined Mg-based AMO-LDO series; measured with a 10 °C.min^{-1} heating rate.

tallite formation values listed above. For the reduction of Cu^{2+} to take place other $M^{\delta+}$-$O^{\delta-}$ bonds in the lattice need to break and reform to allow Cu, which is disperse within the LDH, to leave the lattice. This means the average $M^{\delta+}$-$O^{\delta-}$ bond strength of the lattice should correlate with the temperature required to reduce Cu^{2+}; this is what is observed. Increasing the Mg content, and therefore decreasing the Cu and Zn content, theoretically increases the average $M^{\delta+}$-$O^{\delta-}$ bond strength in the lattice based on the given values for the Gibbs free energy of crystallite formation; the $\Delta G_f^{\ominus}$ for 1 mol of MgO is more negative than the sum of both 1 mol of CuO and 1 mol of ZnO. As expected, Figure 6.11 shows that the temperature of the peaks shift to higher temperature with increasing Mg content in the Mg-LDH series; this shift is almost $\approx +$ 60 °C from 0Mg-LDH to 43.75Mg-LDH.

6.3.5 BET analysis of the Mg LDH/LDO series

The BET surface area of the as-prepared AMO-LDHs initially increases with increasing Mg content, see Figure 6.12; the surface area plateaus between 26.5Mg-

and 52.5Mg-LDHs, at ≈ 320-350 $m^2.g^{-1}$, before dropping off again. As theorised in Section 6.3.2, the BET surface trend is volcano-like in nature; whilst it does not correlate perfectly with either the c parameter or crystallite thickness, it is likely affected by the same effects as those trends.

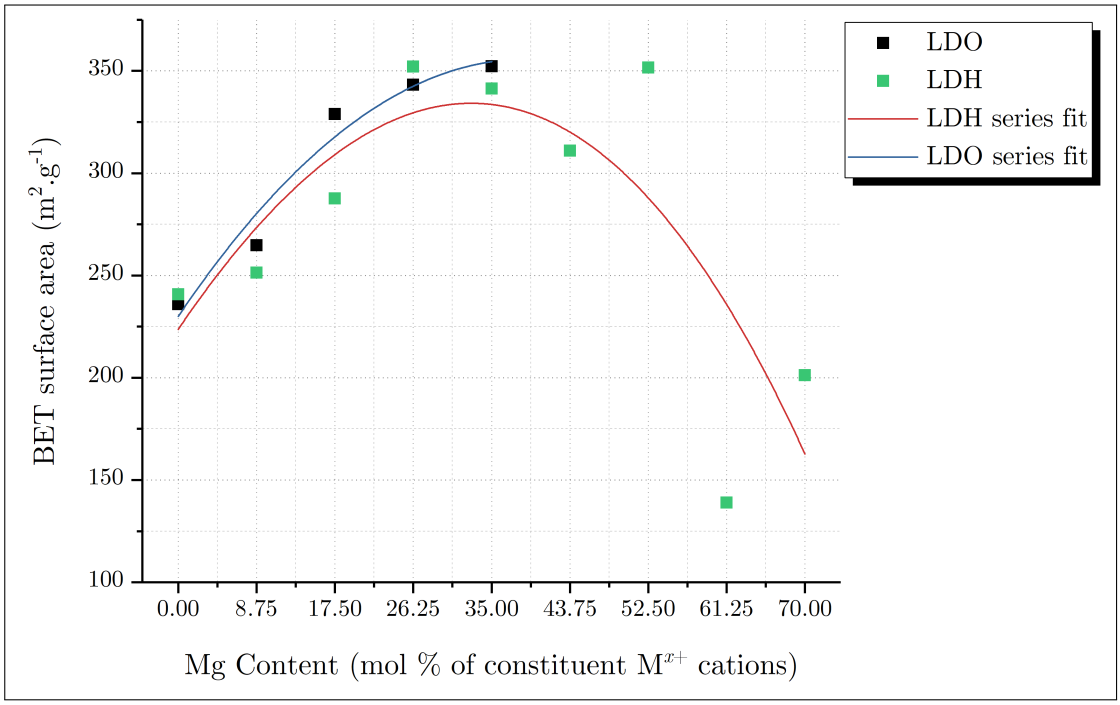


Figure 6.12: The BET surface areas of: Green) the Mg-based AMO-LDH series and Black) part of the Mg-based calcined (LDO) series; the error = ± 1.0 $m^2.g^{-1}$. The red line represents a cubic fit of the LDH where: y = 223.7 + 6.44x - 0.08x^2 - 2.89x^3 and the R^2 value = 0.61. The blue line represents a quadratic fit of the LDO where: y = 230.0 + 6.47x - 0.08x^2 and the R^2 value = 0.96.

The c parameter dominant regime changed around ≈ 52.5Mg-LDH, whereas the analogous change in the crystallite thickness trend occurred at 35Mg-LDH. The BET surface area increases up until 26.25Mg-LDH (see Figure 6.12), therefore the dominant effect is likely the extent of exfoliation; which increases with the Mg content, theoretically because the layers become more polarising and likely achieve higher interlayer acetone concentration during the washing step. The drop in BET surface area after 52.5Mg-LDH is likely due to the increased attractive forces between the interlayer anions and increasingly polarising layers; making exfoliation less thermo-

dynamically favourable. The plateau in between may occur due to a thermodynamic limit on the extent of exfoliation because highly exfolaited layers are higher in potential energy. Alternatively, it could be that the amalgamation of polarisibility, stacking and exfoliation effects (mentioned in Section 6.3.2) cancel each other out, causing the plateau.

Regardless, even the BET surface area of 61.25Mg-LDH, 139 $m^2.g^{-1}$, is very high compared to that of conventional LDHs and mixed metal oxides that have been used as precursors for MSR in literature; for instance, the BET surface areas of two literature active MSR catalyst precursors are 109.6 and 100 $m^2.g^{-1}$ for a $CuZnAlCeO_x$ MMO (with an activity of 19.3 $\mu mol_{H_2}.s^{-1}.g_{cat}^{-1}$ at 240 °C) and a 300 °C-calcined CuZnAl-LDH (with an activity of 6.84 $\mu mol_{H_2}.s^{-1}.g_{cat}^{-1}$ at 250 °C after 25 h), respectively. [85, 106]

It was also theorised that AMO-LDHs would have the potential to experience further surface area increases, upon calcination, consequently having high D_{Cu} % within the lattice. TGA showed that Mg content inversely correlated with thermal stability (see Section 6.3.4). Therefore, it was theorised that the extent of decomposition during calcination may decrease with increasing Mg content; however, the exact extent and effect of partial vs. complete decomposition was not deciphered by TGA. The BET surface area of some of the calcined Mg series was also measured, see Figure 6.12, and in 3/5 cases there was an average $\approx$ 22.5 $m^2.g^{-1}$ surface area increase; whereas, in the other two cases the surface area was $\approx$ 6.8 $m^2.g^{-1}$ lower on average. Thus, the effect of calcination on the surface area of the materials is not clear, perhaps the error in the BET measurement is higher than the instrument readings suggest (the instrument is usually used to record BET surface areas of the order $\approx$ 1000 $m^2.g^{-1}$); regardless, calcination does not appear to degrade the materials in a way that negatively affects their surface area and catalytic potential. Further energy-saving studies

could be carried out to see if the as-prepared LDHs could be directly reduced for catalytic application.

The high surface area of the series makes them good potential precursors for active and selective MSR catalysts; the assessment of the D_{Cu} % and MSR activity for the derived catalysts can be found in Sections 6.3.6 and 6.3.7.

6.3.6 N_2O/H_2 titration of the Mg LDO series

The D_{Cu} % of a sample is an indicator of how many Cu particles there are on the surface of a sample and how thick and wide those particles are; because the D_{Cu} % is determined by the surface:bulk Cu ratio, see Equation:

$$\text{Cu dispersion } \% = \frac{Exposed\ surface\ Cu\ atoms}{Total\ Cu\ atoms\ in\ sample} \times 100$$

Additionally, the higher the D_{Cu} %, the larger the amount of Cu metal/oxide support interface there is (relative to the total amount of Cu).

The initial effect of adding Mg to the structure, from 0Mg-LDO to 8.75Mg-LDO, seems to decrease the D_{Cu} %, see Figure 6.13. Some Cu^{2+} in a LDO sample could be on the face of a non-exfoliated layer or in the bulk of a section that has lost its layered structure. Such an atom, that might be reduced in the 0Mg-LDO sample, might not get reduced in 8.75Mg-LDO. Incorporating Mg increases the required reduction temperature, see Figure 6.11. Therefore, for Cu in that position, which is also surrounded by a higher Mg-O concentration, there may not be enough thermal energy to break the layer's bonds to reduce that Cu atom onto the surface. This effect would mean there is more Cu^{2+} left in the bulk and the sample would have a lower D_{Cu} %. This suggests that the D_{Cu} % of 0Mg-LDO could arise from an incomplete reduction or an anomaly.

Beyond 8.75Mg-LDO the trend in D_{Cu} % correlates with increasing Mg content. The TPR analysis shows the reduction peak can shift closer to $\approx$ 320 °C for LDO

samples with higher Mg content, see Figure 6.11, but the peaks for such samples still have overlap with the experimental reduction temperature, 290 °C. The results from Figure 6.13 indicate that the 2 hour reduction time is sufficient for the majority of Cu^{2+} to be reduced to Cu^0 at 290 °C; because the Cu^{2+} needs to be reduced to Cu^0, before being oxidised to Cu^+ by N_2O, to give a reading in the D_{Cu} % titration experiment.

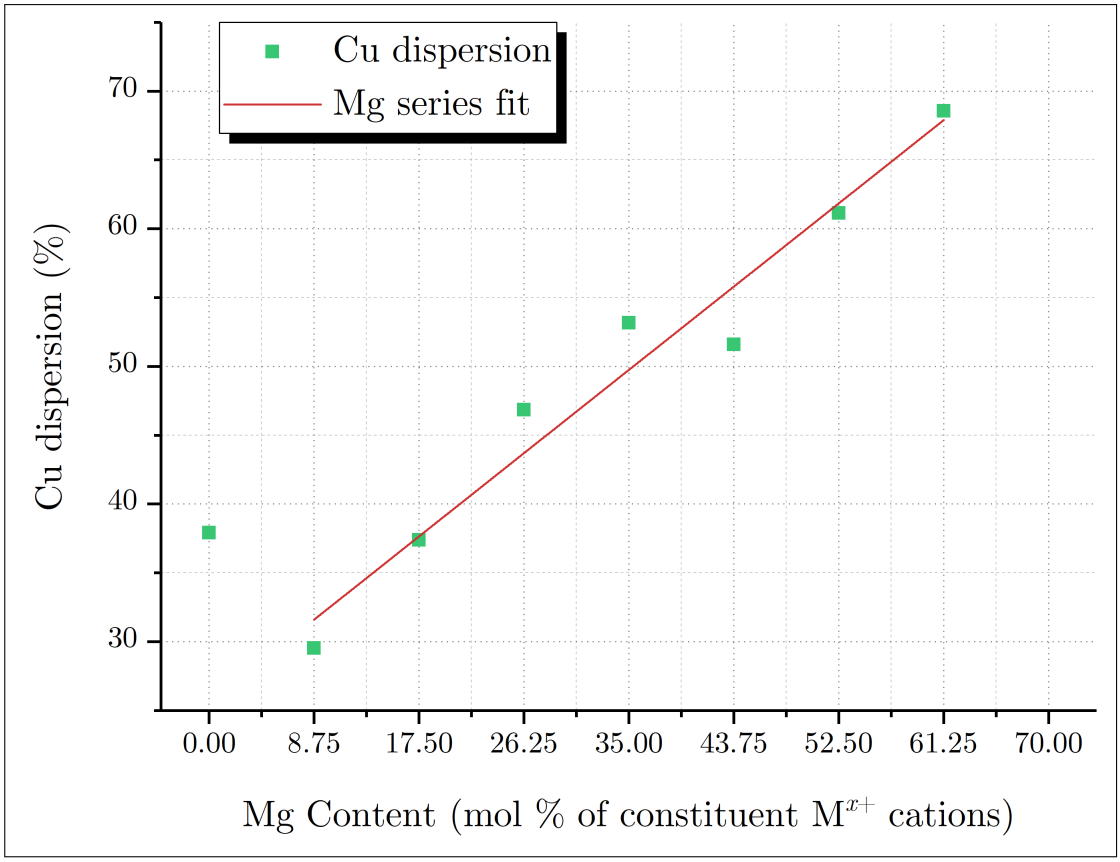


Figure 6.13: The D_{Cu} % of the calcined Mg-based AMO-LDH series; measured via N_2O/H_2 titration. The red line represents a linear fit (ignoring the 0Mg-LDO data point) where: $y = 25.5 + 0.691x$ and the R^2 value = 0.958.

D_{Cu} % increases with Mg content despite the Cu reduction temperature also correlating with the Mg content. This means that the dominant trend from 8.75Mg-LDO to 61.25Mg-LDO is caused by the decreasing Cu concentration in the samples. LDOs topotactically maintain some LDH structure, meaning they likely maintain

the high elemental dispersion; therefore, when the Cu is reduced and comes out of the structure to form metal particles, if the Cu concentration is low, only small particles can form as there are not many other Cu atoms nearby. The size of the particles will also be determined by the reduction temperature because particles need thermal energy to move across the surface and sinter. The reduction temperature is kept constant throughout this work but different samples are seen to have Cu environments that are reduced at different temperatures in TPR (see Section 6.3.4). Smaller particles lead to higher D_{Cu} % because a higher % of the atoms in the particles are on the surface not the bulk (assuming all Cu is reduced out of the lattice).

The size of the Cu^0 particles for the reduced catalysts were not measured directly by TEM or PXRD. However, equations, that can be used to estimate crystallite size from metal dispersion and vice versa, indicate it is reasonable to assume the Cu^0 crystallite size trend in the reduced sample mirrors the D_{Cu} % trend i.e. Cu crystallite size theoretically decreases with increasing Mg content. [243] Experimentally in this work D_{Cu} % correlates with Mg content.

6.3.7 MSR catalytic activity of the Mg reduced series

The Cu-based, AMO-LDH derived catalysts proved active in MSR except for the sample with no Cu content, 70Mg-r; see Figures 6.14, 6.17 and 6.18. As outlined in Section 3.6, the total Cu^0 surface area, D_{Cu} %, amount of support-metal interface and electronic properties of the catalyst can all theoretically affect the MSR catalytic performance. The trend in the hydrogen production of the reduced Mg-based catalyst series is a volcano trend respective to the Mg content; the hydrogen production increases up until 43.75Mg-r and then drops off substantially. The CO production also follows a volcano-like trend, increasing up until 17.5Mg-r and then dropping off after 43.75Mg; however, there is more of a plateau in between. This trend results from an amalgamation of all the trends and properties of the series from throughout

Section 6.3; many of which are likely competing effects that have opposite effects on the MSR activity and CO production.

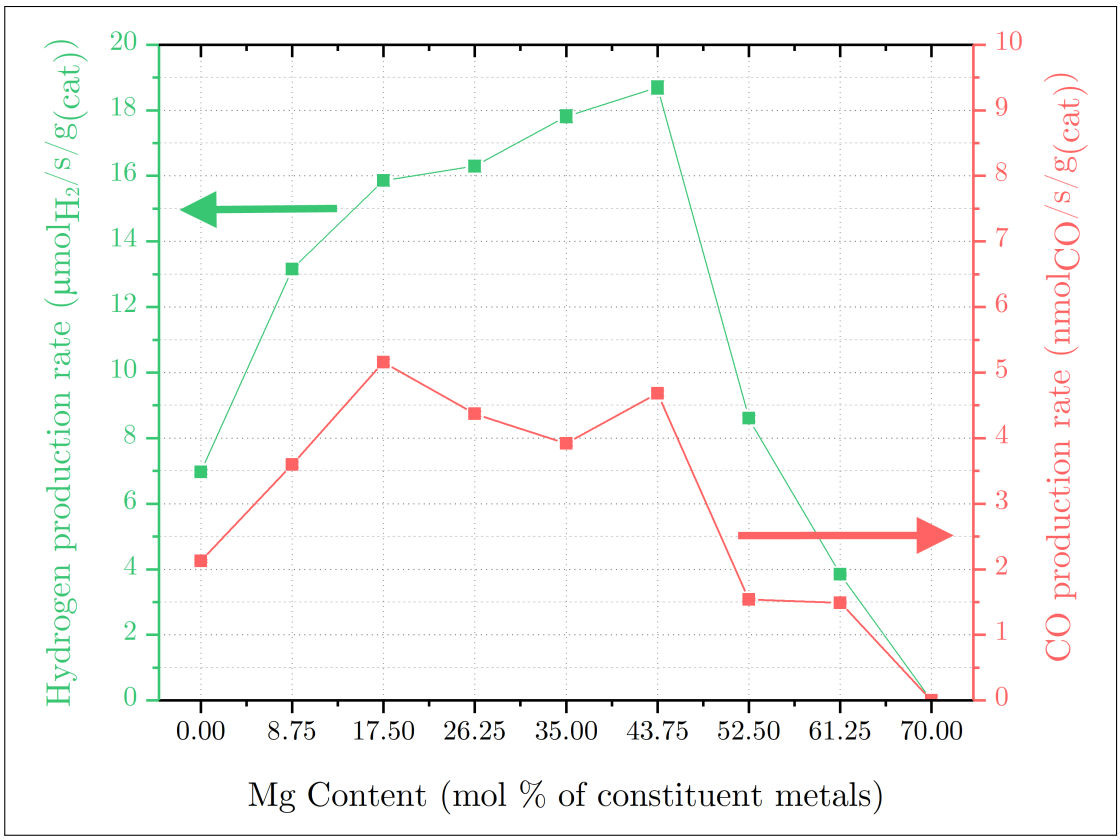


Figure 6.14: The MSR catalytic test results of the reduced Mg-based series; the hydrogen production rate and CO production rate units are $\mu mol_{H_2}.s^{-1}.g_{cat}^{-1}$ and $nmol_{CO}.s^{-1}.g_{cat}^{-1}$, respectively. Tested at 180 °C for 5 hours, with with 75 mg of catalyst, a N_2 gas flow of 10 mL.min^{-1} and a 0.075 mL.min^{-1} liquid flow of water:methanol solution (1.1:1 mol ratio). WHSV = 5.41 h^{-1}.

Some of the largest increases in both H_2 and CO production occur between 0Mg-r and 17.5Mg-r, over the same Mg content region the BET surface area of the precursor LDHs is increasing. As seen in Section 7.3.4 and in literature, the high surface areas of the exfoliated AMO-LDHs are maintained after calcination and could even possibly be increased; therefore, it is likely the same trends in the BET surface area of the LDHs and LDOs apply to the topotactically reduced samples. After the in-situ reduction and 5 hour MSR experiment, reduced catalysts occupy a volume very similar to that of the starting LDO. However, in Figure 6.12, when the BET surface area drops off

by more than half between 52.5Mg-LDH and 61.25Mg-LDH, this does not coincide with the drop in H_2 and CO production. As previously mentioned, there are many competing effects during MSR; in high Mg content regimes, the D_{Cu} % of the series increases with Mg content, whereas BET surface area is decreasing.

The activity of 52.5Mg-r drops off despite its relatively high surface area and D_{Cu} %, this could be due to the sample having a lower total amount of Cu on the surface. The hydrogen production rate should be determined by the MSR rate-determining step (RDS). Lee et al. found the RDS of MSR over a standard commercial Cu/Zn/Al mixed metal oxide catalyst to be the dehydrogenation of adsorbed methanol to bidentate formate; Peppley et al. also found this step to be the RDS. [120, 141] Therefore, in this work the RDS for MSR is considered to involve the oxide support because dioxymethylene/formate formation is theorised to occur at the Cu-support interface (see Figure 3.5). During the RDS a lattice oxygen in the support donates electron density to the adsorbed methoxy group, weakening/breaking some of its bonds with lattice $M^{\delta+}$ as a result. As with the trend in TPR, as Mg content increases so will the average $M^{\delta+}$-$O^{\delta-}$ bond strength. Theoretically, the stronger the breaking interface $M^{\delta+}$-$O^{\delta-}$ bond, the higher the required activation energy for the RDS, which in turn would reduce the MSR rate. This theory can explain the higher Mg content regime and sharp drop off in the rate of hydrogen production (see Figure 6.14). In addition to the RDS, the lower the amount of base level Cu^0, the less sites for methanol adsorption are available to begin the catalytic cycle; which would cap the activity. Therefore high Mg content samples such as 52.5Mg- and 61.25Mg-r are likely less active due to their low Cu surface area combined with their higher lattice energy.

It is proposed the volcano trend in hydrogen production, as seen in Figure 6.14, is dominated by the effects of the increasing total BET surface area and D_{Cu} % during the lower Mg content regime up until 43.75Mg-r. The downwards trend in hydrogen

production from 52.5Mg-r to 70Mg-r is due the decreasing BET surface area, amount of active Cu sites and possibly a decrease in the rate of the RDS step (as a result of Mg increasing the average $M^{\delta+}$-$O^{\delta-}$ bond strength). This trend is also affected by the catalyst stability, see below.

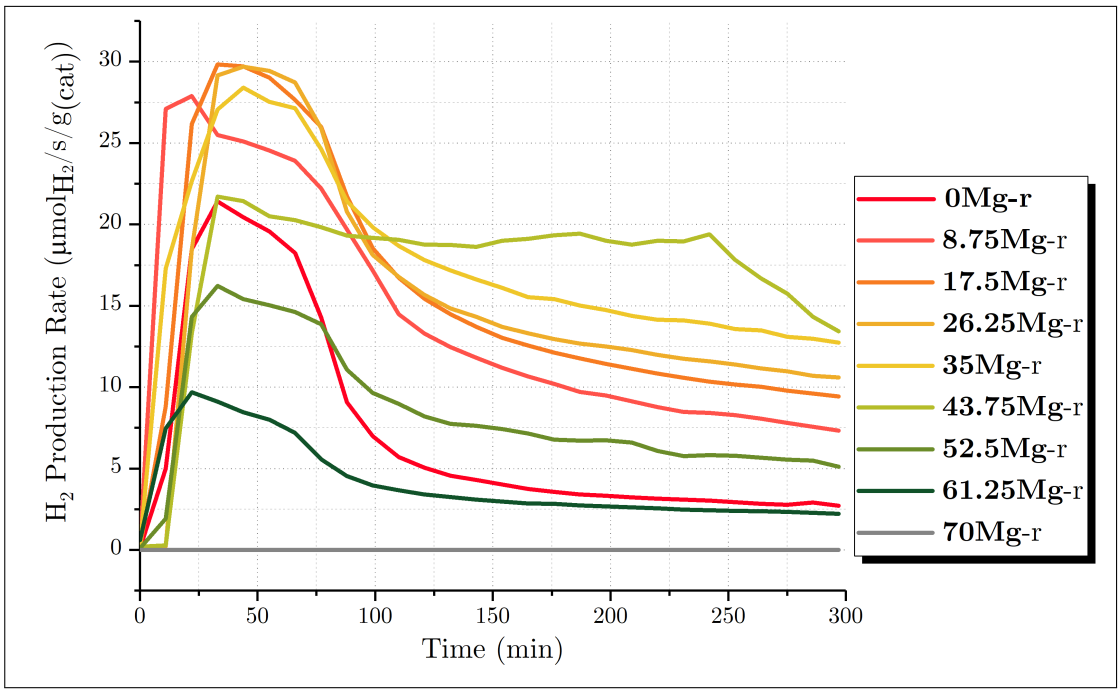


Figure 6.15: The hydrogen production rate ($\mu mol_{H_2}.s^{-1}.g_{cat}^{-1}$) of the reduced Mg-based series shown against time in the x axis (Time = 0, coincides with the start of reactant flow). Tested at 180 °C for 5 hours, with 75 mg of catalyst, a N_2 gas flow of 10 mL.min^{-1} and a 0.075 mL.min^{-1} liquid flow of water:methanol solution (1.1:1 mol ratio). WHSV = 5.41 h^{-1}.

For most reduced Mg-based catalysts in this work, the MSR activity starts to drop off after ≈ 75 minutes at 180 °C (see Figure 6.15). This drop in activity is most likely caused by the sintering of the Cu^0 particles, which involves either, or both, metal particle or atomic movement (see Section 2.5.4) across the support surface that results in the formation of larger Cu^0 particles. The activity drops because Cu^0 surface area, D_{Cu} % and the amount of Cu-support interface decreases as a result of sintering.

As seen in Figure 6.14, the samples that have the highest average hydrogen

production are 35Mg-r and 43.75Mg-r. This is likely because these two samples demonstrate the highest stability against sintering under the reaction conditions. In Figures 6.15 and 6.16 35Mg-r is seen to have a smaller drop in activity than the samples with lower Mg content; whereas, the activity of 43.75Mg-r remains stable for up to ≈ 225 minutes. 52.5Mg-r and 61.25Mg-r have activity drop off that has a smaller range than that of low Mg content samples but their initial activity peak is much lower due to their low amount of Cu^0.

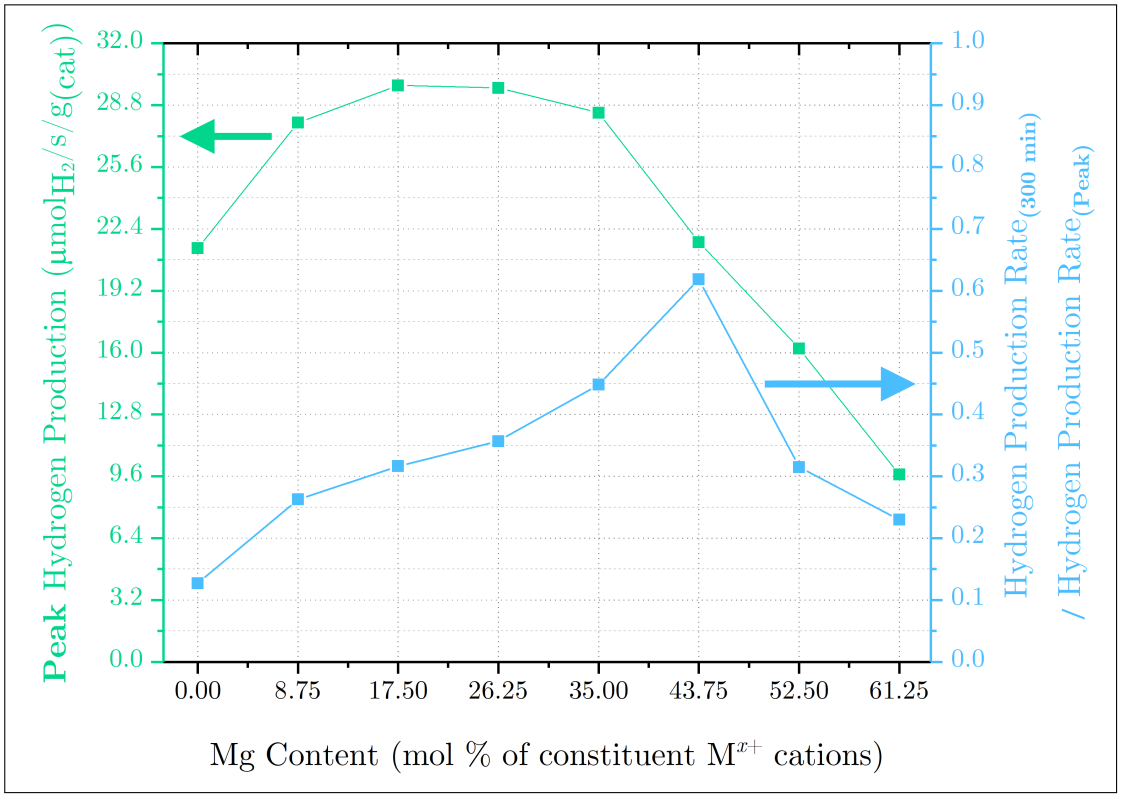


Figure 6.16: The maximum hydrogen production rate ($\mu mol_{H_2}.s^{-1}.g_{cat}^{-1}$) observed for each reduced Mg-based catalyst, shown against the (Hydrogen production rate at 300 mins / The peak hydrogen production rate) ratio. Tested at 180 °C for 5 hours, with 75 mg of catalyst, a N_2 gas flow of 10 mL.min^{-1} and a 0.075 mL.min^{-1} liquid flow of water:methanol solution (1.1:1 mol ratio). WHSV = 5.41 h^{-1}.

Figure 6.16 shows different volcano trends for both the maximum/peak activity and hydrogen production stability for the Mg-based series. The volcano trend in the maximum hydrogen production, seen in Figure 6.16, is likely caused by the same

competing factors as in the case theorised for the average activity (discussed above and shown in Figure 6.14). The hydrogen production rate comparison ratio between the peak activity and the activity at 300 mins is an indicator of the catalyst stability; its trend's shape is reminiscent to the shape seen for the average activity trend in Figure 6.14. Both a combination of the maximum observed hydrogen production rate and the catalyst stability (Figure 6.16) determine the average hydrogen production rate over the 300 minute reaction. The stability of the catalyst is likely the main factor that offsets the maximum H_2 production trend from the average H_2 production trend i.e. 43.75Mg-r is the most active catalyst on average due to its stability more so than its BET surface area and D_{Cu} % (as alluded to previously).

The stability trend in Figure 6.16 is dictated by the catalysts' resistance to harsh conditions and sintering; which in turn, is determined by the morphology/structure of a material and the nature of its metal-support interactions. As mentioned in Section 2.5, bonds need to be broken and formed between the surface and moving entity to allow an atom or particles to diffuse across a surface (to form larger particles with less surface energy); therefore, the rate of sintering can depend on the energy of vacancy formation and the energy required to break the metal-support interaction. [244] Despite the favourable thermodynamics of forming larger heterogeneous particles from smaller ones, sintering is kinectically limited; the Hüttig and Tammann temperatures are used to estimate atomic and crystallite diffusion onset temperatures, respectively, based on the melting points of metals (a good indicator of the strength of attraction between the metal atoms). [54, 244]

In literature, hydroxylation of support oxides has shown to have both increasing and decreasing effects on the adsorption strength of nanoparticles; such effects are very dependent upon the characteristics of the support and nanoparticles. [59] In this work, TGA shows the catalysts are likely dehydroxylated so it is not obvious what

effect, if any, possible, partial retention of hydroxyl surface groups would have on MSR catalysis. The Mg/LDO-based catalysts likely have both a 2D mesoporous structure, as shown with BET (with little 3D connectivity between pores), and a partial layered morphology, both these properties can physically separate Cu particles and limit the extent of sintering. [54, 60] TGA implied samples with lower Mg content were less thermally-stable (see Section 6.3.4) i.e. a larger extent of layer decomposition in the calcinations of samples with lower Mg content may have hindered the ability of the derived catalyst supports to physically limit the sintering of Cu particles.

Whilst many factors affected the stability trend, its resultant volcano shape was theorised to be caused by the combination of two main effects: i) the sintering rate would have been theoretically higher for samples with higher D_{Cu} % and, therefore, higher Mg content (see Section 2.5.4). ii) The thermal stability of the layered morphology, that could physically limit sintering, would have likely increased with an increasing $Mg^{2+}/(Mg^{2+}Cu^{2+})$ % (due to the formation enthalpy of CuO/MgO, Table 6.4).

The trend in CO production partially follows that of hydrogen but levels off between 17.5Mg-r and 43.75Mg-r. As previously mentioned in Section 3.4, CO is produced via two different side reactions, RWGS and MD. Section 3.4 also discussed that WGS and RWGS steps can take place on the support oxide surface; therefore, it was expected that BET surface area would be a dominant factor affecting CO production rate. The volcano trends in the BET surface area (see Figure 6.12) and CO production rate are similar but as with the hydrogen production trend the 52.5Mg-r sample has less production than expected for its BET surface area. This suggests there is a new competing effect that could affect the RDS of the RWGS.

As per literature reports MSR occurs at the Cu-support interface, whereas WGS can occur at any oxide position (see Section 3.5). [245,246] Therefore, the discrepancy

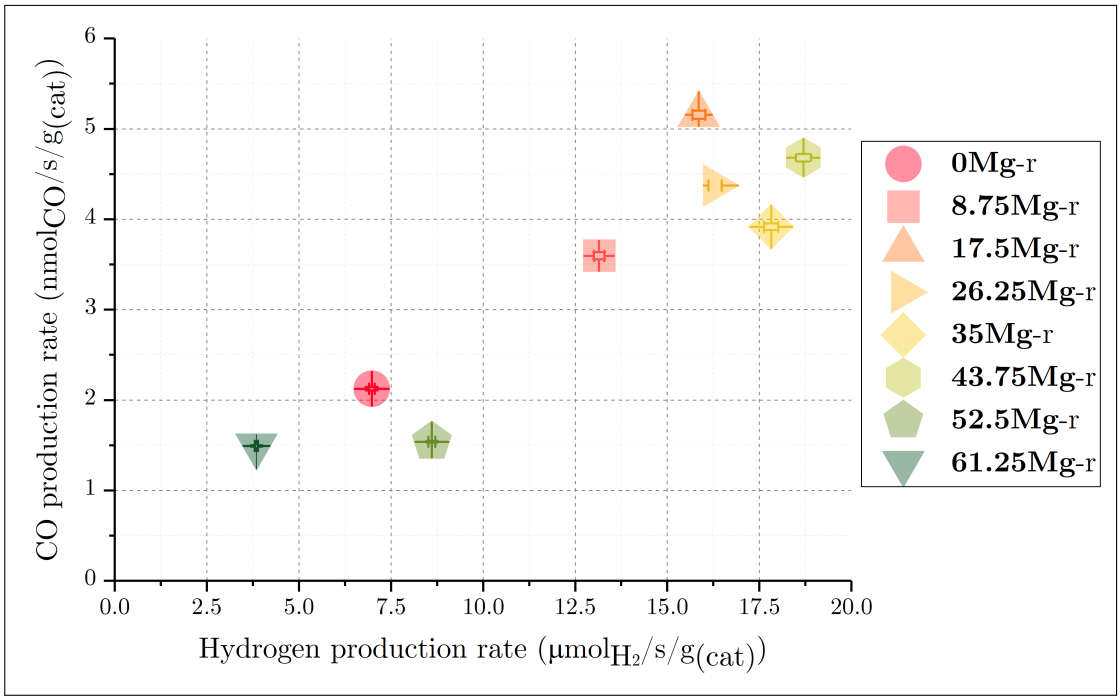


Figure 6.17: A rearranged format of the MSR catalytic test results of the reduced Mg-based series, seen in Figure 6.14; the hydrogen production rate and CO production rate units are $\mu mol_{H_2}.s^{-1}.g_{cat}^{-1}$ and $nmol_{CO}.s^{-1}.g_{cat}^{-1}$, respectively. Tested at 180 °C for 5 hours, with with 75 mg of catalyst, a N_2 gas flow of 10 $mL.min^{-1}$ and a 0.075 $mL.min^{-1}$ liquid flow of water:methanol solution (1.1:1 mol ratio). WHSV = 5.41 h^{-1}. Error bars (x/y) are shown inverted within the data point symbols.

between 43.75Mg- and 52.5Mg-r in both their H_2 and CO production relative to their LDO BET surface area can be explored further by examining each catalyst's stability and D_{Cu} % relative to their H_2:CO selectivity. A low active Cu^0 content and high D_{Cu} % were theorised to cause low peak activity and low catalytic stability, respectively (Figure 6.16). However, it is still possible that the active state of 52.5Mg-r, once it had sintered and reached a steady MSR/WGS rate on-stream, had a higher D_{Cu} % than 43.75Mg-r, in an analogous position, despite still having a lower surface area and lower surface Cu^0 content. Such a scenario could have led to 52.5Mg-r having a much lower H_2 production rate and higher H_2:CO selectivity than 43.75Mg-r (as seen in Figure 6.18); this is because if RWGS/WGS can occur on any surface, whilst MSR can only occur at the interface, then the amount of Cu-support interface, D_{Cu} % or

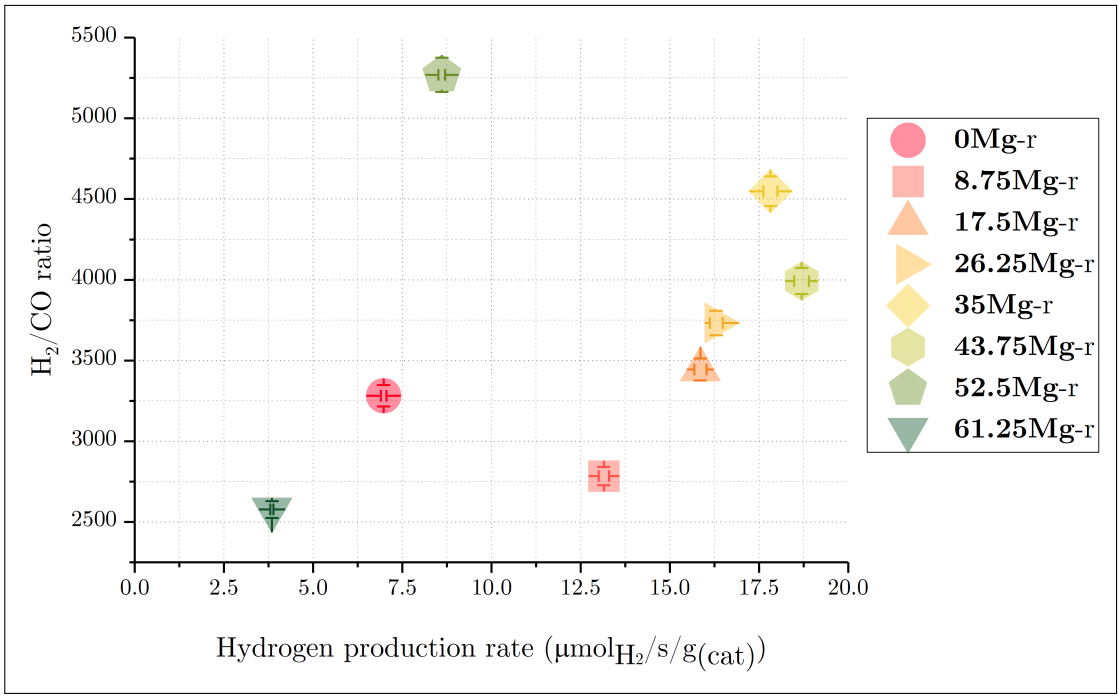


Figure 6.18: The H_2:CO mol ratio produced by the reduced Mg-based series during MSR (as a function of their hydrogen production); the hydrogen production rate's units are $\mu mol_{H_2}.s^{-1}.g_{cat}^{-1}$. Tested at 180 °C for 5 hours, with 75 mg of catalyst, a N_2 gas flow of 10 mL.min^{-1} and a 0.075 mL.min^{-1} liquid flow of water:methanol solution (1.1:1 mol ratio). WHSV = 5.41 h^{-1}. Error bars (x/y) are shown inverted within the data point symbols.

[MSR+WGS]:[WGS] active site ratio, would correlate to the H_2:CO ratio (as seen in Figure 6.18). [20]

The alternative dominant limiting factor or another additional effect that causes the drop in CO productivity of 52.5Mg-r could be thermodynamic, the hydrogen productivity trend will shift the WGS equilibrium, via Le Chatelier's principle, by dictating the hydrogen concentration; this can be seen in Figure 6.14, the CO trend decreases and increases in a similar pattern to the hydrogen productivity. However, this does not account for the H_2:CO ratio.

6.4 Mg chapter summary

Regarding the initial goal of the Mg-based AMO-LDH series, the project was successful in proving some of the active metal content, Cu and Zn, could be replaced by a cheaper and more abundant element, Mg, whilst improving catalytic activity and selectivity; this is most obvious in Figure 6.18. 43.75Mg-r provided a much higher activity than 0Mg-r due to its increased Cu dispersion. The high D_{Cu} % of the Mg series catalysts was achieved due to the combination of lowered Cu content and high BET surface areas. The latter of which was caused by Mg^{2+} increasing the polarising power of the LDH layers and therefore the interlayer acetone concentration during synthesis, leading to a higher degree of layer exfoliation. However, too high a Mg content led to low activity, due to the decrease in active surface Cu^0 species, and a decline in D_{Cu} % stability and BET surface area.

The most resounding success of this project was the high H_2:CO selectivity of catalysts prepared from novel CuZnMgAl AMO-LDHs due to their D_{Cu} %. The highest H_2:CO ratio calculated from literature was 3000 mol_{H_2}:mol_{CO} but, as can be seen from Figure 6.18, the majority of Mg series catalysts improved substantially on this ratio despite using a lower water excess and WHSV. [247] This breakthrough in CO selectivity was continued to be explored and is reported in the next chapters of this work for other MSR catalysts derived from AMO-LDHs.

Chapter 7

Modifying the primary LDH M^{3+} ions

7.1 The goal of M^{3+} ion experimentation

Building upon the success of the CuZnMgAl AMO-LDH derived catalyst series, it was decided that other possible cations in the LDH matrix should be explored. In Section 6.1, the value of metals was discussed specifically in relation to the dilution of an active species; however, AMO-LDH formation requires 'non-active' metals with or without active species dilution. As seen in Section 5.1.1, M^{3+} cations are a vital part of the LDH formula and intentionally or unintentionally alter catalysis via electronic, support-metal interactions or other effects.

Both Ga and Al have been used as components in MSR catalysis literature; predominantly for Cu-based catalysts but not necessarily LDH-derived catalysts. Both metals have been reported to have positive effects in MSR catalysis; however, it is hard to make a cost effective comparison between papers because MSR conditions vary widely across literature (and are not always reported in full detail) and every publication has different priorities. More so than in the case of Cu, Zn and Mg there is a large difference in the pricing of Ga and Al; 217 and 2.85 £/kg, respectively. [248,249] Additionally, Figure 6.1 demonstrates Al is 10^4 orders more abundant

than Ga on Earth making it the more sustainable choice and also the option that is more widely available, produced and in reserve.

In this chapter, the effect of the M^{3+} cation is investigated with the objective of providing insight into which M^{3+}-based LDH, Ga- or Al-, is more suitable for hypothetical, future, MSR-PEMFC systems. This is gauged mainly in terms of catalytic ability i.e. as discussed in Chapter 4, a high H_2/CO production ratio at low MSR temperatures is desirable. In turn that data and analysis could be used by other parties to determine economic feasibility.

7.2 The usage of Ga and Al in steam reforming catalysis

The addition of Al to MMO-based MSR catalysts can physically increase Cu dispersion and the specific surface area of the material. [90] Tang et al. also observed an Al-induced supporting effect, specifically the presence of $CuAl_2O_4$ spinel oxide increased the stability of Cu surface particles. [106] Initial studies by Alejo et al. showed that Al introduction into CuZn-based methanol oxidation catalysts decreased TOF slightly but also increased the catalyst's stability. [250] The observations by Alejo et al. are likely due to the introduction of a harder, more charged cation, Al^{3+}, increasing the M-O bond strength in the oxide; this in turn would increase the energy needed to break adsorption bonds to the active Cu species in the catalytic cycle (decreasing TOF), but also increase the energy required to break lattice bonds (decreasing the amount of lattice breakdown, increasing stability). [7]

These above observations have competing effects on catalytic performance, indicating the amount of Al^{3+} needs to be balanced in CuZn-based MSR catalysts. The stabilising effect of Al oxide supports is limited for Cu particles, partially due to the inherent low thermodynamic stability of Cu^0 against sintering; Thurgood et al. cal-

culated the number of MSR reforming sites of a 'commercially-produced' $CuZnAlO_x$ material halved after 80 hours on stream (at 280 °C, with a 1:1 water:methanol mol ratio). [7, 251]

Due to its higher cost, Ga likely hasn't been used as much as a support in Cu-based MSR catalysts; however, there have been reports of Ga promoting MSR activity when added to Cu/ZnO materials. [252] Toyir et al. report this promotion of activity but it is not clear whether the activity, in $mol.g^{-1}.s^{-1}$, is averaged over the 3 hour reaction time; therefore, it is uncertain if this observed activity increase arises from the Ga stabilising the active Cu particles or by adding new active sites. [252] Ga oxides are more 'reducible' than non-reducible Al oxides, meaning that they more readily form oxygen vacancies, which could be a potential pathway by which Ga addition could introduce new active MSR sites. [66]

Schumann et al. doped ZnO supports with both Ga and Al to support Cu particles for the catalysis of methanol synthesis and RWGS reactions; they theorise both M^{3+} cations structurally promote methanol synthesis, whereas they reduce the activation energy of the RWGS reaction. [253] Below the temperature for bulk ZnO reduction, TPR peaks are seen for the ZnGa-based samples; Schumann et al. attributes this to the reduction of 'special' oxygen defects from the ZnO lattice. [253] Al inclusion does not increase oxygen vacancy formation based on EPR and TPR analyses; likely because it is a harder cation causing stronger average lattice M-O bonds. [253] The XPS data collected by Schumann et al. does not show any Zn^0 as it was performed at low pressures; rather ZnO overlayers on Cu^0 are suggested. Schumann et al. also reported the Al-based material gave a lower RWGS CO formation activation energy and higher methanol formation activation energy compared to the Ga sample, each by 2-3 $kJ.mol^{-1}$ at low pressures. [253]

Li et al. also report Ga-induced promotion of CO_2 hydrogenation activity (akin

to the reverse of MSR), they cite structural promotion (similar to Al support effects) but also propose the formation of an electronic heterojunction; that facilitates the reduction of Zn, forming active CuZn alloy particles (see Section 3.6.2). [169] The theorised type II heterojunction is between $M^{2+}Ga_2O_4$ spinel oxide phase and ZnO, with holes and electrons on the phases, respectively; they propose if the holes (excited oxygen species) were 'long-lived' they could react with hydrogen under reducing conditions and the corresponding electrons would then reduce the ZnO phase. [169] Li et al. display deconvoluted Zn 2p XPS peaks, TEM analysis and EXAFS/DFT modelling of ex-situ, unreacted catalysts as evidence for CuZn alloy formation, it is theorised bcc CuZn alloys stabilise the Cu from sintering and that Ga spinel oxide is required for this phenomena. [169, 170] Kattel et al. investigate CuZnAl catalysts for CO_2 hydrogenation and provide evidence that no Zn^0 forms during the reaction, it was suggested all previous observations of CuZn alloys are better explained by highly disperse ZnO on Cu^0. [173] However, Kattel et al. proposed that the CuZn alloy is unstable at pressures of > 20 bar (MSR atmospheric pressure is not mentioned) and do not have any M^{3+} in their sample; it is shown that CuZn alloy starting catalysts become oxidised under reaction conditions but it is not discussed whether the reduction of Zn into a CuZn alloy (during the pre-reaction reduction step) is what allows the theorised disperse ZnO overlayer to form. [173]

Regardless of the nature of the Ga^{3+} promotion/stabilising effect, doping Ga into Cu-based samples has been observed to decrease the temperature at which the Cu^{2+} is reduced to Cu^0; this can be seen using TPR analysis. [17, 169, 253] This at the very least could conserve energy, making the production of the catalysts more energy efficient; alternatively more reducible Cu could have a significant effect upon the MSR activity. Both Al^{3+} and Ga^{3+} appear to have slightly different strengths in regards to their use in acting as the LDH 3+ cation; in this chapter they will be assessed through the lens of their MSR activity and selectivity.

7.3 The CuZnGa and CuZnAl AMO-LDH series

Two different series of AMO-LDHs were synthesised, one using Ga^{3+} and one using Al^{3+}; the M^{3+} mol % was kept within the stoichiometry range of a theoretical LDH. The Cu^{2+}:Zn^{2+}:M^{3+} mol ratio was 0.45:(0.35-0.25):(0.2-0.3), the trend was designed to follow the effects of replacing Zn^{2+} with Ga^{3+} or Al^{3+} whilst aiming to maintain the high surface areas expected of an AMO-LDH. The Cu amount was kept constant to avoid large differences in the theoretical amount of MSR active sites between catalysts to isolate the M^{3+} effect.

The experimental ratios of metal nitrate hydrates used in the synthesis of the series are displayed in Table 7.1. All samples are labelled as follows: '-LDH' = as-prepared AMO layered double hydroxide; '-LDO' = calcined/LDO sample; and '-r' = reduced sample. Each CuZnAl- or CuZnGa-derived sample is also denoted with its constituent Zn, Al and Ga content expressed as the metal mol % of the respective metal nitrate hydrate (of the total metal nitrate) used in synthesis.

Table 7.1: The constituent metal mol ratios used during the synthesis of the CuZnGa and CuZnAl AMO-LDH series.

Sample	Cu mol % (of total metal mols)	Zn mol % (of total metal mols)	Ga mol % (of total metal mols)	Al mol % (of total metal mols)
35Zn20Al-LDH	45	35	0	20
30Zn25Al-LDH	45	30	0	25
25Zn30Al-LDH	45	25	0	30
35Zn20Ga-LDH	45	35	20	0
30Zn25Ga-LDH	45	30	25	0
25Zn30Ga-LDH	45	25	30	0

ICP-MS analysis shows the amount of metals in the as-prepared LDHs is consistent with the theoretical metal nitrate ratios used in their synthesis, displayed in Table 7.2 (C, O, N and H wt % are not shown but will make up the remainder of each sample to 100 %). The molar masses of Cu, Zn and Ga are almost twice that of Al, hence the Al wt % relative to the Ga wt % of the analagous, mol ratio Ga sample

is much lower; additionally, this causes the % range for both the Cu and Zn wt % in the Al series to be roughly double that of the Ga series i.e. the Cu and Zn have a more weighted effect on the Al series ICP. It is important to note that the Cu mol % is likely very similar in each sample; the Cu wt % changes relative to the average mass of other metals in the LDH. The outlier appears to be 30Zn25Al-LDH, which has a lower Cu wt %, by about 1 %, than expected based on the other ICP trends.

Table 7.2: The ICP-MS analysis results of the CuZnMgAl AMO-LDH and -LDO series.

Sample	Cu (wt %)	Zn (wt %)	Ga (wt %)	Al (wt %)
35Zn20Al-LDH	34.39	26.08	0	7.16
30Zn25Al-LDH	34.41	22.06	0	9.32
25Zn30Al-LDH	36.38	20.30	0	11.50
35Zn20Ga-LDH	31.43	23.82	14.49	0
30Zn25Ga-LDH	31.79	21.48	16.73	0
25Zn30Ga-LDH	32.64	20.18	19.19	0
35Zn20Al-LDO	30.91	24.45	0	6.04
30Zn25Al-LDO	32.32	22.10	0	7.89
25Zn30Al-LDO	31.51	17.67	0	9.10
35Zn20Ga-LDO	33.44	25.90	14.57	0
30Zn25Ga-LDO	32.41	21.52	16.82	0
25Zn30Ga-LDO	32.98	20.59	16.59	0

Table 7.2 also includes the ICP-MS of the calcined samples. Notably outside of the ICP-MS results, upon calcination the mass of all the LDH samples would decrease by about ≈ 33 %; a similar situation was observed in the TGA of the Mg LDH series (see Figure 6.2). The loss in mass due to calcination is due to dehydroxylation and the loss of interlayer water/anions. It was expected that all observed metal wt % values would increase; however this is not the case for the Al-based LDOs, in fact only the Ga-based LDOs' Cu wt % significantly increases. The cause for this unexpected data may be due to the year of storage between calcination and measurement of the LDOs' ICP-MS; the samples may have re-adsorbed water and CO_2 (as carbonate),

exhibiting the LDH memory effect. [254–256] This is still possible due to the prolonged storage, despite the samples being stored under 10mbar vacuum, and the differences between the Ga- and Al-based series may be due to their affinity for LDH memory effect. The TGA analysis of the Mg-based series showed different LDHs had different thermodynamic stability based on their lattice energy; over the course of a year, at room temperature, there might be pronounced differences between the series for the rate of re-hydroxylation and the uptake of water. For the most part, it is unclear what causes the unexpected difference between the LDH and LDO ICP-MS results.

7.3.1 PXRD analysis of the Ga and Al LDH series

Both the $[Cu_{0.45}\,Zn_{(0.35-0.25)}\,Ga_{(0.2-0.3)}\,(OH)_2]^{(0.2-0.3)+}\,(CO_3^{2-})_{(0.1-0.15)}$ and $[Cu_{0.45}\,Zn_{(0.35-0.25)}\,Al_{(0.2-0.3)}\,(OH)_2]^{(0.2-0.3)+}\,(CO_3^{2-})_{(0.1-0.15)}$ series displayed the expected $3R_1$-LDH peaks in their PXRD patterns (see Figure 7.1). However, more LDH peaks are visible for the Ga series compared to the Mg- and Al-based series from Section 6.3.2; these are due to a higher content of the $3R_2$-LDH polytype in the Ga samples. The LDH planes that give a visible PXRD 2θ peak for the Ga-based samples, in Figure 7.1, using Cu K-α X-ray radiation are: (0 0 3) at $\approx$ 11.5 °, (0 0 6) at $\approx$ 23.5 °, (0 0 9) at $\approx$ 33.5 °, (0 1 2) at $\approx$ 34 °, (1 0 4) at $\approx$ 37 °, (0 1 5) at $\approx$ 38.9 °,(1 0 7) at $\approx$ 43.5 °, (0 1 8) at $\approx$ 46.5 °, (1 0 10) at $\approx$ 52.5 °, (0 1 11) at $\approx$ 56 °, (1 1 0) at $\approx$ 59 °, (1 1 3) at $\approx$ 60.5 ° and (1 1 6) at $\approx$ 64.5 °. [115,181,187–193] Two other very small peaks are also observed at $\approx$ 48 ° and $\approx$ 63.5 ° for the 30Zn25Ga- and 25Zn30Ga-LDH smaples; similar small peaks are observed in CuZnAl-LDH PXRD patterns collected by Gao et al. but they were not assigned. [187] It is possible these two small peaks correspond to Wurzite ZnO (0 1 2) and (0 1 3) phases (230511-ICSD). However, if this was the case, or the peaks belonged to a different oxide or hydroxide, more unassigned peaks would be expected. Peaks at $\approx$ 48 ° and $\approx$ 63.5 ° are observed for several 3R LDH phases on the 'Inorganic Crystal Structure Database' (290927- and 86655-ICSD), Mills et

al. assign them (0 0 12) and (1 0 13) Miller-Bravais indices, respectively. [191, 192] The Al-based AMO-LDH series contains almost exclusively the $3R_1$-LDH polytype (see Section 3.7.1); whereas, the Ga-based series contains some $3R_2$-LDH phase. The 30Zn25Ga- and 25Zn30Ga-LDHs have the sharpest PXRD patterns and most visible LDH phases of any LDH sample from Chapters 6 and 7, this is likely due to them being made of the largest LDH crystallites; which can be seen below in the 'crystallite thickness' discussion (also see Figure 7.6).

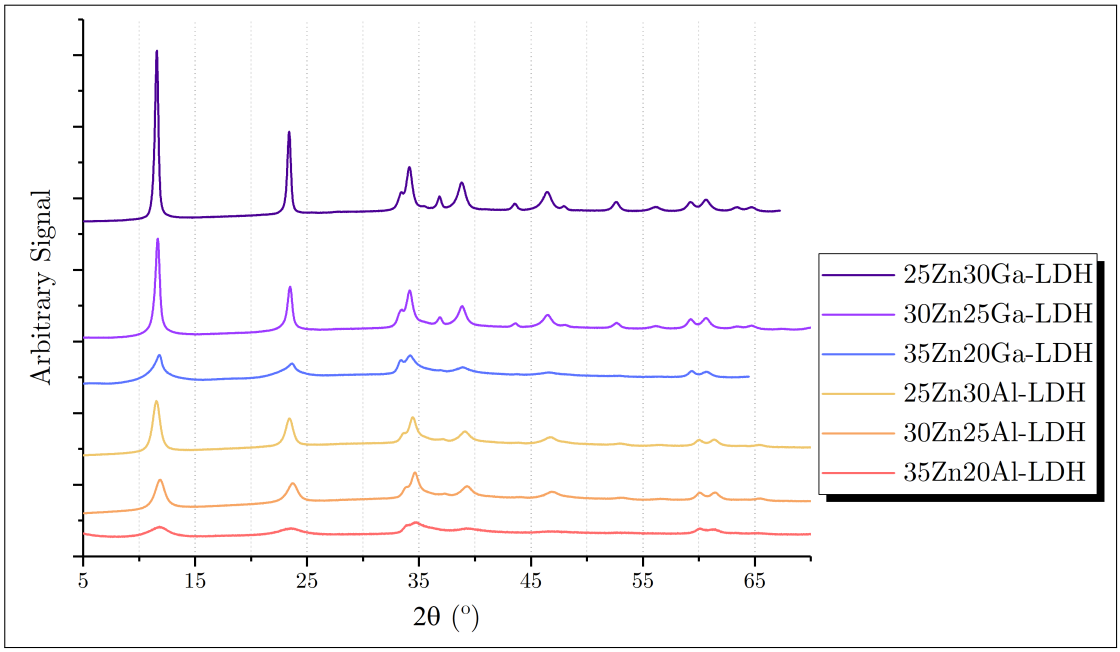


Figure 7.1: PXRD patterns of the Al- and Ga-based AMO-LDH series.

In Figures 7.2 and 7.3, it is clear that the PXRD peaks of the samples with lower M^{3+} content are far less intense and sharp; these broader peaks are linked to the particle size of the material being smaller (as well as other factors), see Section 5.3.1. Therefore, the decrease in peak intensity across the series does not necessarily mean any given sample had a higher or lower percentage of LDH structure. Additionally, there is a shift in their 2θ values between the two series, the Al-based materials give peaks at a 2θ when compared to the analagous planes of a Ga-based material; this is related to the unit cell dimensions, particle size and, therefore, the LDHs' metal

ratios. These factors can be isolated via spacing/Scherrer equations and Bragg's Law calculations (see below).

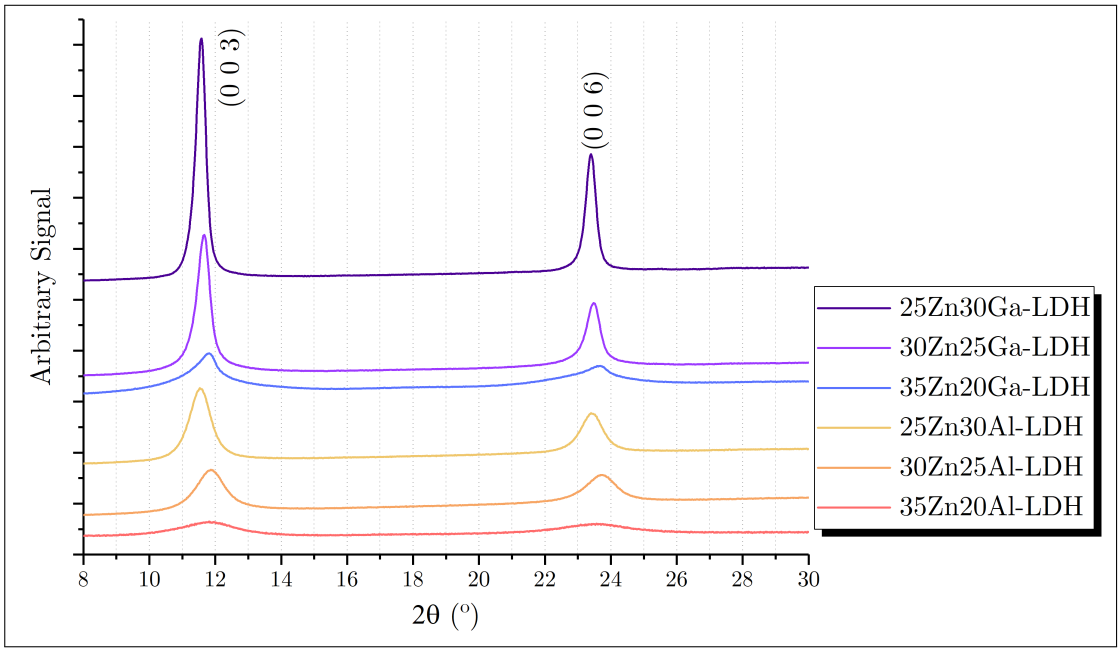


Figure 7.2: PXRD patterns of the Al- and Ga-based AMO-LDH series between 8 ° and 30 ° 2θ; showing the (0 0 3) and (0 0 6) peaks.

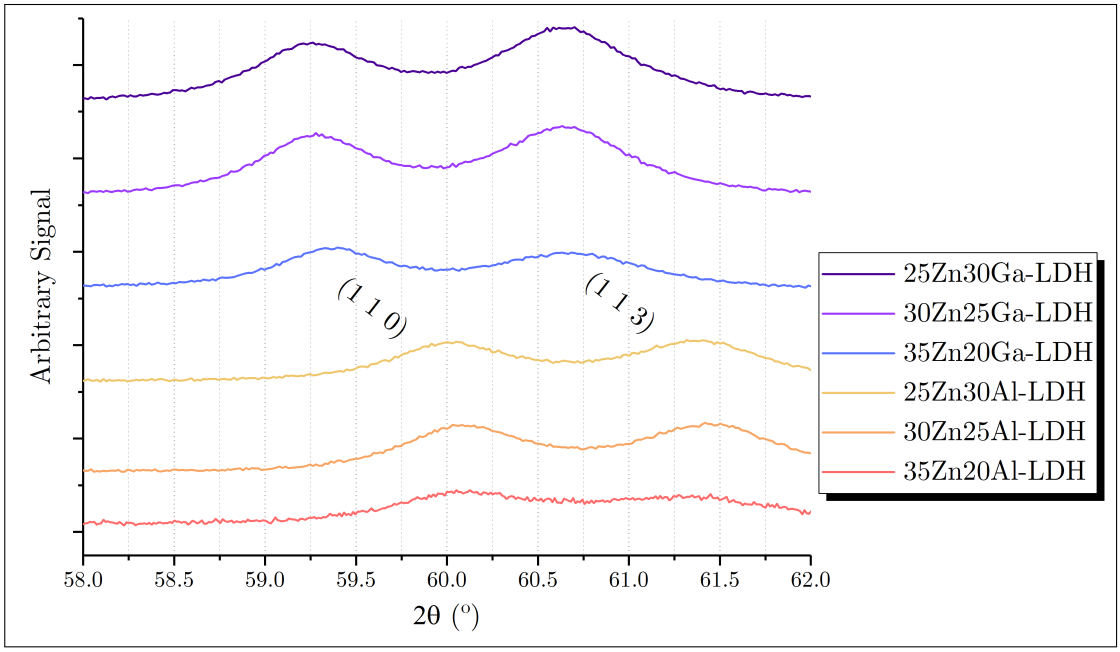


Figure 7.3: PXRD patterns of the Al- and Ga-based AMO-LDH series between 58 ° and 62 ° 2θ; showing the (1 1 0) and (1 1 3) peaks.

Only LDH peaks were observed in the PXRD analysis of the as-prepared materials; so for the calculations, 100 % LDH structure was assumed. In this work and in literature, a hexagonal 'unit' cell is assumed for LDH lattices; therefore, the *a* lattice parameter represents dimensions parallel within the 2D layer and correlates with the average metal ion size. The *c* lattice parameter represents the plane perpendicular to the 2D layers; it correlates with the interlayer distance. As in Section 6.3.2, particle thickness, LDH layers per crystallite and plate diameter, can be derived from these calculations.

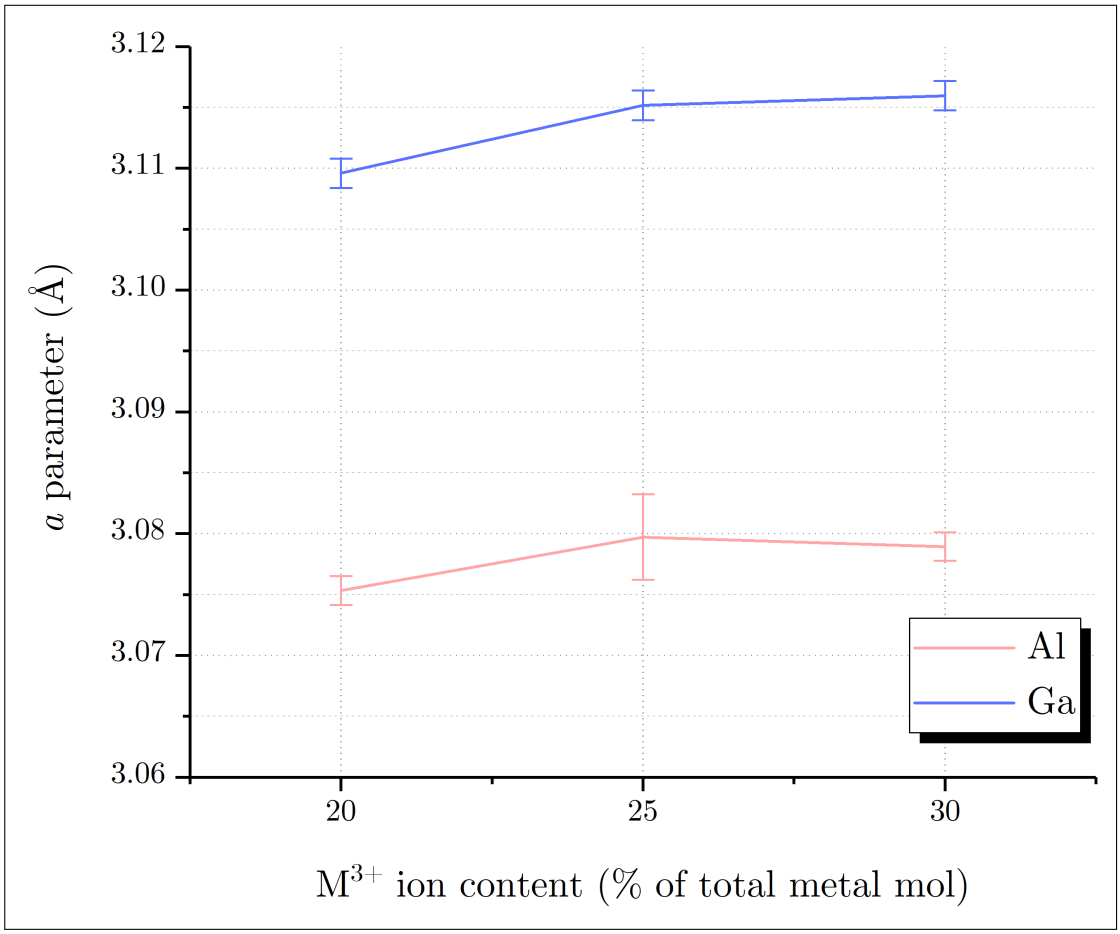


Figure 7.4: The *a* parameters of the Al- and Ga-based AMO-LDH series. Calculated from the PXRD data (Figure 7.1).

Figure 7.4 displays the calculated *a* parameters of both series; within each series the parameter remains almost constant. The standard enthalpies of formation ($\Delta H_f^{\ominus}$)

of Cu^{2+}, Zn^{2+}, Ga^{3+} and Al^{3+} hydroxide (per M-OH bond) are -225, -321, -322 and -426 kJ.mol$^{-1}_{M-OH}$, respectively. [232, 257] Therefore, replacing Zn^{2+} with M^{3+} would be expected to reduce the a parameter by decreasing the average bond length within the lattice (more so for Al^{3+}). This could mean the 10 % mol shift from Zn^{2+} to a M^{3+} cation, across a given series, does not have a large enough effect on the average lattice octahedra size to perturb/decrease the a parameter beyond the error of measurement.

The ionic radii of octahedral Cu^{2+}, Zn^{2+}, Ga^{3+} and Al^{3+} are 0.73, 0.74, 0.62, and 0.54 Å, respectively. [237] There is a slight difference in the a parameter between the two series, ≈ 0.03 Å; if all M^{3+} octahedra sites are Al instead of Ga this appears to introduce an observable difference in the average ionic radii of the lattice due to Al being a smaller ion.

The c parameter data is less consistent with the theorised outcomes. With increasing M^{3+} content, a reduction in the average ionic radius and an increase in the $\delta+$ charge of the layers (causing stronger attractive forces between layers and counterbalance anions) was expected to cause an inverse correlation between the M^{3+} content and c parameter. As can be seen in Figure 7.5, this is not the case and, therefore, the dominant effect is instead likely to be how the interlayer spacing increases with M^{3+} content. This is because more counterbalance anions are required to balance the additional M^{3+} charge; which in turn, causes the interlayer spacing (c parameter) to increase to prevent the introduction of more severe steric and electronic repulsion between anions.

Additionally, in Figure 7.5 the 30Zn25Al-LDH sample appears to be the outlier of a trend where M^{3+} content seemingly correlates with the c parameter. According to the ICP-MS data, see Table 7.2, the 30Zn25Al-LDH is also an outlier in that it has less Cu^{2+} content than the other Al-based samples; therefore, there'd be slightly more Zn and Al content per layer than expected. It is not obvious how such a

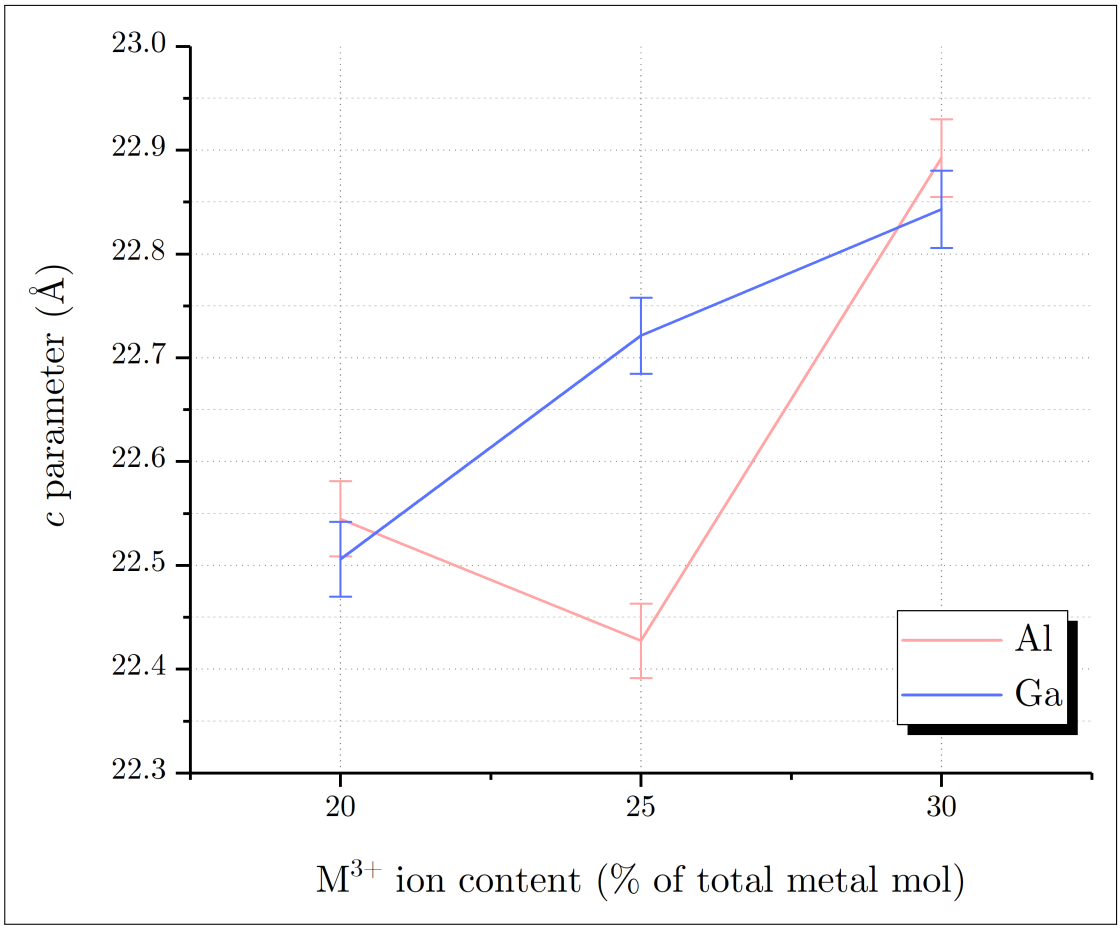


Figure 7.5: The c parameters of the Al- and Ga-based AMO-LDH series. Calculated from the PXRD data (Figure 7.1).

change would cause the observed c parameter decrease. One explanation could be, whilst the Ga series is dictated by one dominant factor, the Al series has different dominant regimes for the competing factors (referred to above), relative to a critical Al^{3+} concentration. The ionic radii change with increasing Al^{3+} content is a more drastic % of the average when compared to the analogous mol % changes in the Ga series; this could account for the decrease in c parameter between 35Zn20Al-LDH and 30Zn25Al-LDH. Then the increase from 30Zn25Al-LDH to 25Zn30Al-LDH would be dictated by the increasing steric interactions between the increasing number of counterbalance anions. Unfortunately, each series size is too small to be able to determine the existence of any critical M^{3+} concentrations, so these arguments are

mostly hypothetical and the analysis of a series, with a larger sample size, is needed.

The c parameter and the crystallite thickness are both measurements of the same plane; in this work, the calculated c parameter corresponds to the dimension of a hexagonal 3R cell (which includes 2 full and 2 half LDH layers, 3 in total). Whereas the thickness of the average LDH crystallite will be affected more by the extent of the exfoliation rather than the average layer thickness; this is discussed in Section 6.3.2 i.e. the degree of exfoliation will not have a large impact on the c parameter unless the crystallites are exfoliated below 3 layers thick in a high number of cases (presumably where the PXRD peaks would become very broad). However, the degree of layer exfoliation is likely very strongly linked to the average crystallite thickness because it determines how many layers are stacked together; the crystallite thickness of both series is shown in Figure 7.6

For both the Ga and Al series the crystallite thickness increases with the M^{3+} content, see Figure 7.6, despite the 3+ cations having smaller ionic radii; therefore, the degree of exfoliation is likely the dominant factor and inversely correlated with M^{3+} content. Increasing the M^{3+} content theoretically increases the concentration of interlayer anions, this can explain the crystallite thickness trend. It would become less energetically favourable to break interlayer attraction and thus exfoliate layers, when the strength of attraction between the layers increases; which it should with increasing M^{3+} and counter anion content.

The crystallite thickness of the Ga AMO-LDH samples is significantly higher than that of the analogous Al samples. As mentioned above, the fact that Ga^{3+} is a larger cation than Al^{3+} does not have a large effect on the c parameter; therefore, it would only have a small effect upon the average crystallite thickness. Arguably the dominant effect should then be something that does not affect the c parameter too strongly; such a factor could be that Al^{3+} and Ga^{3+} have mean electronic polarisibilities of

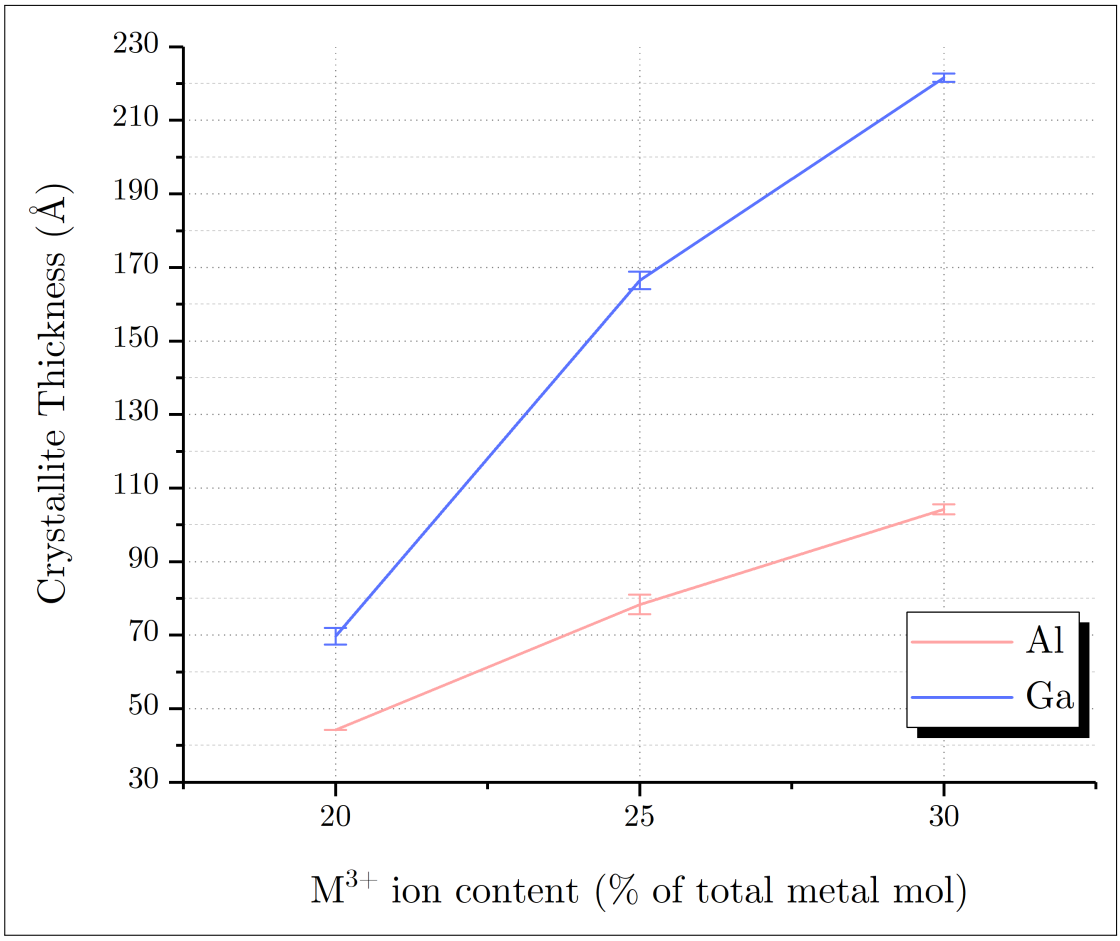


Figure 7.6: The mean crystallite thickness of each AMO-LDH from the Al- and Ga-based series. Calculated from the PXRD data (Figure 7.1) using the standardised Scherrer and integration methods used across this thesis.

0.47-0.53 and 1.5-1.75 Å^3, respectively. [28] This shows that Al^{3+} is significantly more polarising than Ga^{3+}, which in turn would mean that the hydroxide bonds on the LDH surface would be more polarised; theoretically, this would cause acetone to donate more electron density and bond more strongly to the LDH hydroxyl $H^{\delta+}$ during the acetone mixing synthesis step (in the absence of water). Thus the increased extent of exfoliation (and reduced crystallite thickness) for the Al series, relative to the Ga series, is likely caused by the weaker interlayer hydrogen bonding network between the LDH layers during the mixing step; due to a higher amount of acetone entering the interlayer space, bonding to the LDH surface and disrupting the hydrogen bonding

network with methyl groups.

The number of LDH layers per crystallite can also be calculated from the PXRD data, its trend (see Figure 7.7) is almost identical to that of the crystallite thickness trend (Figure 7.6); this was expected as the individual layer thickness and c parameter are expected to be homogeneous across the material. Notably, the average number of layers per crystallite for 35Zn20Ga- and 25Zn30Ga-LDH differ by almost 20 layers, suggesting the M^{3+} content has a significant effect on the extent of exfoliation; this is also evidenced in the BET analysis, see Section 7.3.4).

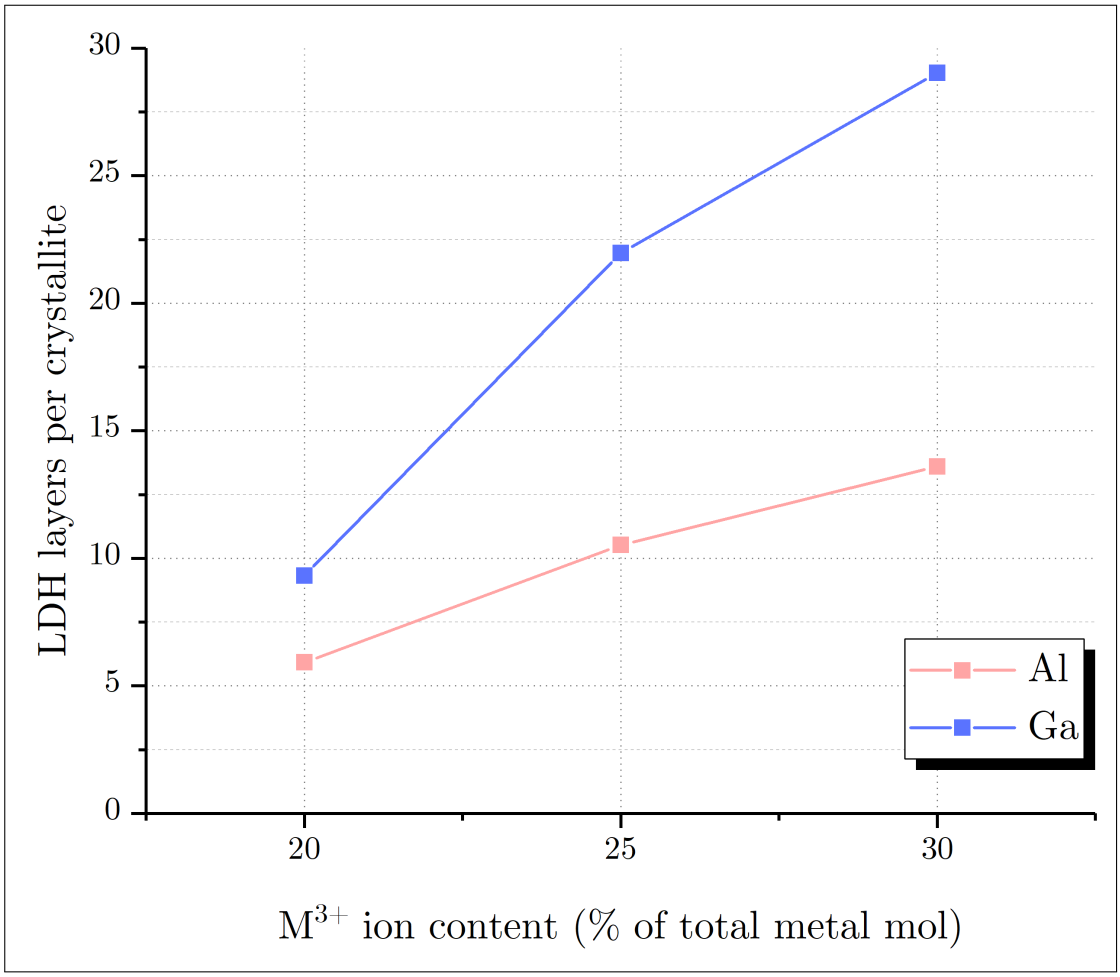


Figure 7.7: The mean no. of LDH layers per crystallite of each AMO-LDH from the Al- and Ga-based series. Calculated from the PXRD data (Figure 7.1).

As was discussed for the Mg-based AMO-LDH series in Section 6.3.2, the error in

the plate diameter of the AMO-LDH materials is quite large when compared to the error for the crystallite thickness; see Figure 7.8. This is because the error measurement compares the difference between manual, human peak integrations and refined, semi-automated peak integrations; the (1 1 0) and (1 1 3) PXRD peaks overlap and the former's FWHM is required in the calculation of the plate diameter. Whereas, the crystallite thickness used two clean peaks, (0 0 3) and (0 0 6), for its calculation, plate diameter uses the FWHM of an overlapped peak; this value varied a lot when manually selected and was more consistent using the semi-automated program. This resulted in larger errors for the plate diameter relative to the errors in the crystallite thickness.

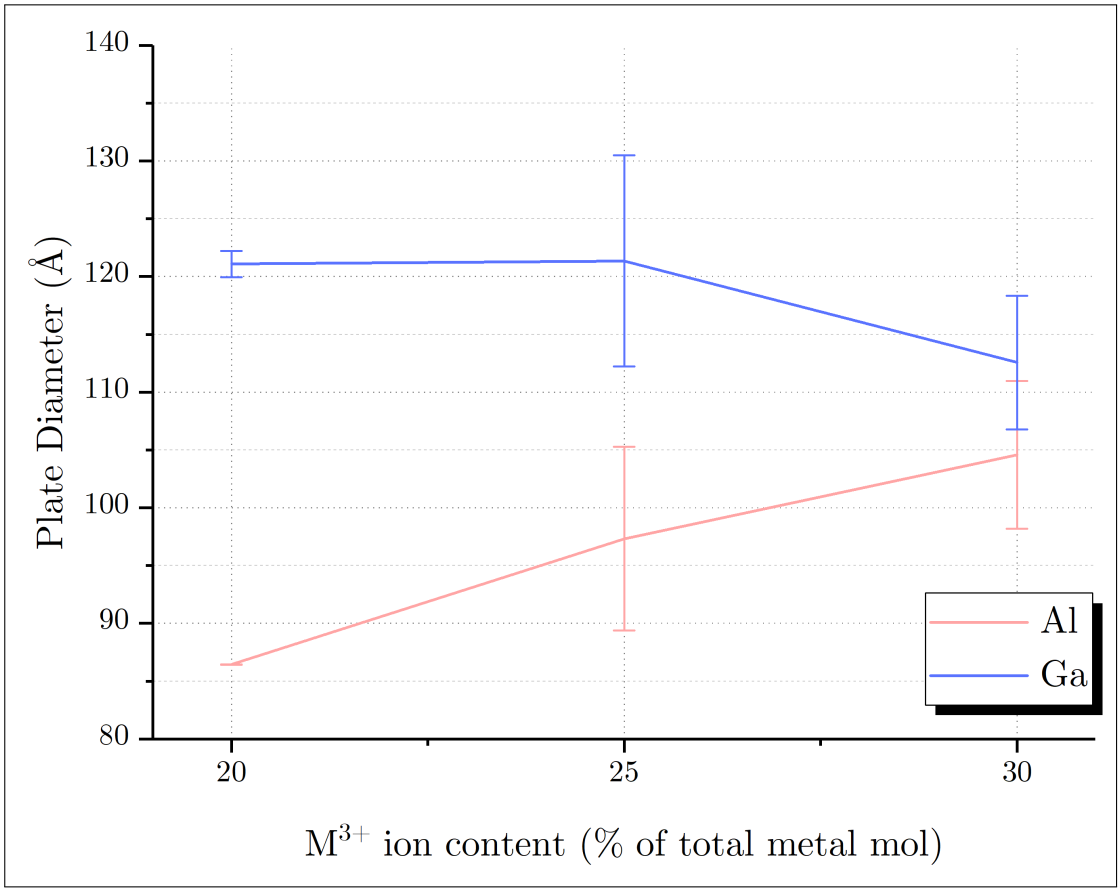


Figure 7.8: The mean plate diameter of each AMO-LDH from the Al- and Ga-based series. Calculated from the PXRD data (Figure 7.1) using the standardised Scherrer and integration methods used across this thesis.

No TEM analysis was performed for the Mg series and it was theorised that the morphology of the AMO-LDHs had ≈ 80-120 Å 'plates' in a flower formation due to using a similar synthesis method to Chen et al. [205] For the Al and Ga series the same AMO-LDH synthesis method was used as for the Mg series and similar plate diameter sizes were achieved; especially between the Al and Mg series, likely because they share a consistent M^{3+} cation (see Figures 6.9 and 7.8). The errors within both the Ga and Al series makes it hard to see the effect of the M^{3+} content upon the plate diameter; however, it is clear the Ga-based AMO-LDHs form larger flowers or plates than the analogous Al-based samples. The layers are exfoliated by acetone disrupting the interlayer regions but this process will not break apart the LDH lattice in the (1 1 0) plane; therefore, the plate or flower size difference is likely determined in the early synthesis steps. The procedure for the synthesis of Al- and Ga-based AMO-LDHs in this work was identical except for the M^{3+} cation; therefore something inherent about Ga means the AMO-LDH layers that are formed are of larger diameter compared to analogous Al-based materials. As mentioned above, the ionic radius of Ga^{3+} is closer in size, than Al^{3+}, to Cu^{2+} and Zn^{2+}. Therefore, one theory could be that the Cu and Zn hydroxide octahedra likely overlap and form unit cells in a more energetically favourable way with Ga's hydroxide octahedra than with Al's. This is theorised because Al's smaller size could cause more strain and distortion on lattice bonds with neighbouring Cu and Zn octahedra i.e. it is proposed that plate or flower growth is more likely to become sterically-unfavourable due to Al^{3+}-induced distortions than for analogous Ga^{3+} concentrations.

Overall, PXRD demonstrates that both Al- and Ga-based AMO-LDHs form the $3R_1$ polytype, whilst for the CuZnGa AMO-LDHs the $3R_2$ polytype can also be observed despite the synthesis being conducted at room temperature and pressure. Ga^{3+} causes the a parameter to increase relative to the smaller Al^{3+} as expected. It was also found that the crystallite thickness correlated with M^{3+} content and

was larger for Ga-based LDHs compared to analogous Al samples. An increase in electrostatic attraction to interlayer anions, due to an increased M^{3+} content, was theorised to cause a decrease in the extent of exfoliation; additionally, Al^{3+} has a higher polarising power then Ga^{3+} so was theorised to increase the extent of exfoliation by increasing the interlayer acetone content during synthesis.

7.3.2 Calcination and Reduction of the Ga and Al series

As discussed in Section 6.3.3, the Al- and Ga-based AMO-LDHs were calcined at 330 °C, in air, in an attempt to further increase their surface area whilst maintaining octahedral and layered morphology. One of the reasons 330 °C was chosen as the calcination temperature of all samples in this work was because Li et al. found their CuZnGa reduced MMO material to have the largest amount of ZnO/MGa_2O_4 interface, via TEM imaging, and highest Zn^0 content, via ex-situ XPS, when 330 °C was used as the calcination temperature; this was deemed important to the catalyst's performance. [180] The other reason was that 330 °C fits the temperature range required for the dehydroxylation of LDHs to LDOs without further breakdown of the layered structure. [177, 206] This temperature of calcination led to the calcined samples (labelled as LDO presumptively) becoming amorphous; see Figure 7.9.

As with the calcined Mg-based AMO-LDHs (see Figure 6.10), both the Ga and Al calcined LDO series only gave one very broad PXRD peak (see Figure 7.9); this peak is at $\approx 35\ ^\circ\ 2\theta$. Coincidentally or not, this could be the remnants of a (0 0 9) peak and the layered morphology; either way, literature suggests low calcination temperatures can maintain layered morphology (see Section 3.7.1), such claims would need to be validated using imaging evidence because the 'LDO' samples do not provide sharp enough PXRD peaks for in-depth synchrotron analysis. As with the Mg series (see Section 6.3.3), the as-prepared Al- and Ga-LDHs were a cyan colour but upon calcination became a dark pine green; likely a mixture of cyan octahedral Cu^{2+} and

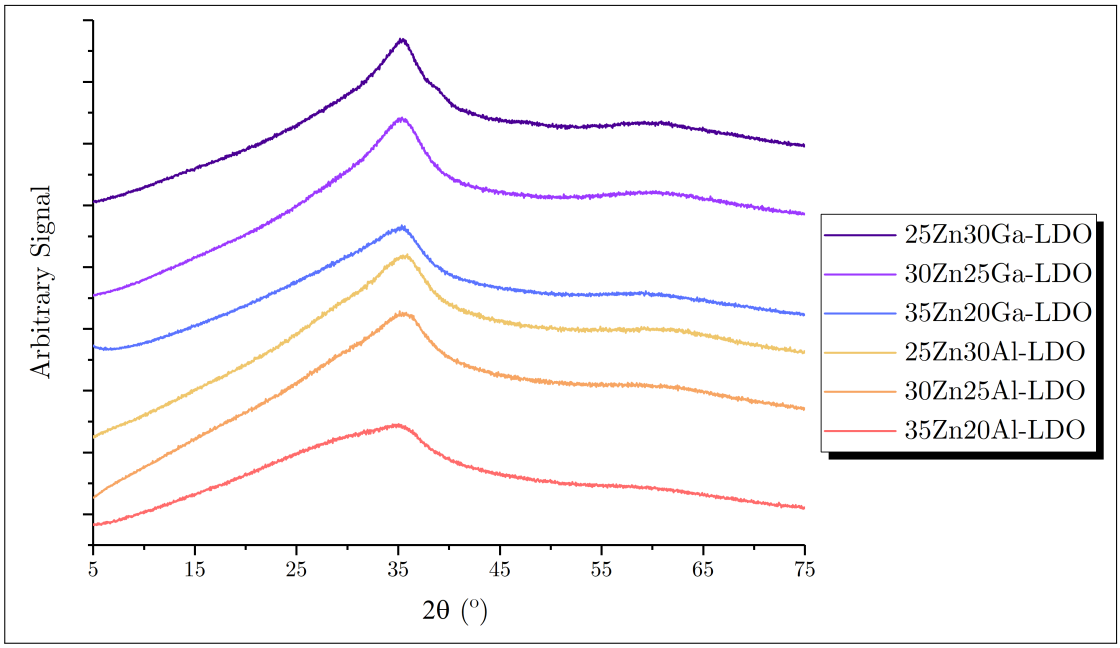


Figure 7.9: The PXRD patterns of the calcined Al- and Ga-based AMO-LDO series.

black CuO.

The PXRD patterns of the reduced sample showed only FCC Cu^0: (1 1 1) at ≈ 43.5 °, (2 0 0) at ≈ 50.5 ° and (2 2 0) at ≈ 74.3 °; and Wurzite ZnO: (0 1 0) at 31.8-32.9 °, (0 1 1) at 36.2-37.1 ° and (1 1 0) at 55.1-57.2 ° (see Figure 7.10). [258,259]

The Scherrer equation was used to calculate the Cu^0 particle size of the ex-situ reduced samples, see Figure 7.11. The trends for both the Ga and Al series are similar but the trend with respect to the M^{3+} content is ambiguous.

Each TPR profile of the Mg AMO-LDH samples shows a single broad peak; all of them, except 61.25Mg-LDO, overlap with the experimental reduction temperature of 290 °C (see Figure 6.11). The conclusion was made that the Mg samples' peaks were caused by a single Cu environment that would fully reduce in the 2 hour 290 °C reduction period because the D_{Cu} % increased with Mg content; notwithstanding the fact that the reduction temperature also correlated with the Mg content. By comparison, the TPR peaks for 30Zn25Ga-, 25Zn30Ga- and 25Zn30Al-LDO are split

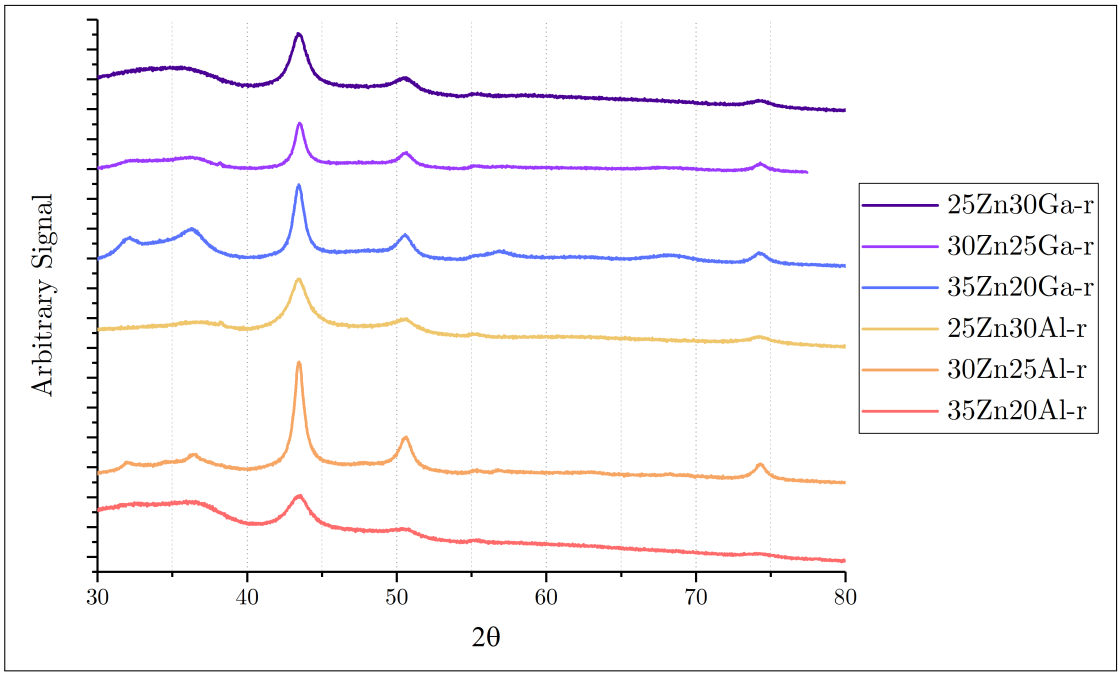


Figure 7.10: The PXRD patterns of the reduced Al- and Ga-based series.

into two peaks, likely representing two Cu environments. Like some of the Mg-LDO samples (that were theorised to be fully reduced using the standardised reduction method), these less reducible Cu environments all had their TPR peak above 290 °C, but unlike those Mg samples, the 30Zn25Ga-, 25Zn30Ga- and 25Zn30Al-LDOs had a much higher Cu content; possibly meaning they may not be fully reduced over the 2 hour reduction. If a sample was not fully reduced then less Cu atoms would be available to form particles and would remain in the oxide/LDO support; this would theoretically lead to smaller Cu^0 particles (assuming consistent support surface area) and a lower D_{Cu} % (because Cu in the support would count towards 'bulk' Cu in calculations). By this logic, if the 30Zn25Ga-, 25Zn30Ga- and 25Zn30Al-LDOs were fully reduced in a longer reduction experiment then they would be expected to form larger Cu^0 particle sizes. This would potentially turn Figure 7.11, with no obvious trend, into a graph that could display an inverse correlation between Cu^0 particle size and BET surface area within both the Al and Ga series; with the Ga series trend giving larger Cu^0 particles relative to the analogous Al samples due to the

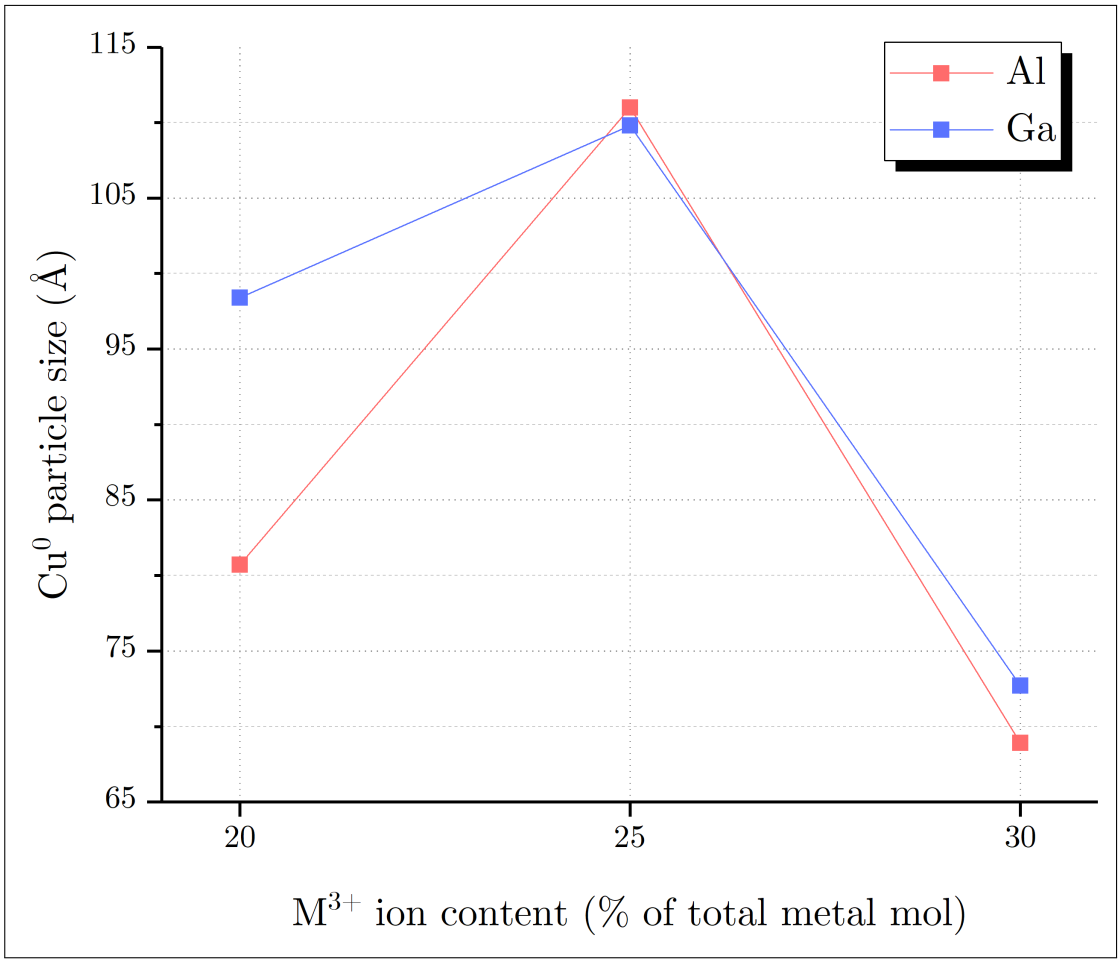


Figure 7.11: The average particle diameter of Cu^0 of each reduced sample from the Al- and Ga-based series. Calculated from the PXRD data (Figure 7.10). The Cu^0 is assumed to be FCC and the calculation error is ± 3 Å.

their lower surface areas. This is a hypothetical argument however, and would need future experiments to disprove or prove it. Such a theory would also suggest a higher reduction temperature would increase the Cu^0 content, and presumably the activity, for 30Zn25Ga-, 25Zn30Ga- and 25Zn30Al-LDO; however, this would make the process less energy efficient overall and would likely break down the LDO morphology further. This is further discussed in relation to D_{Cu} % in Section 7.3.5.

As with the Mg series, calcination led to a loss of crystallinity in the samples; whilst it was shown that the standard reduction procedure used in this work may not have been sufficient to fully reduce LDOs with 30 metal mol % M^{3+} (likely due to an

increase in M^{3+} content causing an increase in lattice energy).

7.3.3 TPR analysis of the Ga and Al LDO series

TPR analysis of the Al and Ga series is shown in Figure 7.12. As mentioned in Section 6.3.4, Cu will have the lowest reduction temperature of any metal present in the samples because the lattice potential energies per mol of M^{x+}-O^{2-} bond (not per mol of oxide) for CuO, ZnO, Ga_2O_3 and Al_2O_3 are +4,135, +4,142, +5,197 and +5,305 $kJ.mol^{-1}_{M-O}$ respectively. [241] Therefore, all TPR peaks in Figure 7.12 are assumed to be caused by different Cu environments.

Some ZnO may be reduced under the standard reduction procedure used (2 hours at 290 °C), as discussed in Section 3.6.2; however, any such reduction peak in the TPR analysis would not be visible under the prominent Cu reduction peaks. Zn reduction would theoretically increase the area of the TPR peaks. Unfortunately, there is not a clear trend in the TPR peak areas, even if they are normalised to the Cu content of the sample; all peaks have a very similar area. This could have been caused by the variation in sample mass used, anywhere between 9 - 39 mg was used for TPR analysis; the results were normalised to Cu content but it is unclear whether the thermal conductivity detector in the TPR set-up was linearly affected by sample mass and its effects on heating and glass flow rate etc. New samples would have to be prepared, and a new line of TPR experiments planned, to investigate the relationship between sample mass and detector signal before Zn content could begin to be estimated by TPR content.

From Figure 7.12, there is a clear trend between the reduction temperature of Cu and the M^{3+} content in both series. Assuming the elements within the samples are well dispersed and almost homogeneous, which is reasonable considering the high elemental dispersions observed later (in Sections 7.3.5 and 8.4.3), then simple electronic effects can describe the differences caused by changing M^{3+} content and ions. As

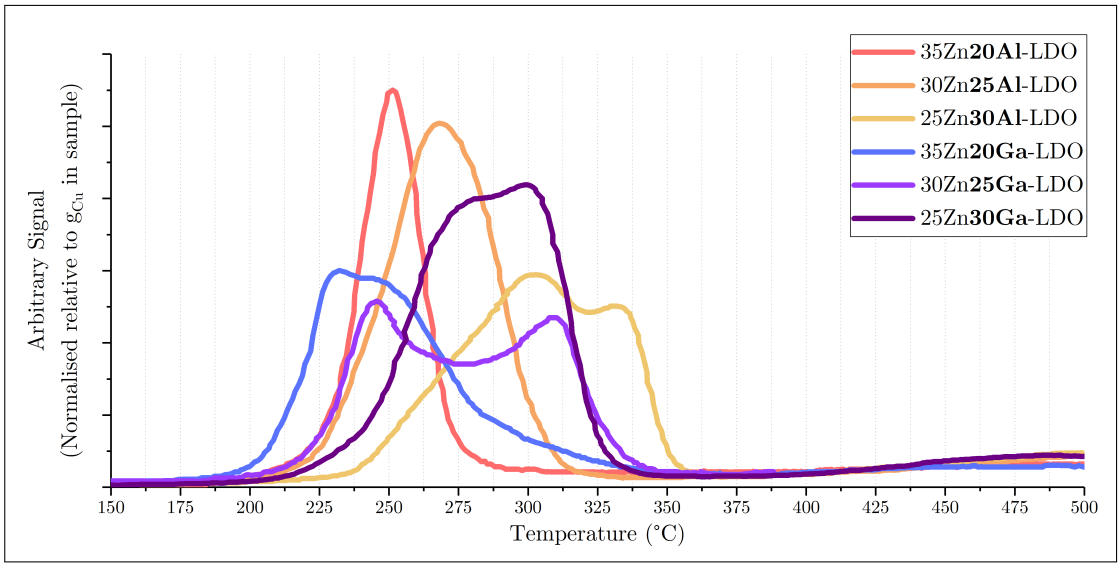


Figure 7.12: The TPR analysis of the calcined Al- and Ga-based AMO-LDO series; measured with a 10 °C.min^{-1} heating rate.

seen above, there are large differences in the standard Gibbs free energy of crystallite formation for the oxides of the elements used in this study. As established, the lattice energy (per M-O bond) trend follows: $Al_2O_3 > Ga_2O_3 > ZnO > CuO$. Therefore, replacing Zn^{2+} with Ga^{3+}/Al^{3+}, or replacing Ga^{3+} with Al^{3+}, in the calcined samples will increase the average M-O lattice bond strength and increase the overall lattice energy; this is because O^{2-} is a small, 'hard', very electronegative anion, meaning it will have more energetically favourable orbital overlap and stronger bonds with cations that are of a similar size and high + charge e.g. Al^{3+}. The lattice around a given Cu^{2+} ion would have to be broken to allow the reduction process to occur, the activation energy required for this initial breaking of lattice M-O bonds theoretically correlates to the temperature of the system. This is what is observed in Figure 7.12, the TPR peaks' temperatures correlate with the M^{3+} content, within the separate Al and Ga series, and the Cu reduction temperature required for a Ga sample is lower than that required for the Al sample with analogous M^{3+} content.

The above, simple, electronic theory can explain the general reduction tempera-

ture order for each sample; however, it cannot fully explain why some TPR profiles are split into two peaks. The split peaks are likely caused by the existence of two Cu environments within one sample, where the local structures around a given Cu environment have different lattice energies. The LDH samples likely have high elemental dispersion as mentioned in Section 3.7 and seen in the EDX analysis of 35Zn20Ga-LDH, see Figure 8.4.3. Despite this, it could be possible other phases exist that were not detected (via PXRD or EDX), or extra phases could of formed during calcination. Nevertheless, the split peaks in the TPR analysis are substantial and often both the peaks for a given sample are similarly sized; implying that both Cu environments are as common as the other. The 35Zn20Al- and 30Zn25Al-LDOs do not exhibit this splitting of the peaks but the broadness of the TPR peak does increase in width with increasing Al^{3+} content; this indicates that the split Cu environments is not an inherent property of the LDH or LDO structure. Additionally, the average, theoretical lattice energy does not seem to be the determining factor in which samples have two Cu environments; the Ga samples have lower lattice energy than analogous Al samples but the sample with the highest theoretical lattice energy, 25Zn30Al-LDO has split peaks as well. It is also impossible to determine the nature of each Cu environment from the TPR peak, it could be possible that the reason for the split peaks could be different for any two samples.

The likeliest explanation for the split peaks is the partial degradation of the LDO structure during calcination. Other phases of oxide may form under the heat treatment and other areas retain their layered morphology; this effect may be a contributing factor to the amorphous PXRD patterns seen for the LDO samples (see Figure 7.9) and may be the reason why layered and more amorphous morphology are observed in the TEM images of 35Zn20Ga-LDO (see Figure 8.25).

Interestingly, the only samples without split TPR peaks, 35Zn20Al- and 30Zn25Al-

LDO, have the two highest BET surface areas (see Figure 7.13). Therefore, perhaps all samples experience this partial degradation but samples that have lower initial surface areas are more susceptible to forming mixed oxide phases, that in turn have lower surface areas. Conversely, the samples with the highest surface areas may form some other non-LDO phases but such phases could have topotactically higher relative surface areas because other potential nearby structures are more exfoliated. In other words the theory is as follows; for samples with lower surface areas the loss of layered structure during calcination creates other oxide phases where Cu is 'buried' further from the surface. Therefore, it requires higher reduction temperatures because more lattice M-O bonds are needed to be broken to reduce the Cu atom. For samples with higher initial surface areas the non-LDO structures that form will be smaller, more disperse and also have higher surface areas, therefore, the Cu atoms will be as 'accessible' as the rest of the LDO structure, meaning there is little difference in the reduction temperatures required and the TPR peaks will not split.

The above theory is only a possible explantion and lacks experimental proof. Of course, much more in depth analysis of the calcined and reduced materials would be needed to identify the different Cu environments in the LDH-derived samples' TPR profiles; such work was not within the immediate scope of determining whether Al of Ga made the most optimal M^{3+} cation for AMO-LDH MSR catalysts. Unfortunately, the calcined materials give amorphous PXRD data and therefore cannot be analysed via synchrotron PXRD (which was attempted). XAS was not extensively used to uncover the structure of the Al and Ga series, as this section of work was more focused on screening which series had more potential catalytically. However, in the next chapter, XAS analysis was performed on reduced LDH samples and gave insight into the structure of very similar LDH-derived materials; see Section 8.4.5 for a further exploration of the structure of reduced AMO-LDH materials that could apply to both the Al and Ga series as well.

In summary, Ga-based AMO-LDHs have a lower Cu reduction temperature than analogous Al samples and Cu reduction temperature increases with increasing M^{3+} content; these trends are dictated by the LDO lattice energy. Some samples exhibit two reducible Cu environments, these environments are postulated to differ because of their distance from the surface of the material.

7.3.4 BET analysis of the Ga and Al LDO series

The BET surface areas of the Al- and Ga-LDOs were measured, see Figure 7.13; notably, the surface area decreases with increasing M^{3+} content and the Al series gives higher surface areas compared to analogous Ga samples with the same M^{3+} content. Additionally, mirroring this figure in the x axis would result in an image resembling the PXRD LDH crystallite thickness trend (Figure 7.6), this is because BET surface area and crystallite thickness are theoretically correlated and inversely correlated, respectively, to the extent of LDH layer exfoliation. The dominant effect within both series is that the increasing M^{3+} content increases the positive charge of each layer, increasing the required counter anion concentration and increasing the strength of ionic bonding between the layers; making them harder to exfoliate and, therefore, less of the LDH layers' surface is exposed.

The same arguments for the trends in crystallite thickness can be made here. Al^{3+} has more polarising power than Ga^{3+}, which leads to the energetics of acetone penetrating the interlayer hydration shell to adsorb to the LDH surface more favourable; leading to a greater degree of exfoliation for an Al sample compared to an analogous Ga sample (for the same exposure time to acetone and same layer size). In addition to this, the Al-based series has smaller plate/flower diameter sizes compared to the Ga series; theoretically, even if both samples had the same strength of interlayer bonds per surface area, then the total energy required to break apart two smaller layers of Al-LDH would be less than the total energy required for two larger Ga layers.

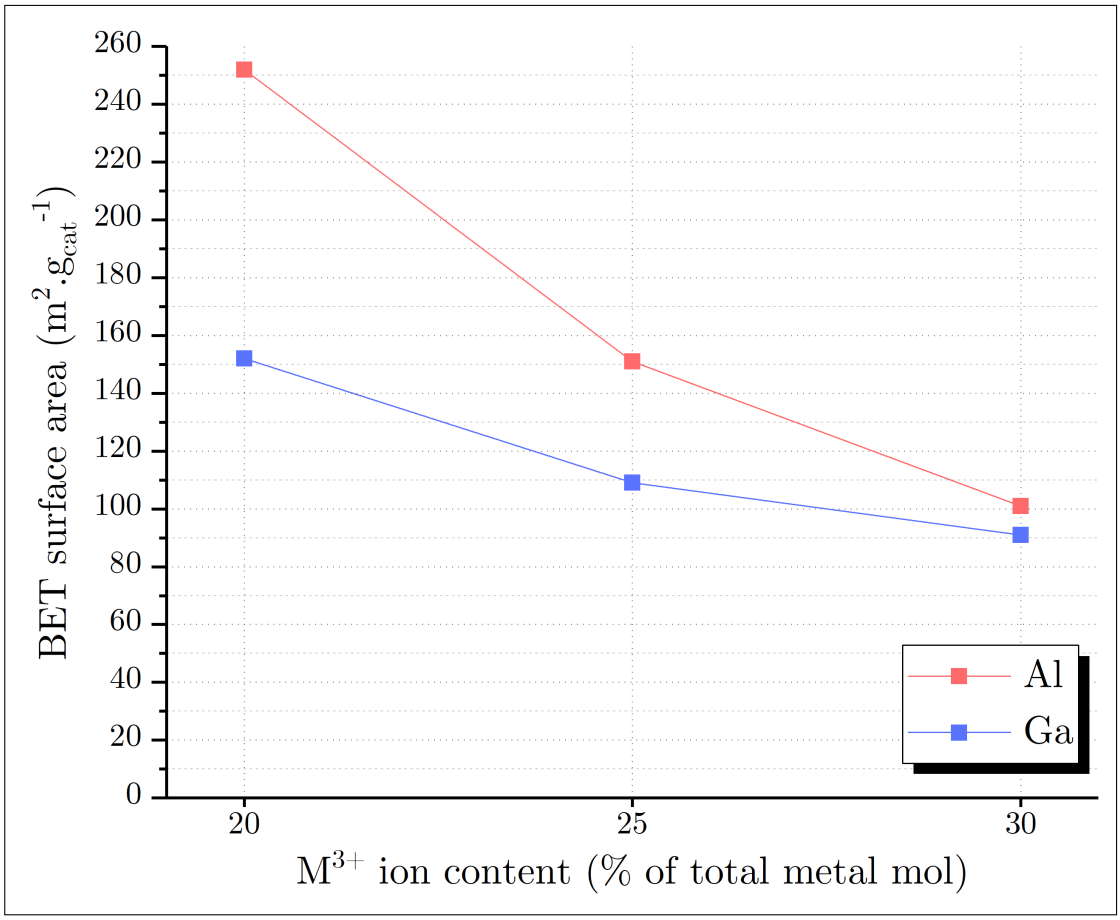


Figure 7.13: The BET surface areas of the calcined Al- and Ga-based series (LDOs); the error = ± 1.0 $m^2.g^{-1}$.

These theories can explain the difference in surface areas between the Al and Ga series but there is also another observation; the % change in the BET surface area, as a result of changing M^{3+} content, is larger across the Al series compared to the Ga series. The exact effect of Al's higher polarising power, compared to Ga, is not theoretically obvious as the interlayer anions, likely NO_3^- and CO_3^{2-}, are larger and 'softer' than hydroxide anions; in addition, the nature of the interlayer bonding network is complicated, with more species (the layers polarising power would affect the hydrogen bonding network). Therefore, the trend in standard enthalpy of formation for Al and Ga hydroxide (shown above in Section 7.3.1) cannot be applied to the interlayer bonding network argument. Increasing M^{3+} content will increase the

overall amount of electrostatic interaction between the layers; this could become the dominant effect on the extent of exfoliation at higher M^{3+} content. Thus, in the 30 % M^{3+} content regime, the Ga LDH layers may be softer and less polarizing allowing them to form stronger electrostatic attractive forces with the 'large' counter anions (compared to analogous Al LDH layers). Whilst, the high polarsing power of the Al LDH samples, which could increase the interlayer acetone concentration during the mixing step, may have a less weighted effect on the extent of exfoliation but, conversely, increase the strength of the hydrogen bonding network; these competing effects could cause the observed closeness of the BET surface area between 25Zn30Al- and 2530Ga-LDO (see Figure 7.13).

Then for the 20 % M^{3+} content regime, the layer-anion electrostatic attraction would have the less weighted effect meaning that Al's increased polarising power, relative to Ga, could have a dominant effect upon the extent of exfoliation i.e. there is a larger % difference in the BET surface area between the Al and Ga samples at lower M^{3+} content. Of course, this system has other types of interactions, including the hydrogen bonding network and interlayer steric interactions; therefore, it is very hard to theoretically discern why the Al series has a larger % difference in its BET surface area compared to the Ga series; expansive computational modelling could possibly be required to explain this observation.

Overall it can be seen that the trends in BET surface area are closely linked to that of the crystallite thickness and the extent of exfoliation i.e. low contents of Al^{3+} cause a higher BET surface area.

7.3.5 N_2O/H_2 titration of the Al and Ga LDO series

The D_{Cu} % trend (see Figure 7.14) of both series indicates a higher percentage of Cu atoms are on the surface, as opposed to the bulk, for samples with lower M^{3+} content. This trend is likely dictated by the BET surface area of the materials be-

cause there are more sites for the reducing hydrogen to adsorb to and more $Cu(OH)_x$ octahedra units are on an exposed surface; this means there are more potential sites where Cu can 'come out' of the lattice to decorate the surface i.e. more sites, with constant Cu content, leads to smaller particles forming and higher D_{Cu} %. Additionally, the distance between Cu^0 particles increases with BET surface area, making it less energetically favourable for the particles to travel across the support surface to amalgamate and form larger particles.

The BET surface area likely has the largest effect on the D_{Cu} % due to the similarities in the BET surface area and D_{Cu} % trends (see Figures 7.13 and 7.14) but competing electronic and thermodynamic effects likely exist.

To summarise the working theory for both the trends in experimental Cu^0 size and D_{Cu} % (Figures 7.11 and 7.14), it is proposed that the M^{2+}:M^{3+} ratio has a large effect on the stability of the Cu^0 particles under reduction conditions (and likely MSR conditions, see later in Section 7.3.6).

At increased temperatures surface Cu particles will have more thermal energy available to break their attractive interactions with the surface; allowing particles to move across the surface and agglomerate, forming larger, more thermodynamically-stable Cu particles (see Section 2.5.4).

The Cu^0 particles do not have an overall charge so the electrostatic attraction to the $\delta+$ support is not a large factor; therefore, most of the attractive interactions between the metal and support will be electron-sharing in nature. Increasing the M^{3+} content, with either Ga or Al, will increase the polarising power of the support. The mean electronic polarisibilities for Zn^{2+}, Cu^{2+}, Al^{3+} and Ga^{3+} are $\approx$ 1.7, 2.2-2.3, 0.47-0.53 and 1.5-1.75 Å^3, respectively; meaning the polarising power trend is as follows: $Al^{3+} > Ga^{3+} > Cu^{2+} > Zn^{2+}$. [28] Therefore, increasing the M^{3+} content will cause the support to favour interactions that are 'harder' and more ionic in nature. Whereas,

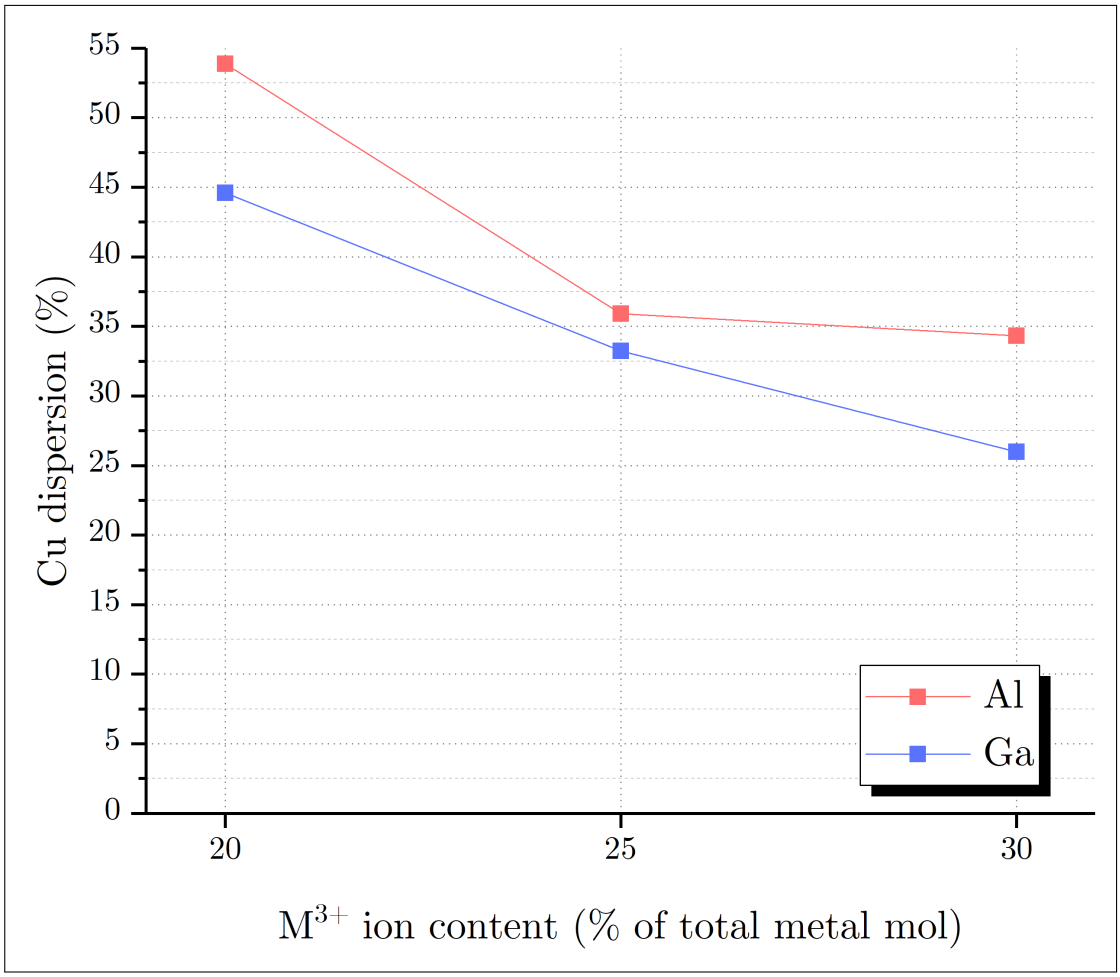


Figure 7.14: The D_{Cu} % of the calcined Al- and Ga-based AMO-LDO series; measured via N_2O/H_2 titration.

the Cu^0 will strongly favour more covalent and intermolecular attractive interactions. The increased polarising power of the LDH layer (caused by higher M^{3+} content, more so for Al^{3+} than Ga^{3+}) will make it less energetically favourable for the less electronegative Cu^0 to donate electron density to the support's, now more polarised, oxygen species; thus, decreasing the strength of electron sharing, and weakening the attractive force, between the support and metal. It is proposed the size of the average, stable Cu^0 particle is smaller for samples with lower M^{3+} content, this is discussed further in regards to the catalytic stability in Section 7.3.6.

Whilst the large BET surface areas of the AMO-LDHs may allow very small

Cu^0 particles to form, more so in the case of Al than for Ga; electronic properties (M^{2+}:M^{3+} ratio) of the support dictate the stable and optimal size of the Cu^0 particles. Therefore, it is proposed that M^{3+} content correlates with the Cu^0 particle size. However, this trend is not fully observed because at higher M^{3+} contents the dominant effect upon the Cu^0 particle size is the Cu reducibility; not as much Cu is reduced (see Section 7.3.1) and larger particles cannot form i.e. 30Zn25Ga-, 25Zn30Ga- and 25Zn30Al-LDO give lower Cu^0 particle size values than expected.

The BET surface area has a large effect upon the D_{Cu} % trend. The non-complete reduction of the 30 % M^{3+} samples explain why they have low dispersion but small Cu^0 particle size. Additionally, from the TPR trend, see Figure 7.12, the Ga series has more reducible Cu when compared to analogous Al samples; this could possibly explain why the dispersion of analogous Al and Ga samples are only $\approx$ 10 % apart despite the Al samples having much higher BET surface areas and smaller Cu^0 particle sizes i.e. more Cu leaves the support and more Cu particles are formed increasing the surface:bulk Cu ratio. Alternatively, small Cu^0 particles could be less stable over more polarising AlO_x compared to GaO_x. As previously mentioned, a series of tailored experiments with varying reduction times and temperatures could potentially be set up to fully explain this series of complicated competing effects; however, the scope of this work was to determine the best catalyst recipes for a given set of energetically-favourable conditions.

7.3.6 MSR catalytic activity of the Al and Ga reduced series

All AMO-LDHs in both the Al and Ga series could be calcined, then reduced into materials that exhibited both MSR activity and side CO production under MSR conditions at 180 °C; see Figures 7.15, 7.16 and 7.17. Only N_2 (carrier gas), H_2O/CH_3OH (reactants), H_2, CO and CO_2 species were observed via both TCD and 'methanizer'-FID detectors after the reactor and gas chromatography columns. The mechanism of

Cu-based, metal/oxide MSR catalysts was discussed in Section 3.4 and it is theorised these reduced AMO-LDO materials' performance would be dictated in a similar way i.e. the BET surface area, thermal stability, reducibility, amount of defects, D_{Cu} % and metal-surface interactions all likely have substantial effects on their catalysis. As per Chapter 4, the best potential MSR catalyst will be the material that achieves the highest H_2:CO mol production ratio whilst remaining stable over long reaction times; this is because CO poisons down-line hydrogen fuel cells and increases in stability improve the economic potential and sustainability of MSR.

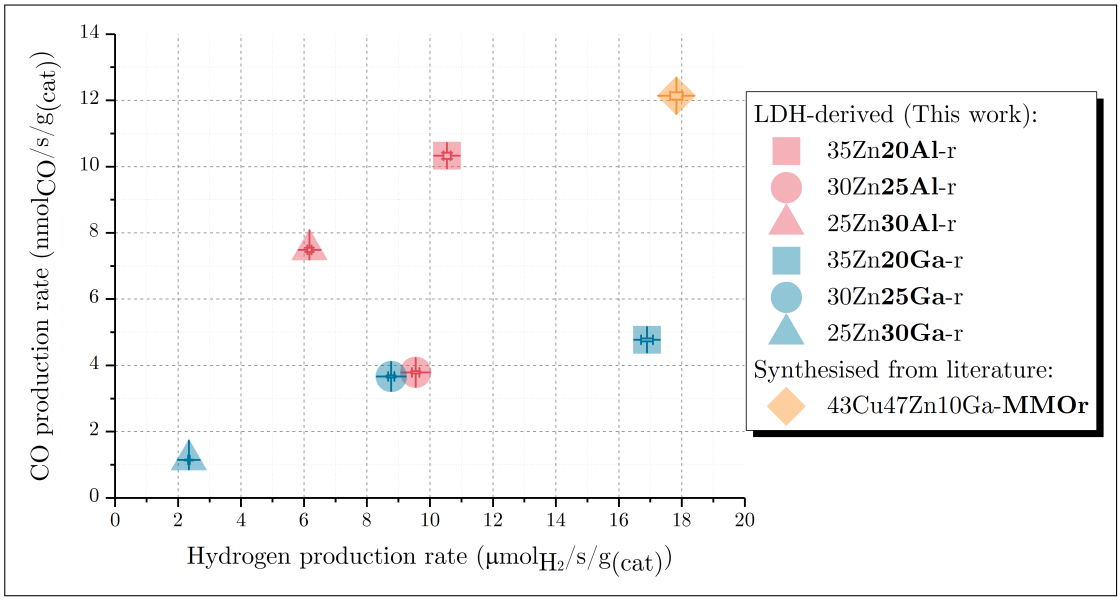


Figure 7.15: The MSR catalytic test results of the reduced Al- and Ga-based series; the hydrogen production rate and CO production rate units are $\mu mol_{H_2}.s^{-1}.g_{cat}^{-1}$ and $nmol_{CO}.s^{-1}.g_{cat}^{-1}$, respectively. Tested at 180 °C for 5 hours with 200 mg of catalyst, a N_2 gas flow of 10 mL.min^{-1} and a 0.1 mL.min^{-1} liquid flow of water:methanol solution (1.1:1 mol ratio). WHSV = 2.70 h^{-1}. Error bars (x/y) are shown inverted within the data point symbols.

From Figure 7.15 it can be seen that the most active MSR catalyst from both series is the 20 % M^{3+} sample; it is clear 35Zn20Ga-r has a substantially higher average H_2 production rate over the reaction time, and each Ga-based sample has lower CO production than the analogous Al sample. However, the range in activity across the Ga series is much larger. Therefore, plotting the H_2:CO production ratio against

the average H_2 production rate can put the effect of the WGS/RWGS equilibrium into context (see Figure 7.16) i.e. due to Le Chatelier's principle, the average H_2 production rate (proportional to the average CO_2 production rate, 3:1) will also have a shifting effect on the position of the equilibrium; thereby affecting the CO production rate.

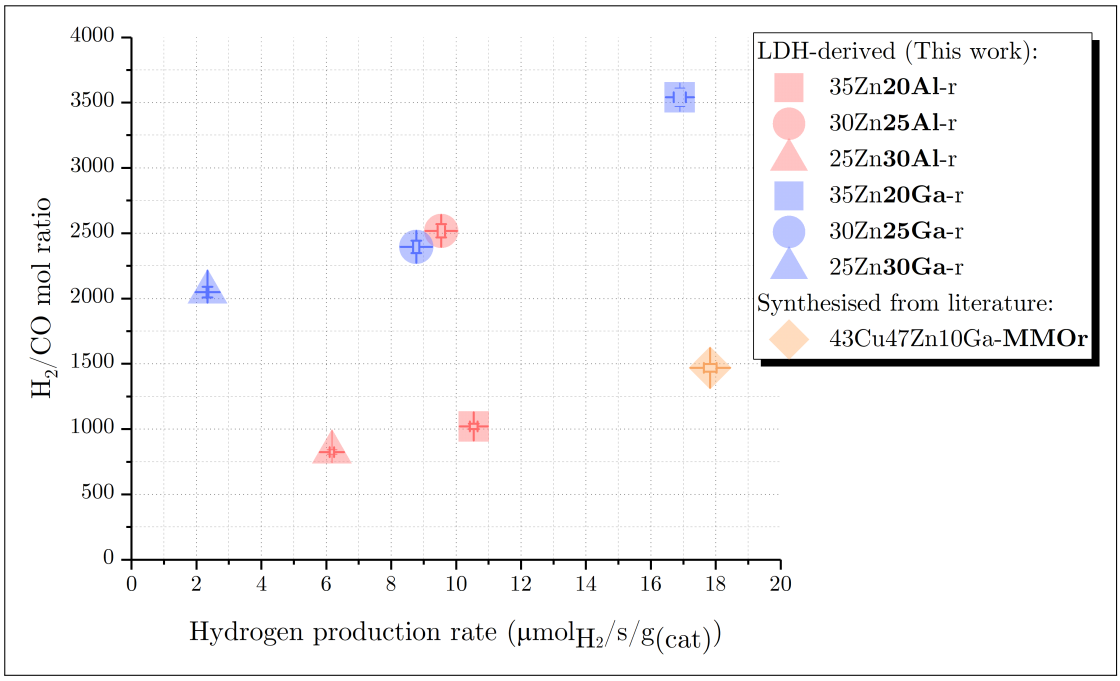


Figure 7.16: The H_2:CO mol ratio produced by the reduced Al- and Ga-based series during MSR (as a function of their hydrogen production); the hydrogen production rate's units are $\mu mol_{H_2}.s^{-1}.g_{cat}^{-1}$. Tested at 180 °C for 5 hours, with 200 mg of catalyst, a N_2 gas flow of 10 mL.min^{-1} and a 0.1 mL.min^{-1} liquid flow of water:methanol solution (1.1:1 mol ratio). WHSV = 2.70 h^{-1}. Error bars (x/y) are shown inverted within the data point symbols.

Arguably, the trend in H_2 production is simpler to explain than the CO production trend owing to only 'non-reversible' MSR being able to produce H_2 under the 180 °C/atmospheric pressure conditions used; methanol decomposition begins to occur at higher temperatures (see Section 2.7.1). Additionally, as mentioned in Section 3.6, for Cu-based MSR catalysts the active site is the Cu^0-oxide interface; whereas, the likely source of CO, RWGS, has more potential active sites, across all oxide surfaces,

and a more complicated equilibrium under the flow reactor conditions. The trend in H_2 production is discussed first.

The MSR activity likely has an inverse correlation with the M^{3+} content of the samples for several reasons. Primarily, the D_{Cu} % and BET surface area (of the LDO precursor) decrease with increasing M^{3+} content, this reduces the number of surface Cu^0 and Cu^0-support sites available for MSR catalysis (assuming the proposed mechanism in Section 3.4). Additionally, a lower BET surface area reduces the amount of reactants that can adsorb to the material's surface per unit time; all these factors combine to physically limit the rate of MSR for a given flow of methanol and water. It is assumed the reduced materials' BET surface areas follow a similar trend to that of the LDO series due to the fact that the reduction process is short, likely topotactic and occurs at a lower temperature than the calcination; additionally, the D_{Cu} % values imply that samples with analogous M^{3+} content will lose a similar amount of Cu from the lattice during reduction.

The reducibility of the Cu in the sample could also potentially affect the MSR catalysis because the catalytic cycle involves the oxidation of Cu, via methanol adsorption, followed by the regeneration of Cu^0 (reduction) in later catalytic steps. Samples with higher M^{3+} content were observed to have less reducible Cu in TPR analysis due to increased lattice energy. However, the energetics of Cu reduction will only affect the MSR rate if its reduction is involved in the rate-determining step; which, as discussed in Section 3.4, is likely not the case for Cu-based MSR catalysts. In the kinetic model developed by Peppley et al., the MSR rate-determining step for a CuZnAl MMO-derived catalyst was determined to be the dehydrogenation of the adsorbed methoxy group. [120] Tong et al. and Yong et al. proposed a bidentate formate species intermediate at the Cu-support interface is formed by the dehydrogenation of the adsorbed methoxy species. [20,131] So the MSR rate-determining step

does not appear to involve the reduction of Cu but rather a bond formation between a support oxygen species and the methoxy carbon; such a process involves the oxygen species donating electron density, weakening the lattice bonds of that oxygen to the rest of the lattice. The lattice energy argument used to explain the reducibility of the Cu in Section 7.3.3, also has relevance here; the higher the content of 'hard' cations with a high polarising power, in a given lattice, the stronger the average M-O bond in that lattice. In this case (see Figure 7.16), the higher the M^{3+} content, the higher the activation energy cost is for 'weakening' the M-O lattice bonds (at the interface) during bidentate formate intermediate formation i.e. because this step is the rate-determining step, increasing M^{3+} content slows the overall observed MSR rate. This is just a theory based on literature MSR kinetic data and this work's TPR analysis. The quantitative ratios between contributions of the effects caused by lattice energy, BET surface energy and D_{Cu} % on the MSR catalytic activity are unknown but each appears to fit the observed trend that MSR activity decreases with M^{3+} content. To put forward a kinetic model would require further in-depth experimental study using a series with more M^{2+}:M^{3+} ratios, in conjunction with specific, calorimetric, and possibly in-situ experiments.

The difference of activity between the Al and Ga series and also the range of activity within each series does not present an immediate clear trend. Analogous M^{3+} content Al and Ga catalysts have very similar D_{Cu} % values, whilst the Al LDOs have higher BET surface areas than analogous Ga LDOs; therefore, neither of these properties appear to cause the difference between the two series, but that is not to say they don't have an effect. In Figures 7.15 and 7.16, 35Zn20Ga-r has been shown to have the highest activity of the LDH-derived catalysts; as per the rate-determing step theory above, the 35Zn20Ga-r may have the lowest lattice energy (according to the TPR theory) and, therefore, requires less activation energy to stabilise the bidentate formate intermediate during the rate-determining step i.e. making it the most

active catalyst. However, the other five catalysts' MSR activity does not completely correlate to the reducibility of their Cu (TPR trend); for instance, 35Zn20Al-r is more active than 30Zn25Ga-r and 25Zn30Al-r is more active than 25Zn30Ga-r, which is not what the TPR trend would imply. Of course, the TPR trend is confused by the split peaks and it is not obvious if the area under the TPR peaks corresponds to the mass of Cu measured (see Section 7.3.3); perhaps for these five catalysts the LDO BET surface area may start to become a more limiting factor. No combination of these effects seems to give a clear theory to explain the observed trend; therefore, it is important to remember that the data displayed in Figures 7.15 and 7.16 represents the production rates' averages over the 5 hour reaction.

Figure 7.17 displays the hydrogen production rate of the same 5 hour experiments that gave the averages in Figures 7.15 and 7.16; however, each reading, taken every $\approx$ 11 minutes is shown. The activity of all samples does not reach peak activity instantaneously because the evaporation of the reactant liquids takes time to reach its maximum rate, it also takes time to saturate the catalyst surface with adsorbed species. The existence of a 'peak' activity is most likely caused by the sintering and agglomeration of the active Cu metal species under the MSR reaction conditions; where Cu atoms or Cu metal particles break and reform bonds with the surface to move across the surface and form energetically more stable larger particles (see Section 2.5.4). This thermal process results in the loss of Cu surface area and D_{Cu} % (the amount of exposed Cu^0); hence why it is theorised to be the cause of activity loss in many metal catalyst literature studies. The peak activity for most catalysts, in this chapter, occurs around the 50 - 70 minute mark after starting the flow of reactants.

From Figure 7.17, 35Zn20Al-r is seen to have the highest peak in MSR activity; it is clear the maximum observed (peak) hydrogen productivity trend correlates to the LDOs' BET surface area trend i.e. 35Zn20Al- > 35Zn20Ga- > 30Zn25Al- >

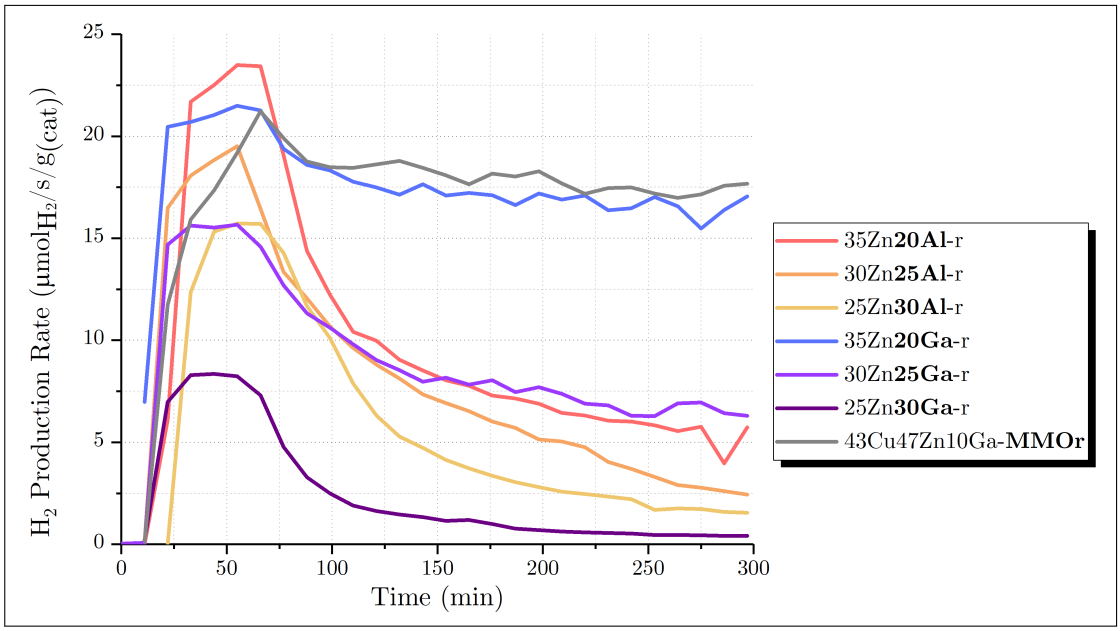


Figure 7.17: The hydrogen production rate ($\mu mol_{H_2}.s^{-1}.g_{cat}^{-1}$) of the reduced Al- and Ga-based series shown against time in the x axis (Time = 0, coincides with the start of reactant flow). Tested at 180 °C for 5 hours, with 200 mg of catalyst, a N_2 gas flow of 10 mL.min^{-1} and a 0.1 mL.min^{-1} liquid flow of water:methanol solution (1.1:1 mol ratio). WHSV = 2.70 h^{-1}.

30Zn25Ga- ≈ 25Zn30Al- > 25Zn30Ga-. Importantly, the Ga catalysts can be seen to have a higher stability of their activity; relative to the peak activity, the activity of the Al catalysts drops off substantially. Figure 7.18, displays the ratio of the maximum observed MSR activity compared to activity after 5 hours.

From Figure 7.18, the Al catalysts series are observed to have a higher peak MSR activity than the analogous M^{3+} content Ga catalysts, this is theorised to be caused by their presumably higher BET surface areas (based on the LDO BET surface area trends) and slightly higher D_{Cu} %; causing the Al catalysts to have a higher initial amount of metal-support interface. However, it appears that the stability of the Ga catalysts is a more ample explanation for their higher averaged MSR activity compared to the analogous Al catalysts.

35Zn20Ga- and 30Zn25Ga-r have a much higher stability, in terms of their (H_2

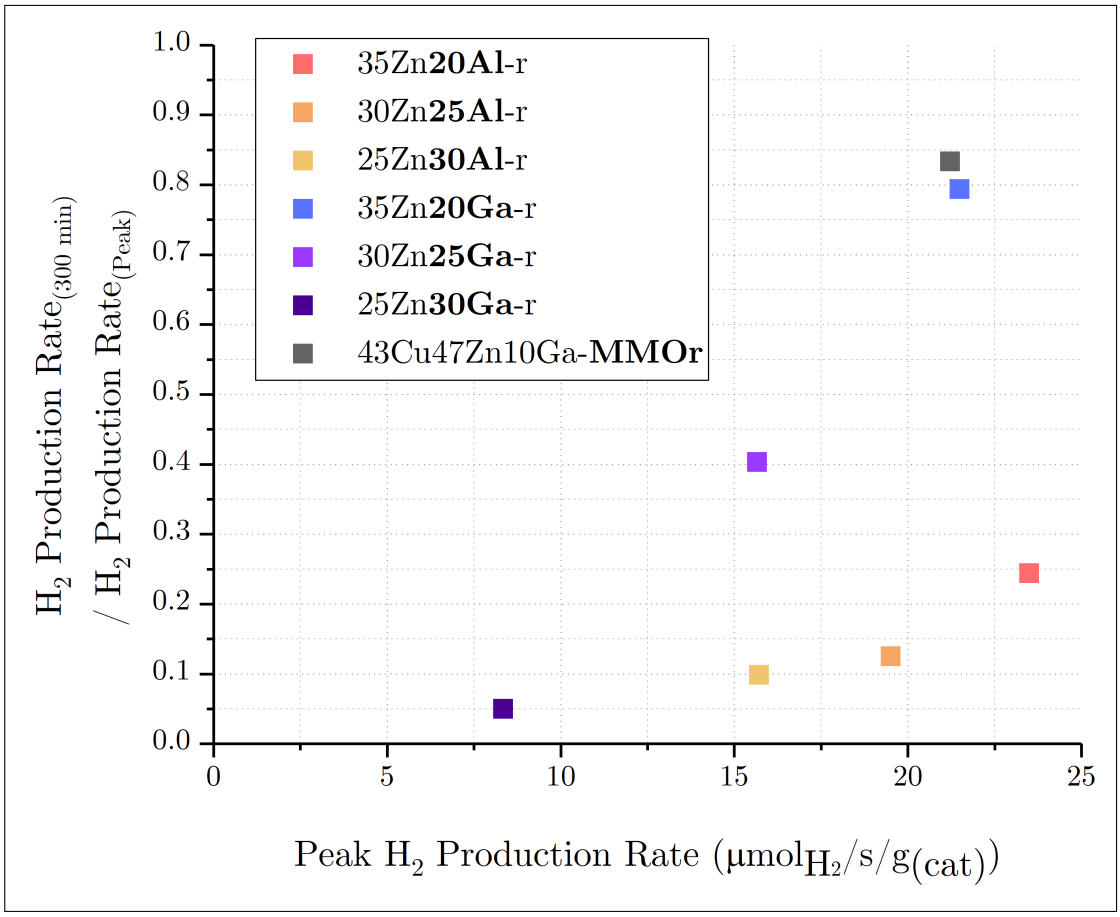


Figure 7.18: The maximum hydrogen production rate ($\mu mol_{H_2}.s^{-1}.g_{cat}^{-1}$) observed for each reduced Al- and Ga-based catalyst, shown against the (Hydrogen production rate at 300 mins / The peak hydrogen production rate) ratio. Tested at 180 °C for 5 hours, with 200 mg of catalyst, a N_2 gas flow of 10 mL.min^{-1} and a 0.1 mL.min^{-1} liquid flow of water:methanol solution (1.1:1 mol ratio). WHSV = 2.70 h^{-1}.

production$_{300mins}$/H_2 production$_{Peak}$) ratio, than the analogous Al-based catalysts. In Section 7.3.3, the average lattice M-O bond strength for a Ga sample was theorised to be less than that for an analgous Al sample; this lower lattice energy would imply that the Ga-based lattice should be less stable at elevated temperatures. However, 180 °C is not a high enough temperature to breakdown the LDO morphology, see Section 3.7.1 and the theorised loss in activity, sintering, is not caused by a breaking of the lattice bonds; rather a weak attraction between the metal and support. It was theorised in Section 7.3.5 that samples with less M^{3+} content have a smaller size of

average, stable Cu^0 particle due to the polarising power of the support. Additionally, Al^{3+}'s higher polarising power than Ga^{3+} theoretically causes Al^{3+} to 'pull' more electron density away from the support O species it forms ionic bonds with; in turn, these support O species donate less electron density to the Cu^0 metal compared to the same species in the Ga-based material. Due to the presumable high elemental dispersion within the support (see the EDX analysis for 35Zn20Ga in Section 8.4.3), to sinter across the surface any Cu species must break and remake some form of bonds with evenly distributed sections of Zn and Al/Ga oxide species. The activation energy for breaking such bonds will theoretically determine, and inversely correlate with, the sintering rate; therefore, it is proposed the sintering rate of Cu on a given metal oxide support will follow the opposite trend to that of the mean electronic polarisibility of that metal: $AlO_x > GaO_x > ZnO_x$. This trend also explains why the catalyst stability is observed to decrease with increasing M^{3+} content in Figure 7.18.

The higher $3R_2$ polytype content of the Ga series is unlikely to play a large role in the increased catalytic stability unless both calcination and reduction are highly topotactic. It would be interesting to study the experimental minimal Ga^{3+} content required to synthesise an AMO-LDH to see if the stability could be enhanced further.

Coincidentally, the literature catalyst (43Cu47Zn10Ga-MMOr) that was chosen for comparison with the materials in this work, based on its low-temperature MSR catalytic performance, was derived from a $CuZnGaO_x$ MMO precursor with a relatively low $\approx$ 10 % wt Ga^{3+} content. This literature catalyst was originally published by Yu et al. and Tong et al. and achieved a H_2 production rate of 0.0045 $\mu mol_{H2}.s^{-1}.g_{cat}^{-1}$ (equivalent to 22.5 % methanol conversion, the highest in its original series) and an incalculable H_2:CO ratio, on account of no detectable CO being observed, at 150 °C and under a 0.01 $mL.min^{-1}$ flow of methanol:water solution (1:2 mol ratio). In line with original work by Tong et al., 43Cu47Zn10Ga-MMOr produced detectable CO at

180 °C in this work, 235 ppm_{CO}. In fact, this work's 35Zn20Ga-r gave a very similar average H_2 production rate, peak H_2 production rate and stability profile to the reproduced 43Cu47Zn10Ga-MMOr catalyst; this is likely a coincidence. There are a large number of potential competing effects on the MSR activity of the two samples, such as large differences in morphology, synthesis conditions, Zn^{2+}/Ga^{3+} content and presumably the properties achieved as a result of exfoliation, such as high BET surface areas and D_{Cu} %; Tong et al. reported the D_{Cu} % of 43Cu47Zn10Ga-MMO to be 30.5 %, whereas the D_{Cu} % of 35Zn20Ga-LDO was 47.5 %. The most important difference between the two catalysts, is the CO production, seen in Figures 7.15 and 7.16. The H_2:CO mol production ratio of 35Zn20Ga-r is more than double that of 43Cu47Zn10Ga-MMOr; the trends and factors that affect CO selectivity are discussed below.

As discussed in Section 3.4, CO is a side product under MSR conditions, arising from the reverse water gas shift ($CO_2(g) + H_2(g) \longrightarrow CO(g) + H_2O(g)$) and methanol decomposition ($CH_3OH(g) \longrightarrow 2\,H_2(g) + CO(g)$). Unfortunately, the CO production rate is too low for the difference in the H_2:CO_2 mol ratio, between the hypothetical cases of RWGS and methanol decomposition CO production methods, to be observable within reasonable error; primarily because the CO content is 10^3 mol orders below that of H_2 and CO_2. In literature at MSR temperatures below 260 °C, methanol decomposition has been reported to be insignificant. [112, 140, 141] Therefore, it is assumed all CO content in this work arises from the RWGS reaction.

Each Ga-based catalyst gives a lower CO production rate than the analogous Al sample with the same M^{3+} content (see Figure 7.15). As was discussed in Section 3.4 and for the Mg-based catalysts (see Section 6.3.7), WGS and RWGS have been proposed to occur on Cu, oxide and/or interface (see Section 3.4). Therefore, it is not clear which active sites catalyse RWGS for these LDH-derived materials. For the

Mg-based series, Section 6.3.7, the CO production correlated with the BET surface area until the surface area and stability became the limiting factor.

Multiple theories can be proposed to explain the difference in CO production between the Al and Ga series. Schumann et al. found the activation energies for RWGS CO formation to be 87, 89, 98 and 99 kJ.mol^{-1} for Cu supported on $ZnAlO_x$, $ZnGaO_x$, $ZnMgO_x$ and ZnO_2, respectively; Schumann et al. theorised Ga^{3+} and Al^{3+} were electronic promoters. [253] As previously mentioned, the RDS for RWGS when using the LDH-derived catalysts is likely to be the CO_2 dissociative adsorption. [260, 261] The first theory, depending on the active site for RWGS, follows a generic polarising power argument, whereby Al^{3+} is more polarising than Ga^{3+}. Therefore, CO_2 forms stronger bonds with the 'harder' cations in the support when adsorbing on the oxide support at the oxide interface. However, this theory would have to involve the breakdown of microreversibilty between WGS and RWGS catalysis.

A second, more tenuous theory, is that Ga-based samples have more paramagnetic 'oxygen vacancies' than Al-based samples, with analogous M^{3+} content, due to their larger EPR signals (as discussed in Section 10.3 and these additional oxygen vacancies can help stabilise a higher concentration of [Cu^+] during MSR; Turco et al. proposes Cu^+ binds more strongly to CO than Cu^0 i.e. CO molecules have a longer effective residence time, increasing the forward WGS rate and lowering [CO] concentration. [163] Yu et al. proposed a similar theory, where more oxygen vacancies are formed in CuZnGa MMOs due to the metals' similar ionic radii and increased 'site swapping', it was theorised if the support oxide is more reducible then it is more energetically favourable to lose oxygen via oxidising CO. [17] Again this would involved the breakdown of microreversibility.

The most likely theory, for explaining the difference in CO production of the Ga- and Al-based series, can be postulated if the RWGS reaction can occur on the oxide

surface, not involving the Cu^0 metal, as proposed by Tong et al. [20, 142] The D_{Cu} % of Ga and Al samples, with analogous M^{3+} content, are almost equivalent, implying a similar amount of metal-support interface sites; assuming these sites have similar selectivity for the MSR vs RWGS reactions, then the catalyst with more additional oxide support surface area would provide more oxide sites for just the WGS/RWGS. These WGS sites favour a higher RWGS rate under the MSR conditions used in this work because in a flow reactor equilibrium cannot be reached and the [CO] concentration is continuously decreased. Al-based samples have higher BET surface areas than Ga-based samples, with analogous M^{3+} content, so may have a higher [RWGS only]:[RWGS+MSR] active site ratio active sites. Subsequently, allowing a faster rate of both WGS and RWGS reactions that lets the observed concentration of [CO] shift towards the thermodynamic equilibrium concentration (which is not normally reached in low-temperature MSR literature). [17, 75, 76] Additionally, the Ga-based series has a higher resistance to thermal sintering as per Figure 7.18 and, therefore, will have a higher effective D_{Cu} % averaged over the MSR reaction time (relative to their original D_{Cu} % at time = 0) compared to Al-based catalysts.

Within the Ga series, the M^{3+} content seems to inversely correlate with the H_2:CO production mol ratio (see Figure 7.16); the case for the Al series is complicated due to 30Zn25Al-r being an apparent anomaly. Further study of more Al series samples is needed to better understand the relationship between M^{3+} content and CO production in that series.

7.4 AlGa chapter summary

Gallium was shown to be the favourable M^{3+} cation, rather than aluminium, for use in AMO-LDH MSR catalyst precursors, in terms of the CO production rate. This chapter also showed that the minimal possible M^{3+} content, for creating an AMO-LDH (20 %), is optimal for creating a catalyst precursor that will give high MSR activity at low temperatures. 35Zn20Ga-r proved to be the most active LDH-derived catalyst by far, 16.89 $\mu mol_{H_2}.s^{-1}.g_{cat}^{-1}$, and provided a very high H_2:CO mol production ratio, 3,541 mol_{H_2}:mol_{CO}. It is important to note that a 2.70 h^{-1} WHSV was used for this chapter as opposed to the 5.41 h^{-1} WHSV used for the Mg series, therefore reactants had a longer residence time in this chapter allowing a higher yield of the RWGS reaction. Therefore, 3,541 mol_{H_2}:mol_{CO} is a very impressive selectivity as it is higher than the previous literature best, which was achieved at 7.09 h^{-1}. [247]

The good CO selectivity of 35Zn20Ga-r can be attributed to its high sintering-resistance under MSR conditions and, therefore, its high in-situ D_{Cu} % which allows a higher ratio of MSR and WGS active interface sites relative to just WGS oxide active sites. The higher activity stability of the Ga catalysts was theorised to be caused by stronger Cu-support interactions due to the lower polarising power of Ga^{3+} compared to Al^{3+}. Additionally, the AMO method proved very effective at synthesising very high surface area precursors that led to catalysts with high D_{Cu} % and, therefore, high MSR activity at low temperatures.

The lower price and higher abundance of Al may still be the economic best option, even after factoring in downstream processes that specifically oxidise CO; and as seen in Section 6.3.7, in CuZnMgAl LDH-derived catalysts, the doping of Mg can offset the weaknesses of Al. 43.75Mg-r increased the stability ($Activity_{(300mins)}$/$Activity_{(Peak)}$) and H_2:CO mol production ratio compared to 0Mg-r (40Cu30Zn30Al-r) by $\approx$ 4.87 and 1.22 fold, respectively. Indeed the preparation of chemical reactor facilities is ex-

tremely complicated, but hopefully this chapter provides some data for consideration when planning future MSR projects.

To explore CO selectivity in greater detail, the CuZnGa AMO-LDH was selected for further study, due to it having the lowest observable CO production in the M^{3+} cation study; in this further study, Ce was doped into the lattice to affect the oxide reducibility and, potentially, the concentration of oxygen vacancies. In addition to this, in-situ DRIFTS, TEM, EDX, EXAFS, XANES, XPS and DFT modelling were performed on precursors, LDOs, reduced samples and samples during certain stages of reaction; to develop more insight into how 'low-CO' MSR catalysts can be developed.

Chapter 8

Doping CuZnGa AMO-LDHs with Cerium

8.1 The usage of Ce in catalysis

Ceria or cerium oxide, CeO_2, is used as a support in many catalytic processes owing to its 'reducible' nature. It also has a similar abundance on the Herfindahl-Hirschman Index to Cu/Zn (see Figure 6.1) and as such Ce metal is relatively cheap, 3.28 £/kg. [262] A 'reducible' oxide is an oxide that only requires relatively mild conditions to be reduced (see Section 2.6). [66] Ceria is considered reducible because there is a relatively strong steric repulsion between the large soft Ce^{4+} cations in the oxide making the formation of defects more favourable as these reduce steric strain and increase entropy; therefore, ceria is known to have high 'oxygen mobility'. [66] Theoretically upon reduction, some Ce^{4+} becomes Ce^{3+} and oxygen is lost i.e. oxygen vacancies form. Ceria has been shown to contribute to TPR signals whereas other lanthanide series oxides (La and Sm) have not. [263] Doping Ce into other oxides, such as iron oxide, has been reported to introduce more oxygen vacancies. [264]

As discussed in Section 3.4, oxygen vacancies are theorised to play an important role in the MSR reaction mechanism; they likely provide adsorption sites at the metal-support interface for water and formate intermediates. It was also discussed in

Section 7.3.6, that oxygen vacancies at the interface have been proposed, in literature, to stabilise Cu^{+} in the active catalyst, likely increasing the adsorbed residence time of CO (more so than for Cu^{0}); then because ceria is a reducible oxide, lattice oxygen can oxidise CO in an energetically favourable process. [17, 163]

The introduction of Ce into LDH-precursors for MSR catalysts was highlighted as a possible strategy for lowering CO content in the product feed; this was backed up by the fact that Cu/CeO_2 materials are often used as catalysts for WGS reactions and the preferential oxidation of CO. [265] Konsolakis et al. implied that the catalytic Ce-Cu interactions can be extremely complex and challenging to analyse depending on the additional species present, structure permutations, crystallinity of the catalyst, surface defects and the type of catalytic process. [265] The WGS reaction especially was noted as complicated (as touched on in Section 6.3.7), both a redox mechanism, where CO is oxidised by oxygen from dissociatively adsorbed water, and an associative mechanism, which involves the reaction of CO with surface hydroxy species, have been proposed. There are many kinetic analyses of WGS in literature and the rate determining step is thought to be the dissociation of water for low temperature and pressure conditions. [245, 246, 265]

Stacchiola et al. observed that $Cu(1\ 1\ 1)/CeO_x$ was a more active WGS catalyst than just Cu(1 1 1) and contained both Ce^{4+} and Ce^{3+}; *in-situ* ambient pressure XPS showed stabilised $CO_2{}^{\delta-}$ species occured for only the $Cu(1\ 1\ 1)/CeO_x$ catalyst. [266] Stacchiola et al. proposed WGS proceeds via an associative mechanism when CeO_x is introduced. Stacchiola et al. cite that metals have a weak interaction with water and a strong interaction with CO (the opposite was theorised for oxides). [266]

As mentioned in Section 3.5, WGS/RWGS can likely occur over oxide surfaces due to hydrogen spillover. Wang et al. used *in-situ* XAS and DRIFTS to show water dissociation could occur on any oxygen vacancy oxide site during WGS catalysis over

Cu/CeO_x materials; they proposed Cu helped facilitate the oxygen vacancy formation. [144] This agrees with observations of Rodriguez et al., that materials with oxygen vacancies can lower the activation energy of water dissociation, therefore increasing the WGS rate. [267] Wong et al. imply CeO_2 helped increase the strength of CO chemisorption to Cu^0 but do not offer a non-Ce comparison. [145]

Lu et al. also used DFT calculations, it was found that the doping of 3 mol % of Cu into ceria decreased the activation energy required for the formation of oxygen vacancies in the oxide; this was attributed to the difference in cationic radii 'relaxing' the structure and reducing unfavourable steric interactions. [268] The lower oxidation state of the Cu^{2+}, compared to Ce^{4+}, also reduced the difficulty of fulfilling the charge imbalance created by the oxygen vacancy; however, no Cu^+ was observed in the models. [268] However, Cu^+ and Ce^{3+} have both been observed experimentally under WGS conditions for CeCu-based catalysts. [265, 267, 269]

CuCe materials were also used in other research areas, besides WGS catalysis, owing to the activity of Cu^0. Senanayake et al. used *in-situ* XPS and infrared reflection absorption spectroscopy to study CuCe- and CuZn-based CO_2 hydrogenation catalysts, it was proposed that the formation of Ce^{3+}/oxygen vacancies provide sites for the carbon dioxide adsorption and help stabilise a ${CO_2}^{\delta-}$ intermediate; Cu/CeO_x were more active than Cu/ZnO_x catalysts. [269] For the dimethyl ether steam reforming process, Oar-Arteta et al. found higher contents of ceria in the support of noble metal catalysts led to increased H_2 and CO_2 yields, and a lowered CH_4 yield; this was attributed to ceria promoting WGS activity. [90]

The use of CuCe-based catalysts in MSR is relatively uncommon in literature. Early work by Liu et al. found that Cu/CeO_2 was a more active MSR catalyst than various CuZnAl oxides over a range of 220 - 260 °C; the Cu/CeO_2 material had the highest surface area but it was also theorised that Cu^+ could be formed via redox

with Ce in the support. [104] As evidence for this, Liu et al. posited the split peaks in TPR profiles were caused by Cu^{+} and Cu^{2+}, and that the Cu^{+} was important for 'efficient' MSR catalysis without much elaboration; besides the citation of a study by Idem et al., wherein the Cu^{0}: Cu^{+} ratio is observed to affect activity. [104, 270]

Patel et al. synthesised one of the most active MSR catalysts found in literature and it contained Ce, the CuZnAlCe MMO-derived catalyst achieved an activity of 244 $\mu mol_{H_2}.s^{-1}.g_{cat}^{-1}$ at 260 °C. [101] Unfortunately, the H_2:CO mol production rate was low, only ≈ 500, despite a high excess of water being used (1.4 = H_2O:CH_3OH); however, the CO mol % in the product feed was lower than that of non-Ce catalysts in the same study. [101] Patel et al. proposed the role of ceria was to increase D_{Cu} %, increase thermal stability and to provide 'mobile oxygen' to oxidise coke and prevent its build-up. [101] Yang et al. also saw that the addition of Ce, into CuZnAl catalysts, increased D_{Cu} % and MSR activity; Cu^{+} was observed in Auger XPS and it was proposed higher Cu surface areas and lower Cu reduction temperatures increased the MSR activity. [85]

Ceria was also used as a support in PtInCe-based MSR catalysts by Liu et al., the ceria was attributed with providing oxygen and lower CO:CO_2 ratios compared to other catalysts during TPD experiments. [83] The TPD experiments by Liu et al. also revealed Ce promoted the chemisorption of water at lower temperatures; this was correlated to increased hydrogen production, via the increased activation of water and methanol. [83]

From the literature reports, Ce appeared to be a promising potential dopant to improve the CO selectivity of a MSR catalyst; however, it was not clear what effect introducing Ce cations into a CuZnGa or CuZnAl LDH lattice would have. Ce, lanthanides and other large cations have previously been used in the synthesis of LDHs but in the majority of papers PXRD, BET, ICP-MS, FTIR and TEM analysis has

only been used to infer the position of the dopant, inside or outside the LDH lattice; often the materials are too amorphous. [138,271–278] Suárez-Quezada et al. only use a shift in the LDH (1 1 0) peak as evidence of Ce incorporation in the lattice, whilst Posati et al. base their Eu-incorporation claims on the materials' thermal stability, luminescence brightness and selected-area electron diffraction patterns. [276,279] Gao et al. observed that increasing Y^{3+} content, in a series of CuZnAl LDHs, decreases the LDH content; implying too much distortion of the LDH lattice, due to the larger ionic radius of Y^{3+}, could cause the adoption of a different amorphous structure. [187] Al-aani et al. synthesised 'Ce-doped' CuMgAl-LDHs but did not attempt to identify the Ce location in great detail and the samples were calcined at high temperatures into MMOs before catalysis; however, a Ce/Cu redox interaction was theorised (Ce^{3+} + $Cu^{2+} \rightleftharpoons Ce^{4+} + Cu^{+}$). [212]

The most compelling evidence for lanthanide inclusion in the LDH lattice was provided by Stumpf et al., Eu^{3+} was attempted to be doped into MgAl-LDHs, LDH PXRD peak broadening was detected but more importantly EXAFS analysis was conducted of the Eu^{3+} L_3 edge; the data fitting revealed there were no Eu-Eu interactions in a sample containing 10 % metal mol Eu, indicating no $Eu(OH)_3$ was present. [280] Time-resolved laser fluorescence spectroscopy analysis of the same sample was also taken and two different emission peaks were detected after being excited by 394 nm wavelength light at 10 K. [280] Using data of the emissions' decay lifetime and excitation selection rules, Stumpf et al. calculated there was a low-symmetry Eu environment and a high-symmetry environment that were coordinated to ≈ 5 and 3 water molecules, respectively. For the high-symmetry environment, 3 water molecule quenchers were equivalenced to 6 hydroxyl groups (-OH); it was theorised this was a Eu environment substituted into the LDH lattice. [280] Furthermore, the EXAFS analysis distinguished there were two different types of Eu-Al coordination, the shorter Eu-Al distance was assigned a low-symmetry Eu environment bound to

the LDH surface; whereas, the longer Eu-Al is associated to the lattice Eu environment. [280] Lower Al and O coordination numbers from the EXAFS analysis are interpreted to mean the larger radius of Eu distorts the LDH structure somewhat or that Eu does not replace Mg/Al in the same lattice locations. [280]

Gao et al. found that doping 2.5 mol % of Ce or Zr into conventional CuZnAl LDH materials increased the BET surface area; in addition, they observed an increase in the number of sites that strongly bound CO_2 in TPD. [271] Gao et al. assigned these sites as 'coordinately unsaturated O^{2-} ions', as opposed to hydroxyl groups or lattice Zn-O or Al-O bonds. [271] Gao et al. suggested the increase in the number of these sites was caused by a decrease in thermal stability, as a result of the doping, or due to the 'higher net electronic charge of the layers' caused by M^{x+}. [271] Gao et al. observed a correlation between the number of strongly basic sites and CO_2 hydrogenation activity (and methanol selectivity over CO); it was proposed CO_2 adsorbed on these sites was more likely to react with other surface species than to dissociate into CO via the RWGS. [271]

8.2 The goal of doping MSR catalyst LDH-precursors with Ce

The CuZnGa AMO-LDH series proved to be good precursors for MSR catalysts due to their high surface area, elemental dispersion and stability. The goal was to improve upon these catalysts' already-good CO selectivity so that they could be used as a lone, efficient catalyst for powering methanol-fed PEMFCs or in a process that required a H_2 feed without CO. As per Section 8.1, Ce's role in preferential CO oxidation and WGS catalysis was reportedly to: provide oxygen vacancies to lower the activation energy of water dissociation (increasing the RDS of WGS); provide active oxygen species for the oxidation of CO and coke; cause a Ce/Cu redox system whereby Cu^+ binds more strongly to CO than Cu^0 and to act as a structural promoter

(increasing BET surface area and D_{Cu} %). If one of these roles could be utilised in MSR catalysis, improvements would be expected by doping Ce into the CuZnGa AMO-LDH series. It is not clear how the Ce inclusion would affect the growth of the LDH lattice or the exfoliation step and the subsequent physical properties of the catalyst; judging by other work in literature some LDH phases still formed with lanthanide inclusion and the report by Stumpf et al. showed large Eu^{3+} cations could occupy sites within the lattice and on the surface. [280] Nonetheless, pilot tests were carried out to see how Ce would affect the MSR catalytic performance of 35Zn20Ga-r.

In this chapter, Ga was replaced with Ce content in a series of CuZnGaCe AMO-LDHs; the Ga^{3+} was chosen to be replaced as it has the highest net charge of the cations in the lattice. The series was designed to follow the empirical formula: $[Cu_{0.45}\,Zn_{0.35}\,Ce_{0-0.1}\,Ga_{0.1-0.2}\,(OH)_2]^{x+}\,(CO_3^{2-})_{x/2} \bullet yH_2O \bullet zCH_3COCH_3$ (where y and $z < 10$ theorised by Chen et al.). [181] The goal was to implement the AMO-LDH precursors as they were in the previous chapters and attempt to identify how Ce affected the catalytic performance; ideally it was theorised that Ce doping could further increase the MSR H_2:CO ratios.

8.3 The CuZnGaCe AMO-LDH series

The Ce mol % used during synthesis of the Ce series spans from 0 - 10 % (including the comparison of 35Zn20Ga-LDH from Chapter 7), the intervals are not equal because initially only 0.5, 1 and 2 % were screened; after the MSR performance of 19Ga1Ce-r, higher Ce loadings were attempted at 5, 7.5 and 10 % and the 0.75 % loading was attempted due to the differences observed between the 19.5Ga0.5Ce- and 19Ga1Ce-LDH samples. The formulas used during the synthesis of the Ce series are shown in Table 8.1. All samples are labelled as follows: '-LDH' = as-prepared AMO layered double hydroxide; '-LDO' = calcined/LDO sample; and '-r' = reduced sample. Each CuZnGaCe(Ln)-derived sample is also denoted with its constituent Ga

and lanthanide content expressed as the metal mol % of the respective metal nitrate hydrate (of the total metal nitrate) used in synthesis.

Table 8.1: The constituent metal mol ratios used during the synthesis of the CuZnGaCe AMO-LDH series.

Sample	Cu mol % (of total metal mols)	Zn mol % (of total metal mols)	Ga mol % (of total metal mols)	Ce mol % (of total metal mols)
19.5Ga0.5Ce-LDH	45	35	19.5	0.5
19.25Ga0.75Ce-LDH	45	35	19.25	0.75
19Ga1Ce-LDH	45	35	19	1
18Ga2Ce-LDH	45	35	18	2
15Ga5Ce-LDH	45	35	15	5
12.5Ga7.5Ce-LDH	45	35	12.5	7.5
10Ga10Ce-LDH	45	35	10	10

Not all the ICP-MS analysis was conducted for the Ce-based LDH series but it was completed for the LDO series since it was of higher priority because it was used in D_{Cu} % calculations. In all cases the analogous metal wt % ratio for a given LDH was less than that for the LDO, as was expected due to dehydroxylation and the loss of interlayer water/anions.

Table 8.2: The ICP-MS analysis results of selected as-prepared CuZnGaCe AMO-LDHs and the whole series of calcined CuZnGaCe AMO-LDOs.

Sample	Cu (wt %)	Zn (wt %)	Ga (wt %)	Ce (wt %)
19.5Ga0.5Ce-LDH	31.82	24.12	13.09	0.86
19Ga1Ce-LDH	30.23	23.26	12.15	1.61
18Ga2Ce-LDH	30.44	23.70	11.87	2.88
19.5Ga0.5Ce-LDO	35.92	25.55	13.62	0.87
19.25Ga0.75Ce-LDO	35.89	25.37	13.72	1.21
19Ga1Ce-LDO	31.59	24.85	13.60	1.73
18Ga2Ce-LDO	32.19	25.77	12.41	3.28
15Ga5Ce-LDO	32.31	23.47	10.05	7.44
12.5Ga7.5Ce-LDO	32.99	23.20	8.57	11.07
10Ga10Ce-LDO	31.60	22.71	6.81	14.20

Table 8.2 shows the Ce wt % trend for the Ce-based LDO series is in line with the

theoretical ratios used during the synthesis. As are the rest of the metal trends which generally decrease with Ce content due to the higher molar mass of Ce, although there are some anomalies; these could arise from irregularities in setting up the calcination process and/or differences between the conditions and operators for the various, off-site ICP-MS sessions.

8.4 Analysis of the Ce-doped LDH structure

8.4.1 PXRD analysis of the Ce LDH series

PXRD analysis and subsequent standardised integration methods/calculations were conducted for the Ce-doped AMO-LDH series as they were for the Mg, Al and Ga series. The PXRD patterns were collected using Cu K-α X-Ray radiation and only peaks of LDH planes were visible: (0 0 3) at $\approx$ 11.5 °, (0 0 6) at $\approx$ 23.5 °, (0 0 9) at $\approx$ 33.5 °, (0 1 2) at $\approx$ 34 °, (1 0 4) at $\approx$ 37 °, (0 1 5) at $\approx$ 38.9 °, (1 0 7) at $\approx$ 43.5 °, (0 1 8) at $\approx$ 46.5 °, (0 0 12) at $\approx$ 48 °, (1 0 10) at $\approx$ 52.5 °, (0 1 11) at $\approx$ 56 °, (1 1 0) at $\approx$ 59 °, (1 1 3) at $\approx$ 60.5 °, (1 0 13) at $\approx$ 63.5 ° and (1 1 6) at $\approx$ 64.5 °. [181, 187–189, 191, 192] Like the Ga-based AMO-LDH series in Chapter 7, a mixture of the $3R_1$ and $3R_2$ polytypes are present (see Section 3.7.1). These PXRD patterns are sharp and show very similar peak definition to the 30Zn25Ga- and 25Zn30Ga-LDHs; this is likely because the LDH crystallites are even thicker than that of the Ga series (see Figure 8.6).

Only LDH phase peaks are observed in the PXRD patterns of the Ce-doped AMO-LDH series. This does not exclude the possibility that other very small phases, such as CeO_2, are present; if particles are small enough, line broadening could render their diffractions unobservable. The LDH phase peaks do not shift in a significant way with respect to the Ce content, see Figures 8.2 and 8.3; however, the peak intensity does decrease significantly with increasing Ce content. To explain these trends, the lattice parameters and crystallite thickness were calculated using the PXRD data.

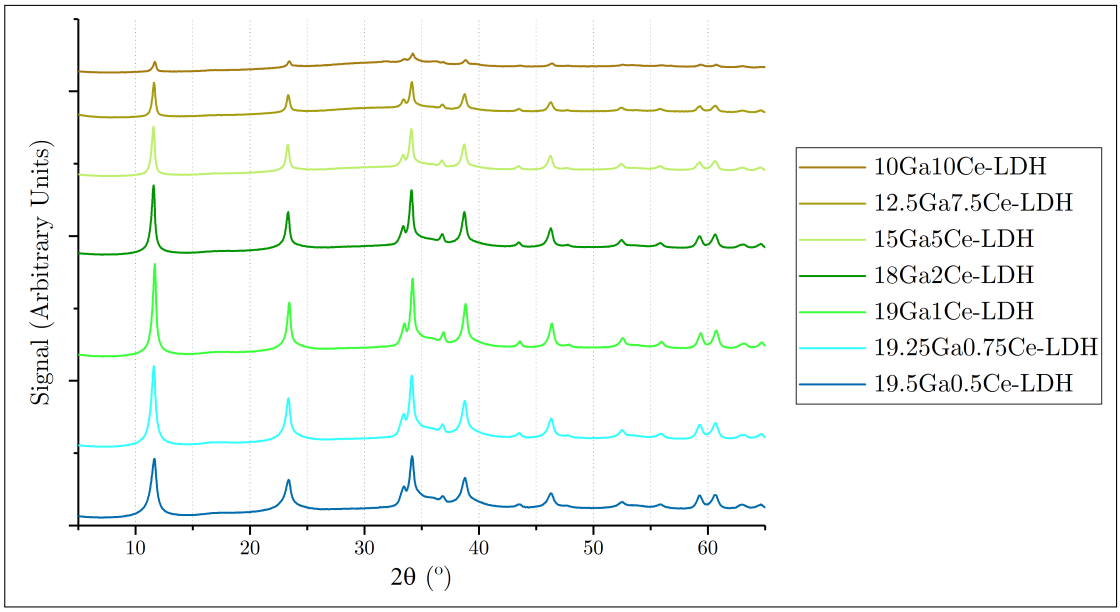


Figure 8.1: PXRD patterns of the Ce-based AMO-LDH series.

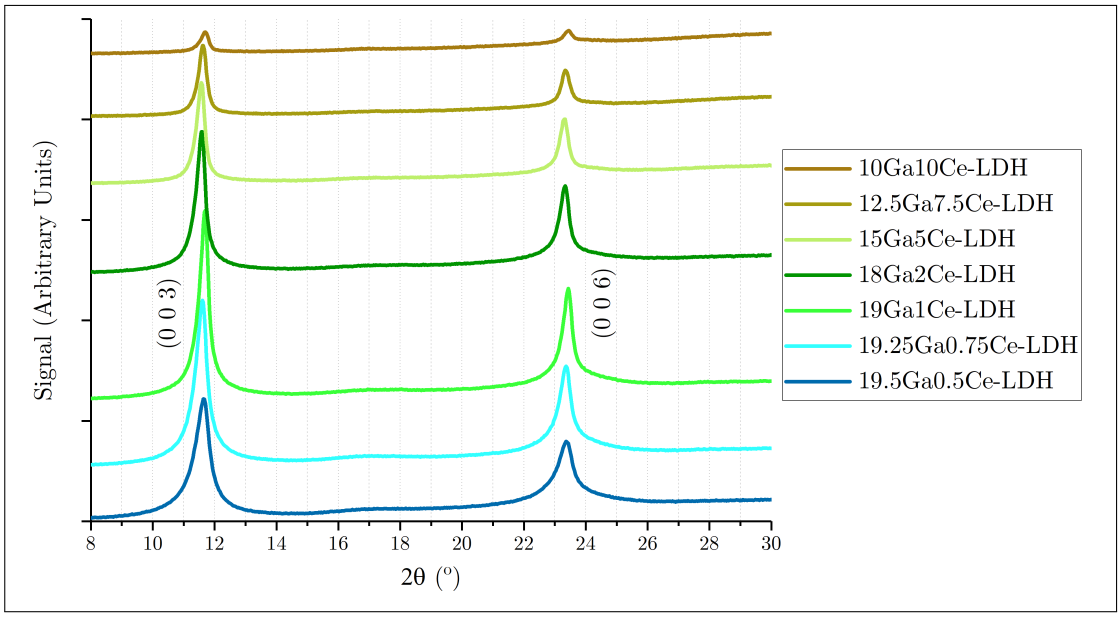


Figure 8.2: PXRD patterns of the Ce-based AMO-LDH series between 8 ° and 30 ° 2θ; showing the (0 0 3) and (0 0 6) peaks.

The lattice and other physical parameters of the Ce-doped AMO-LDHs were calculated using the (0 0 3), (0 0 6) and (1 1 0) LDH phase peaks from Figure 8.1; the series was also compared to the 35Zn20Ga-LDH from Chapter 7. Whilst this cannot provide information of the percentage of Ce atoms that are included in a LDH

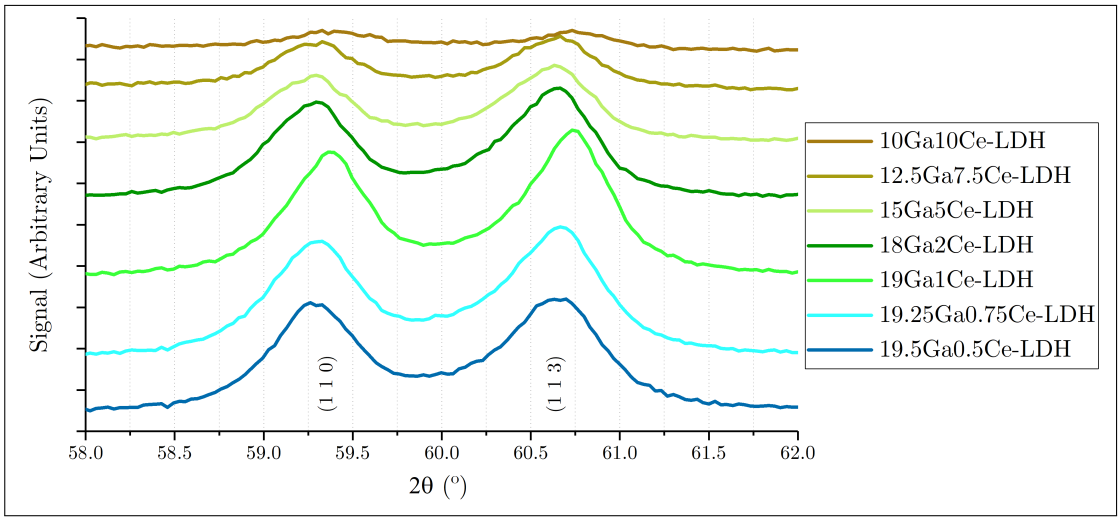


Figure 8.3: PXRD patterns of the Ce-based AMO-LDH series between 58 ° and 62 ° 2θ; showing the (1 1 0) and (1 1 3) peaks.

lattice it can show how any LDH lattices present are affected by the presence of Ce. Figure 8.4 represents the trend in the a parameter of the Ce series, the error in the measurement is relatively large compared to the differences in a parameters between the various samples. For 19.25Ga0.75Ce-LDH the error bar is dominated by the difference in 2θ between each phases' peaks across two different PXRD measurements (random error); whereas, for the other samples the error bars are all a very similar size because they are seemingly dominated by an analysis method or diffractometer error. Not all samples had their PXRD patterns collected experimentally twice but all samples had their spectra analysed via two different methods (the standardised, semi-automated method and a manual peak/baseline assignment method).

The trend in the a parameter of the Ce-series is complicated, especially in the low Ce content regime below 1 mol %. The a parameter of all Ce-doped samples is higher than that of the 35Zn20Ga-LDH as expected because the widest theoretical Ce ionic radii range is from 0.87 Å, for 6-coordinate Ce^{4+}, to 1.14 Å, for 8-coordinate Ce^{3+} (both these oxidation state/coordination number combinations are not typical); these sizes are larger than Cu^{2+}, Zn^{2+} or Ga^{3+}. [237] This difference is nowhere near as

pronounced as the ≈ + 0.035 Å increase in the *a* parameter that is seen when all Al^{3+} is 'substituted' for Ga^{3+}, see Figure 7.4. On one hand this is not surprising for low Ce content samples where only a small percentage of the metal cations in the lattice are 'enlarged'. However, the increase in radii from Al^{3+} to Ga^{3+} is ≈ 0.08 Å, whereas the increase in radii from Ga^{3+} to Ce^{x+} is ≈ 0.25 - 0.52 Å; therefore, a much larger *a* parameter increase above 35Zn20Ga-LDH was expected for the higher Ce content samples. Figure 8.1 displays that the *a* parameter increases slightly upon addition of Ce into the CuZnGa LDH structure, but it tends to decrease slowly when Ce content increases further. This implies that there is a 'critical' amount of Ce that can occupy Cu, Zn or Ga positions in the 35Zn20Ga-LDH whilst maintaining a LDH phase; but the *a* parameter cannot elucidate what structure the excess Ce forms because no other phase peaks are detected. This is because the *a* parameter is specifically a unit cell dimension of the layered double hydroxide lattice, as it is solely calculated using the LDH (1 1 0) peak. The Ce could still be 'within' the materials' layers where it forms breaks in the LDH phase and causes defects and amorphous structural sections or very small/disperse particles of ceria could decorate the surface of an almost pure LDH phase, or it could be a mixture of both cases.

The *c* parameter, like the *a* parameter, is a unit cell dimension of the LDH lattice calculated from the (0 0 3) and (0 0 6) phase peaks from the PXRD patterns; therefore, a *c* parameter is only measurable and applicable for sections of stacked LDH layers. Like the trend in the *a* parameter, the *c* parameter trend is complicated and there is no obvious correlation; the *c* parameter increases with Ce doping compared to the 35Zn20Ga-LDH sample. The Ce-doped LDHs have *c* parameters in a very similar range to that of 30Zn25Ga- and 25Zn30Ga-LDH, for the Ga series it was observed that the *c* parameter increased with increasing net layer + charge (M^{3+}:M^{2+} ratio) because more anions are required in the interlayer space. The initial increase in *c* parameter with Ce doping could be caused by the Ce cation's increased size (Ce^{3+})

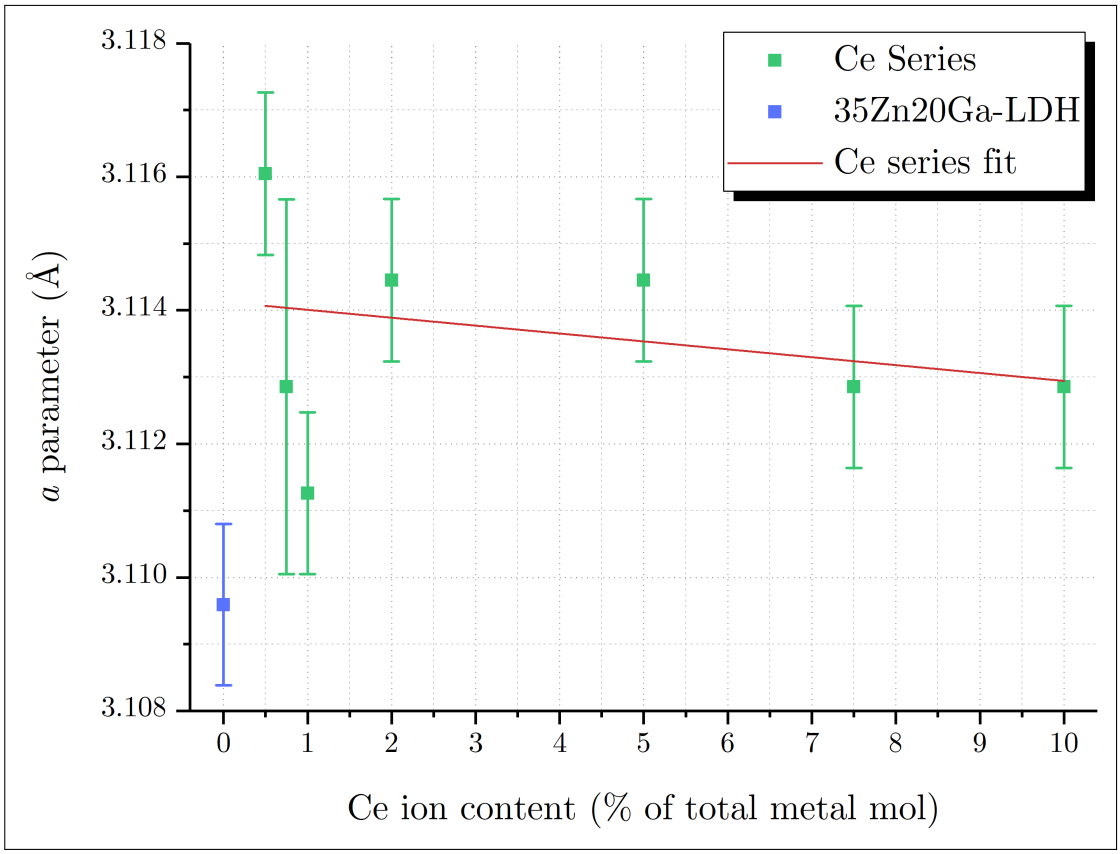


Figure 8.4: The a parameters of the Ce-based AMO-LDH series. Calculated from the PXRD data (Figure 8.1). The red line represents a linear fit where: y = 3.11 - $(1.18\times10^{-4})x$ and the R^2 value = 0.076.

and/or charge (Ce^{4+}) compared to that of Ga^{3+}. However, if Ce continued to occupy LDH lattice positions, a correlation would be expected between the Ce content and the c parameter. Therefore, again this is likely evidence that there is a critical Ce content that can occupy a given mol of LDH lattice before the Ce either forms ceria particles or amorphous, 'LDH-adjacent' defects that have their net charges balanced. Such a theory is more likely than all Ce being in the (3+) oxidation state and inside the layer, causing the lack of c parameter increase; this is because Ce^{3+} in a LDH lattice position would have a large effect on the a parameter.

The FWHM of the PXRD peaks are used for the calculation of particle size in the different dimensions depending on the *hkl* plane of the peak; this is why smaller

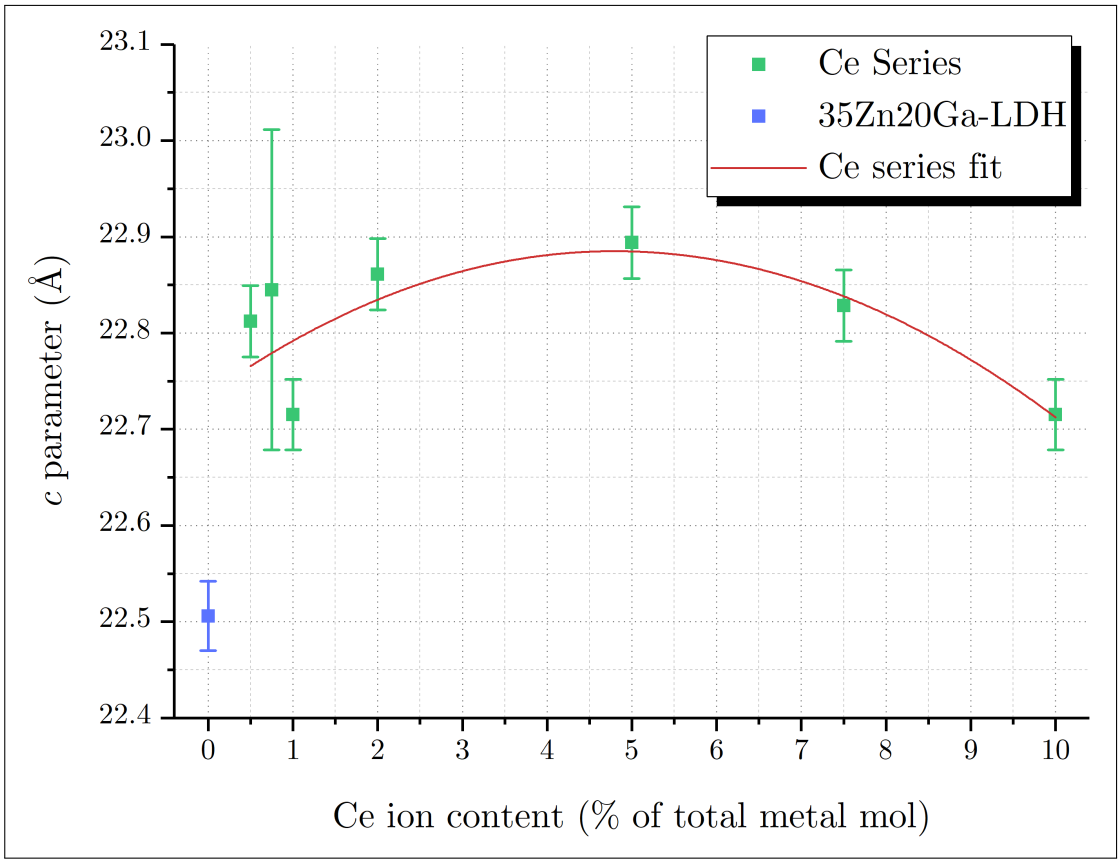


Figure 8.5: The c parameters of the Ce-based AMO-LDH series. Calculated from the PXRD data (Figure 8.1). The red line represents a cubic fit where: y = 22.74 + 0.062x - 0.006x^2 + (1.15×10^{-5})x^3 and the R^2 value = 0.67.

particles give broader peaks, see Section 5.3.1. The three parameters calculated from the Scherrer equation (crystallite thickness, LDH layers per crystallite and plate diameter) all follow trends with plateaus at high Ce content from 18Ga2Ce-LDH onwards, see Figures 8.6, 8.7 and 8.8.

In the case of the crystallite thickness, at low Ce content the degree of LDH exfoliation during the acetone mixing step is likely inversely correlated to the Ce content due to the difference in polarising power of Ga^{3+} and Ce^{3+}; the mean electronic polarisibilities for Ga^{3+} and Ce^{3+} are ≈ 1.5-1.8 and 3.5-4.4 Å^3, respectively. [28]. For the Ga- and Al-LDH series (see Section 7.3.1) the analogous Al samples experienced higher extents of exfoliation; this was theorised to occur because Al^{3+} is more polar-

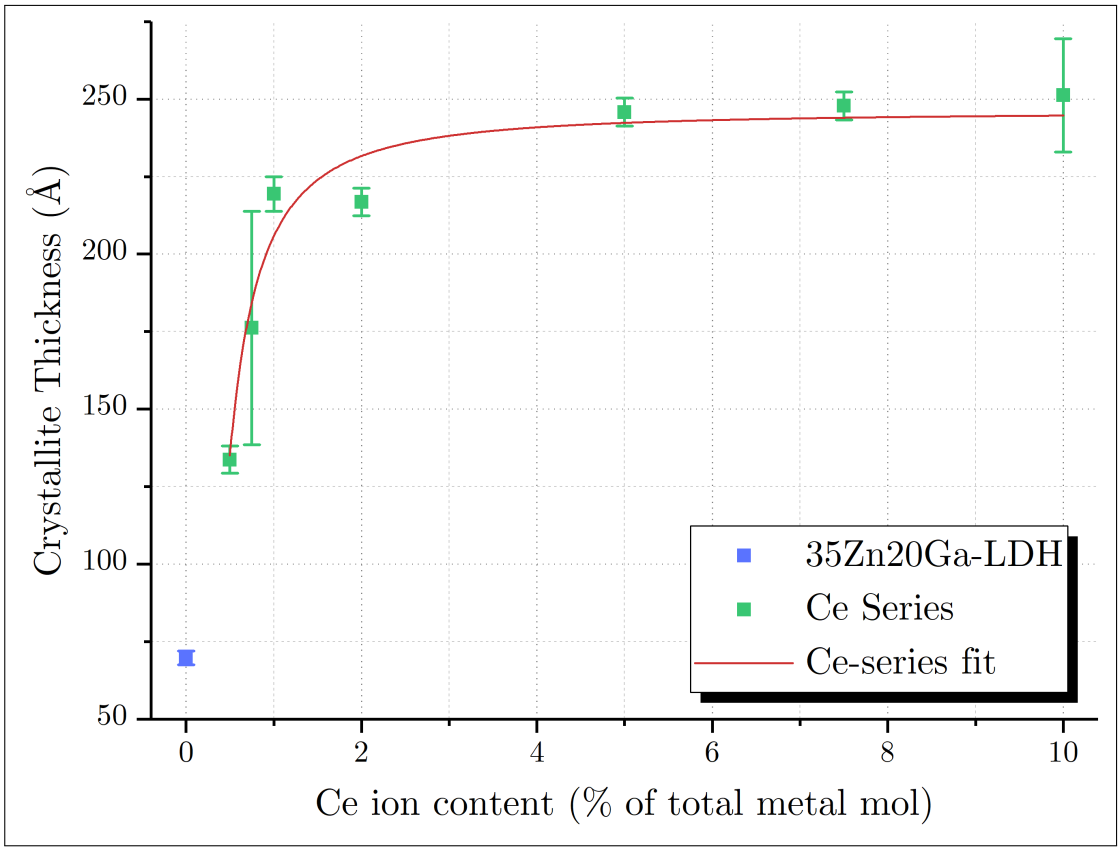


Figure 8.6: The mean crystallite thickness of each AMO-LDH from the Ce-based series. Calculated from the PXRD data (Figure 8.1) using the standardised Scherrer and integration methods used across this thesis. The red line represents a sigmoidal fit where: y = 246 - $\frac{1986}{1+(\frac{x}{0.065})^{1.5}}$ and the R^2 value = 0.92.

ising than Ga^{3+} and would form stronger hydrogen bonds with acetone during the acetone washing step (after the removal of water), increasing the interlayer acetone concentration and, therefore, the extent of exfoliation (this is described in more detail for the Mg series in Section 6.3.2). In this section, it is theorised that replacing Ga^{3+} with Ce^{3+} would decrease the polarising power of the LDH layers, decreasing the extent of exfoliation during the acetone washing step, and subsequently increasing the crystallite thickness. If Ce was assumed to be in the more polarising (4+) oxidation state, the crystallite thickness would still be expected to increase with Ce content because the overall increase in electrostatic charge from Ga^{3+} to Ce^{4+} would increase the interlayer electrostatic attractions, making exfoliation less thermodynamically-

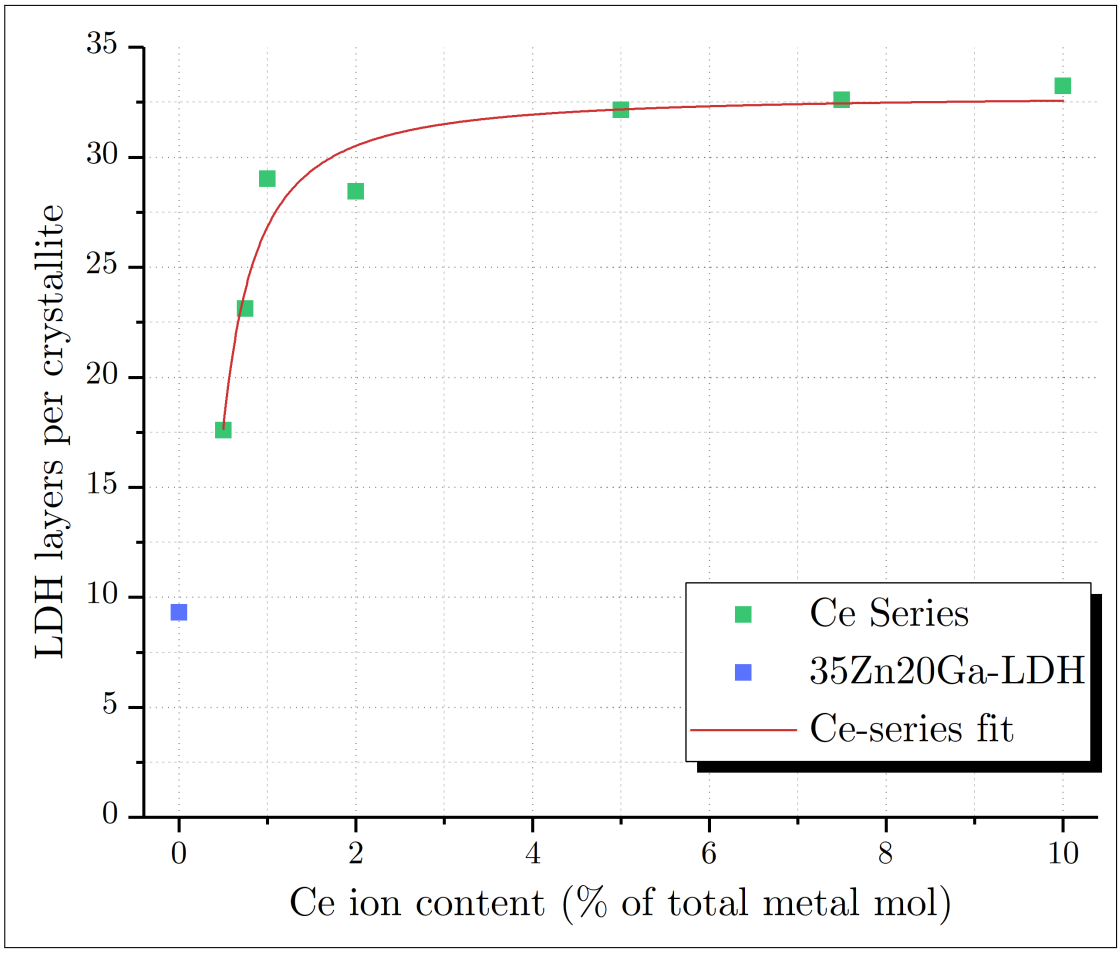


Figure 8.7: The mean no. of LDH layers per crystallite of each AMO-LDH from the Ce-based series. Calculated from the PXRD data (Figure 8.1). The red line represents a sigmoidal fit where: y = 32.8 - $\frac{170}{1+(\frac{x}{0.074})^{1.4}}$ and the R^2 value = 0.90.

favourable.

The lack of increase in crystallite thickness above 1 % total metal mol of Ce indicates Ce is not in the LDH lattice. As brought up before, the excess Ce could be in ceria particles or defects in the LDH layers. Small ceria particles could decorate the LDH particles, not affecting the crystallite thickness and plate diameter. However, the materials were synthesised by a simultaneous co-precipitation of all the metals' nitrates; therefore, because the lack of PXRD peaks indicate any potential ceria particles are much smaller than the LDH particles, it would be expected that these small particles would decorate LDH layers as they were growing, interrupting particle

growth/layer stacking or expanding the c parameter, neither of these scenarios are observed. Therefore, the excess Ce likely occupies an amorphous structure/defect site that does not affect the growth of the LDH particles.

The trend in the number of LDH layers per crystallite, Figure 8.7, mimics the crystallite thickness trend shape, Figure 8.6, because the c parameter is not significantly affected by the Ce content.

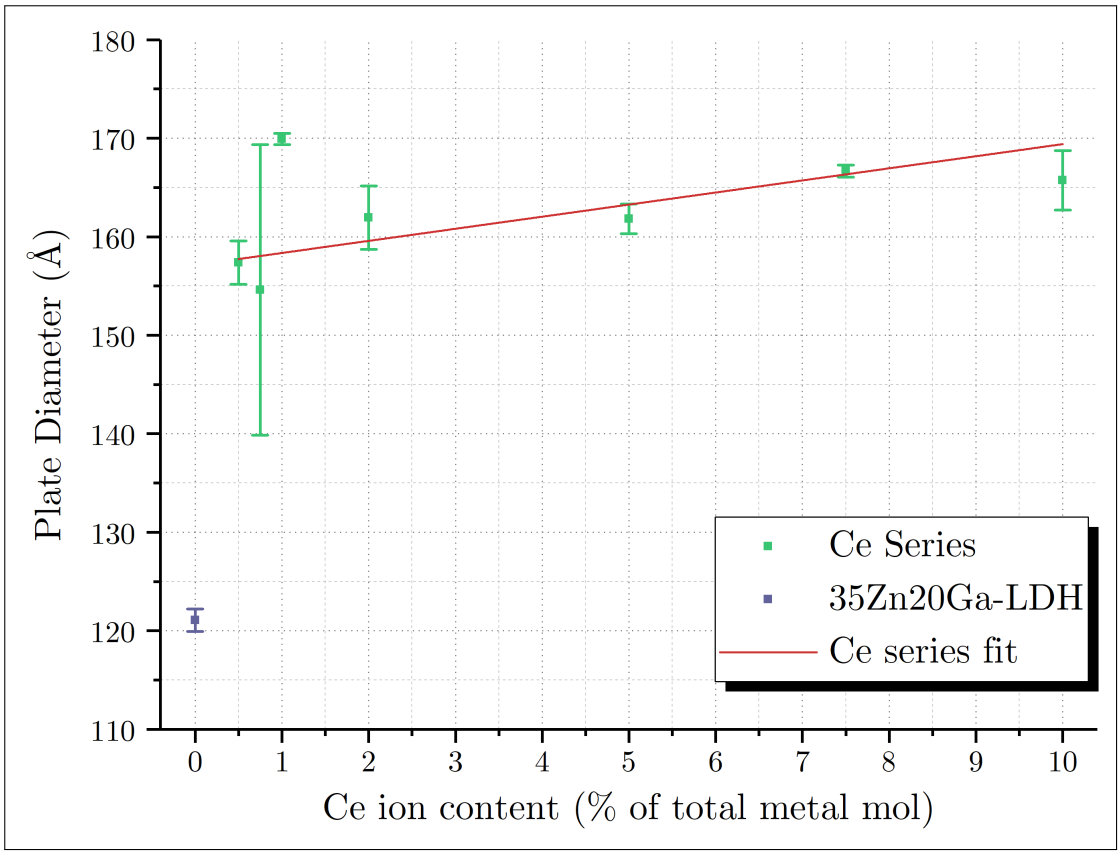


Figure 8.8: The mean plate diameter of each AMO-LDH from the Ce-based series. Calculated from the PXRD data (Figure 8.1) using the standardised Scherrer and integration methods used across this thesis. The red line represents a linear fit where: y = 157 + 1.23x and the R^2 value = 0.87.

A critical/maximum Ce content, that can occupy a given amount of LDH lattice, again could be the cause of the absence of a correlation between the particle plate diameter and the Ce content (beyond 1 % metal mol Ce). As with the situation for the crystallite thickness the excess Ce, that does not reside in a LDH lattice position, has

no observable effect on the growth of the LDH particles. Below the proposed critical Ce content the particle diameter does fluctuate but this could be due to random error in measurement due to the large error bars; therefore, the critical Ce content may not be specifically relevant and it could be proposed that the doping of any content of Ce does not have a large impact on the plate diameter.

The PXRD data for the Ce series indicates that a small amount of Ce can occupy LDH lattice cation positions but when Ce accounts for above $\approx$ 1 - 2 % mol of the total metal in the sample it has no further effect on the LDH unit cell or how the LDH particles grows. The Ce still remains within the sample as shown by the ICP-MS results of both the as-prepared LDHs and calcined LDOs (see Section 8.3). The FWHM of the LDH peaks were not substantially affected above this critical Ce content either, indicating that the PXRD signal loss with increasing Ce content, observed in Figure 8.1, was caused by a reducing amount of LDH phase; which makes sense if Ce cannot replace the Ga^{3+} positions that are being emptied up the series, a LDH needs a minimum of $\approx$ 20 % mol of its total metal ions to be M^{x+}. No other phases or structures form particles visible in the PXRD patterns and, subsequently, it is hard to theorise how amorphous or defective Ce-containing structures form in-situ alongside the LDH particles; especially when the LDH particle sizes in all dimensions remains relatively constant from 18Ga2Ce- to 10Ga10Ce-LDH. Therefore, further investigation was required via EDX and XAS to determine more about the position and environment of the Ce within the samples.

Additionally, it is posited that the cause(s) for this 'critical' Ce content per mol_{LDH} arises from Ce^{x+} cations putting steric strain on the local LDH structure due to their large size and/or from Ce^{4+} increasing the LDH layers' net + charge. The Ce size effect could cause different interatomic distances in the LDH layer to decrease or increase in the local structure around Ce, which is not energetically favourable

because it can cause increased interactions between ions of the same charge and it can also limit the geometries of certain bonds, not allowing orbitals to overlap in the most energetically favourable way. Similarly, it is not energetically favourable to have high charge densities due to repulsive electrostatic attractions between charges of the same polarity; increasing the average oxidation state of the metals in an LDH would cause more +/+ interactions within the layer and also more -/- interactions in the interlayer space due to the forced increase in counterbalance anions to keep the overall charge of the system balanced. Both these effects could be the reason why there is a thermodynamic limit on how many Ce cations can occupy LDH sites before other phases start to form where Ce can be coordinated in a more energetically favourable manner.

In summary the only visible PXRD patterns for the Ce-doped series are those of $3R_1$ and $3R_2$ LDH polytypes. The LDH PXRD signal intensity, but not the FWHM, decreases with increasing Ce content. The a/c parameter and plate diameter trends are relatively flat throughout the series but fluctuate far more below 2 % metal mol Ce. The crystallite thickness increases drastically with Ce content initially as expected due to the decreasing polarising power of the average M^{3+} cation in the LDH layers causing a lower interlayer acetone concentration during synthesis and, therefore, a lower extent exfoliation. Importantly, this trend plateaus around > 1-2 % metal mol Ce, suggesting that additional Ce added during coprecipitation no longer occupies a LDH lattice position; this was denoted as a 'critical' Ce content and that Ce in excess of this concentration occupied disperse, defective and/or amorphous phases.

8.4.2 TEM analysis of the Ce LDH series

In this section TEM images of the as-prepared 35Zn20Ga-, 19.25Ga0.75Ga- and 12.5Ga7.5Ce-LDH samples are compared. The images feature zoom levels from 2 - 1000 nm and most were collected using a HAADF-STEM microscope.

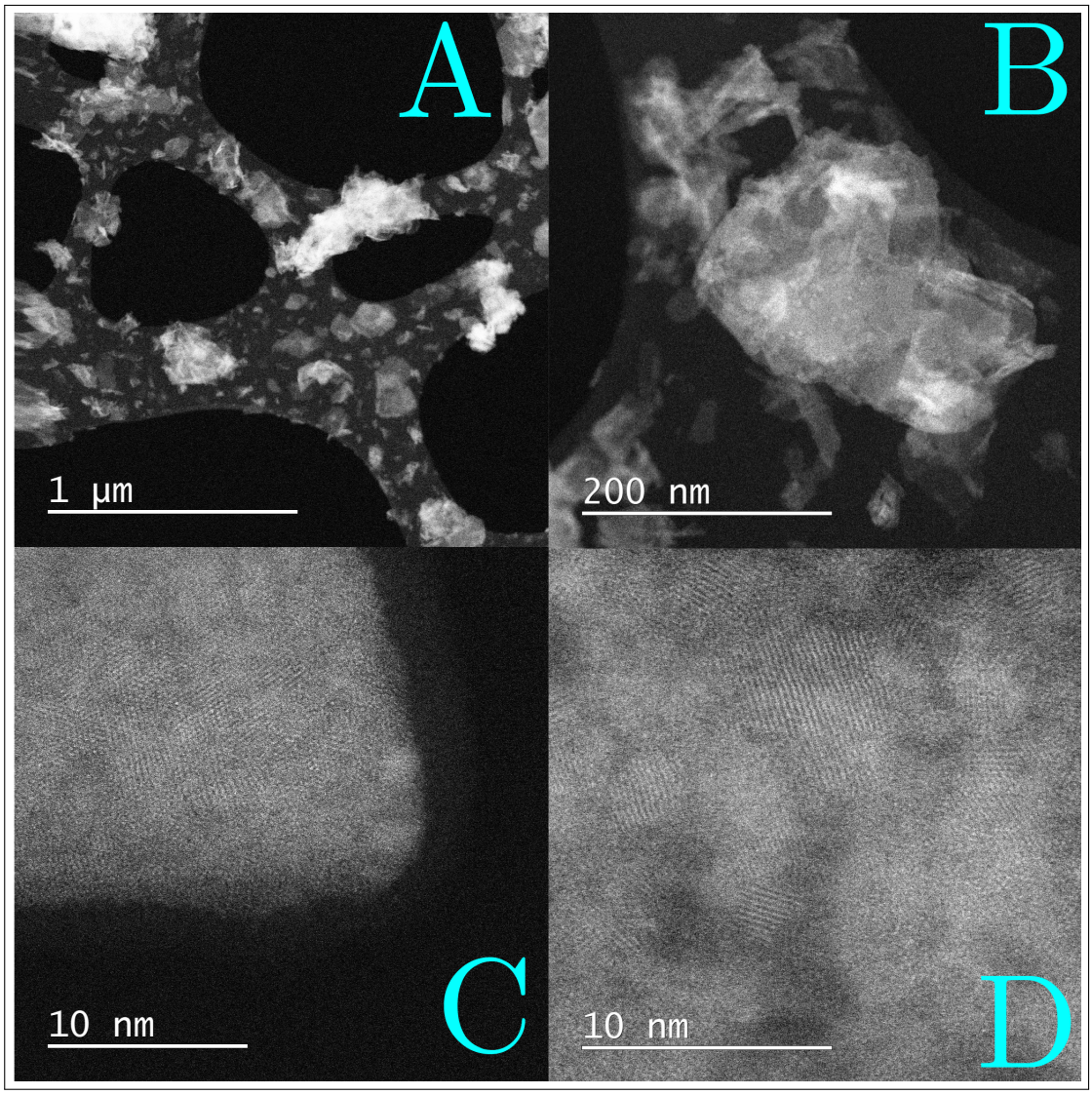


Figure 8.9: Dark-field TEM images of 35Zn20Ga-LDH.

Figure 8.9.A shows a low zoom of 35Zn20Ga-LDH heterogeneously dispersed on a holey carbon TEM grid, the pure black parts of the image are holes in the grid (as is the case for all images in this section); the brighter the area of an image, the higher the amount of sample that has aggregated to that part of the grid. It can be seen that dispersing, not dissolving, 35Zn20Ga-LDH in acetone before applying the solution to the TEM grid did lead to an inhomogeneity in the aggregation of the crystallites. This is the case for all samples in this section too, however it was preferable to introducing the samples to a high water content; because this method

minimised the re-stacking of layers and the LDH memory effect (in the case of the calcined samples). Nonetheless, some crystallites were well dispersed on the grid and could give good resolution images for qualitative analysis.

Figure 8.9.B shows a typical, 200-400 nm crystalline, plate-like section of the sample. Figures 8.9.C and 8.9.D demonstrated that the 35Zn20Ga-LDH sample is highly crystalline and that '3D nano-crystallinity' was present because separate particles/phases have different orientations. [281] 35Zn20Ga-LDH has a crystallite thickness and plate diameter of 6.9 and 12.1 nm, respectively, as per the PXRD Scherrer analysis (see Section 7.3.1); these are roughly the dimensions visible for the different particles/phases in Figure 8.9.D. The crystallite thickness and plate diameters from all LDH samples across this work range from $\approx$ 2.5 - 25 nm and 8 - 18 nm (including the Mg AMO-LDH series), respectively; therefore, similar 3D nano-crystallinity was expected for these other LDH samples too.

Figures 8.10.A, 8.10.B, 8.10.C and 8.10.D all show large plate-like crystallites, about 300-700 nm in length, for 19.25Ga0.75Ce-LDH. These plates are similar to that of the non-doped Ce LDH shown in Figure 8.9.B; however, more overlap, folds crimps and defects (with high image intensity) seem to be visible compared to Figure 8.9.B. This is likely due to the small sample size of the images taken for 35Zn20Ga-LDH but Ce could also be introducing defects or new phases to the layered structure.

In Figures 8.10.E and 8.10.F, 19.25Ga0.75Ce-LDH exhibits mostly areas of crystalline material but there also appear to be more amorphous sections. Notably, some phases or sections of visibly crystalline material appear to be smaller in dimension than the crystallite thickness and plate diameter measured by PXRD, which is 17.6 and 15.5 nm respectively. This was also the case in Figures 8.9.C and 8.9.D for 35Zn20Ga-LDH but the degree of amorphous sections relative to the calculated Scherrer dimensions does seem to be higher for 19.25Ga0.75Ce; perhaps from Ce inclusion

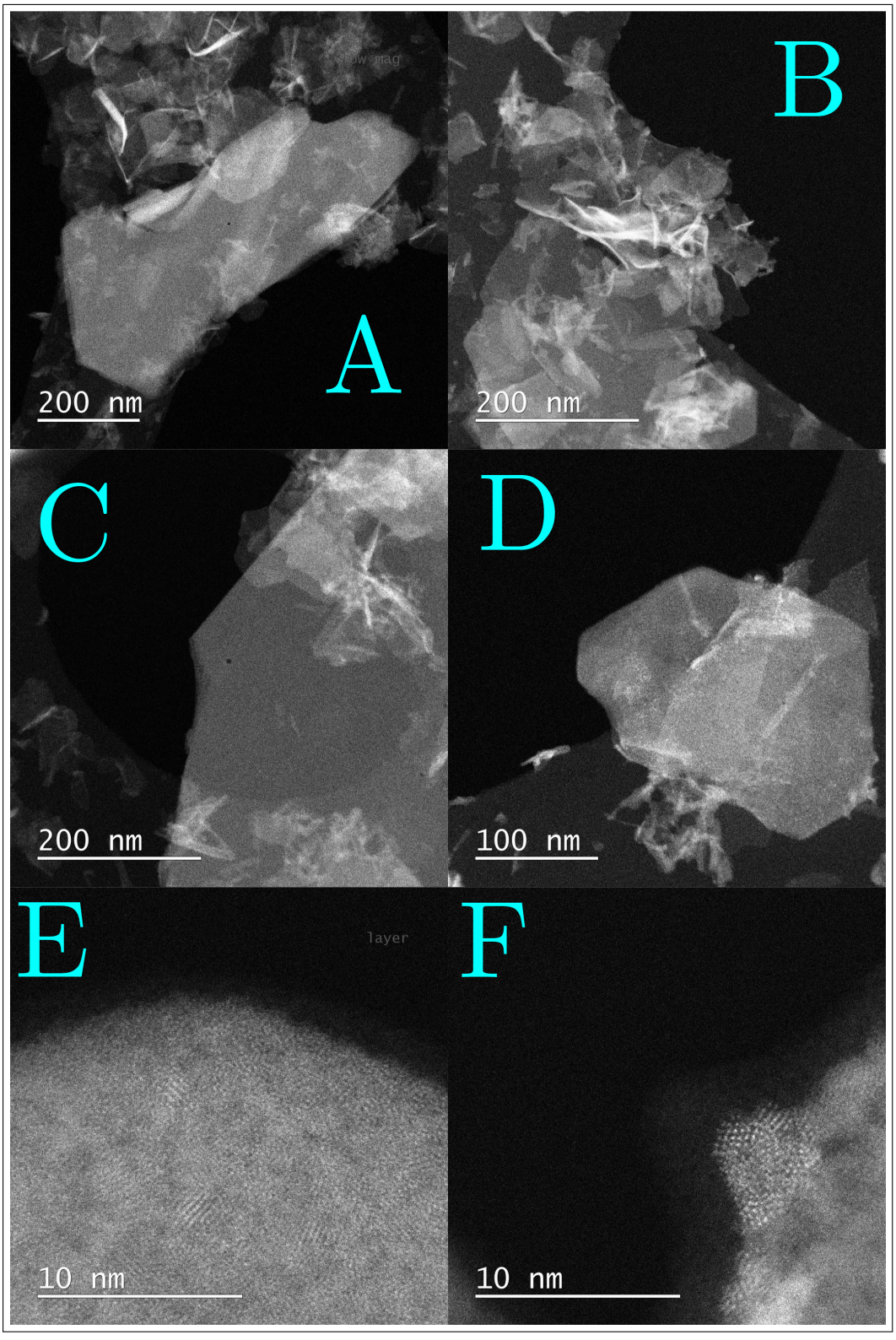


Figure 8.10: Dark-field TEM images of 19.25Ga0.75Ce-LDH.

in the material preventing high-order layer stacking and growth.

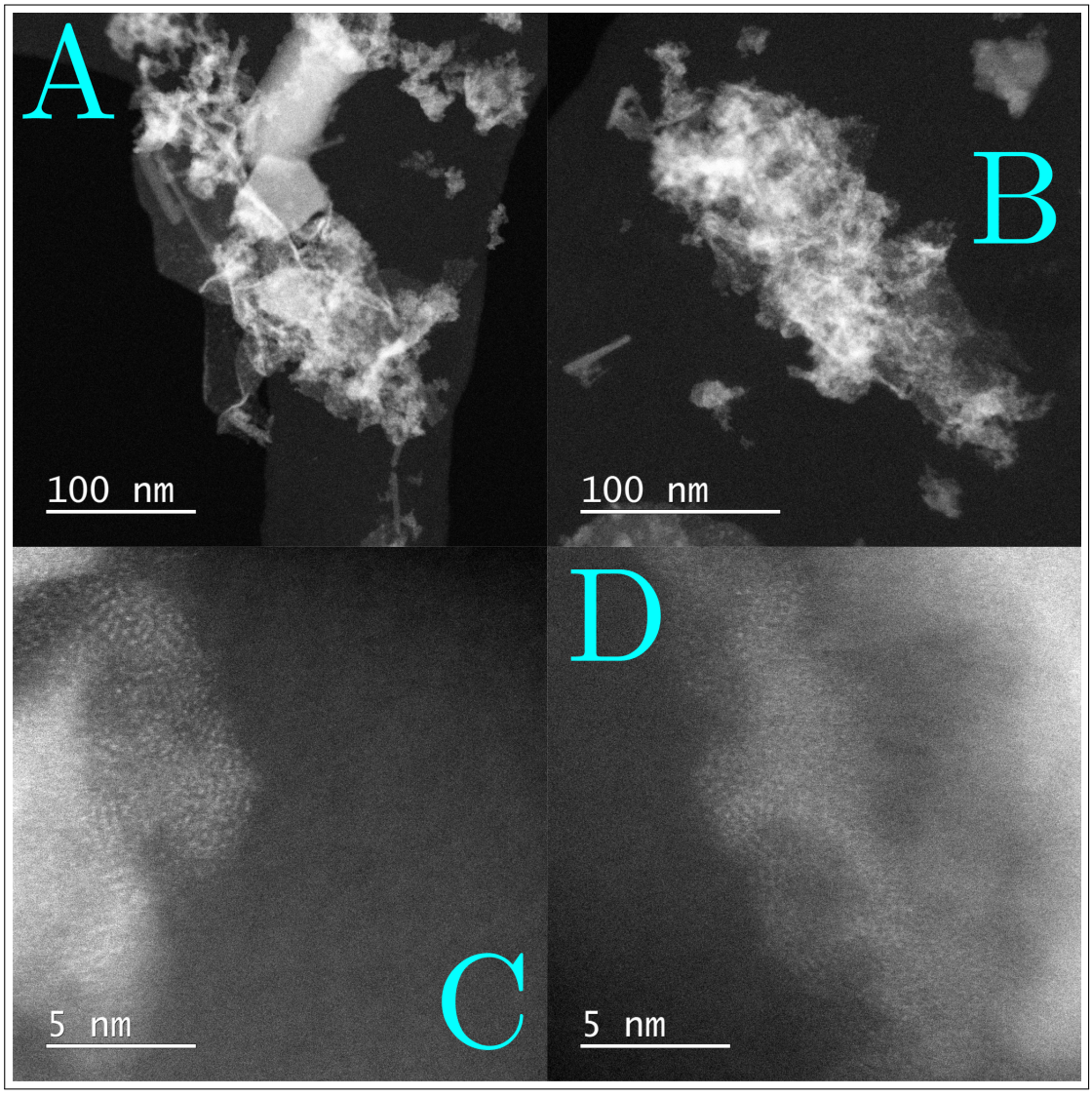


Figure 8.11: Dark-field TEM images of 12.5Ga7.5Ce-LDH.

Figures 8.11.A and 8.11.B show 12.5Ga7.5Ce-LDH has a much less ordered structure than either 35Zn20Ga- or 19.25Ga0.75Ce-LDH; only partial plate-like morphology is visible, 12.5Ga7.5Ce-LDH appears to have a lot of layer overlap and folds. Whilst Figures 8.11.C and 8.11.C are close-ups of more plate-like sections of morphology; there are still crystalline areas but it definitely appears more areas are amorphous than for 19.25Ga0.75Ce-LDH.

TEM demonstrates an increase in Ce doping of the LDH layers appeared to cause a decrease in crystallinity.

8.4.3 EDX analysis of the Ce LDH series

EDX analysis was performed at a different facility to the TEM analysis using a high-sensitivity silicon drift detector X-ray spectrometer; it allowed the elemental mapping of the 35Zn20Ga-, 19.25Ga0.75Ce- and 12.5Ga7.5Ce-LDH samples.

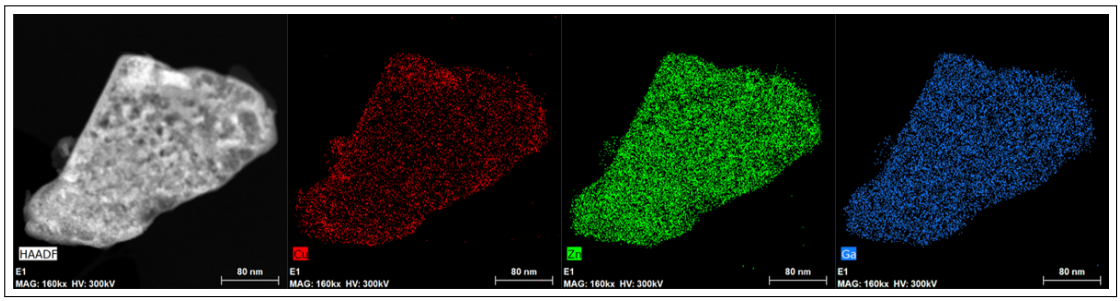


Figure 8.12: EDX imaging analysis of 35Zn20Ga-LDH.

All EDX images, in Figures 8.12, 8.13 and 8.14, show that all elements are well dispersed throughout the samples; Cu, Zn, Ga and O are especially homogeneously dispersed. Ce is also homogeneously dispersed in Figure 8.13, as expected it is notable that there is far less Ce present in 19.25Ga0.75-LDH's EDX image compared to 12.5Ga7.5Ce-LDHs'.

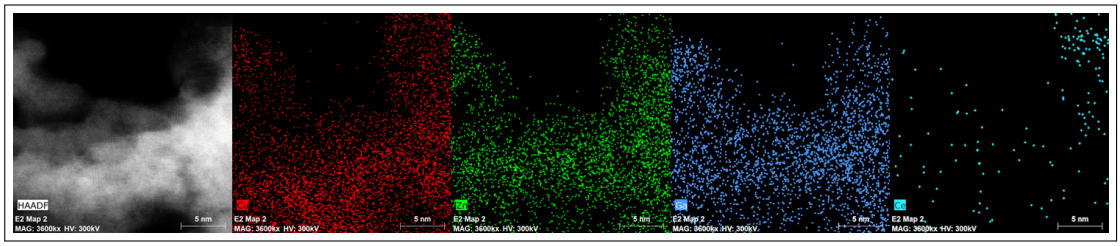


Figure 8.13: EDX imaging analysis of 19.25Ga0.75Ce-LDH.

The Ce mapping in Figure 8.14 displays a very homogeneous Ce dispersion for 12.5Ga7.5Ce-LDH. It is very hard to make conclusions using only a few qualitative images but in all cases the elemental dispersion is effectively homogeneous wherever

the HAADF detector shows sample; this agrees with literature observations of high elemental dispersion in as-prepared LDHs (see Section 3.7).

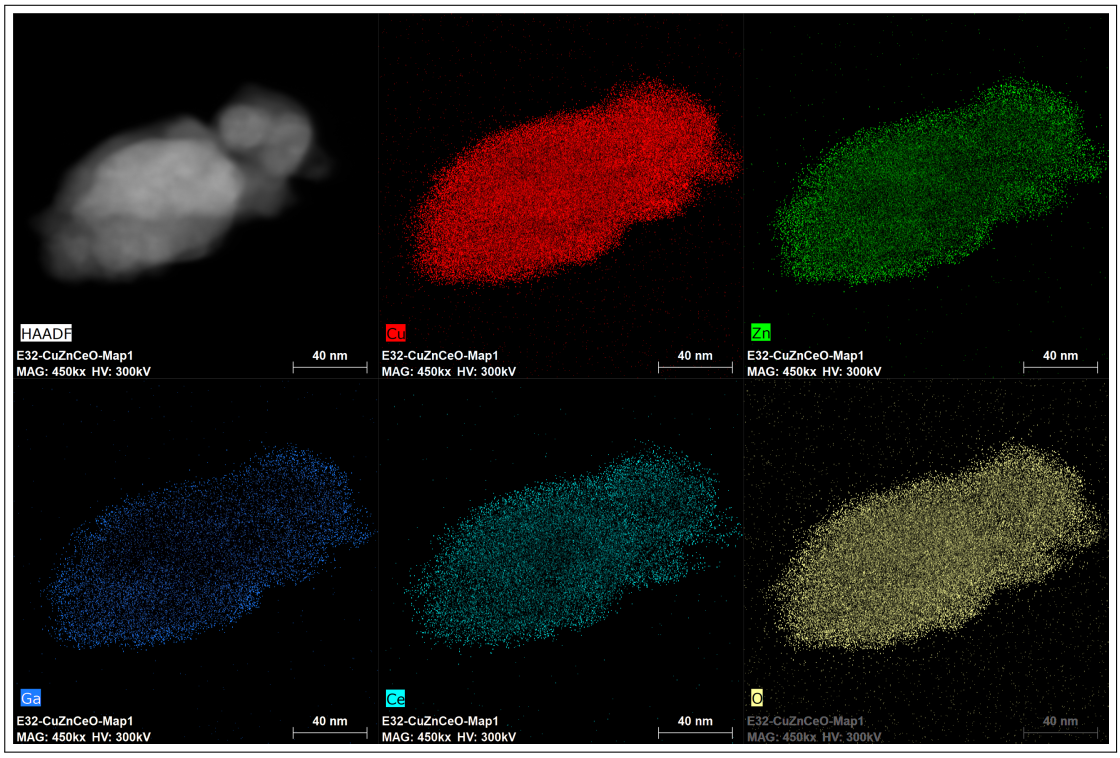


Figure 8.14: EDX imaging analysis of 12.5Ga7.5Ce-LDH.

Overall, Ce is very well dispersed in each particle investigated with EDX mapping.

8.4.4 XPS analysis of the Ce LDH series

XPS analysis was performed for 35Zn20Ga-LDH and also two Ce-doped AMO-LDHs for insights into if the Ce-doping affected the oxidation states of the metals on the surface of the LDH material. Figures 8.15, 8.16, 8.17 and 8.18 show the XPS spectra of 35Zn20Ga-, 19.25Ga0.75Ce- and 12.5Ga7.5Ce-LDH; the peaks were fitted with standard Shirley backgrounds and the resultant envelopes were also plotted.

Table 8.3 summarises the Zn 2p peak data from the samples' XPS spectra. As discussed in Section 5.10.1, a p orbital would be expected to give a doublet XPS peak where the ratios between the higher B.E. signal to lower B.E. signal would be 1 to 2,

Table 8.3: XPS Zn binding energy data for 35Zn20Ga-, 19.25Ga0.75Ce- and 12.5Ga7.5Ce-LDH. Data from Figures 8.15, 8.16 and 8.17.

Sample	Zn $2p_{3/2}$		Zn $2p_{1/2}$	
	B.E. peak position (eV)	% of total peak area	B.E. peak position (eV)	% of total peak area
35Zn20Ga-LDH	1021.2	66.9	1044.2	33.1
19.25Ga0.75Ce-LDH	1021.5	64.8	1044.6	35.2
12.5Ga7.5Ce-LDH	1021.6	68.7	1044.6	31.3

respectively. This is what is observed when the percentages of total peak areas are analysed, for the Zn 2p orbital in Table 8.3 and also for the Ga 2p orbital in Table 8.4.

Table 8.4: XPS Ga binding energy data for 35Zn20Ga-, 19.25Ga0.75Ce- and 12.5Ga7.5Ce-LDH. Data from Figures 8.15, 8.16 and 8.17.

Sample	Ga $2p_{3/2}$		Ga $2p_{1/2}$	
	B.E. peak position (eV)	% of total peak area	B.E. peak position (eV)	% of total peak area
35Zn20Ga-LDH	1117.2	67.6	1144.1	32.4
19.25Ga0.75Ce-LDH	1117.5	68.74	1144.3	31.3
12.5Ga7.5Ce-LDH	1115.0	66.4	1141.8	33.7

Unfortunately for both Ga and Zn, the difference in B.E. energy between 2p orbitals for different oxidation states is very hard to distinguish due to the other factors that affect binding energy (such as co-ordination environment); this problem also exists for the 2s orbital peaks. [282–284] Therefore, it is hard to distinguish Zn^0 from Zn^{2+} or the less common Ga^+ from Ga^{3+} using XPS. Modified Auger parameters of the $L_3M_{45}M_{45}$ peaks for transition metals have been proposed for tracking changes to oxidation states. [283] Bourque et al. reviewed Auger XPS analysis of Ga^0, Ga^+, Ga^{2+} and Ga^{3+} compounds but only observed a 2 and 6 eV range across all oxidation states in the values of the $2p_{3/2}$ and $L_3M_{45}M_{45}$ peaks, respectively; which is too small a margin to assign accurately to the asymmetric Ga auger peaks in this work. [285] For Zn there is a similar problem and the B.E. of Zn 2p in XPS can be affected by the conductivity of support oxides and the size of the constituent particles being on

a nm scale. [283] In addition, the use of Auger parameters was proven inaccurate for several transition metals, therefore the possible role of Zn^0 in MSR was investigated via XAS; see Section 8.5.5. [286] The position of the peak maxima and symmetrical nature of peak shapes in XPS spectra of Zn and Ga evidence that they are in (2+) and (3+) oxidation states, respectively. This was expected for the LDHs precursors before calcination and reduction.

Table 8.5: XPS Cu binding energy data for 35Zn20Ga-, 19.25Ga0.75Ce- and 12.5Ga7.5Ce-LDH. Data from Figures 8.15, 8.16 and 8.17.

Sample	Cu $2p_{3/2}$		Cu $2p_{1/2}$	
	B.E. peak position (eV)	% of total peak area	B.E. peak position (eV)	% of total peak area
35Zn20Ga-LDH	934.1	39.6	953.9	19.6
19.25Ga0.75Ce-LDH	934.2	42.6	954.1	18.9
12.5Ga7.5Ce-LDH	934.3	39.8	954.0	19.7

The XPS spectra for Cu 2p differs from that of Zn and Ga due to the presence of 'satellite peaks'. These peaks are caused by 'shake-up', this is where some of the kinetic energy from a photoelectron leaving the ion is used to excite other electrons in the outer d or f orbitals. Shake-up peaks appear at a higher B.E. compared to the original transition peak because the X-ray source is a constant energy i.e the higher the kinetic energy of the photoelectron, the lower the required ionisation energy. [287] This is common for paramagnetic ions and is extensively, qualitatively studied for Cu in literature; Cu^{2+} gives intense satellite peaks, Cu^+ often only gives satellite peaks that are barely visible above the background noise (they are due to the presence of some Cu^{2+}) and Cu^0 has no satellite peaks. [283] Unfortunately it is very complicated to quantify all 3 oxidation states (Cu^0, Cu^+ and Cu^{2+}) from one spectrum, this is because for calculating the Cu^{2+}:Cu^+ or Cu^{2+}:Cu^0 ratio for a given sample involves the assumption that both the Cu^+ or Cu^0 species gives no satellite peaks. [283,288] A reference sample with only Cu^{2+} content, such as $Cu(OH)_2$, is also required for such calculations.

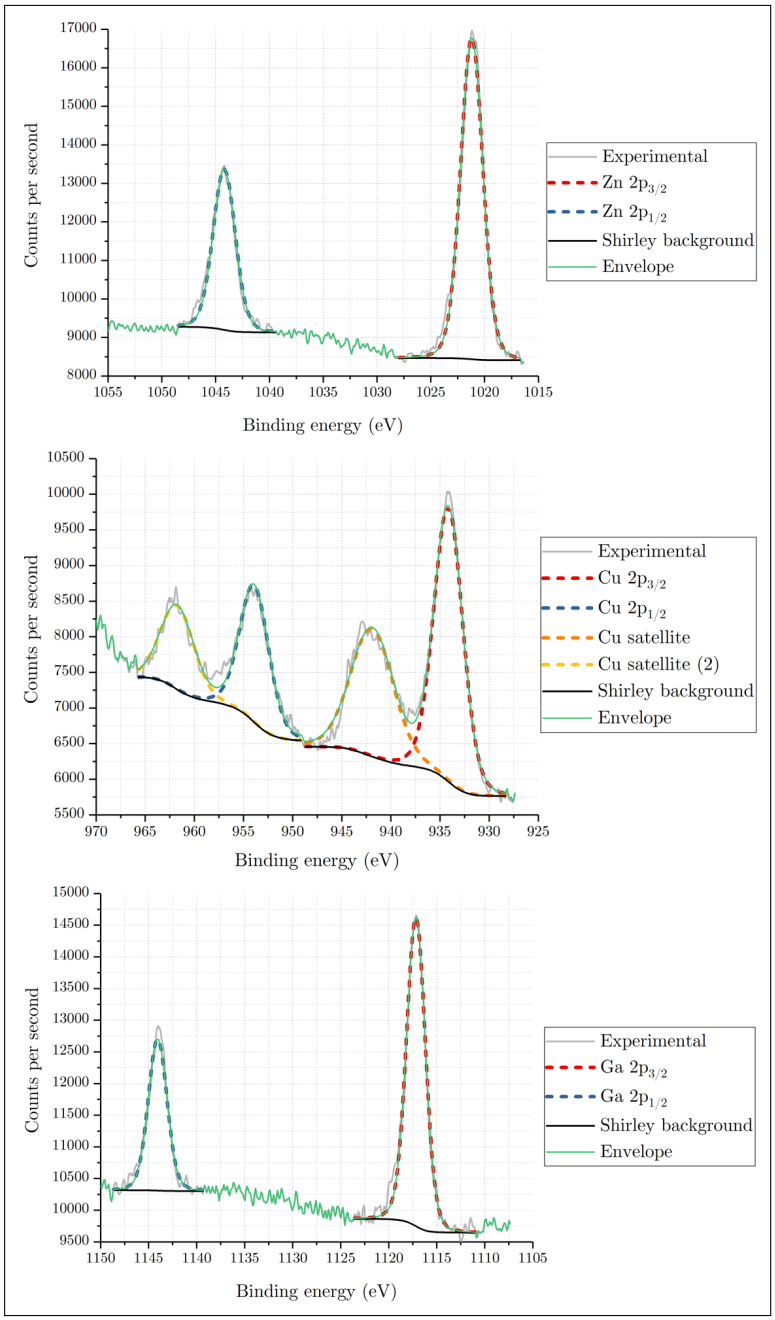


Figure 8.15: XPS spectra of 35Zn20Ga-LDH. Top) Zn B.E. Middle) Cu B.E. Bottom) Ga B.E.

Qualitatively Figures 8.15, 8.16 and 8.17 appear to show a high Cu^{2+} content due to the strong satellite peaks; this was expected for the as-prepared LDHs because they had not been reduced. None of the Cu $2p_{3/2}$ peaks have a non-satellite shoulder which is indicative of having a high concentration of one oxidation state present. [283]

As expected no Cu^0 or Cu^+ was observed for the LDHs; their presence under MSR conditions would have to be investigated by in-situ XPS or XAS experiments in future work.

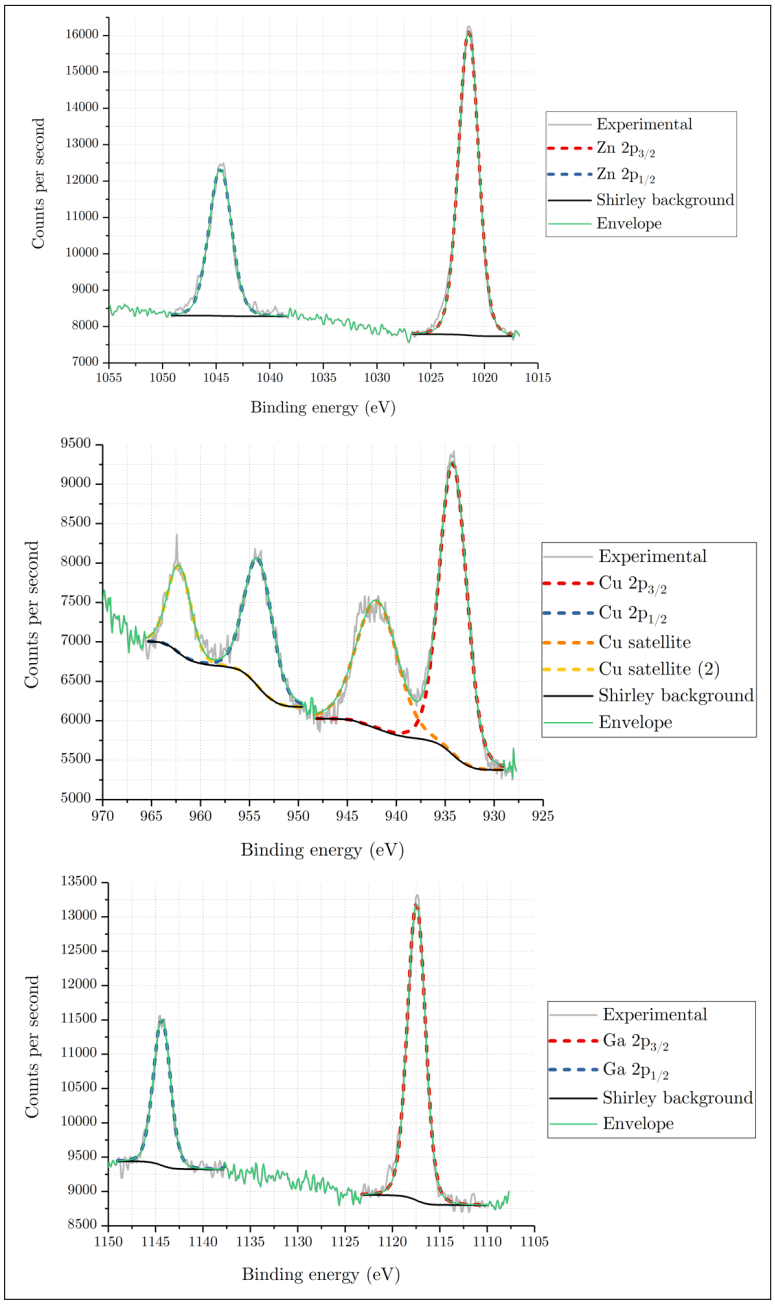


Figure 8.16: XPS spectra of 19.25Ga0.75Ce-LDH. Top) Zn B.E. Middle) Cu B.E. Bottom) Ga B.E.

The Ce 3d peaks for 19.25Ga0.75Ce-LDH were not quantifiable due to the signal

to noise ratio; this likely occurred due to the low concentration of Ce in the sample correlating to a low amount of Ce electrons and, therefore, low XPS counts per second.

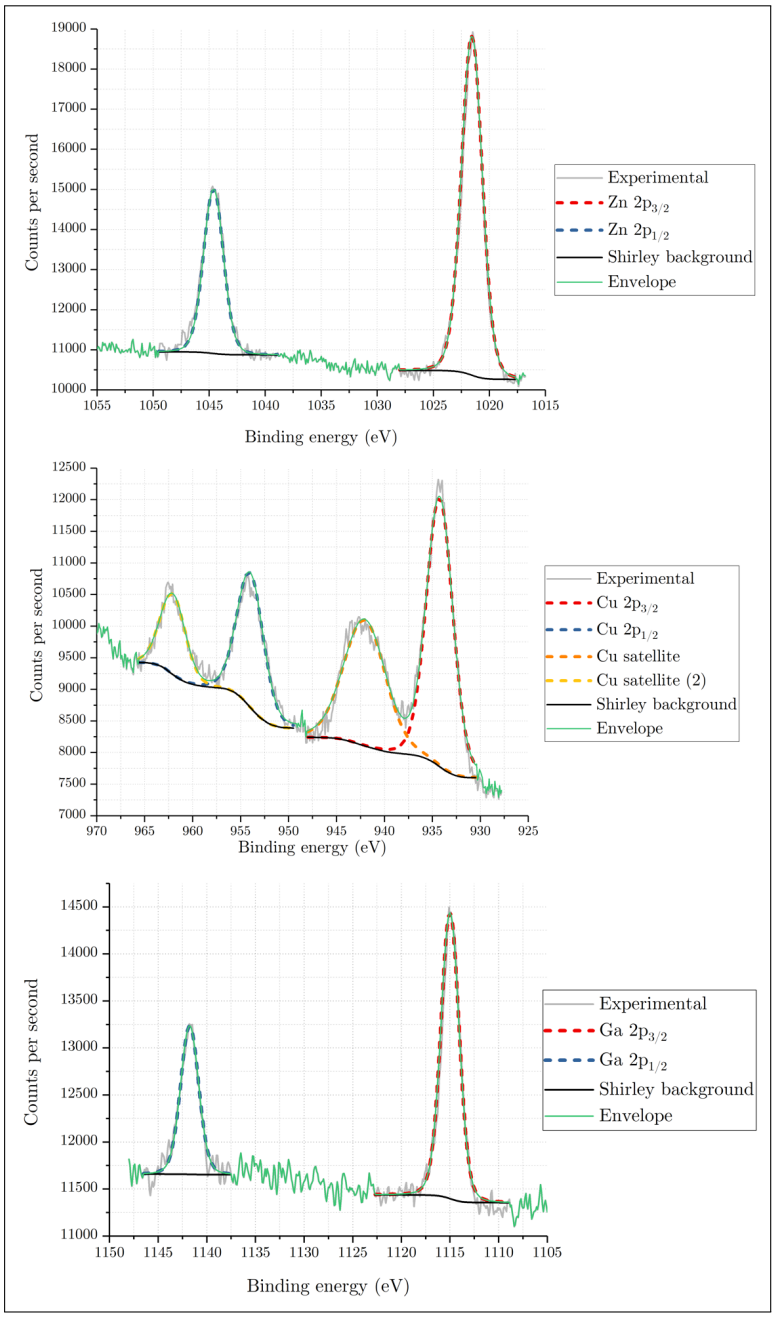


Figure 8.17: XPS spectra of 12.5Ga7.5Ce-LDH. Top) Zn B.E. Middle) Cu B.E. Bottom) Ga B.E.

Figure 8.18 displays the Ce 3d XPS peaks for 12.5Ga7.5Ce-LDH, such peaks have been analysed in literature and a mixture of both Ce^{3+} and Ce^{4+} give a complicated

spectrum. Initial work by Burroughs et al. used u and v notation for the $3d_{3/2}$ and $3d_{5/2}$ XPS peaks, respectively. [289] Later Wang et al. assigned the Ce 3d peaks to the 'final states' (the electronic configurations after ionisation) as follows: u'''/v''' as the doublet for the Ce^{4+} final state; u''/v'' as the doublet for hybridised Ce^{4+} $3d^9 4f^1$ / O $2p^5$; u'/v' as the doublet for the Ce^{3+} final state; u/v as the doublet for hybridised Ce^{4+} $3d^9 4f^2$ / O $2p^4$; and u^0/v^0 as the doublet for hybridised Ce^{3+} $3d^9 4f^1$ / O $2p^6$. [290]

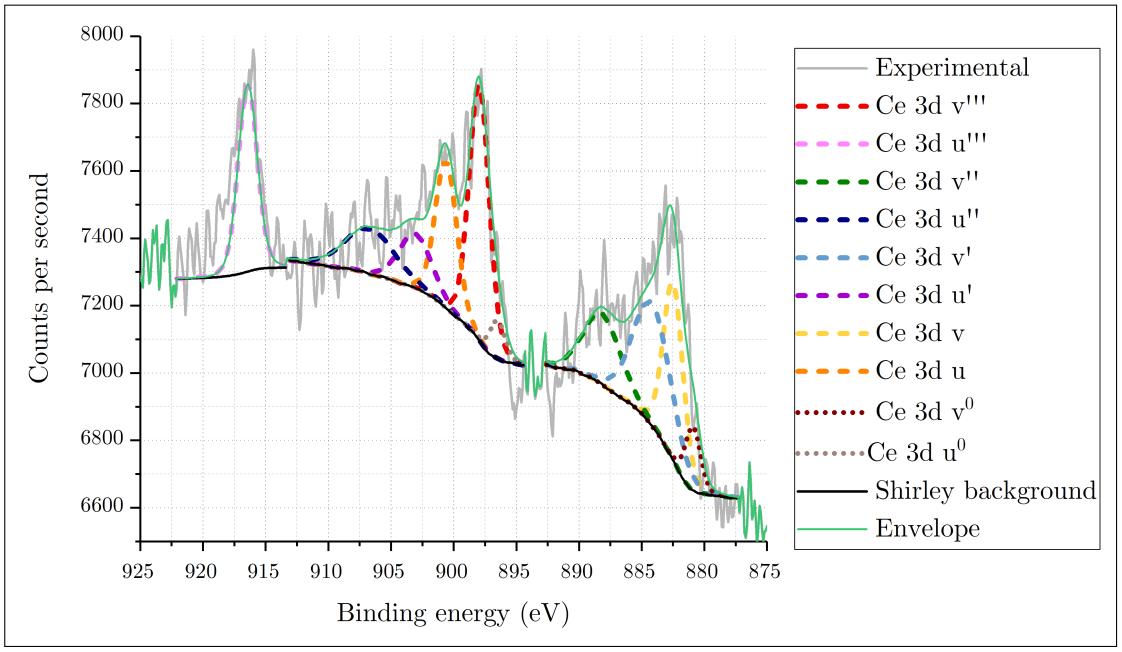


Figure 8.18: XPS spectrum of Ce binding energies for 12.5Ga7.5Ce-LDH.

Jaffari et al. used an equation to calculate Ce^{3+} content from the 3d XPS data. [291]. A version of that equation was applied for 12.5Ga7.5Ce-LDH's XPS 3d data (Table 8.6) and is shown below:

$$\frac{Ce^{3+}}{total\ Ce} = \frac{u^0+u'+v^0+v'}{Total\ Ce\ peak\ area} \times 100 = \frac{837.81}{837.81+2726.07} \times 100 = 23.5\ \%$$

Therefore, it is estimated that 23.5 % of Ce, in as-prepared 12.5Ga7.5Ce-LDH, is in the Ce^{3+} oxidation state (the remainder is Ce^{4+}). It should be noted that Kumar et al. have estimated, via models backed by experiments, that the measured amount

Table 8.6: This table displays the assignment and integration of the 12.5Ga7.5Ce-LDH Ce 3d XPS peaks (from Figure 8.18).

XPS peak (Ce 3d)	B.E. peak position (eV)	Peak area (% of total peak area)
v'''	898.0	18.3
u'''	916.4	12.7
v''	884.2	16.4
u''	906.7	7.9
v'	888.2	9.3
u'	903.0	6.2
v	882.5	12.5
u	900.6	11.2
v^0	880.9	3.4
u^0	896.5	2.1

of Ce^{3+} can be increased by a factor of 1.10 - 1.15 due to X-ray radiation-induced reduction during XPS analysis; therefore, the calculated Ce^{3+} % for 12.5Ga7.5Ce-LDH may be slightly inflated compared to the true as-prepared value. [292]

8.4.5 XAS analysis and DFT modelling of Ce-doped LDHs

Ce L_3 edge XAS analysis was performed for both 19.25Ga0.75Ce- and 12.5Ga7.5Ce-LDH. Unfortunately, the Ce content in 19.25Ga0.75Ce-LDH did not provide a strong enough signal for modelling and analysis. A single-electron excitation transition cannot explain Ce L_3 edge XANES spectra. [293] Both Ce^{3+} and Ce^{4+} oxidation states were also found to contribute to the XANES spectra. [294] In Section 8.4.4 it was calculated from XPS data that 12.5Ga7.5Ce-LDH had a $Ce^{3+}/(Ce^{3+} + Ce^{4+})$ content of $\approx$ 23.5 %.

Gaussian fittings of the 12.5Ga7.5Ce-LDH XANES spectrum were performed following the methods of Fernandes et al. and Shanin et al. (see Figure 8.19 and Table 8.7). [294,295] The XANES spectrum of CeO_2 was shifted to a higher energy than that of the experimental spectrum for 12.5Ga7.5Ce-LDH, this indicates that Ce in CeO_2 is in a higher oxidation state because a change in the electronic configuration changes

what electron transitions are available upon absorption of X-Rays. [296,297] Soldatov et al. found that the Ce L_3 XANES spectrum for CeO_2 electrons could be excited to mixtures of O anion 2p orbitals and Ce 4f/5d orbitals. [298] Figure 8.19 shows the experimental XANES spectrum for 12.5Ga7.5Ce-LDH fitted with four Gaussian peaks (a, b, c and d) which represent the transitions listed in Table 8.7. [294,295] The $2p_{3/2} \longrightarrow$ 4f Gaussian peak, at $\approx$ 5721 eV (d), is forbidden by dipole selection rules; as a result it often has low intensity but adds a pre-edge shoulder. [295] The Gaussian peak, at $\approx$ 5727 eV (c), was found to correspond to the fraction of Ce^{3+}. [294,295]

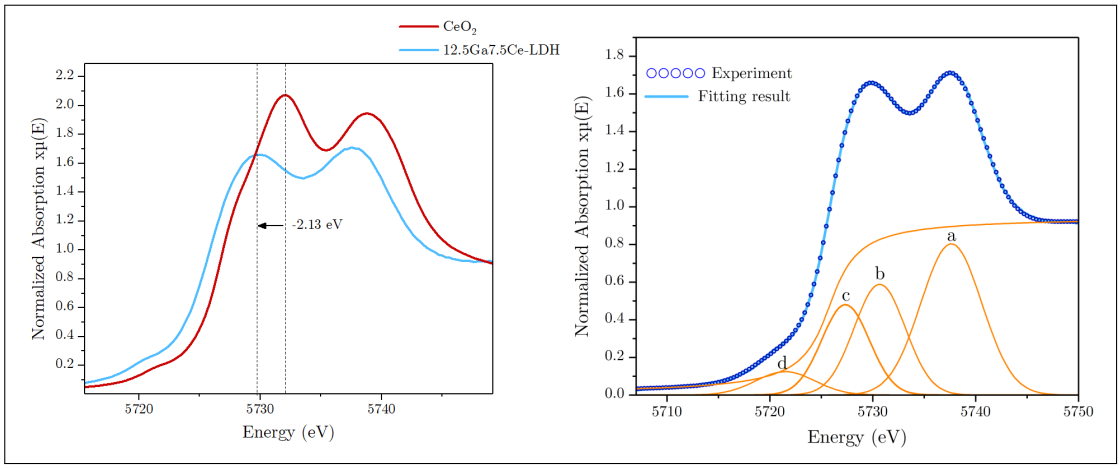


Figure 8.19: Left) Experimental Ce L_3 edge XANES spectra of 12.5Ga7.5Ce-LDH and CeO_2. Right) The Gaussian fitting of the 12.5Ga7.5Ce-LDH XANES spectrum using the literature-known $a/b/c/d$ Ce^{x+} transitions.

Table 8.7 summarises the results of the quantitative Gaussian LCF fitting from Figure 8.19. Using the peak areas, the Ce^{3+} content can be estimated: [294,295]

$$\frac{Ce^{3+}}{total\ Ce} = \frac{Area_c}{Area_{a+b+c+d}} \times 100 = \frac{2.803}{0.895+2.803+3.677+5.982} \times 100 = 21.0\ \%$$

This Ce^{3+}:Ce^{4+} ratio is in close agreement with the value found via XPS, see Section 8.4.4.

Figure 8.20 displays experimental Ce L_3 edge FT-EXAFS analysis of 12.5Ga7.5Ce-LDH, such analysis can be used to reveal information of the local structure around absorbing Ce atoms (see Section 5.11.1). Initially the experimental and simulated

Table 8.7: Gaussian function analysis summary of the 12.5Ga7.5Ce-LDH XANES spectrum (Figure 8.19).

Peak label	Transition(s)	Peak position (eV)	Peak area
a	$2p_{3/2} \longrightarrow 4f^0 5d^*$	5737.642	5.982
b	$2p_{3/2} \longrightarrow 4f^1 5d^*L$ ($O2p^5$)	5730.680	3.677
c	$2p_{3/2} \longrightarrow 4f^1 5d^*L$ ($O2p^5$)	5727.351	2.803
	$2p_{3/2} \longrightarrow 4f^2 5d^*L$ ($O2p^4$)		
d	$2p_{3/2} \longrightarrow 4f^*$ (forbidden)	5721.502	0.895

FT-EXAFS data was fitted for many common Ce oxides and precursors such as bulk CeO_2, $Ce(OH)_x$ and $Ce(NO_3)_3$, all fitting models were used from models from the 'Materials Project'. [216] Of these fittings only CeO_2 with a P63/mmc spacegroup gave a reasonable fitting R-value of 1.35 %; this fit is displayed in Table 8.8. It is important to note that when simulated FT-EXAFS spectra are fitted to an experimental spectrum, a statistical R-value closer to 0 % represents a closer fit. Other parameters must be considered during simulated FT-EXAFS fitting as well. The Debye-Waller factor (σ^2) represents an averaged physical value of atomic thermal/mechanical displacement and it reflects how 'rigidly placed' an atom in the fit is i.e. a higher Debye-Waller factor value reflects an atom or bond with a higher freedom of movement within the modelled fit and high values indicate a poor model fit. Debye-Waller factors vary depending on atom mass and factors such as differences in surface and bulk models; however, they should be comparable throughout Table 8.8 because the models and atoms used are similar.

Unlike the experimental CeO_2 XANES, 12.5Ga7.5Ce-LDH displayed simpler and weaker Ce L_3-edge XANES features/signals (Figure 8.19), this suggests Ce is more disperse and/or in an amorphous phase with a short-range coordination environment. The Debye-Waller factor and R-value parameters for P63/mmc bulk CeO_2 did not fit as well as other modelled Ce-doped LDH structures (see Table 8.8). This indicates that Ce is well dispersed throughout the 'LDH' structure, in agreement with the

EDX analysis (see Section 8.4.3), and interacts with other transition metals in close proximity.

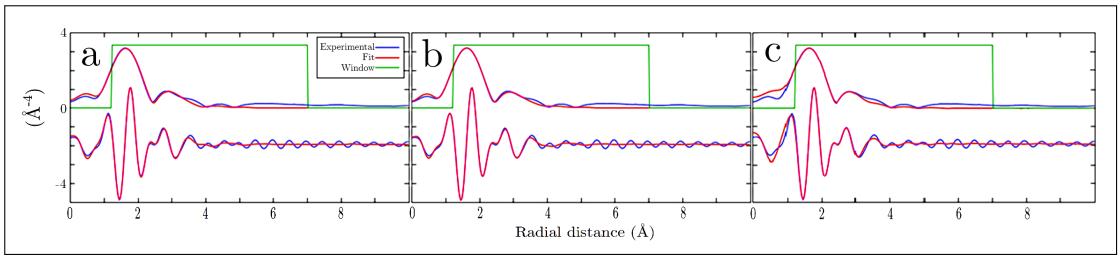


Figure 8.20: Blue line) Experimental Fourier-transformed $|\chi(R)|$ (above) and filtered back-Fourier Transformed $R_e|\chi(R)|$ (below, which is used to remove effects from higher coordination shells) EXAFS spectra of 12.5Ga7.5Ce-LDH. The red line represents simulated EXAFS spectra for the following models: a) 'monolayer' $Ce^{4+}O_2$ b) 6-coordinate Ce^{3+} substituted in LDH lattice position c) 8-coordinate Ce^{4+} substituted in defective layered lattice position.

After the fittings of known Ce structures were performed, three classes of hypothetical models were constructed via DFT and used to simulate FT-EXAFS spectra via the finite differences method. These models were constructed by modifying a database single layer MgAl-LDH model to a pure Zn-LDH layer; this was done because the calculations became significantly more complicated and time consuming when having to account for all likely combinations of the three elements (Cu, Zn, Ga) in various positions. [216] This was a reasonable simplification to apply because it was found that the differences in models of Cu-, Zn-, Ga- and CuZn-LDH models was minimal (see the differences in the 6-coordinate substitution models in Table 8.8); this is because Cu, Zn and Ga all have similar radii in the muffin-tin approximation (which disregards 'unimportant' volume to save computational power). Overall, the Zn-LDH monolayer usually led to the best model fits to experimental data, this was likely because it possessed the median ionic radius of the possible metal cations. Therefore, most models used a pure Zn-LDH model as a base; of course such a structure could not be real due to real required M^{2+}:M^{3+} ratio for thermodynamically-favourable LDH formation. The first class of hypothetical models (adsorbed) treated a small Ce

oxide particle with 3 Ce atoms and varying Ce-O coordination numbers as if it was 'adsorbed' to an LDH surface i.e. no LDH surface bonds and hydroxyl groups were broken or dissociated compared to that of the pure-Zn model. The second class (O-sharing) treated such Ce oxide particles on the surface of a Zn-LDH layer as sharing oxygen groups with the LDH at the interface; however, most models were of poor fit and reverted to adsorbed-like models. The third class of models (substituted) used a single Ce atom, with varying coordination/oxidation environments, to replace a Zn atom in the LDH single layer.

All DFT-calculated models were constructed using a full-electron relativistic approach. The effective core potential of the calculated models converged to a minimum with successive iterations of the calculations (ground state approximation). The resultant 3D models and simulated FT-EXAFS fitting data to the experimental 12.5Ga7.5Ce-LDH spectrum are displayed in Figure 8.21 and Table 8.8, respectively. The bulk P63/mmc CeO_2, substituted 6-coordinate and substituted 8-coordinate models' simulated FT-EXAFS spectra are also shown in Figure 8.20.

Table 8.8: EXAFS fittings of the simulated models. In each case the 1^{st} shell is either O^{2-} or OH^{-}; the 2^{nd} shell is another metal. Discarded fits are listed in the top section and unsuitable fits are listed in the middle section; whilst good R-value fits, with σ^2 within reasonable limits, are listed in the bottom section. σ^2 values denoted as 'N/A' were calculated as negative.

Model	1^{st} shell					2^{nd} shell				R value
	Ce-X	N	σ^2[Å]	R_{fit}(Ce-O)$_1$[Å]	R_{fit}(Ce-O)$_2$[Å]	Ce-X	N	σ^2[Å]	R_{fit}[Å]	[%]
Adsorbed $Ce_3^{4+}O_x$	Ce-O	6	N/A	1.96	2.36	Ce-Zn	1	N/A	5.63	36.81
Adsorbed $Ce_3^{4+}O_x$	Ce-O	7	N/A	2.15	2.45	Ce-Zn	1	N/A	5.30	10.40
Adsorbed $Ce_3^{4+}O_x$	Ce-O	8	N/A	2.21	2.45	Ce-Zn	1	N/A	4.43	28.24
Adsorbed $Ce_3^{4+}O_x$	Ce-O	9	N/A	2.10	2.60	Ce-Zn	1	N/A	2.90	7.81
O-sharing $Ce_3^{4+}O_x$	Ce-O	6	0.050	1.71	2.06	Ce-Ce	2	0.055	2.93	5.65
O-sharing $Ce^{4+}O_9$	Ce-O	9	0.030	2.30	-	Ce-Zn	1	0.008	2.75	3.99
Bulk P63/mmc $Ce^{4+}O_2$	Ce-O	9	0.040	2.20	2.66	Ce-Ce	5	0.066	3.72	1.35
'Monolayer' $Ce^{4+}O_2$	Ce-O	6	0.010	2.22	-	Ce-Ce	6	0.010	3.46	2.68
Substituted Ce^{3+}	Ce-OH	6	0.005	2.22	-	Ce-Cu	6	0.021	3.04	0.73
Substituted Ce^{3+}	Ce-OH	6	0.004	2.30	-	Ce-Zn	6	0.016	3.20	0.98
Substituted Ce^{4+}	Ce-O	8	0.026	2.12	2.26	Ce-Zn	6	0.027	3.00	0.61
Substituted Ce^{4+}	Ce-O(H)	8	0.002	2.31	2.71	Ce-Zn	6	0.014	3.35	0.69

From Table 8.8 it can be seen that including -OH groups instead of just O atoms at for the LDH anions improved the fit, this is best seen when comparing the two 8-coordinated substitution models. The adsorption models have very poor R value fits as expected because the bonding between the CeO_2 and Zn-LDH layer is effectively a weak hydrogen bonding interaction. It is theorised the forming of such an 'adsorbed' structure and bond is likely thermodynamically unfavourable under coprecipitation conditions because a stronger hydrogen bonding network and electrostatic interactions can be formed from the formation of another LDH layer and subsequent interlayer gallery. Unfortunately, only two oxygen-sharing models between CeO_2 and LDH surfaces resulted in a structure that didn't revert to models akin to the adsorbed models via the iterative method. These two models were of surface Ce_3O_6 and CeO_9 particles that shared oxygen with $Zn(OH)_6$ octahedra from the LDH layer; however, the R value fits for these models were also poor (see Table 8.8).

PXRD analysis of Ce-doped LDHs only showed that the particles large enough to give a diffraction signal were LDH phases and subsequent analysis of the crystallite thickness suggested that there was 'critical Ce content' above which Ce no longer occupied a conventional LDH lattice position (see Section 8.4.1). 12.5Ga7.5Ce-LDH had a Ce content well above the theorised critical amount and EDX analysis suggested that Ce was very well dispersed throughout 12.5Ga7.5Ce-LDH (see Section 8.4.3); all this evidence points towards Ce occupying non-LDH or defective phases that are well dispersed amongst the LDH phases. The coordination number of Ce is very flexible and has been known to be 6, 7, 8, 9 or higher in various compounds. [299, 300]

In literature CeO_2 (with a Fm -3 m spacegroup) has an average bond distance of 2.35 Å; this is not far from the bond distances for the simulated bulk CeO_2 model despite the different space group. [301] From Table 8.8 it is apparent that Ce substituted into the LDH layer gives good Debye-Waller factors relative to bulk CeO_2 and the best

statistical R value fits. As can be seen in Figure 8.21 the 8-coordinated Ce^{4+} substitution model introduces more oxygen into the lattice creating a different structure to the LDH lattice; whereas, the 6-coordinated Ce^{3+} model retains the LDH phase with slight distortion. As theorised in Section 8.4.1 and throughout this chapter, when more than a critical content of Ce is doped during the synthesis ($\approx$ 1 mol %) the LDH crystallite sizes do not change and there is a lower ratio of crystalline LDH phase observed with increasing Ce content. Additionally, XPS and EDX analysis suggest Ce in the precursor LDH material is very highly dispersed and predominantly in the (4+) oxidation state. These models support the theory that 6-coordinate Ce^{3+} could occupy lattice positions initially but that the favoured state is Ce^{4+} with a coordination number of 8. The defective model of 8-coordinated, substituted Ce^{4+} could also explain why higher contents of Ce do not appear to effect LDH phase-specfic PXRD parameters and could be responsible for the high dispersion of Ce seen in EDX and low crystallinity seen in TEM (Figure 8.14 and 8.11, respectively). Disperse particles of CeO_2 could also cause a similar effect; however, even CeO_2 particles with a diameter of 5 nm would still be expected to give broad PXRD peaks at 28.5 °, 33.1 °, 47.5 ° and 56.3 °; the only peak that doesn't coincide with a $3R_1$ or $3R_2$-LDH PXRD peak is the 28.5 ° CeO_2 peak, which is not seen for any Ce-LDH sample. [301, 302]

The XANES edge for several models was also simulated for further insight (see Figure 8.22). Unfortunately, like the experimental CeO_2 XANES spectrum, the 8-coordinated, substituted Ce simulated XANES spectrum does not completely match that of experimental 12.5Ga7.5Ce-LDH. Initially, it was theorised that Green function Muffin-tin approximation caused the inaccuracy of the second peak due to fact that simulated XANES spectra often only fit well up to above $\approx$ 15 eV above the edge ($\approx$ 5735 eV for Ce L_3). [298] Notably, the fit was massively improved when the XANES edge was simulated using a 20:80 ratio of the 6-CN-Ce^{3+}:8-CN-Ce^{4+} models; this ratio was chosen based on the Ce^{3+}:Ce^{4+} ratio estimated by XPS and XANES Gaussian

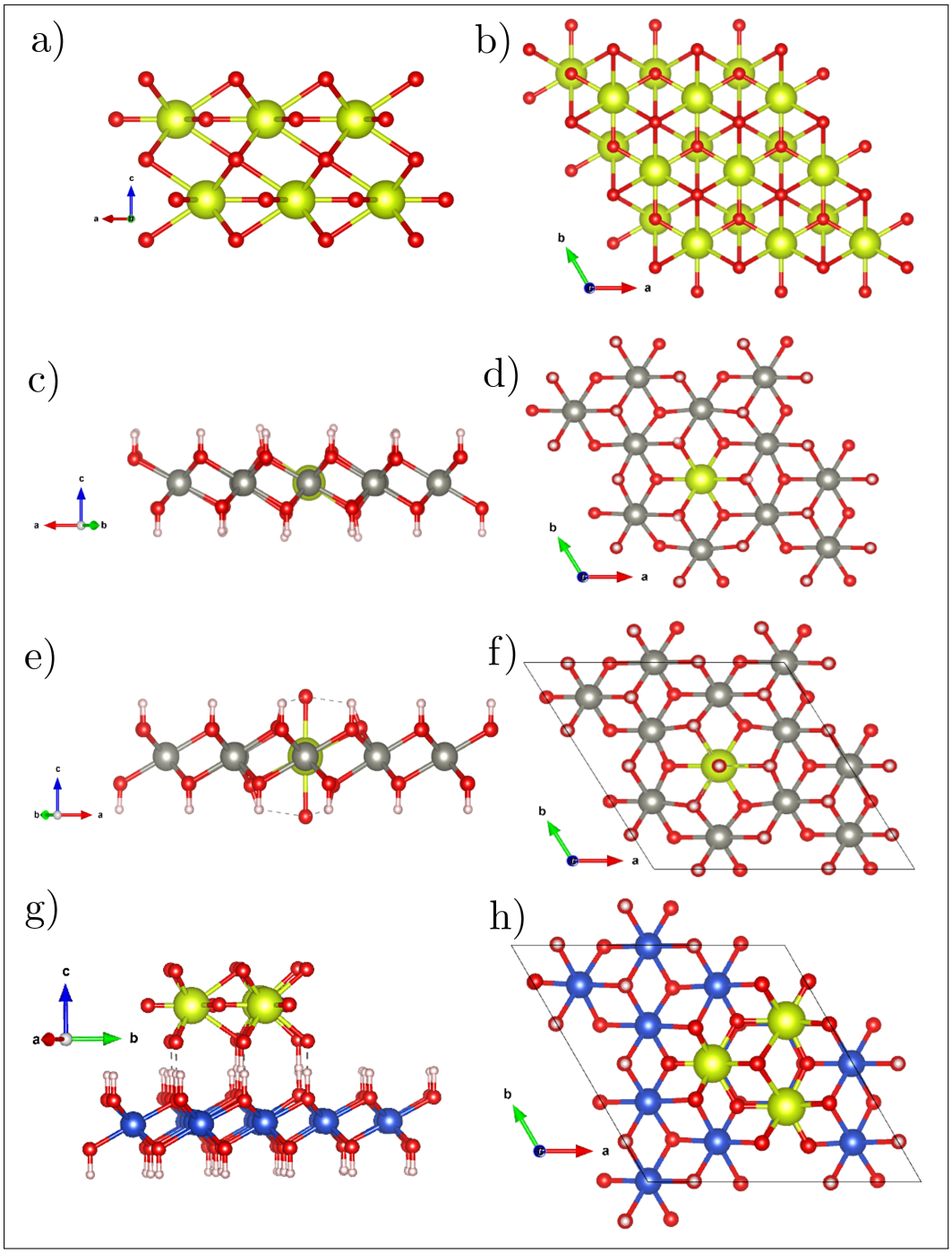


Figure 8.21: a/b) Different angles of the bulk $Ce^{4+}O_2$ model (no LDH layer). c/d) Different angles of the 6-coordinate Ce^{3+} substitution model. e/f) Different angles of the 8-coordinate Ce^{4+} substitution model. g/h) Different angles of an adsorbed $Ce_3^{4+}O_x$ model. Models viewed with VESTA software (K. Momma and F. Izumi, "VESTA 3 for three-dimensional visualization of crystal, volumetric and morphology data, *J. Appl. Crystallogr.*, 2011, **44**, 1272-1276).

fitting experiments of 12.5Ga7.5Ce-LDH.

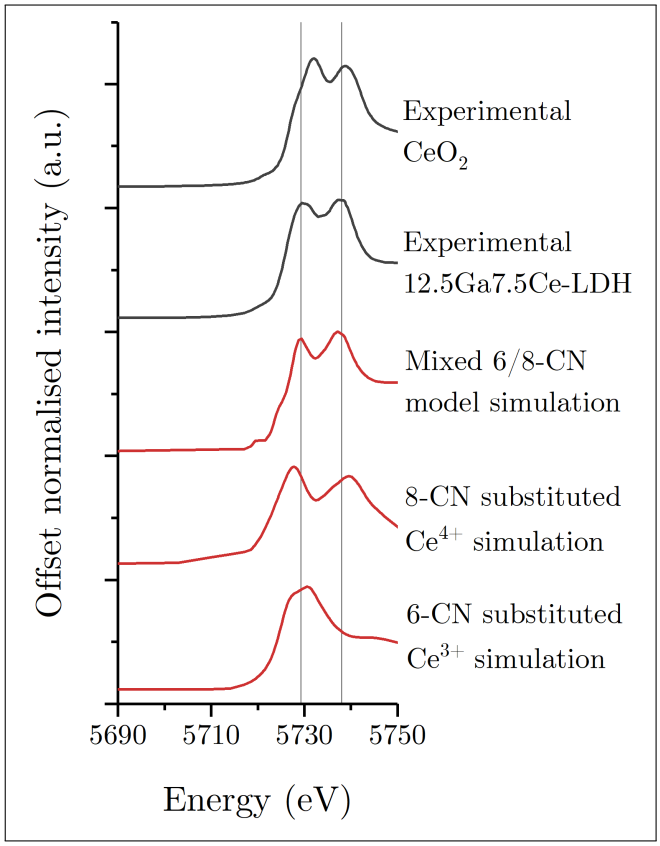


Figure 8.22: XANES spectra of the simulated 8-coordinated Ce^{4+}- and 6-coordinated Ce^{3+}-substituted models compared to experimental results. The 'mixed 6/8-CN model' XANES spectra was simulated for a mixture of 20 mol % of the 6-coordinated Ce^{3+}- and 80 mol % of the 8-coordinated Ce^{4+}-substituted models (reflecting the experimental oxidation state mixture estimated via XPS and Gaussian XANES fitting analysis).

Using EXAFS and XANES analyses in combination with direct EDX imaging, it is theorised that during coprecipitation initially Ce^{3+} from the Ce(III) nitrate precursors incorporate into LDH lattices alongside the other copreciptating metal cations. However, the steric bulk of the large Ce^{3+} cations likely distorts the LDH layer, decreasing the lattice energy by decreasing the layer stacking efficiency. Therefore, above a critical Ce LDH-layer content, Ce forms defect sites in the layers with additional oxygen atoms that allow a shorter, in-layer Ce-OH bond to form (see Table 8.8). It is unlikely these Ce^{4+} groups terminate LDH particles in an ordered or crystalline

fashion because no CeO_2 is seen by PXRD and high-resolution EDX shows there is a very high Ce dispersion. Synchrotron pair-distribution function analysis is planned for this Ce-based AMO-LDH series for further insight into the structure.

As per the XAS-based modelling, for 12.5Ga7.5Ce-LDH it is theorised that ≈ 1-2 % metal mol Ce occupies a LDH lattice position in the (3+) oxidation state whereas ≈ 5.5-6.5 % metal mol Ce (≈ 80 % of total Ce) occupies defective layer positions in the (4+) oxidation state and introduces extra oxygen 'adatoms' due to its 8-coordination number. This occupation ratio corresponds to the critical Ce content observed in the crystallite thickness trend and the Ce^{3+}:Ce^{4+} signal component ratios (determined by XANES Gaussian fitting and XPS analysis). Despite the bulk CeO_2 model EXAFS fitting having a higher R value, the presence of very disperse CeO_2 surface particles can not be ruled out on this basis alone; further experimental evidence is required.

8.5 Analysis of the calcined and reduced Ce series

8.5.1 PXRD analysis of the Ce LDO/reduced series

As with the Mg, Al and Ga series the calcination of the Ce-doped LDHs transformed the materials from crystalline to amorphous, see Figure 8.23. Following the other calcined samples in this work, the amorphous peak occurs around ≈ 35 ° 2θ and not much information can be gleaned besides the calcined materials are amorphous; other minor peaks/bumps can be seen on the PXRD patterns of 19.5Ga0.5Ce- and 19Ga1Ce-LDO but they are almost indistinguishable from the baseline and could be speculated to be almost any oxide or LDH peak.

The PXRD patterns of the reduced Ce series also resemble that of the reduced Al and Ga series, only FCC Cu^0 and ZnO Wurzite PXRD peaks were observable (see Figure 8.24).

The Cu^0 particle sizes calculated, via the Scherrer equation, for the ex-situ re-

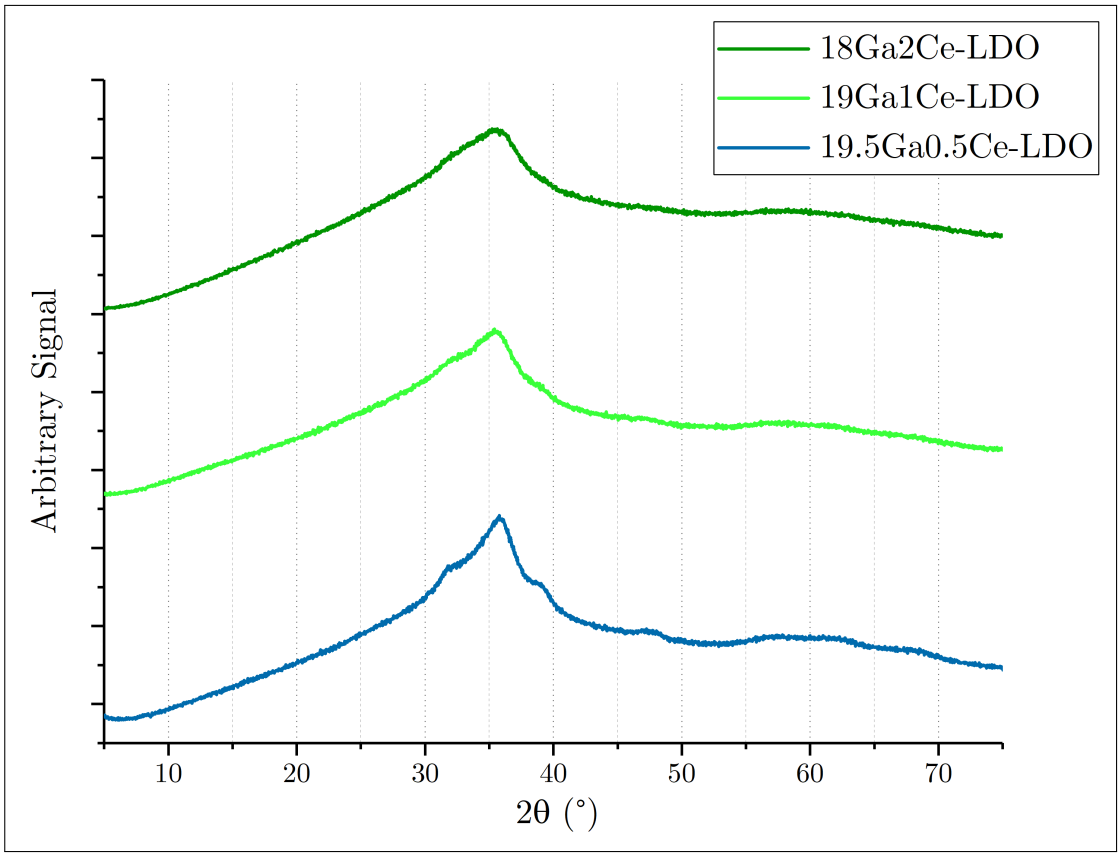


Figure 8.23: The PXRD patterns of the calcined Ce-based AMO-LDO series.

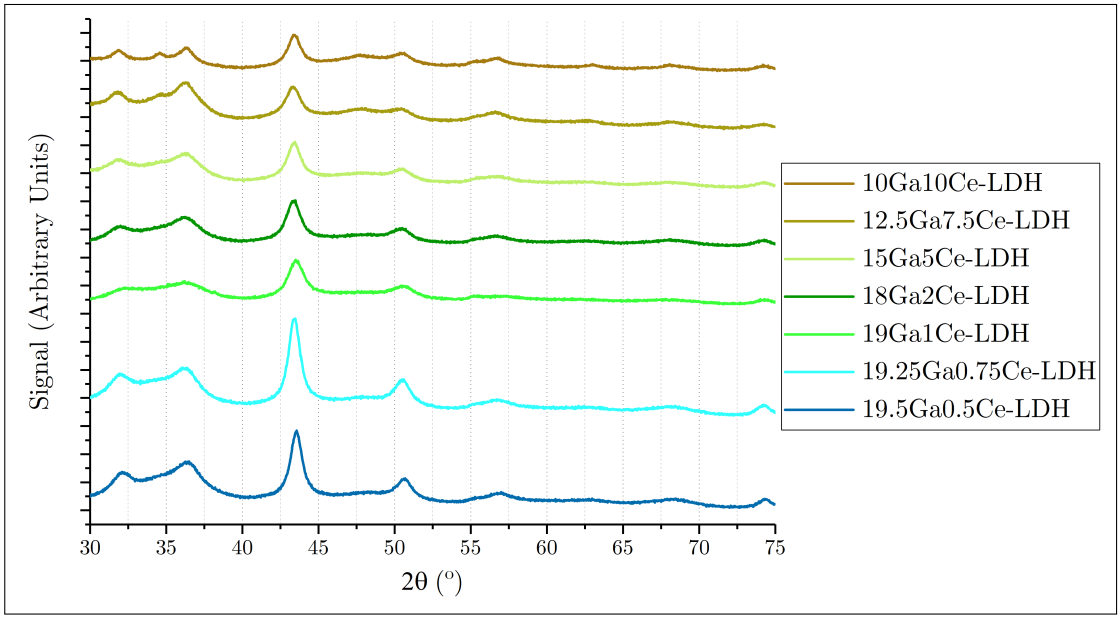


Figure 8.24: The PXRD patterns of the reduced Ce-based series.

duced Ce-doped series do not fit an observable trend; indicating that the Ce content could have multiple competing effects upon the Cu reduction process. Due to the unclear effect that Ce doping has upon the LDH structure, the potential for ceria particles to decorate the LDH surface and the possible redox reactions of Ce^{3+}/Ce^{4+}, the unknown effects upon Cu reduction could be a mix of both electronic and physical/structural trends.

To summarise, PXRD data could not be used to conclusively discern how doping Ce content into CuZnGaCe AMO-LDHs affected the structures of the calcined and reduced materials; therefore, TEM, EDX, TPR, BET, N_2O/H_2-titration, and DFT analyses were required if the materials' structures were to be solved.

8.5.2 TEM analysis of the Ce LDO series

In this section TEM images of the calcined 35Zn20Ga- and 19.25Ga0.75Ga-LDO samples are compared. The images feature zoom levels from 2 - 1000 nm and most were collected using a HAADF-STEM microscope; whilst one image, Figure 8.25.A, is from a bright-field microscope (see Section 5.9.2).

Figures 8.25.A and 8.25.B show bright- and dark-field images of calcined 35Zn20Ga-LDO, respectively; ≈ 200-500 nm plate-like morphology is still visible. However far more layer overlap, folds and crimps are visible for 35Zn20Ga-LDO than 35Zn20Ga-LDH, this is likely due to a partial breakdown of the LDH lattice and exposure to atmospheric water (causing layer agglomeration) that occurs during the calcination process. Despite this, areas of layered morphology can still be clearly identified, in Figure 8.25.C individual layers, of presumably LDO, can be distinguished; matching reports of topotactic thermal transitions from literature (see Section 3.7.1). Figure 8.25.D shows a high zoomed image of a individual 'LDO' layer from the 35Zn20Ga-LDO sample, it shows nano-crystallinty with phase/particle size similar to that of the LDHs imaged in Figures 8.9.D and 8.10.E; however, the symmetry/order of the

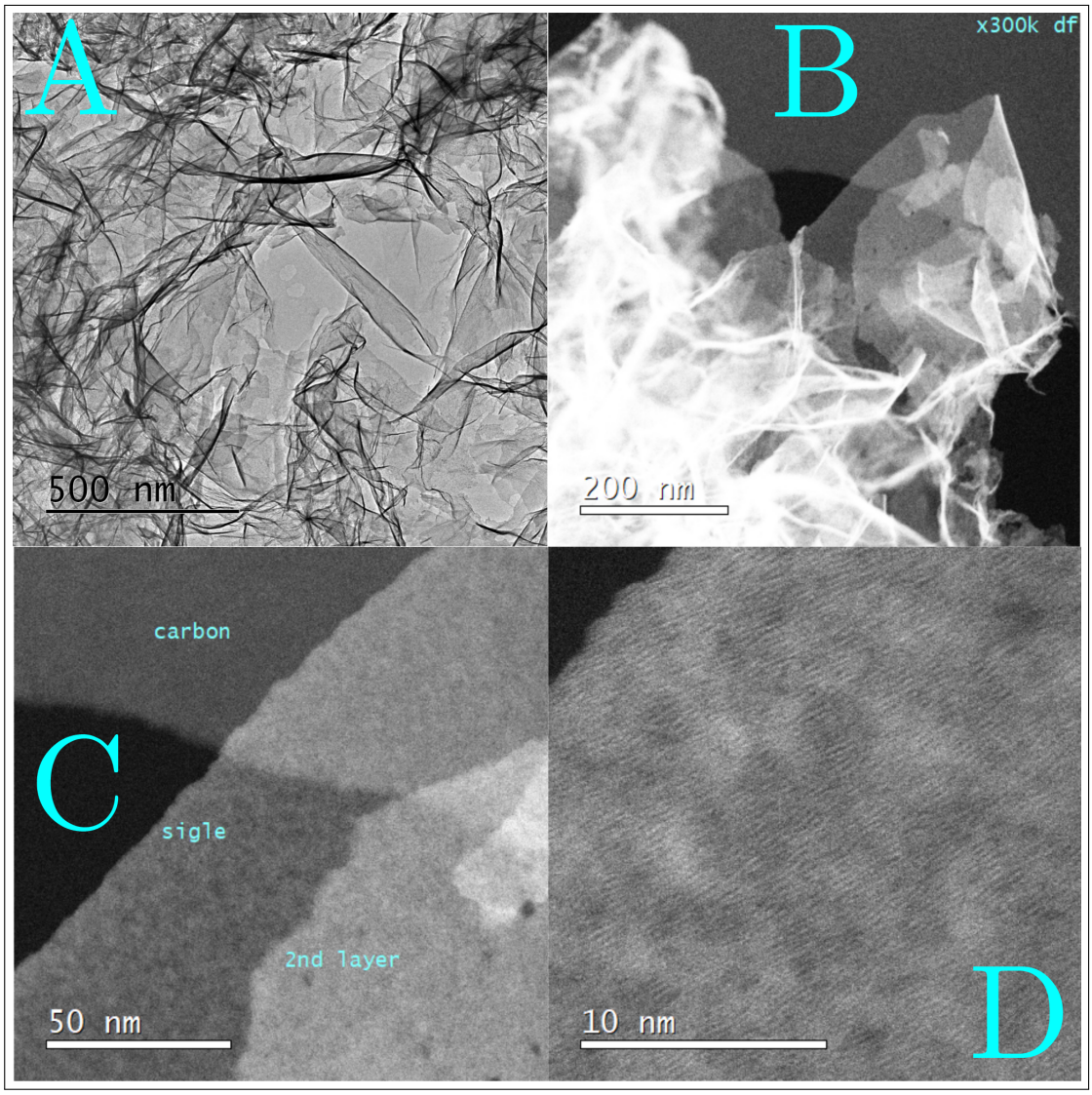


Figure 8.25: a) Light-field TEM image of 35Zn20Ga-LDO. b/c/d) Dark-field TEM images of 35Zn20Ga-LDO.

crystalline sections seems to be lower. The crystalline patterns in Figure 8.25.D seem to be more 'wavy' or 'fuzzy' compared to the analogous LDH images, again this is only qualitative analysis based on a few images; the cause for this may be a loss of order in the structure (due to calcination) but the images are not conclusive.

TEM images of 19.25Ga0.75Ce-LDO can be seen in Figure 8.26, the calcination process' effect appears to be similar to the one that occurs for 35Zn20Ga-LDH/LDO i.e. partial layered morphology is maintained but other amorphous phases seem to

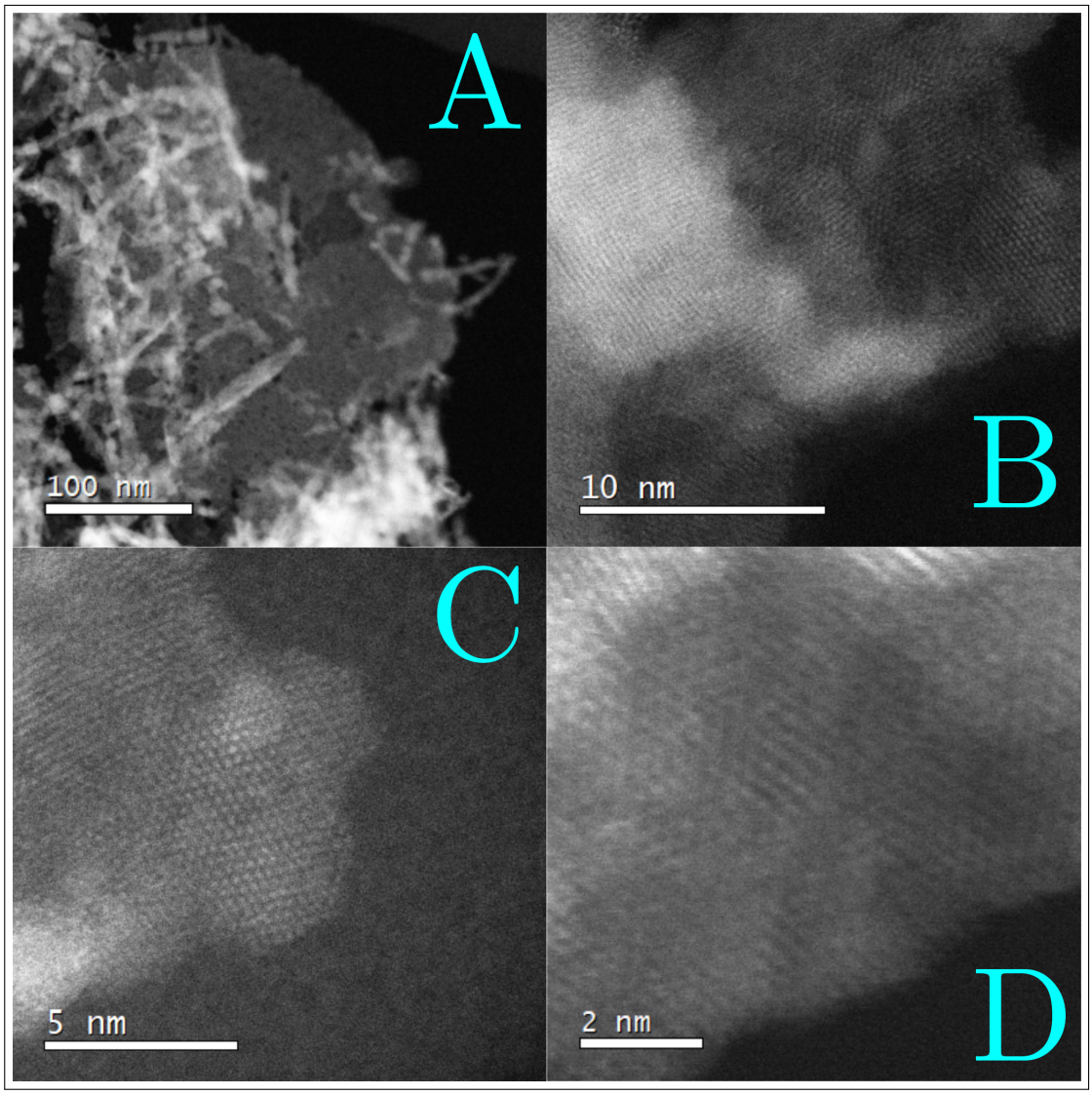


Figure 8.26: Dark-field TEM images of 19.25Ga0.75Ce-LDO.

form. Figure 8.26.A shows there is a 200 - 300 nm section of layered crystallite surrounded by amorphous folds, defects or phases. Figures 8.26.B, 8.26.C and 8.26.D show various sections of the material at high zoom, both areas of crystallinity and more amorphous sections can be seen.

TEM demonstrates that layered morphology can be at least partially retained after calcination as expected due to the topotactic nature of LDH thermal transitions (see Section 3.7.1).

8.5.3 BET analysis of the Ce LDO series

The BET surface areas of the Ce-doped LDO series and 35Zn20Ga-LDO are shown in Figure 8.27. The main feature of the trend is the sudden drop in surface area between 19.5Ga0.5Ce- and 19.25Ga0.75Ce-LDO, after this the surface area increases slightly for 19Ga1Ce-LDO and then plateaus with increasing Ce content; however, 19.5Ga0.5Ce-LDO may be anomalous. The large initial changes in surface area at low Ce contents, 0-1 %, coincide with the largest increases in crystallite thickness/plate diameter and erratic changes in the a and c parameters. These changes do not correlate exactly, mainly because the 19.25Ga0.75Ce-LDO has a lower surface area than 19Ga1Ce-LDO; however, it is apparent the largest changes in the precursor structure all occur in this range. A critical Ce content was proposed in Section 8.4.1, whereby after a certain point Ce would no longer occupy a Ga^{3+} LDH lattice position but rather form another amorphous phase or occupy defect sites in the layers.

The LDH PXRD layers per crystallite trend almost mirrors the LDO surface area trend along the y=0 axis, this is because greater exfoliation of the LDH layers leads to thinner LDH crystallites and higher surface area LDHs. Which in turn, are calcined to higher surface area LDOs, assuming some layered morphology is topotactically retained. Despite the LDH particles remaining a similar size with increasing Ce content, it was expected that the BET surface area would decrease with Ce content because the total amount of layered phases was decreasing (as per the LDH PXRD signal intensity, see Figure 8.1). However, it was observed that the BET surface area plateaus at Ce content above 1 %, this implies other surface area effects were present that competed with the LDH phase loss effect; for instance, the potential amorphous phase formed by the excess Ce could have a similar surface area to the LDO phase and/or the Ce^{x+} has a higher possible N_2 coordination number compared to the smaller Ga^{3+} ions it replaces.

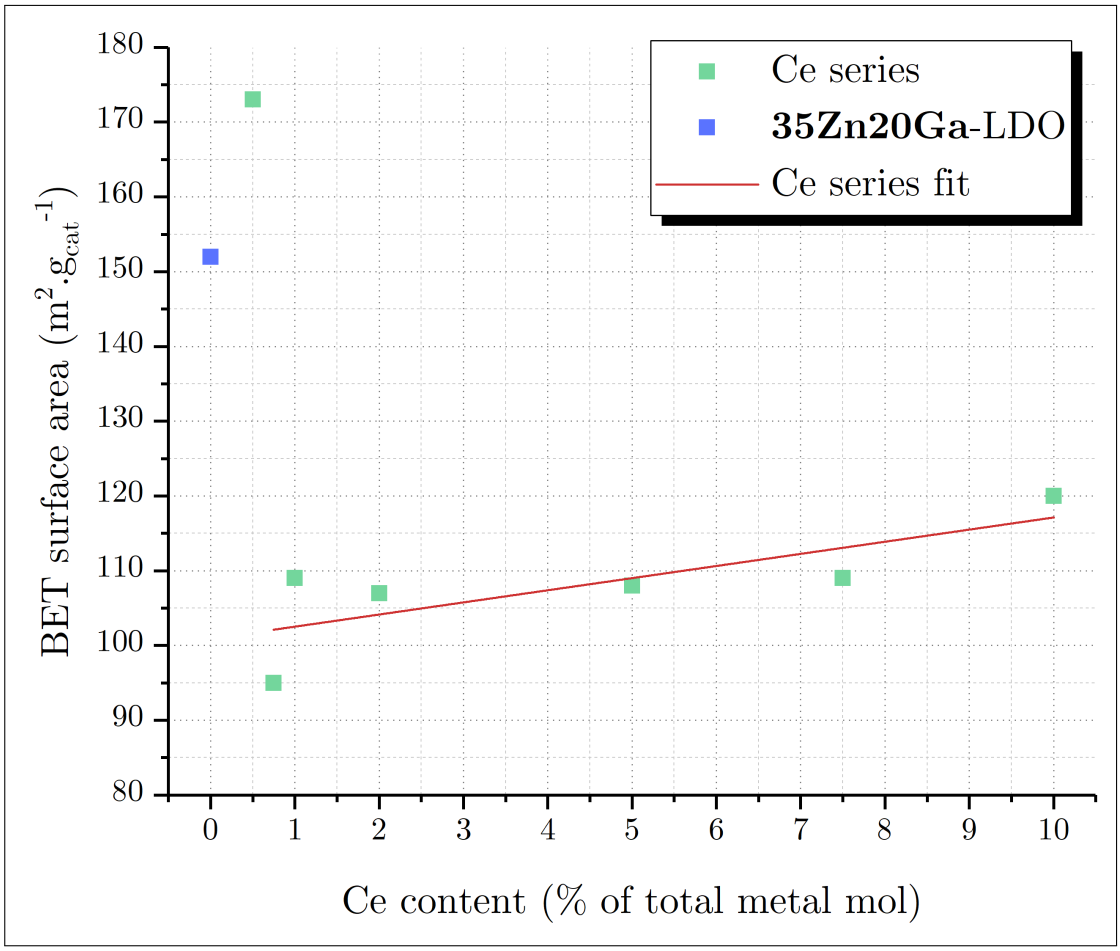


Figure 8.27: The BET surface areas of the calcined Ce-based series (LDOs); the error = ± 1.0 $m^2.g^{-1}$. The red line represents a linear fit (ignoring the 19.5Ga0.5Ce-LDO data point) where: y = 100.9 + 1.62x and the R^2 value = 0.60.

A trend in both the pore diameter and desorption BJH pore volume of the Ce-doped LDOs can be seen in Figure 8.28. The modal pore diameter (the pore diameter with the highest BJH pore volume) decreases from 650 to 230 Å with increasing Ce content from 35Zn20Ga- to 10Ga10Ce-LDO, respectively. Additionally, the total BJH pore volume of the series appears to follow a volcano trend with respect to the Ce content, where the highest pore volume plateaus between 0.5 - 2 Ce metal mol %; these trends are represented quantitatively in Figure 8.29.

BJH pore analysis assumes pores are perfectly cylindrical, which may introduce a consistent systematic error when calculating the pore size for the layered LDOs with

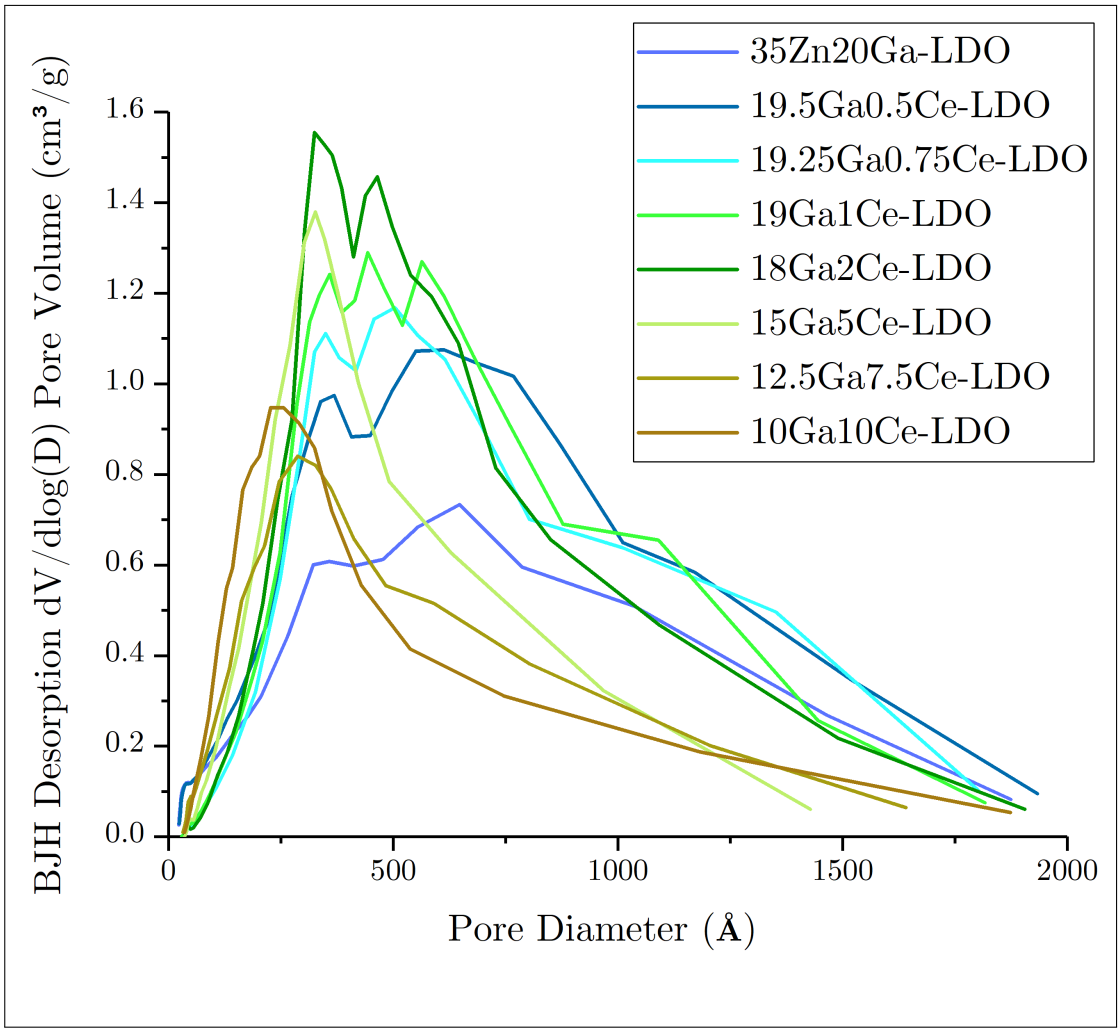


Figure 8.28: BJH desorption pore volume and pore diameter for the Ce-based LDO series (data from Figure 8.27).

an unknown pore structure. The adsorption and desorption hysteresis loops from the BET analysis of the Ce LDO series can be seen in Figure 8.30; their shapes imply all samples have a type IV BET adsorption isotherm. [303, 304]

The samples also have a H3 hysteresis loop because the adsorption and desorption isotherms are almost parallel in both vertical and horizontal positions, this isn't immediately obvious in Figure 8.30 because only a small section of the x axis is shown (this was done for better figure visibility due to the number of samples). [305] Figure 8.31 demonstrates the profiles of the hysteresis loops, displaying both axes fully; the

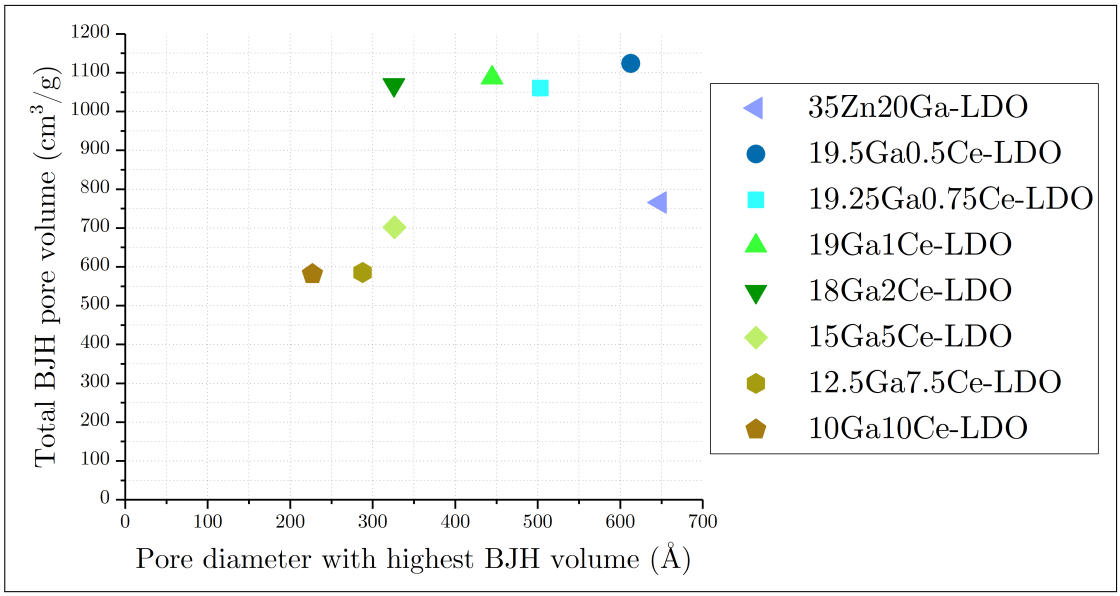


Figure 8.29: The total BJH pore volume and modal pore diameter for the Ce-based LDO series (data from Figure 8.27).

amount of parallel vertical components in the loop suggest there may be some H1 hysteresis loop character, this is often caused by 'more rigid' mesoporous oxides. [305] Both type II and IV isotherms initially follow a similar trend at low P/P_0 values as the monolayer and multilayers of N_2 adsorb but differ because type IV isotherms have a hysteresis loop. [304] Sing et al. propose the cause for most hysteresis loops is that mesopores cause 'capillary condensation', this is where the formation of multilayers of adsorbed N_2 has a lower required condensation pressure. Condensation of N_2 within a mesopore allows a meniscus to form at the liquid-vapour interface. [306] Subsequently, the largest rate in desorption will occur at a lower P/P_0 relative to the highest adsorption rate (forming the hysteresis 'loop' on a graph) because N_2 is trapped behind the meniscus, where it will have a lower saturation vapour pressure due to the increased van der Waals forces in the mesopore. [305] H3 hysteresis loops are often given by non-rigid, aggregated plate-like particles, such as montmorillonite (comprised of layered alumina and silica), when they adsorb non-polar gases, such as nitrogen. [305, 307] LDHs from literature, that also formed plate/flower morpholo-

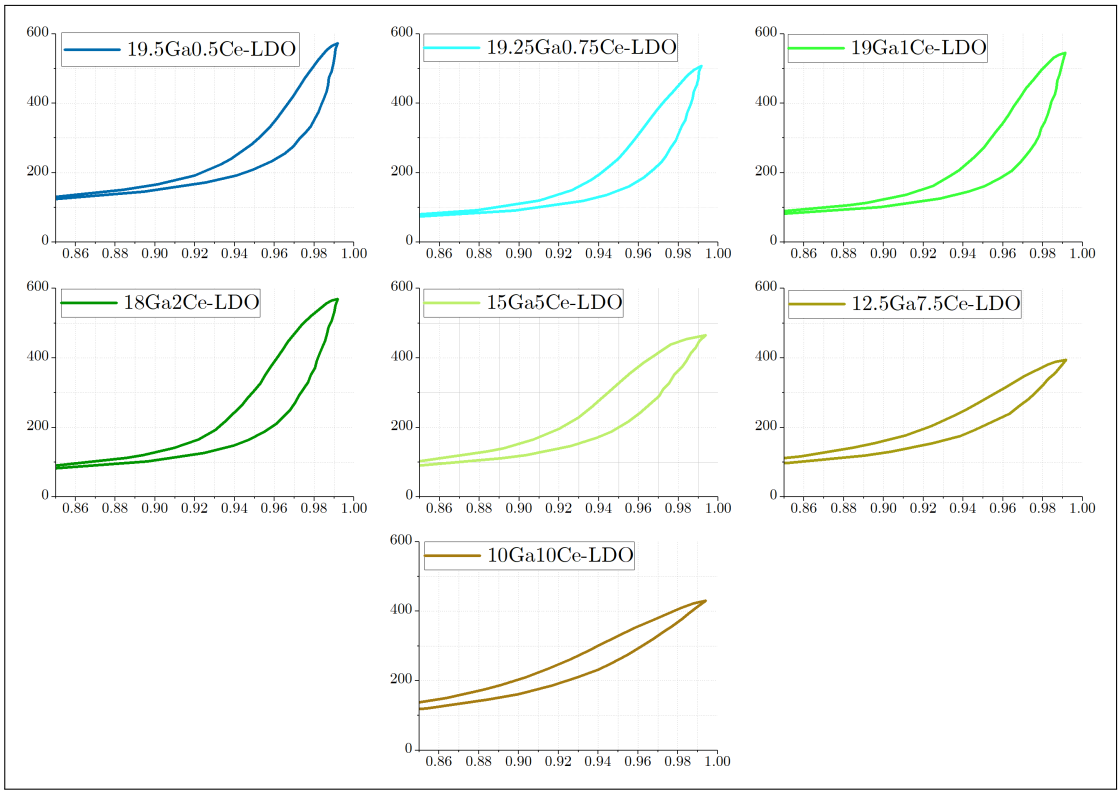


Figure 8.30: Hysteresis loops for the Ce-based LDO series in the upper relative pressure regime. x axis = relative pressure (P/P_0), y axis = amount adsorbed ($cm^3.g^{-1}$). Data from Figure 8.27.

gies, gave similar IV isotherms and H3 hysteresis loops to those observed for the Ce-based LDO series. [308, 309] This indicates that the calcined Ce-series maintains a layered plate/flower-like morphology from their LDH precursors and, therefore, the BJH pore calculation assumptions that pores are perfectly cylindrical may not be highly accurate. However, this would likely be a systematic error and it is probable Ce doping still relates to pore volume in a volcano trend and pore diameter in an inverse correlation.

Interestingly, as Ce content increases the hysteresis loop shape becomes slightly less parallel in the vertical axis and more so horizontally (see Figure 8.30), which is unlikely to be caused by a lower effective BET surface area since the BET surface area trend plateaus (see Figure 8.27). It is possible that the hysteresis loop types

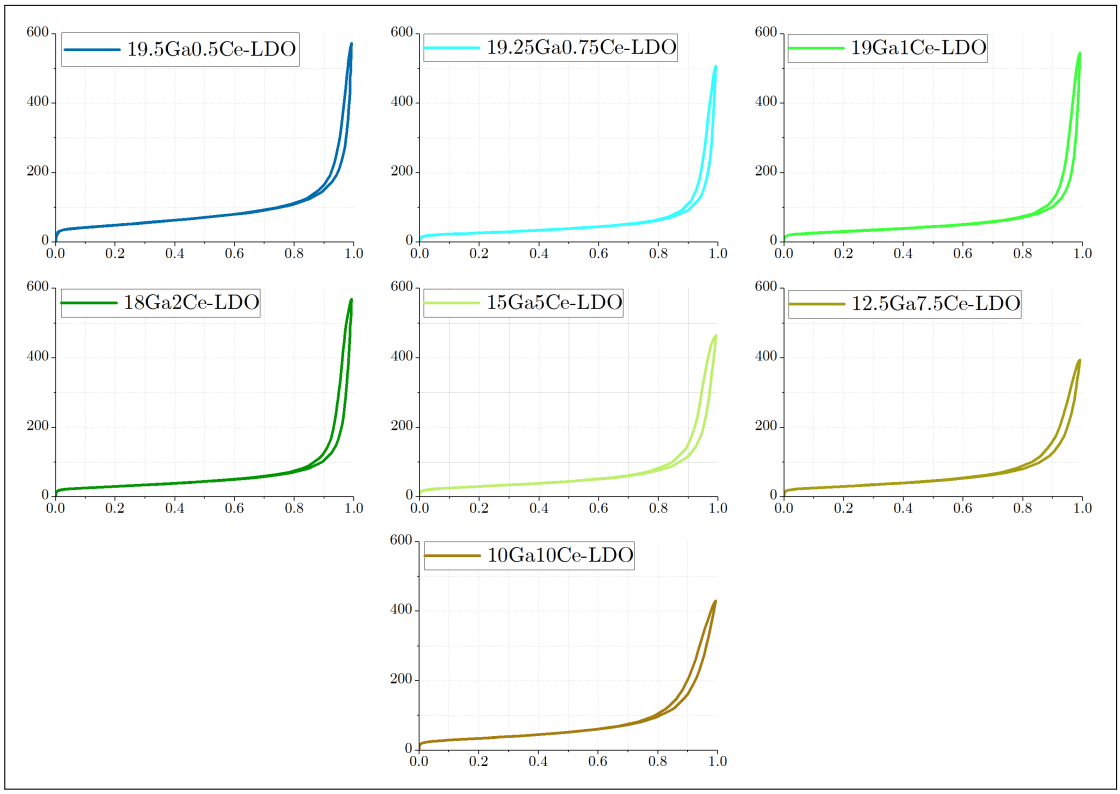


Figure 8.31: Hysteresis loops for the Ce-based LDO series across all relative pressure regimes. x axis = relative pressure (P/P_0), y axis = amount adsorbed ($cm^3.g^{-1}$). Data from Figure 8.27.

shifts closer to H4 from H3 with increasing Ce content; Long et al. have observed an LDH with a H4 hysteresis loop in literature. [310] H4 hysteresis loops typically close at 0.4 P/P_0 and are often more microporous; however, even the hysteresis loop for 10Ga10Ce-LDO closes at $\approx$ 0.75 P/P_0 and has a large vertical parallel component, see Figure 8.31. [311] Therefore, any shift to H4 hysteresis loop character is very small and the majority of all samples can be considered layered, plate-like, non-rigid structures (with H3 hysteresis loops).

In summary, BET surface area analysis shows that all Ce samples are mesoporous and have a similar surface area (that is much lower than that of non-doped 35Zn20Ga-LDO). Interestingly, the modal pore diameter seems to decrease in size with increasing Ce content.

8.5.4 N_2O/H_2 titration of the Ce LDO series

The first thing to note when reviewing the D_{Cu} % data for the Ce-doped LDO series is that all of the calcined LDO samples for D_{Cu} % analysis were exposed to the atmosphere for up to half a year after the vacuum desiccator grease seal failed (as was the cause for a portion of the samples in the Ce series TPR analysis). This likely led to the intake of water, O_2 and CO_2 by both LDH and LDO samples in the desiccator, LDOs likely experienced at least a partial memory effect (whereby LDH morphology is reformed) and the exfoliated LDH layers probably lost surface area as the atmospheric water could have formed new interlayer regions when layers stacked together in a more energy efficient way to remove charge density. Most analysis was performed before this happened, such as the BET analysis, but the N_2O-H_2 data still reflected trends in the analysis of those fresh samples. However, lower than expected D_{Cu} % values were still obtained due to the stacking of layers and loss of surface area. This was demonstrated by the D_{Cu} % measurements for 35Zn20Ga-LDO before and after the long exposure to atmosphere, 47.5 and 30.3 %, respectively.

The trend in D_{Cu} % of the Ce series follows a similar trend to that of the BET surface area, see Figures 8.32 and 8.27, the D_{Cu} % of the Ce-doped samples is lower than that of 35Zn20Ga-LDO and plateaus with increasing cerium content. Initially the relationship between these two trends makes sense because the surface area determines how close together the forming Cu^0 are; the lower the surface area, the less energy is required for a Cu^0 particle to move across the surface to amalgamate with the nearest other Cu^0 particle to form a more energetically stable larger particle. Therefore, the lower the surface area, the lower the expected D_{Cu} %. However, there are two discrepancies, the first and major one is the contrast between the BET surface area and the D_{Cu} % of 19.5Ga0.5Ce-LDO. The second one is related to the theory that the Ce coordination number was a partial cause for the plateau in the BET surface

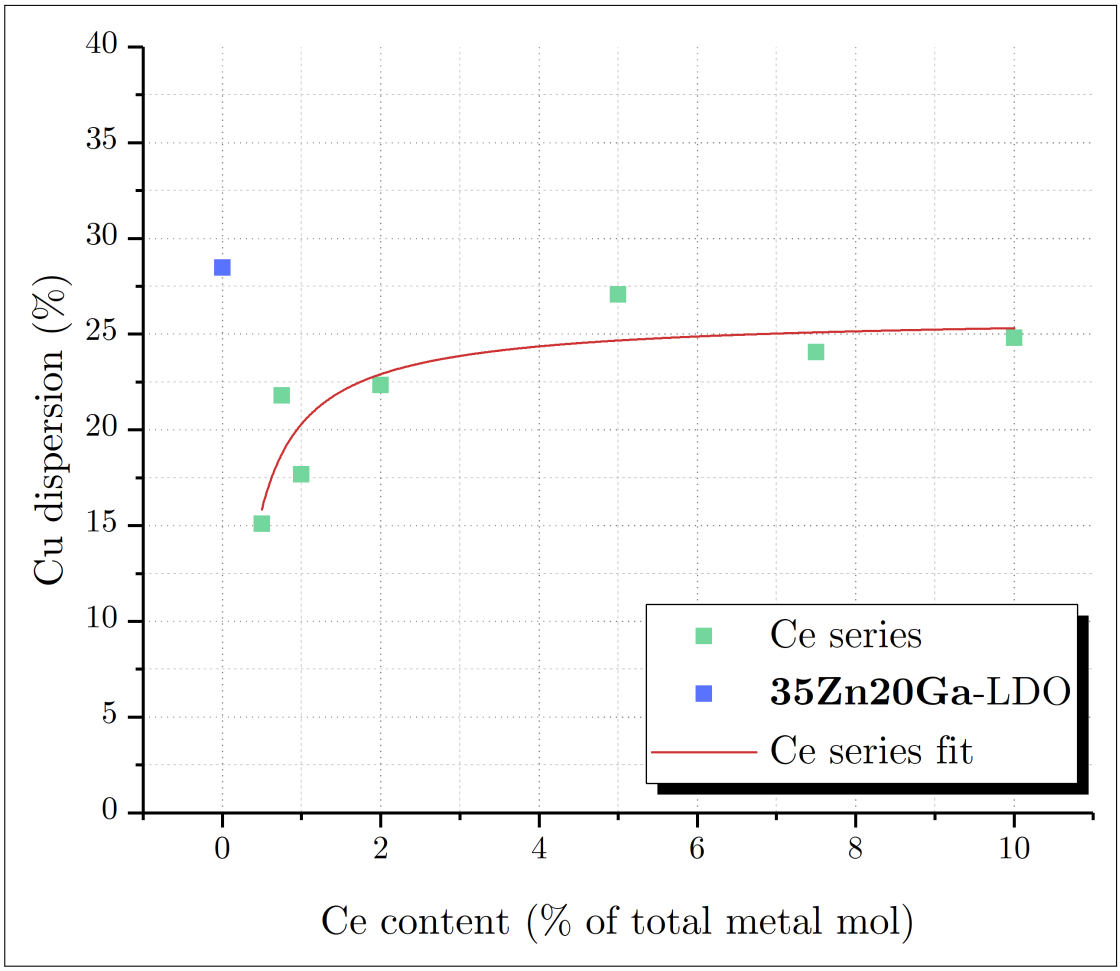


Figure 8.32: The D_{Cu} % of the calcined Ce-based AMO-LDH series; measured via N_2O/H_2 titration. The red line represents a sigmoidal fit where: y = 26.0 - $\frac{20.7}{1+(\frac{x}{0.07})^{0.93}}$ and the R^2 value = 0.53.

area. This theory cannot apply to the D_{Cu} % trend because the potential Cu^0-support interfacial area between the particles would not increase solely because Ce^{x+} favours a higher ligand coordination number than the Ga^{3+} it would be replacing.

The D_{Cu} % of 19.5Ga0.5Ce-LDO is lower than expected relative to its BET surface area because when it was exposed to the atmosphere for a prolonged time its calcined LDO morphology partially transformed back into a re-stacked LDH morphology (with a lower surface area than its original exfoliated LDH form). During D_{Cu} % measurement the sample is reduced again over a 2 hour period at 290 °C and then

oxidised by pure N_2O for one hour at 60 °C, however it is unclear if this would remove any LDH hydroxyl groups and reform the LDO morphology because the system was kept air-tight and no oxidant was introduced at 'calcining' temperatures. Additionally, the reduction temperature of Cu is higher for the samples that were exposed to the atmosphere for half a year (see Figure 10.1), implying that Cu^0 particles are less stable on a partially hydroxylated LDO support. The lower surface area and the potentially less-stabilising hydroxyl sections of support are observed to give a lower D_{Cu} % for the exposed samples; however, this applies to all samples in the Ce-series, presumably to a similar % extent. So the exposure to atmosphere does not explain why 19.5Ga0.5Ce-LDO is in very different trend locations in the BET surface area and D_{Cu} % trends. The pore size distribution trend is also not correlated to this anomaly (see Figure 8.28), both 35Zn20Ga- and 19.25Ga0.75Ce-LDO have similar average pore diameters but they do not experience such a large estimated % drop in D_{Cu} % relative to their BET surface area trend. At the time of writing this anomaly has no evidence-based explanation.

As previously mentioned, the potential of surface Ce to adsorb more coordinating N_2 in BET experiments likely doesn't contribute to the plateau in the D_{Cu} % trend. In Section 8.5.3 it was proposed that the amorphous defects (caused by excess Ce that does not occupy LDH lattice positions) have a similar surface area to the LDO morphology; this would also explain the plateau in the D_{Cu} % trend (in Figure 8.32).

In summary, Ce doping is observed to decrease the D_{Cu} % to varying degrees relative to 35Zn20Ga-r; unfortunately this data may have been affected by the LDH memory effect and BET surface area loss due to atmospheric exposure.

8.5.5 XAS analysis of reacted catalysts

The WGS reaction mechanism was investigated for both 35Zn20Ga-r and 12.5Ga7.5Ce-r by exposing both reduced catalysts to water vapour then CO subsequently (or CO

then water vapour); the reactions were kept at 180 °C, under an argon atmosphere and were purged with argon in between each step. At each step, in which water or CO was introduced, some sample was portioned off for XAS testing; these samples were labelled as H1, C2, C1 and H2 to denote their exposure order. A reduced sample that was exposed to just water vapour was labelled as '-rH1' and a reduced sample that was exposed to water then CO was labelled as '-rC2'. This is the opposite for the second permuatation of the experiment, a reduced sample that was exposed to only CO was labelled as '-rC1'; whereas, a reduced sample that was exposed to CO and then water was labelled as '-rH2'. Cu K edge XANES, Zn K edge EXAFS/XANES and Ce L_3 edge EXAFS/XANES was performed for all samples.

The same Gaussian-fitting method used to analyse the Ce L_3 XANES of 12.5Ga7.5Ce-LDH (see Section 8.4.5), using transitions assigned by Fernandes et al. and Shahin et al., was used to determine the Ce^{3+} content for the reduced and reacted samples in this Section. [294, 295] The Gaussian-fitting results are shown in Table 8.9 alongside LCF fitting data of $Ce(NO_3)_3$ and CeO_2 experimental EXAFS spectra (also collected on the I20 beamline using the same parameters as the samples from this work). The Ce L_3 edge of 19.25Ga0.75Ce-r was also analysed but it required 17 repeats of EXAFS due to its low Ce content; whereas, three repeats of the EXAFS analysis were only needed for 12.5Ga7.5Ce-r before the spectra were merged.

Table 8.9 shows that the LCF EXAFS fitting of experimental standards estimates a higher Ce^{3+} content than the XANES Gaussian fitting; however, the trends are in good agreement. As per Table 8.9, the standard reduction procedure used for all catalysts is estimated to reduce a substantial amount of Ce above that in the analogous LDH precursor e.g. the XANES Gaussian fitting for 12.5Ga7.5Ce-LDH and 12.5Ga7.5Ce-r are 21.0 and 31.1 %, respectively (see Section 8.4.5). Additionally, 19.25Ga0.75Ce-r has almost double the Ce^{3+} content than 12.5Ga7.5Ce-r; this could

Table 8.9: Ce L_3 edge XANES Gaussian-fitting and EXAFS LCF fitting of reduced and WGS-reacted 12.5Ga7.5Ce- and 19.25Ga0.75Ce-r samples.

Sample	XANES Ce^{3+} Gaussian component, signal ratio % of total [Ce^{3+} + Ce^{4+}]	EXAFS $Ce(NO_3)_3$ standard LCF component, signal ratio % of total [$Ce(NO_3)_3$ + CeO_2]
19.25Ga0.75Ce-r	63.0	86.3
12.5Ga7.5Ce-r	31.1	47.8
12.5Ga7.5Ce-rH1	36.8	46.4
12.5Ga7.5Ce-rC2	59.1	74.1
12.5Ga7.5Ce-rC1	65.0	76.1
12.5Ga7.5Ce-rH2	60.6	74.7

reflect that the majority of the Ce in 19.25Ga0.75Ce-LDH precursor was already in a Ce^{3+} 6-coordinated LDH substitution morphology, in line with the topotactic nature of LDH thermal transitions and the proposed critical Ce content theory (see Section 8.4.1).

On average for both the XANES and EXAFS fits for the transition from 12.5Ga7.5Ce-r to 12.5Ga7.5Ce-rH1 (Table 8.9) it appears that water exposure does not have a large effect on the oxidation state of Ce^{3+} when it was expected that water exposure would oxidise the catalyst. Throughout this section it is seen that water has a relatively small effect compared to the changes in oxidation state induced by CO; it is theorised that this is because the relative pressure of water in the experiment was much lower than that of CO because water was only introduced via a room temperature nitrogen bubbler. However, water is seen to oxidise Ce in the transition from 12.5Ga7.5Ce-rC1 to 12.5Ga7.5Ce-rH2. Upon exposure to CO, in both cases Ce is reduced substantially where the Ce^{3+} % of total Ce increases by $\approx$ 25 - 35 %. Whilst it was expected that CO would reduce some Ce that had previously been oxidised by water at 180 °C, it was surprising that CO reduced such a large content of Ce directly after the standard reduction procedure with 5 % H_2/N_2 (g) at 290 °C. This suggests that Ce-containing supports in the active catalyst have a high activity towards oxidising CO with labile

oxygen species because such supports are more reducible i.e. the formation of oxygen vacancies is more thermodynamically-favourable (Section 2.6). By comparison, the Zn and Cu oxidation states do not appear to follow a trend relative to the introduction of water or CO; see Table 8.10 and Figure 8.33.

Table 8.10: Ce L_3 edge EXAFS LCF fitting of reduced and WGS-reacted 12.5Ga7.5Ce- and 35Zn20Ga-r samples. The LCF components included simulated Zn (hcp) and ZnO (wurzite) spectra.

Sample	EXAFS model Zn^0 LCF component, signal ratio % of total [Zn^0 + ZnO]
35Zn20Ga-r	65
35Zn20Ga-rH1	56
35Zn20Ga-rC2	54
35Zn20Ga-rC1	58
35Zn20Ga-rH2	50
12.5Ga7.5Ce-r	51
12.5Ga7.5Ce-rH1	54
12.5Ga7.5Ce-rC2	62
12.5Ga7.5Ce-rC1	-
12.5Ga7.5Ce-rH2	56

The Zn K EXAFS spectra were fitted using the LCF of bulk hcp Zn metal and wurzite ZnO simulated EXAFS spectra; the results are shown in Table 8.10. Upon first impressions the Zn^0 signal components seem excessively high considering no Zn^0 is observed in the reduced PXRD patterns of 35Zn20Ga- or 12.5Ga7.5Ce-r (see Figure 8.24). Moreover Kattel et al. suggested Zn^0 was not stable under CO_2 hydrogenation conditions which would have an increased hydrogen partial pressure (highly reducing) relative to MSR; however, Kattel et al. did not investigate atmospheric pressures. [173]

It is possible Zn^0 is very disperse on the surface but unfortunately this data could not be compared to a Gaussian fitting of the Zn K edge XANES spectra because no conventional fittings were found in literature. Table 8.10 displays that all samples have a Zn^0 signal of component 50 - 65 % and that all that introduction of both

CO and water oxidise the sample; the only exception is when CO is introduced in the transition for 12.5Ga7.5Ce-rH1 to 12.5Ga7.5Ce-rC2. Additionally it appears that the Zn^0 is oxidised less relative to the original reduced sample Zn^0 content when Ce is doped into the catalyst; however, the 35Zn20Ga-r has a 11 % higher Zn^0 signal component than 12.5Ga7.5Ce-r to begin with. Unfortunately, the Zn K edge data file for 12.5Ga7.5Ce-rC1 was corrupted so the potentially-reducing effect of CO on Zn in Ce-doped catalysts cannot be confirmed and the accuracy of the entire Zn^0 signal component data cannot be compared to other estimations. Further analysis of the Zn K EXAFS spectra for the reduced and WGS-reacted catalysts is required in future work; such work would likely require using a wide range of experimental comparisons and Zn-containing models (that more accurately fit the real, expected structure of the reduced catalysts).

LCF fittings of the Cu K edge EXAFS for the reduced and WGS-reacted samples suggested the samples were all Cu^0. However, despite pre-edge analysis being a developing field, Giordanino et al. have theorised that the Cu K edge pre-edge peak at $\approx$ 8982 - 8984 eV incident energy is caused by the Cu^+ 1s $\longrightarrow$ 4p transition. [312] Experimentally this peak is seen in all experimental Cu K edge XAS spectra in Figure 8.33; including for the Cu^0 reference foil. Therefore, it is proposed that all Cu in the samples is in the Cu^0 oxidation state because all Cu XAS are very similar.

XAS analysis of the CuZnGa(Ce) LDH-derived catalysts under various WGS conditions has shown that the Ce^{x+} in the sample can partake in redox reactions with both water and CO. No trends in the redox of Cu^+/Zn^0 were seen, whilst Zn^0 was observed in some capacity, it is uncertain how stable it would be in MSR conditions considering the high excess of water compared to the experiments in this section. In-situ MSR experiments need to be conducted to determine the effect, if any, that Zn^0 has upon activity/selectivity.

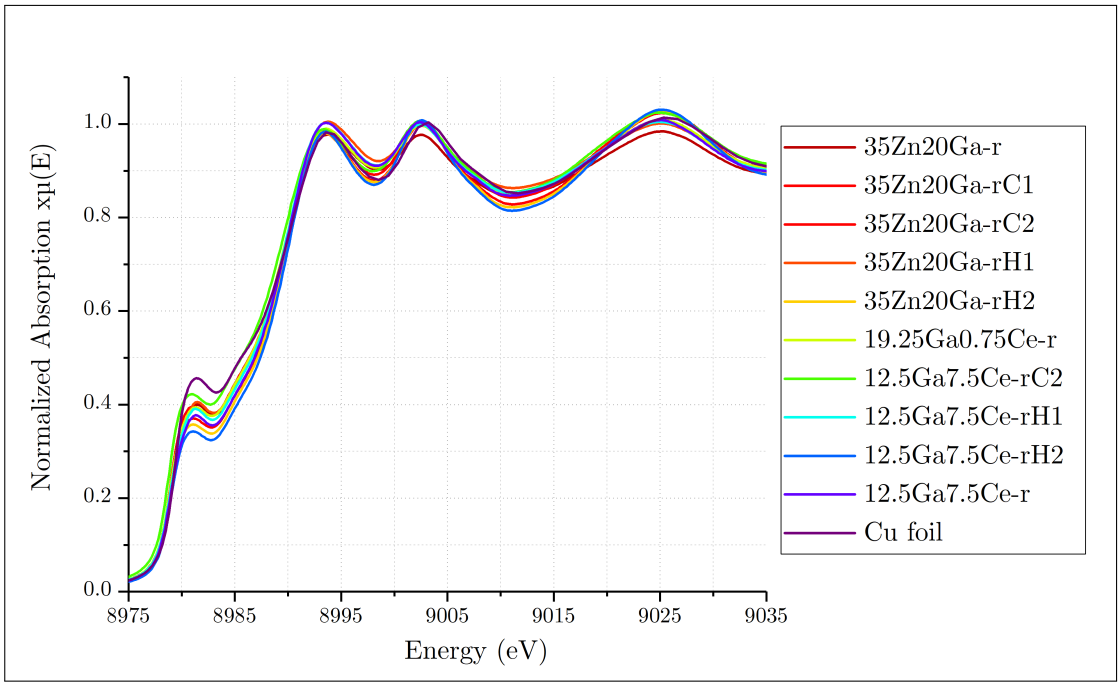


Figure 8.33: The experimental Cu K XAS analysis of the reduced/WGS-reacted catalysts and Cu foil.

8.5.6 MSR catalytic activity of the Ce reduced series

The Ce-doped AMO-LDHs were calcined and reduced to yield active MSR catalysts; the hydrogen production rate, CO production rate and H_2:CO mol ratio from the catalytic tests are displayed in Figures 8.34 and 8.35. The reactant flow rate in the catalytic tests for the Al and Ga series was slightly higher than that used for the Ce-doped series; therefore, both the 0.075 and 0.1 mL.min^{-1} H_2O/CH_3OH flow rates were used with 35Zn20Ga-r to allow for comparison. When the reactant flow is slowed (or the WHSV is decreased) the residence time of the reactants in the reactor, and on the catalyst surface, is increased. [313, 314] Therefore, the MSR and RWGS reactions were expected to have higher conversion percentages compared to the Al and Ga series i.e. both H_2 and CO production rates were expected to increase with a decrease in flow rate for the same weight of catalyst. [313, 314] This is what was observed for the 35Zn20Ga-r catalytic tests at the different flow rates, see Figure 8.34.

In addition to the Ce-doped catalysts series, a physical mixture of 35Zn20Ga-r and CeO_2 (that was ground together in a mortar and pestle) was tested for its MSR activity; the Cu:Ce wt % ratio of the physical mixture was approximately equivalent to 19.25Ga0.75Ce-LDO (based on ICP-MS data and the molar mass of pure ceria). Surprisingly this catalyst was less active and produced more CO than 35Zn20Ga-r, as did 19.5Ga0.5Ce-r. For the physical mixture the reduction in MSR activity could have been caused by the decrease in Cu content relative to pure 35Zn20Ga-r that came with balancing the Cu:Ce ratio. The increase in CO content for the physical mixture may arise due to an increase in catalyst volume (increasing residence time) and/or the introduction of an oxide surface that is not in contact with Cu^0. In literature it was theorised the WGS and RWGS reactions could happen on an oxide surface, whereas a metal-support interface is required for MSR (see Sections 3.4 and 3.5); therefore, reducing Cu content and introducing pure CeO_2 could have reduced the (MSR+WGS):WGS active site ratio. [20]

All of the Ce-doped catalyst series decreased both MSR activity and CO production relative to 35Zn20Ga-r (at the same WHSV) except for 19.5Ga0.5Ce-r; it does fit the inverse correlation of Ce content with MSR activity but it produced more CO than 35Zn20Ga-r. 19.5Ga0.5Ce samples have been anomalous throughout the study e.g. in the BET surface area analysis. Figure 8.35 demonstrates that a 0.75 - 2 % mol doping of Ce into a CuZnGa AMO-LDH-derived catalysts can significantly increase the H_2:CO production ratio. The most selective catalyst, 19.25Ga0.75Ce-r, increased the H_2:CO ratio by + 47.6 % but decreased the H_2 production rate by 19.3 % compared to 35Zn20Ga-r (at the same WHSV). The prominent observations are that an increase in Ce content correlates with a decrease in MSR activity and that an optimal Ce loading can suppress RWGS CO formation.

The Ce series have a lower BET surface area and D_{Cu} % than that of the

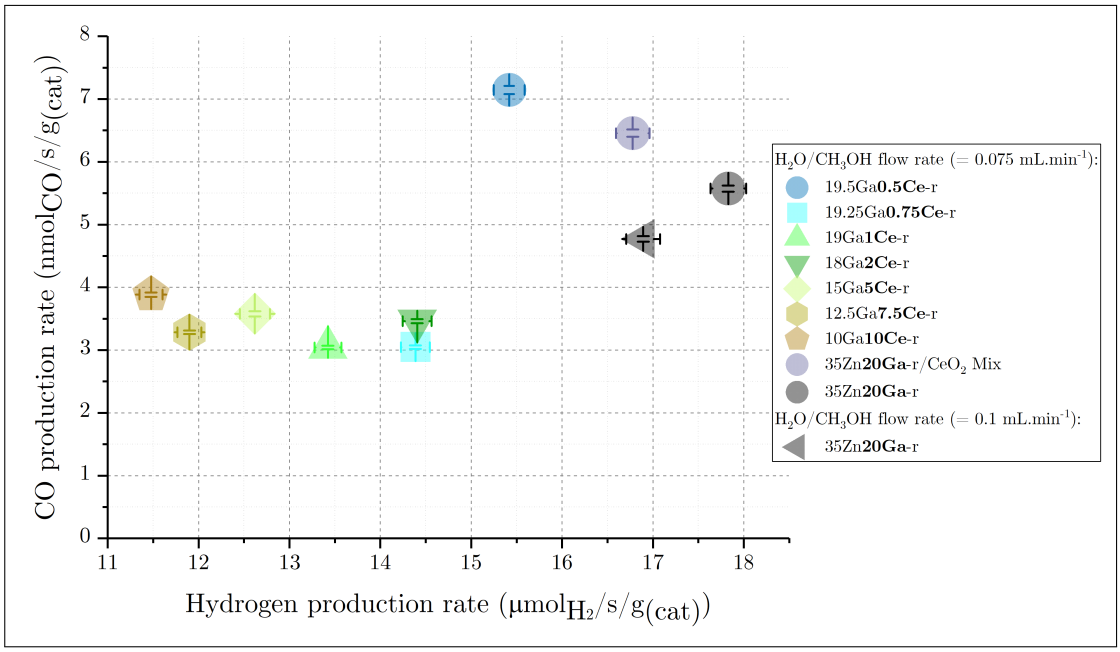


Figure 8.34: The MSR catalytic test results of the reduced Ce-based series; the hydrogen production rate and CO production rate units are $\mu mol_{H_2}.s^{-1}.g_{cat}^{-1}$ and $nmol_{CO}.s^{-1}.g_{cat}^{-1}$, respectively. Tested at 180 °C for 5 hours with 200 mg of catalyst, a N_2 gas flow of 10 mL.min^{-1} and a 0.075 mL.min^{-1} liquid flow of water:methanol solution (1.1:1 mol ratio). WHSV = 2.03 h^{-1}. Error bars (x/y) are shown inverted within the data point symbols.

35Zn20Ga-r which explains why they have less MSR activity under the same conditions. Within the Ce series the MSR activity decreases with increasing Ce content. The BJH pore modal diameter of the LDO series decreases with Ce content (see Section 8.5.3), which theoretically would lead to an increase in internal mass transfer limitations in the heterogeneous catalytic system assuming a partially-topotactic reduction i.e. gaseous reactant movement through catalyst pores to active sites becomes sterically less favourable. [315] Karadeniz et al. use computational modelling to show how a decrease in catalyst pore diameter, from 500 to 250 Å, decreases the WGS activity (when other conditions are kept constant). [316]

PXRD and XAS modelling suggest a substantial amount of Ce^{4+} occupies non-LDH structures in the precursors but upon reduction and surface reactions with water and CO, a Ce redox reaction can occur where a higher Ce^{3+} content forms

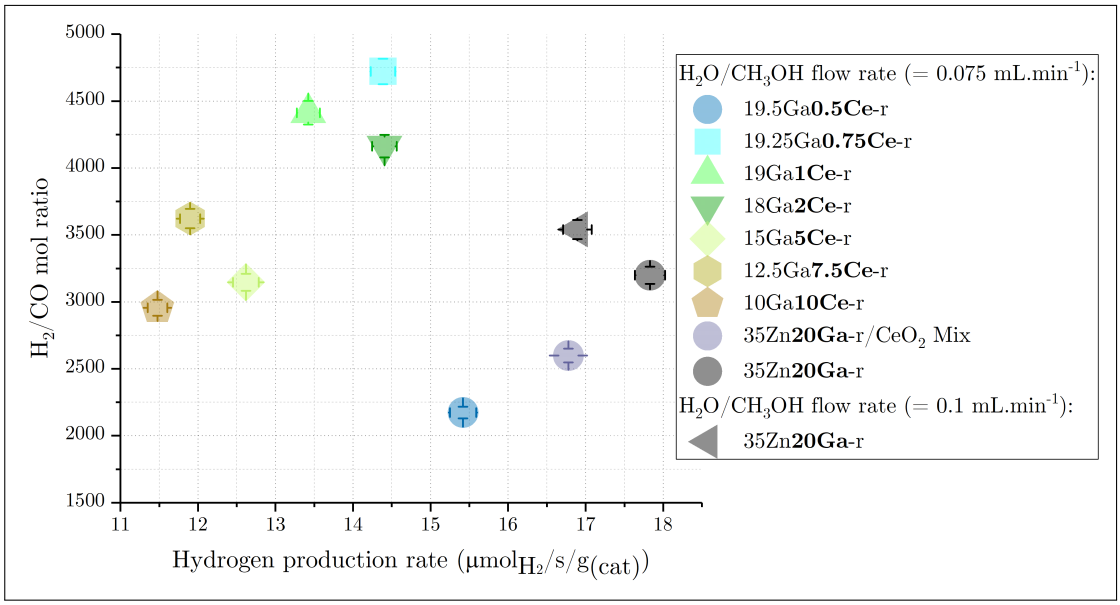


Figure 8.35: The H_2:CO mol ratio produced by the reduced Ce-based series during MSR (as a function of their hydrogen production); the hydrogen production rate's units are $\mu mol_{H_2}.s^{-1}.g_{cat}^{-1}$. Tested at 180 °C for 5 hours, with 200 mg of catalyst, a N_2 gas flow of 10 mL.min^{-1} and a 0.075 mL.min^{-1} liquid flow of water:methanol solution (1.1:1 mol ratio). WHSV = 2.03 h^{-1}. Error bars (x/y) are shown inverted within the data point symbols.

(see Sections 8.4.1, 8.4.5 and 8.5.5). Unfortunately the structure of the reduced Ce catalysts has not been observed or modelled and no Ce phases were seen in the reduced materials' PXRD. Therefore, it is possible surface Ce_xO_y particles could form on the surface of the active catalysts blocking Cu active sites and decreasing the H_2:CO ratio by decreasing the ratio of (MSR+WGS):WGS active sites; this would fit with both the trends of H_2 production and H_2:CO, which decrease with increasing Ce content (seen in Figure 8.35). However, further investigation of the reduced catalysts and modelling of their EXAFS data would be required to confirm this theory. Nonetheless, BJH pore modal diameter gives a partial experimental explanation for the decrease in MSR activity with increasing Ce content.

Despite an excess of Ce having a negative effect upon both activity and selectivity, there appears to be an optimal ratio of Ce doping, 0.75 - 2 mol % of the AMO-LDH

precusor (just above the critical Ce content that forms non-LDH structures), that suppresses CO production relative to a non-doped CuZnGa catalyst. Using XAS analysis, in Section 8.5.5, it was observed that the Ce content in 12.5Ga7.5Ce-r could readily oxidise CO in a redox reaction at 180 °C; whereas, the Zn^0 trend did not seem to be affected much by the prescence of Ce.

As such, it is theorised that the H_2:CO ratio decreases with increasing Ce content because there is a decrease in the Cu-support interface and the (MSR + WGS):(WGS) active site ratio. However, there is a peak in H_2:CO ratios at low Ce content relative to the non-doped CuZnGa catalysts because Ce increases the oxygen mobility of the catalyst, breaking the WGS microreversibilty principle by altering the catalyst surface and providing a higher affinity for CO oxidation on the surface using oxygen provided via the dissociation of excess water.

Figure 8.36 shows that the peak MSR activity of the each catalyst in the Ce-based series follows a similar trend to that of its BET surface area and D_{Cu} % as expected (see Figures 8.27 and 8.32). Additionally, it can be observed that Ce-doping does not seem to have a positive or negative effect upon the catalytic stability of 35Zn20Ga-r (see Figure 8.36). This is likely because the BET surface area of the Ce-based AMO-LDO is dictated by the layered morphology of the CuZnGa-LDO phase (assuming topotactic reduction), which indicates that the non-LDH phase that Ce forms above the critical Ce content does not decrease the thermal stability of the catalyst. It could be possible that the introduction of extra O^{2-} adatoms (and M-O bonds) by the 8-coordinated Ce^{4+} substituted defect model (as proposed in Section 8.4.5) could possibly offset the loss of lattice energy caused by Ce-induced sterically-unfavourable distortions.

8.5.7 Other lanthanide dopants

Other lanthanide series elements were doped into CuZnGa AMO-LDHs using

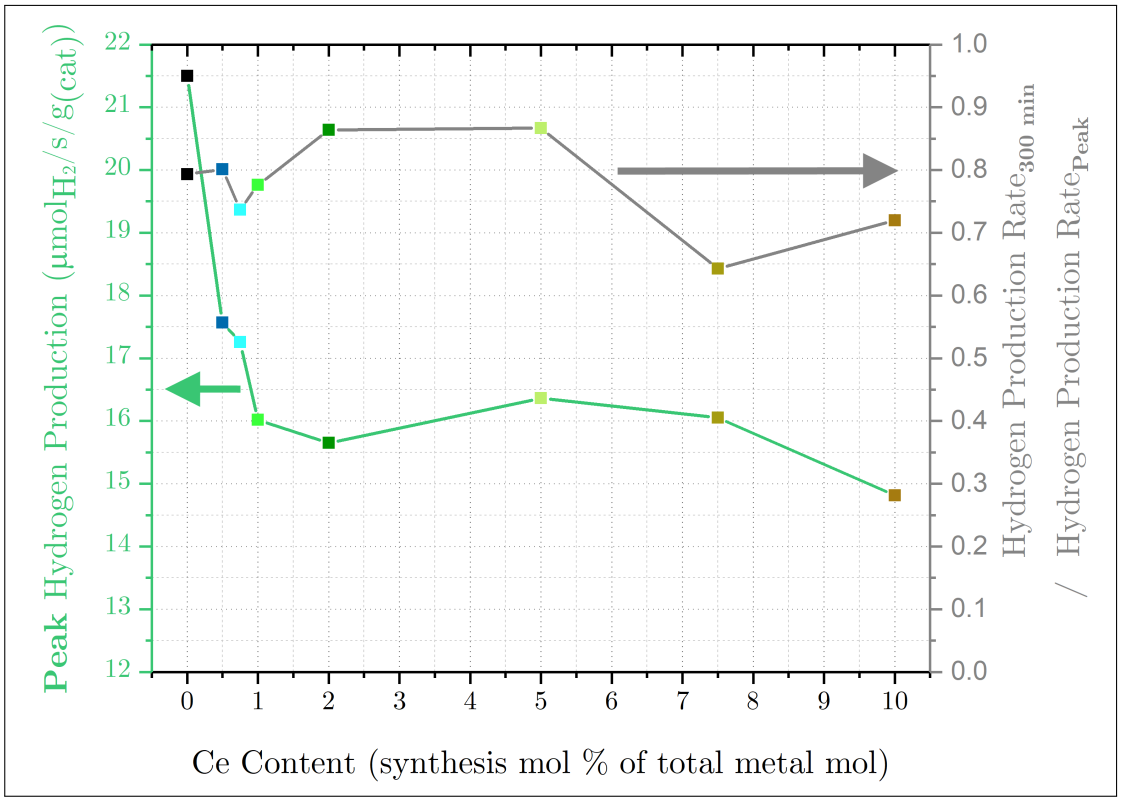


Figure 8.36: The maximum hydrogen production rate ($\mu mol_{H_2}.s^{-1}.g_{cat}^{-1}$) observed for each reduced Ce-based catalyst, shown against the (Hydrogen production rate at 300 mins / The peak hydrogen production rate) ratio. Tested at 180 °C for 5 hours, with 200 mg of catalyst, a N_2 gas flow of 10 mL.min^{-1} and a 0.075 mL.min^{-1} liquid flow of water:methanol solution (1.1:1 mol ratio). WHSV = 2.03 h^{-1}.

the standard coprecipitation method and metal nitrate hydrate precursors; the same doping ratio as Ce in 19.25Ga0.75Ce-LDH was used. This was investigated to see if other lanthanides would have a similar effect on the MSR activity via structural and/or electronic effects (compared to 19.25Ga0.75Ce-r). All crystalline structures in the lanthanide-doped AMO-LDHs were composed of $3R_1$ and $3R_2$ LDH polytypes (see Figure 8.37). The non-Ce, lanthanide-doped catalysts gave much lower H_2:CO selectivity in MSR catalysis (see Figure 8.38).

All the non-Ce, lanthanide-doped catalysts have a very similar H_2:CO production rate that is similar to that of non-doped 35Zn20Ga-r, $\approx$ 3200 mol_{H_2}:mol_{CO}; whilst, all catalysts except 19.25Ga0.75La-r have an activity substantially lower than 35Zn20Ga-

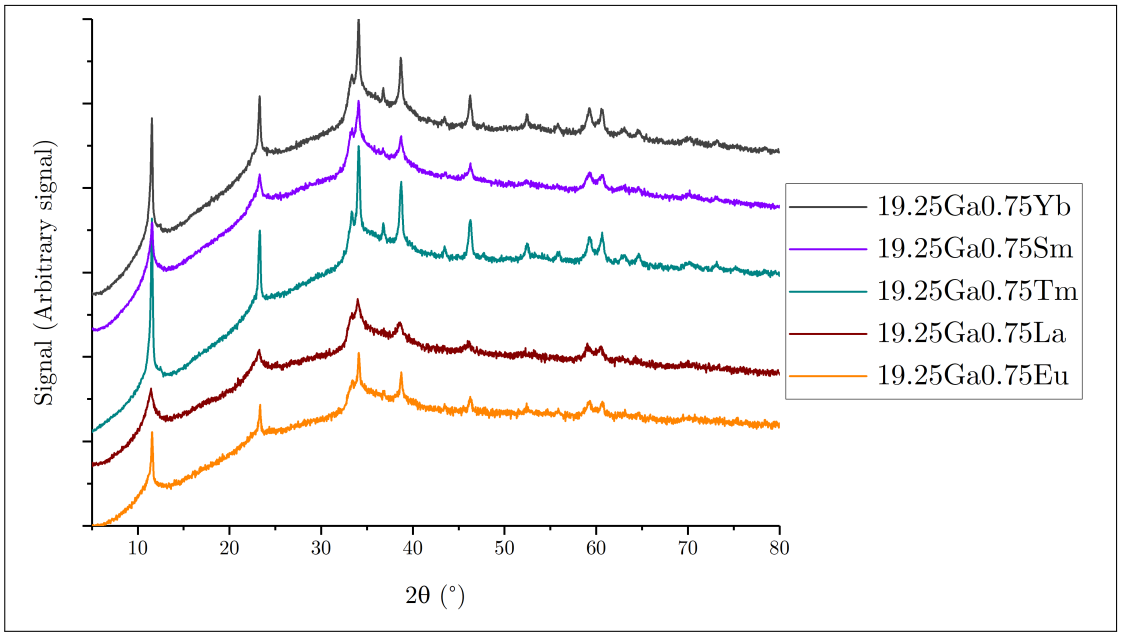


Figure 8.37: PXRD patterns of the Ln-based AMO-LDH series.

r (see Figure 8.38). This indicates that the CO suppressing effect that an optimal Ce content can introduce to a CuZnGa-based catalyst, is not shared by other lanthanide oxides. This is likely because other lanthanide oxides do not have as high an oxygen mobility, or cannot participate as readily in redox with CO (as CeO_2 can); similar observations in other oxidation catalytic reactions have been observed (see Figure 8.39). [317]

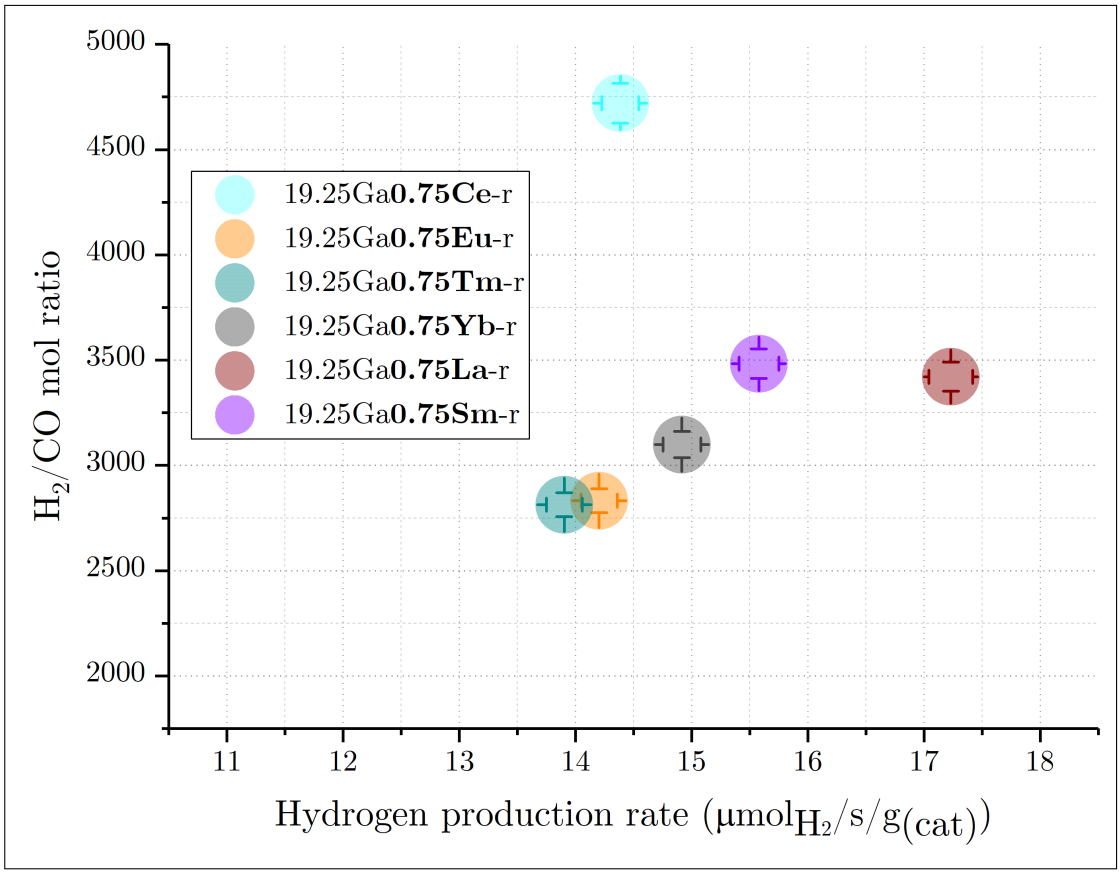


Figure 8.38: The MSR catalytic test results of the reduced lanthanide-doped, LDH-derived series; the hydrogen production rate and CO production rate units are $\mu mol_{H_2}.s^{-1}.g_{cat}^{-1}$ and $nmol_{CO}.s^{-1}.g_{cat}^{-1}$, respectively. Tested at 180 °C for 5 hours with 200 mg of catalyst, a N_2 gas flow of 10 mL.min^{-1} and a 0.075 mL.min^{-1} liquid flow of water:methanol solution (1.1:1 mol ratio). WHSV = 2.03 h^{-1}. Error bars (x/y) are shown inverted within the data point symbols.

8.6 Ce chapter summary

It can be concluded that an optimal Ce doping can further improve upon the H_2:CO selectivity of the CuZnGa LDH-derived catalyst series despite the Ce series being tested at a lower WHSV, 2.03 h^{-1}. This selectivity is theorised to be improved by the Ce decreasing the kinetic and/or thermodynamic energy cost associated with oxygen vacancy formation and oxygen mobility across the support; increasing the rate of CO oxidation in a way that breaks the microreversibility principle associated with the catalysis of WGS. It is suggested that further, in-depth kinetic studies of in-situ

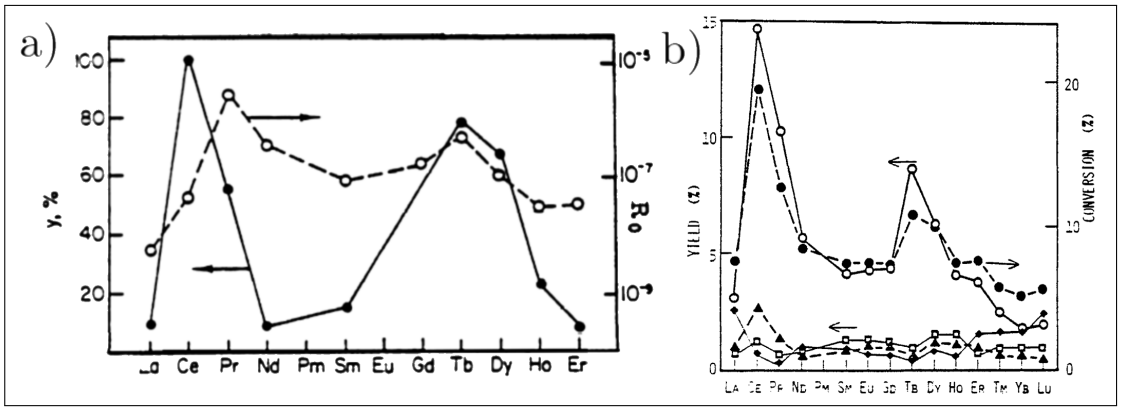


Figure 8.39: a) Propylene oxidation activity of lanthanide oxides; y = overall yield and R_0 = initial reaction rate. b) n-butane oxidation activity of lanthanide oxides; filled circle = n-butane conversion, empty circle = CO_2 yield, empty square = CO yield, filled triangle = hydrocarbon yield, filled diamond = n-butenes. Figure used with permission from: M. P. Rosynek, *Catalysis Reviews*, 1977, **16**, 111-154.©1977 Informa UK Ltd.

MSR reactions catalysed by these Ce-doped materials are required to fully explain this phenomenon.

Unfortunately, Ce doping was found to decrease the overall H_2 production rate of the catalysts; this was likely due to decreases in the pore diameter or D_{Cu} % via thermally-induced Ce-containing phase decoration.

Interestingly, XAS, EDX, PXRD and DFT analysis alluded to the existence of a 'critical Ce content', above which Ce no longer occupied LDH lattice positions and favoured disperse, amorphous phases. EXAFS modelling suggests this phase is a defective, 8-coordinated Ce^{4+} centre within the LDH layer. A simulated fit of 20 % 6-coordinated Ce^{3+} (in LDH lattice positions) and 80 % 8-coordinated Ce^{4+} (in defective layer positions) was modelled and found to match the experimental XANES spectrum of 12.5Ga7.5Ce-LDH well; which correlated with the Ce^{3+}:Ce^{4+} ratio determined by experimental XPS and XANES Gaussian fittings, 23.5 and 21.0 %, respectively. This was the first time in literature that a lanthanide-doped LDH structure was analysed in-depth with techniques other than PXRD or time-resolved

photoluminescence analysis. Further experimental investigation is required to rule out the existence of bulk CeO_2 decoration (synchrotron X-ray pair distribution function analysis is planned at the time of writing) and the reduced structure of the catalysts is yet to be investigated.

Chapter 9

Conclusion

This work has shown that the high elemental dispersion and surface areas of novel AMO-LDHs have allowed the synthesis of highly active and selective MSR catalysts. This was possible via the topotactic thermal transitions of LDHs. All experiments were carried out at low temperatures to screen their usefulness for proton exchange membrane fuel cell applications; but at high enough temperatures to observe the inherent CO production trends of each catalyst.

It was found that the active copper phase could be diluted with magnesium to make the catalysts more economically viable whilst increasing copper dispersion and MSR activity.

The use of gallium as the layered double hydroxide backbone, alongside a minimal M^{3+} content in the LDH layer, was discovered to increase Cu^0 particle stability during MSR catalysis leading to a higher average MSR activity over a 5 hour reaction.

A small, optimal amount of cerium doping was found to increase the H_2:CO selectivity during MSR catalysis. This CO suppression effect was likely due to a cerium-specific redox reaction, that was uncovered during X-ray absorption spectroscopy analysis under water gas shift reaction conditions.

Most importantly, the highest H_2:CO production ratios in MSR literature were

achieved (see Table 9.1), despite using longer residence times and lower water content (that increase RGWS CO production) compared to the literature studies.

Table 9.1: The highest H_2:CO mol ratios in MSR literature.

Reference	Catalyst	Temperature (°C)	Reactant H_2O:MeOH (mol ratio)	WHSV* (h^{-1})	H_2 Productivity* ($\mu mol_{H_2}.s^{-1}.g_{cat}$)	Product H_2:CO* (mol ratio)
[104]	Cu/CeO_2	220	1	3.09	37.3	747
[106]	CuZnAl-MMO	250	1.3	1.03	N/A	1250
[104]	CuZnAl-MMO	220	1	3.09	19.8	1500
[77]	$Cu/ZrAlO_x$	220	1.5	7.09	128	3000
This work	35Mg-r	180	1.1	5.41	17.8	4548
This work	35Zn20Ga-r	180	1.1	2.70	16.9	3541
This work	19.25Ga0.75Ce-r	180	1.1	2.03	14.4	4721

* = calculated in this work (unless exact H_2/CO compositions given), using data from the reference, the ideal gas equation and assuming CO (mol %) = $\frac{CO\ mol}{CO\ mol + CO_2\ mol\ (+\ hydrocarbon\ product\ mol)}$, as is reported in most literature reports. [76, 79, 84–86]

Recent advances in the studies of PEMFC electrodes include the observations of Lee et al., where a PtRuNi/C anode showed a 52 % higher current density (in a 0.6 V PEMFC system), than a standard Pt/C anode, when the CO concentration in the feed was 10 ppm. [318] Despite such advances, Sung et al. clearly demonstrated for a similar 'CO-resistant' 0.6 V low temperature PEMFC system (with a PtRu anode), 25 ppm of CO can almost half the current density compared to a pure hydrogen feed. [319] In this work's research plan a low CO production was targeted as the main goal; therefore, 10 ppm was chosen as the limit. [20, 21, 141]

Additionally, the research plan highlighted the 'Toyota Mirai 2017®' hydrogen fuel cell powered car as a hydrogen production benchmark; it requires ≈ 137,000 $\mu mol_{H_2}.s^{-1}$. [201] Unfortunately, based on the H_2 production rates achieved in this work; only much less powerful applications would be currently feasible. For example, a 500 W electrical device that is powered by an on-board MSR-PEMFC system would require ≈ 5,000 $\mu mol_{H_2}.s^{-1}$, still with a maximum CO concentration of 10 $ppm.s^{-1}$.

250 g of MSR catalyst with an activity of 18 $\mu mol_{H_2}.s^{-1}.g_{cat}^{-1}$ MSR catalyst and

a 1,280:1 H_2:CO ratio, using a scaled-up version of the MSR catalytic method used in this work (see Section 5.15), could almost achieve the required 500 W with < 10 ppm CO. However, it must also be considered that the H_2 and CO concentrations are heavily dependent on the addition of an inert carrier gas. Springer et al. modelled a PEMFC at constant 0.6 V and the results show an almost exponential drop in current density with a decreasing hydrogen mol fraction; from 0.4 to 0.05 H_2 mol fraction the current density drops by $\approx$ 45 %. [320] The H_2 mol fraction in the gas stream, of the aforementioned example of a scaled-up version of this work, would be ≈ 0.013 i.e. much lower than the H_2 mol fractions modelled by Springer et al., so it would likely result in a very low current density.

It is unlikely LDH-derived MSR catalysts will be commercially viable any time soon. However, this work applied a novel aqueous miscible organic solvent method, elucidated the structure of the previously unsolved lanthanide-doped layered double hydroxide and produced the best MSR H_2:CO ratios in literature; it also has contributed significant insights into how this selectivity was achieved. Overall, this research project can be considered successful because it provides new avenues for catalyst development and a strong basis for any future methanol steam reforming research.

Chapter 10

Appendix

This appendix includes work that had no clear outcome or experimental conclusion e.g. TPR of the Ce LDO series was made invalid by inconsistent sample exposure to atmospheric conditions (throughout the series).

10.1 TPR analysis of the Ce LDO series

The TPR analysis of the Ce-doped LDO series yielded complicated results, see Figure 10.1, as with the Ga-based series (from Section 7.3.3) multiple peaks were visible.

The areas of the peaks were not consistent with the Cu content of the samples; it is possible that Zn or Ce reduction could contribute to the TPR signal but neither Zn nor Ce correlated with the TPR peak area. Zn and Ce oxidation states for both the 19.25Ga0.75Ce- and 12.5Ga7.5Ce-r samples were also investigated by XAS, see Section 8.5.5. In literature, higher surface area ceria has a lower reduction temperature shoulder than lower surface area ceria, these shoulders are $\approx$ 400 and 450 °C for /*approx* 44 and 3 $m^2.g^{-1}$ BET surface area CeO_2 respectively, so it is not unreasonable to assume that reduction of very disperse Ce^{4+} in the Ce-doped LDOs contribute, in an unknown extent, to the TPR profiles in Figure 10.1. [321,322] More importantly, as discussed in Section 7.3.3, it was not established how the mass of

sample used affected the error in TPR peak area measurement; therefore, the peaks cannot be quantified to give accurate data. However, the TPR peak positions can still be used to determine the reducibility of major Cu species in the sample.

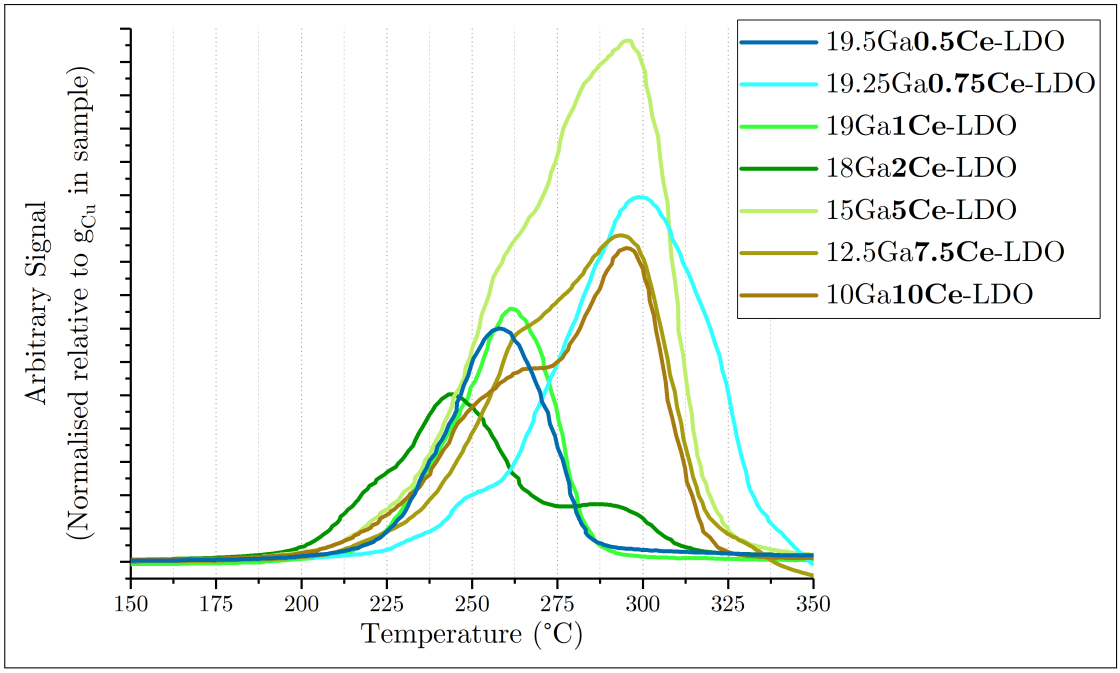


Figure 10.1: The TPR analysis of the calcined Ce-based AMO-LDO series; measured with a 10 °C.min^{-1} heating rate.

Each Ce-doped LDO appears to have two reducible Cu environments, one at ≈ 240-260 °C and a second at ≈ 280-300 °C; 18Ga2Ce-LDO also has a reduction shoulder starting at 200 °C. The non-doped 35Zn20Ga-LDO sample had a 200 °C reduction shoulder and two peaks at ≈ 230 and 245 °C (see Figure 7.12). It is not immediately obvious why 18Ga2Ce-LDO has a reduction shoulder that resembles that of the non-doped LDO when the other Ce-doped LDOs do not. Additionally, 19.25Ga0.75Ce-LDO appears to give an anomalous spectra in regards to its shape and position, its TPR profiles more resembles the other TPR profiles of 15Ga5Ce-, 12.5Ga7.5Ce- and 10Ga10Ce-LDO as opposed to the other lower Ce content LDOs. It is worthwhile to note that 19.25Ga0.75Ce-, 15Ga5Ce-, 12.5Ga7.5Ce- and 10Ga10Ce-LDO were analysed via TPR analysis half a year, or more, after their synthesis, over

this time period the ChemBET apparatus used for the analysis was repaired multiple times. It is unlikely the TCD and thermometer set-up in the TPR equipment changed very significantly for the temperature (°C) measurement but the TCD signal sensitivity may have changed with the introduction of a new detector despite a calibration being performed for each experiment. The factor that likely causes the anomaly is the half year delay in the samples' measurements, the calcined samples were kept in a sealed vacuum desiccator. However, after a half a year of the vacuum desiccator not being opened, its grease seal may have failed because the usual audio prompts of a vacuum filling upon opening the desiccator's glass tap could not be heard (normally this sound lasts 30 seconds or so). All the samples were left on a continuous 10 mbar vacuumed overnight but the calcined samples may have reabsorbed water and CO_2 from the atmosphere. Literature PXRD studies of the LDH 'memory' effect have shown that calcined LDH samples (even when calcined at high temperatures to MMOs) can reabsorb water from the atmosphere and reform LDH structures over the course of days or months depending on the humidity. [254–256] Therefore, the TPR analysis of 19.25Ga0.75Ce-, 15Ga5Ce-, 12.5Ga7.5Ce- and 10Ga10Ce-'LDO' may be more akin to the TPR profiles for their respective, defective LDH structures.

Regardless, the TPR profiles of the 19.5Ga0.5Ce-, 19Ga1Ce- and 18Ga2Ce-LDOs indicate that the lower-temperature Cu reduction peak occurs at a higher temperature for Ce-doped samples compared to 35Zn20Ga-LDO. The lattice potential energies per mol of M^{x+}-O^{2-} bond (not per mol of oxide) for Ga_2O_3, Ce_2O_3 and CeO_2 are +5,197, +4,221 and +4,814 kJ.mol$^{-1}_{M-O}$, respectively. [241] This indicates Ga^{3+} forms stronger bonds with oxygen than $Ce^{3+/4+}$ due to it being a smaller, harder cation with electron orbitals that can overlap more efficiently with those of hard O^{2-} anions. Based on this, it would be expected that the replacement of Ga with Ce in the structure would reduce the reduction temperature because the activation energy required to break the average lattice M-O bond in the structure, to release/reduce the disperse CuO_x units,

would decrease. However, as shown by the DFT models modelled from XAS results, in Section 8.4.5, the introduction of Ce^{4+} likely introduces extra oxygen species in the form of defects, which is in-line with the expected co-ordination number of Ce^{4+} in oxides; introducing extra M-O bonds would have an effect on the lattice energy and, therefore, the energy to remove Cu from the lattice. The lattice potential energies per mol of metal cation (not per mol of oxide) for Ga_2O_3, Ce_2O_3 and CeO_2 are +7,796, +6,332 and +9,628 $kJ.mol^{-1}_{metal}$, respectively. [241] It can now be seen that ceria has the highest lattice energy per mol of metal. The situation is far from simple, as each Cu environment in the LDO structure may have a slightly different number and type of bonds that need to be broken to access it; additionally, it is not clear whether redox of Ce or Zn could occur alongside the reduction of Cu. Additionally, if the excess Ce, that resides outside of the LDH/LDO structure, decorates the LDO surface then the Cu in the LDO is less accessible for reduction because more energy will be required to break the required bonds for it to leave the 'buried' lattice position; as mentioned in Section 8.4.1 the Ce lattice position is not known for the LDO materials and further techniques are needed to understand it.

Based on the experimental TPR data from Figure 10.1, it is observed that Ce-doping into CuZnGa AMO-LDHs appears to slightly increase the reduction temperature for the initial reduction of Cu^{2+} to Cu^0 for the LDO materials; this could be caused by the additional O^{2-} added to the calcined, amorphous LDO/MMO materials via the introduction of Ce^{4+}. The oxidation and co-ordination states of the materials are explored further in the XAS and DFT modelling analysis, see Scetion 8.4.5.

10.2 DRIFTS analysis of the Ce reduced series

In-situ DRIFTS experiments were screened for quantifiable differences in the time-lapsed spectra; the goal was to try and obtain insight into the MSR reaction for the non-doped and Ce-doped CuZnGa LDH-derived catalysts. Figure 10.2 displays

four experimental screenings using various combinations of catalyst and isotope labelled reactants. The catalysts were reduced under reaction conditions, next the cell temperature was set at a constant 180 °C, then saturated with methanol vapour; the methanol flow was stopped before a flow of water vapour in nitrogen was started at the same time as the DRIFTS collection. Figure 10.2 shows that frequencies associated with methanol decrease with time, as was expected. Figure 10.3 displays selected peaks' maxima in the x and y axis, from Figure 10.2, and was plotted to track shifts and intensity changes of different infra-red transitions. Figure 10.3 was also baseline corrected so that the effect H_2O concentration had on the signal of the methanol signals was minimised.

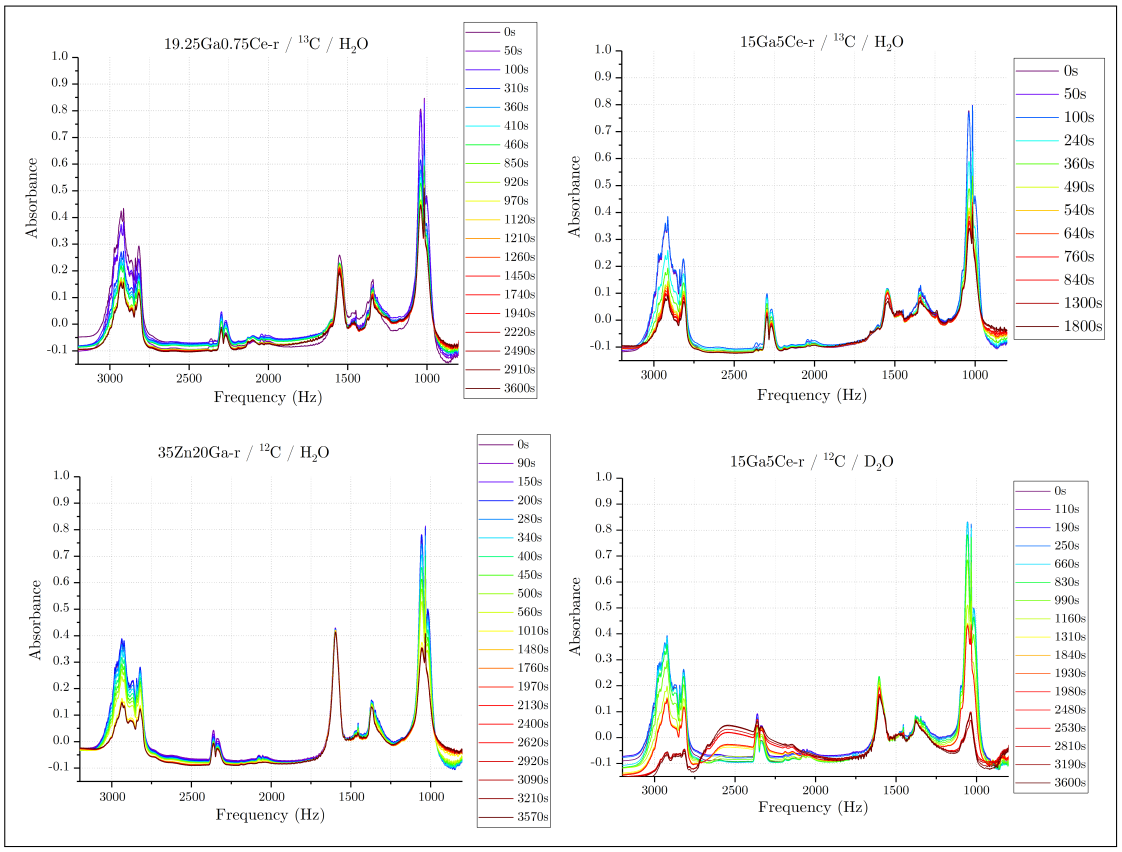


Figure 10.2: Baseline-corrected DRIFTS spectra for various LDH-derived catalysts at 180 °C. Each sample was saturated with a flow of $^{12/13}CH_3OH/N_2$ (g) before measurement. Time = 0 s coincides with the replacement of the $^{x}CH_3OH/N_2$ (g) flow with a $^{1/2}H_2O/N_2$ (g) flow.

The notable transitions in Figures 10.2 and 10.3 include methanol C-H stretching (2800 - 2980, ≈ 2050 and 1455 - 1479 cm^{-1}) methanol C-H bending (≈ 1450 cm^{-1}), methanol O-H bending (1300 - 1400 cm^{-1}), methanol C-H rocking (1050 - 1100 cm^{-1}), methanol C-O stretching (1010 - 1030 cm^{-1}), water O-H bending (1654 cm^{-1}) and background noise (2250 - 2350 cm^{-1}). [323] When ^{13}C-isotope methanol was used in the DRIFTS experiments most infra-red peaks associated with C-H stretching/bending and C-O stretching shifted to slightly lower frequencies by ≈ 5 - 20 cm^{-1}, this was most prominent for signals at 1060 cm^{-1} or lower; this difference in the IR spectra of $^{12}C/^{13}C$-methanol was also observed by Ott et al. [324] These shifts occur because the frequency of the C-X stretching mode correlates to the square root of the reciprocal of the C-X system's reduced mass; therefore, increasing the isotopic mass of C will decrease the stretching frequency. An even more noticeable isotope effect is observed in Figure 10.2 when D_2O is introduced; the O-D stretching frequencies are very broad and appear at 2000 - 2600 cm^{-1}.

Beyond the isotopic effects no significant difference in the methanol stretching, bending or rocking modes was observed between the experiments. 19.25Ga0.75Ce-r and 15Ga5Ce-r were both tested under the exact same DRIFTS conditions with ^{13}C-methanol and H_2O but no effect related to the Ce concentration was observed. The rates of change in the DRIFTS signals is not a very reliable metric to quantify any effect on the MSR mechanism step rates; this is because the room temperature and the gas flow rates (through the liquid bubblers) were not kept constant between experiments due to the completely manual nature of the gas flow valves and bubbler set-up. Unfortunately, the water and methanol DRIFTS screening experiments in Figures 10.2 and 10.3 did not provide any insight into Ce's effect on the MSR mechanism; however, improved experiments with consistent flow rates and a lower amount of changing variables may be able to offer insight in the future.

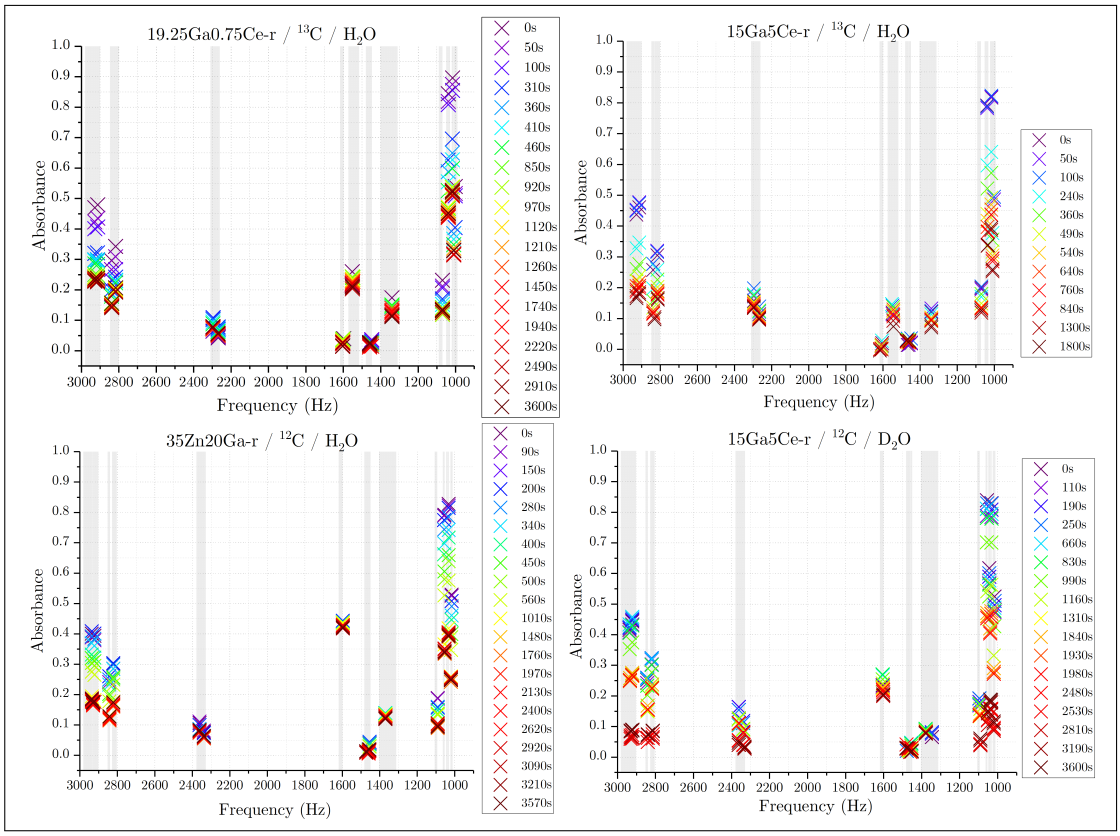


Figure 10.3: A representation of Figure 10.2 where the peaks of various IR absorptions are highlighted.

Similar experiments were conducted where the catalysts were reduced under reaction conditions, before the cell temperature was set at a constant 25 °C, then saturated with 1 % CO/N_2; the CO flow was stopped before a flow of water vapour in nitrogen was started at the same time as the DRIFTS collection. Figure 10.4 displays the collected data in these experiments, the increase in water O-H stretching (3200 - 3600 cm^{-1}) and bending (1654 cm^{-1}) modes with time is obvious and expected. These DRIFTS experiments were planned to observe any potential differences in the adsorbed CO infra-red signals related to the catalyst. In literature Schumann et al. investigated Cu^0 supported on $ZnAlO_x$ or MgO with CO as a probe and assigned DRIFTS signals at 2125 and 2090 - 2112 cm^{-1} to $Zn^{\delta+}$-CO and Cu^0-CO, respectively. [325]

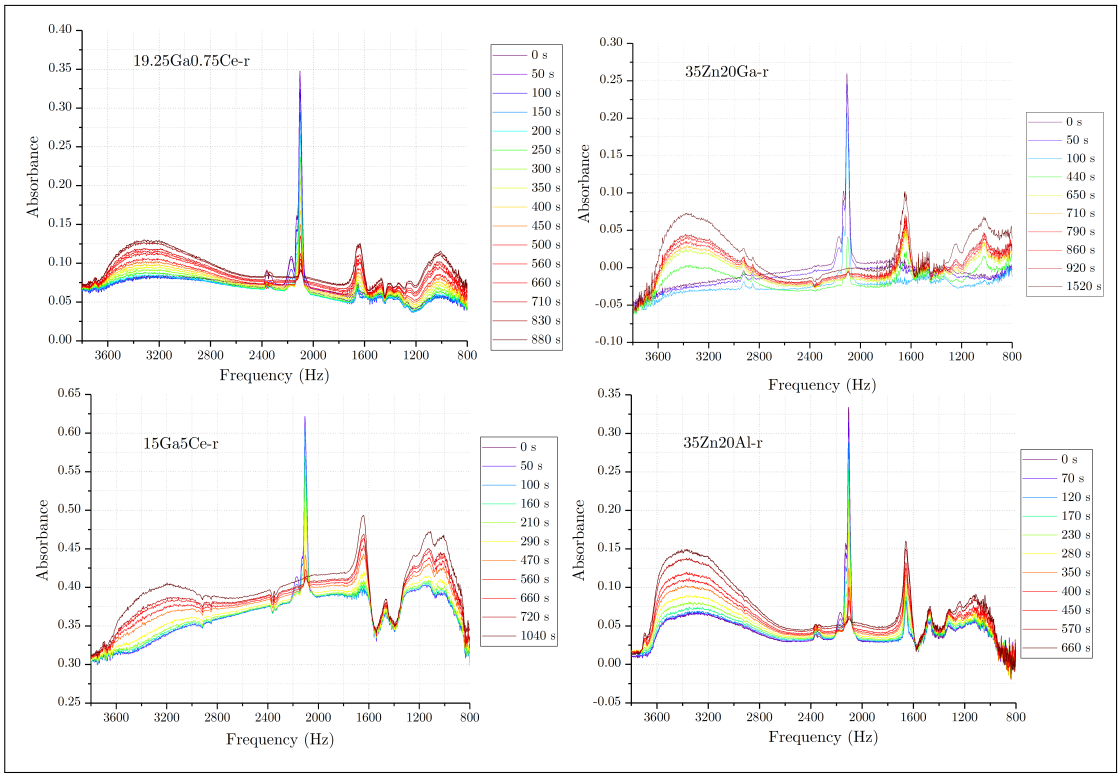


Figure 10.4: Baseline-corrected DRIFTS spectra for various LDH-derived catalysts at 25 °C. Each sample was saturated with a flow of 400 ppm CO/N_2 (g) before measurement. Time = 0 s coincides with the replacement of the CO/N_2 (g) flow with a H_2O/N_2 (g) flow.

Figure 10.5 shows the frequency range often associated with CO IR modes, the shape of the spectra are very similar to those measured at 300 K by Schumann et al. for reduced $Cu^0/ZnAlMgO_x$ catalysts. [325] As with the methanol DRIFTS data the total absorbance and rates of change in absorbance may have fluctuated depending on the manually controlled gas flow rates that varied from experiment to experiment. However, the relative absorbance between peaks in the same experiment can be compared because they were under the same conditions. As per the assignment by Schumann et al. the large signals at ≈ 2100 cm^{-1} likely correspond with the linear adsorption of CO to Cu^0 whilst the smaller peak around 2130 cm^{-1} corresponds to CO adsorbed on the support oxide; the broad least intense peaks at 2175 cm^{-1} are caused by the free CO gas which causes a doublet signal around 2150 cm^{-1} (so half

of its signal likely overlaps with those of the adsorbed CO).

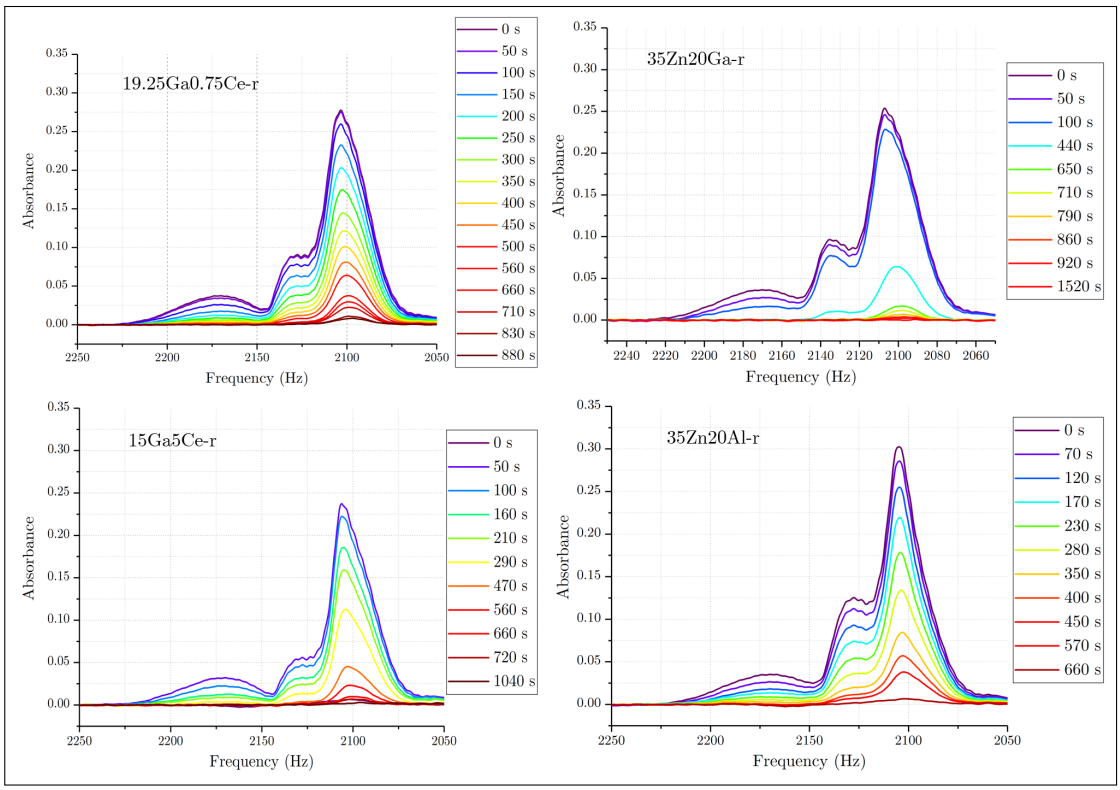


Figure 10.5: A representation of Figure 10.4 over the 2050 - 2250 Hz range; depicting CO adsorption modes.

No shifts in the frequency of the 3 different CO signals were significant (Figure 10.5); the frequencies at 2169 and 2105 cm^{-1} did not change (at t = 0 s), ± 1 cm^{-1}. The signal assigned to CO adsorbed on an oxide had four very small peaks at 2123, 2127, 2131 and 2135 cm^{-1} for every catalyst tested (at t = 0 s), typically for all samples the peaks at 2127 and 2131 cm^{-1} had almost equal intensity, with 2127 cm^{-1} being the maxima; however, for 35Zn20Ga-r the maxima was at 2135 cm^{-1}. These peaks could correspond to the different elements that CO can adsorb to on the oxide surface because different ions will donate different electron density to the CO anti-bonding orbital, causing different C-O bond lengths and, therefore, different IR frequencies. It is hard to find a trend in these finer signal patterns, the nature of the metals in the oxide may alter the frequency but the combination of potential

electronic, steric and mass effects make it too hard to predict these slight differences in the $M^{\delta+}$-CO signal. Assuming all $M^{\delta+}$-CO signals have similar standard deviation curve shape around their maxima then the ratio of CO adsorbed to the oxide support and the Cu^0 particles can be estimated.

The maxima signal ratios, $\frac{M^{\delta+}-CO}{Cu^0-CO}$, for 35Zn20Al-, 35Zn20Ga-, 19.25Ga0.75Ce- and 15Ga5Ce-r are 0.415, 0.380, 0.327 and 0.237, respectively. There is no trend in the absolute $Cu^0 - CO$ peak intensity due to the slightly differing flow rates from experiment to experiment. This implies the amount of CO adsorption on a given surface follows the trend $Cu^0 \gg AlO_x > GaO_x > CeO_x$. Whilst all samples have a similar overall Cu wt %, they have a different amount of exposed Cu^0 and oxide surface; their D_{Cu} % and BET surface area trend is as follows: 35Zn20Al-LDO > 35Zn20Ga-LDO > 15Ga5Ce-LDO > 19.25Ga0.75Ce-LDO. Increasing D_{Cu} % theoretically would increase the relative amount of $Cu^0 - CO$, whilst an increase in BET surface area should increase both $M^{\delta+}$-CO and Cu^0-CO peaks. Back electron donation from the metal to the $2\pi^*$ CO anti-bonding orbital is often the deciding factor in C-O bond strength; if net charge is the deciding factor for the amount of electron donation and orbital overlap efficiency with CO (based on the metal size) is the second most important factor then the M-CO adsorption bond strength would likely follow this trend: $Cu^0 \gg Al^{3+} > Ga^{3+} > Ce^{4+}$ (the opposite of this trend would fit the C-O bond IR frequency). [326, 327] Whilst electron donation of the different elements predominantly dictates the IR frequency, it could also affect the affinity for adsorption; the differences between C-O bond strength for the different metals in the oxide may not be very severe, hence why their peaks merge at ≈ 2130 cm^{-1} and the M-CO adsorption and C-O bond strength are much stronger and weaker, respectively, with Cu^0.

In summary, DRIFTS does not reveal whether, BET surface area, D_{Cu} % and/or

CO adsorption strength determines the signal ratios between the different CO peaks at 2150 and 2105 cm^{-1}; other techniques are required in tandem with DRIFTS for insight into the MSR activity and selectivity of the Ce-doped catalysts (see Section 8.5.6).

10.3 EPR analysis of the Al and Ga LDO series

Cu^{2+} is paramagnetic because it has an unpaired electron in a 3d orbital, this electron can absorb microwave radiation, during EPR analysis, to change spin state and produce a peak on the EPR spectrum. In literature, Cu^{2+} ions in oxide have been reported to give an EPR signal between $\approx$ 3200 - 3600 G, or around a g factor of $\approx$ 1.90 -2.17 when measured using the X EPR band. [72, 328–331] This range is very broad as Cu^{2+} can adopt tetrahedral, octahedral or Jahn-Teller distorted octahedral geometry; different mixes and orientations of these geometries relative to other elements in the structure, especially large ions such as transition metals, can have a large influence on the effective magnetic field felt by the unpaired electron and hyperfine and superhyperfine coupling interactions. For most oxide or nanoparticle structures that contain more than 2 wt % Cu, the broadening of the Cu paramagnetic electron EPR signal will occur due to dipolar coupling between different Cu^{2+} nuclei in various different environments. [329] Applying the 1st derivative to EPR peak absorptions often translates the peaks into their 'positive' and 'negative' gradient peaks, these shapes and intensities can vary based on the how the effective magnetic field felt by the electron varies with structural orientation; however, in the case of the Al and Ga LDO seriers measured in this work only the negative 1st derivative peak is observed in Figure 10.7. Such large isotropic peaks that partially or fully obscure the hyperfine splitting or even other EPR signals, seemingly like the positive 1st derivative gradient peak in this work, have been observed in literature for $Cu/ZrO_2/Al_2O_3$, $CuZnGaO_x$, $CuGaO_x$, $CuZnAlO_x$, $CuZnZrAlO_x$ and $CuAlO_x$. [72, 328–331] In all cases the large

amount of possible Cu sites and interactions between such Cu environments leads to a broad range of observed signals because the effective magnetic field felt by any given electron can vary greatly across the structure. [329, 330] Bellido et al. and Yu et al. independently managed to observe Cu^{2+} environments that displayed axial EPR 1st derivative peak patterns, where by $g_z > g_y = g_x$, and also some hyperfine splitting patterns; this was achieved by using Cu contents lower than 5 wt % and/or low temperatures, 77 K. [328, 329] A well resolved axial pattern is displayed in Figure 10.6.c, the hyperfine splitting for $g_{\parallel}$ can be observed but no splitting is visible for $g_{\perp}$ (this is indicative of an elongated z axis). [332] Lots of similar Cu environments and orientations within an oxide lattice would all give similar EPR spectra if the Cu centre was isolated, but the combination and overlap of all these signals generates a net result of one very broad peak originating from the combination of each spectra's most dominant feature, the large negative gradient of $g_{\perp}$ (see Figures 10.6.a and 10.6.b). [332] This is what is theorised to be the case for each LDO's EPR spectra, shown in Figure 10.7.

Unlike other simpler cases in literature, the observed experimental peaks in this work are too broad to allow the assignment of specific Cu environment geometries; this is not surprising, as the nature of the calcined materials is already theorised to contain surface, bulk, distorted, octahedral, exfoliated and/or near-defect Cu environments. [330] Whilst the EPR data cannot elucidate on the specific geometries of the Cu in the LDOs, the EPR signal could still correlate to the amount of paramagnetic Cu^{2+}. Evidently, this is not the case upon comparison of the EPR 1st derivative signal intensity trends (see Figure 10.7) and the Cu wt % ICP-MS data for the samples (see Table 7.2); presumably due to other competing effects. Bulk CuO is EPR silent due to the antiferromagnetic coupling that occurs between the unpaired electrons of square planar Cu^{2+} cations, removing the paramagnetism. The degradation of a LDH with high elemental dispersion would unlikely lead to structures of pure square planar

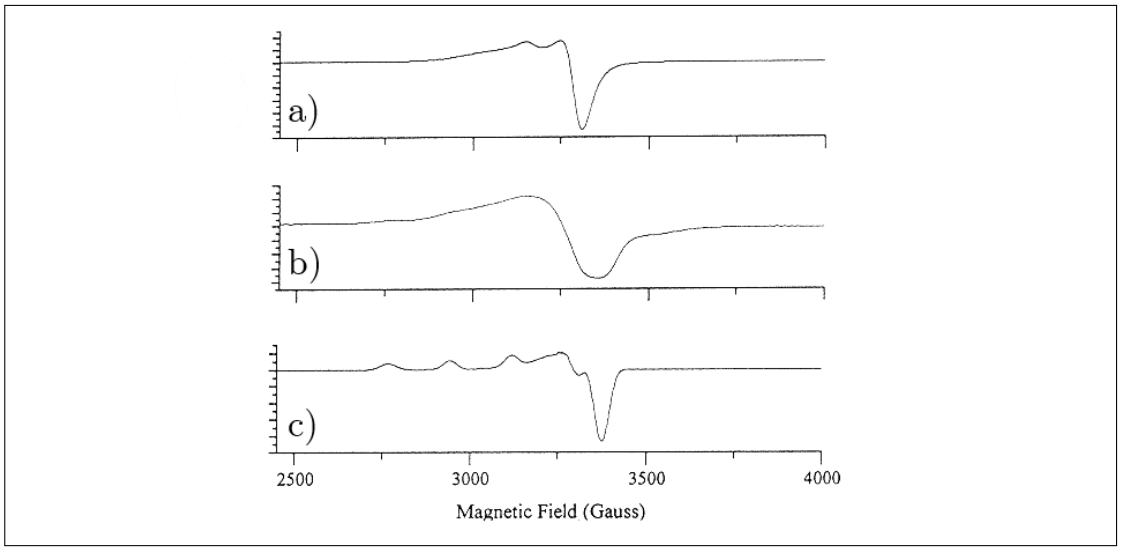


Figure 10.6: Experimental X-band EPR spectra, measured at 77 K, for a monomeric Cu complex, with organic ligands, under different conditions: a) Pure crystalline powder. b) Dissolved in chloroform. c) Dissolved in dimethyl-formamide, in this scenario the Cu centres do not interact with each other; therefore, there is well resolved hyperfine splitting. Figure used with permission from: P. Subramanian, E. Suresh, D. Srinivas, *Inorganic chemistry*, 2000, **39**, 2053 – 2060.©2000 American Chemical Society.

CuO, rather various mixed metal oxide geometries; therefore pure CuO content is not likely correlated with the signal intensity.

It is observed 35Zn20Ga- and 30Zn25Ga-LDO give more intense EPR signals than the analogous Al samples; whilst 30 % M^{3+} samples give the lowest intensity. None of the analysis in this chapter can elucidate how the LDO composition, surface area etc affect any potential antiferromagnetic coupling in the sample; therefore the EPR data trends cannot be discussed with a complete set of evidence, qualitative or quantitative. In literature, oxygen vacancies that trap one electron and are therefore paramagentic have been theorised to occur between g factors of 1.96 - 2.01 and their amount has been theorised to correlate with EPR signal intensity; unfortunately, they can be mistaken for transition metal impurity signals and are often only qualitatively correlated to photoluminescence studies of defects. [333, 334]

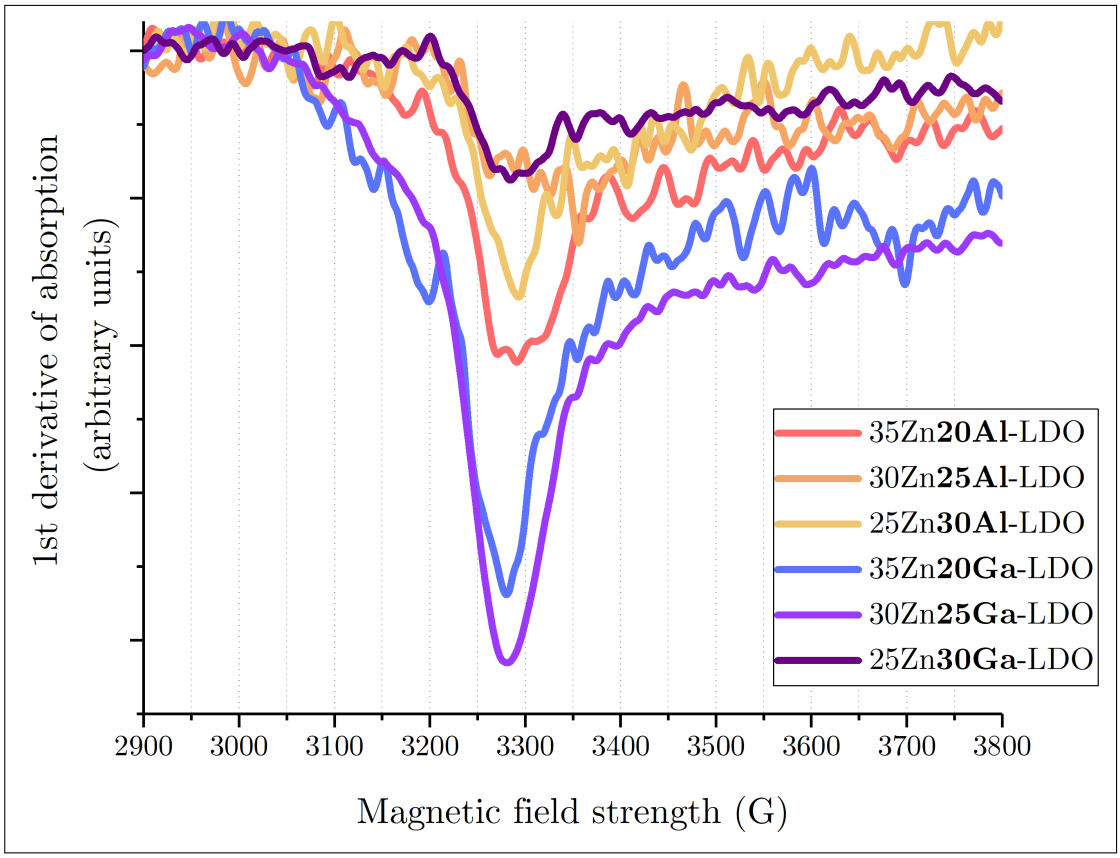


Figure 10.7: Electron paramagnetic resonance analysis of the Al- and Ga-LDO series

To summarise the EPR data, the broad peaks likely occur from the overlap of several paramagnetic species (different Cu^{2+} environments and oxygen vacancies); however, the lack of hyperfine splitting structure and peak definition mean the trends in signal intensity for the Al and Ga series cannot be easily assigned. The increased EPR signal for 35Zn20Ga- and 30Zn25Ga-LDO could be due a higher density of oxygen vacancies and/or less antiferromagnetic coupling inherently occurring due to their structure and/or the total Cu wt % of the samples. Unfortunately, this renders EPR analysis not very useful when it comes to discerning which of these catalyst series would make better MSR catalysts. As with other analytic techniques in the study of these materials (for instance the TPR and reduced PXRD analysis) but to a greater extent for EPR; to discern the exact quantitative contributions of all the competing effects, would require a large standalone study of all the potential Cu environments,

likely involving the modelling and measuring of a wide ranging EPR sample set.

10.4 EPR analysis of the Ce LDO series

In Section 10.3 the EPR spectra of the Al- and Ga-LDOs were discussed; it was theorised that the very broad singular peak was the combination of the large negative g gradients from multiple Cu environments. It was also put forward that EPR peak intensity could possibly correlate to the amount of oxygen vacancies, however the structure and Cu content could also affect the signal via antiferromagnetic coupling. The EPR peaks for the Ce-LDOs are extremely similar to those of the Al- and Ga-LDOs, the only difference is they have a higher signal intensity. There is no signal trend that correlates with Ce content and the signal for 10Ga10Ce-LDO was anomalously large but all Ce-doped LDOs have larger signal intensity than the Al- and Ga-based materials. To reiterate, the analysis of this EPR data is highly qualitative due to experimental data, baseline quality and number of Cu environments. Therefore, there could be a combination of several reasons for the Ce > Ga > Al signal intensity trend.

Ce introducing more oxygen vacancies into the catalyst was one of the targets of the Ce doping into the AMO-LDHs based on literature reports; however, Ce altering the LDO structure or reducing the samples' Cu wt % could also cause differences in signal intensity and the EPR data does not give any indication of which scenario or scenarios is most likely.

EPR analysis of the lanthanide-doped series showed very similar spectra and EPR signal intensity to that of 19.25Ga0.75Ce-LDO (see Figure 10.9); possibly indicating similar Cu and oxygen vacancy structures; however, the EPR analysis in this work was highly qualitative.

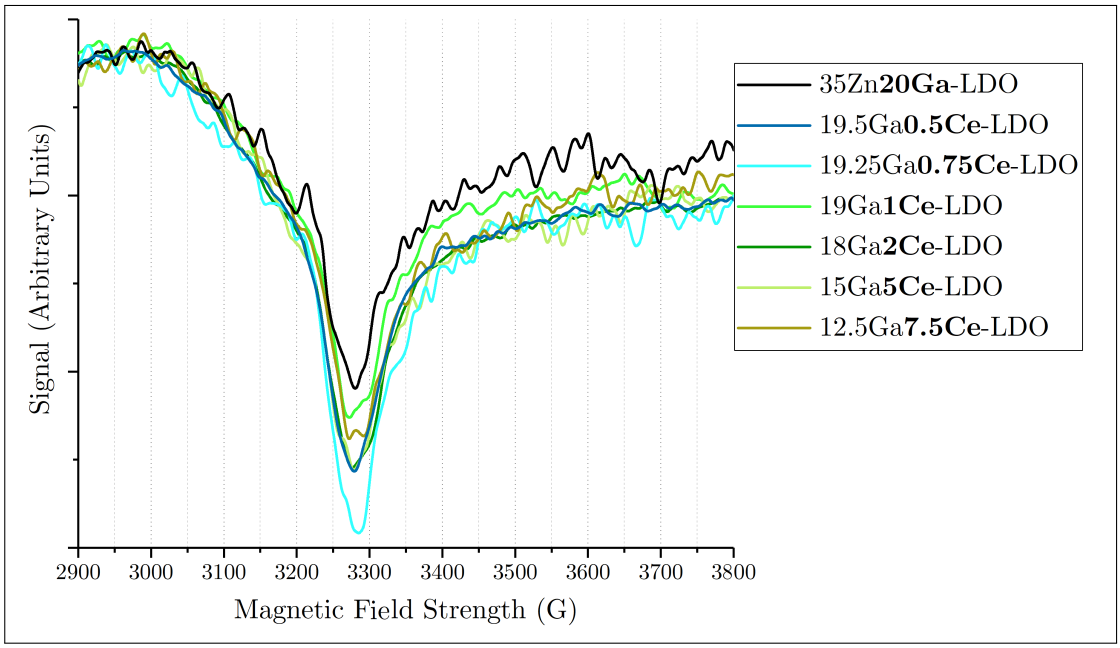


Figure 10.8: Electron paramagnetic resonance analysis of the Ce-LDO series

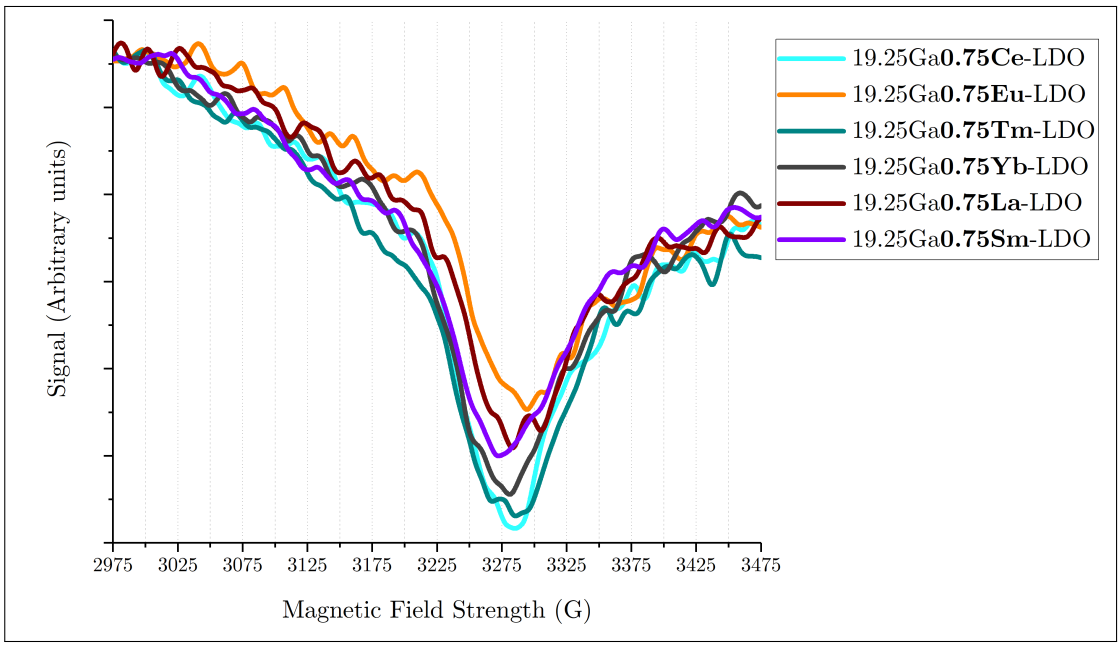


Figure 10.9: Electron paramagnetic resonance analysis of the Ln-LDO series

Bibliography

[1] P. Atkins, T. Overton, J. Rourke, M. Weller, F. Armstrong in *Shriver and Atkins' Inorganic Chemistry 5th ed.*, OUP, Oxford ; New York, 2009, p. 152.

[2] A. M. Oliveira, R. R. Beswick, Y. Yan, *Current Opinion in Chemical Engineering*, 2021, **33**, 100701.

[3] J. Bowman, *Land use policy*, 1990, **7**, 101–108.

[4] IEA, *Hydrogen Report, https://www.iea.org/reports/hydrogen (Accessed: 03/12/2021).*

[5] L. Schlapbach, A. Züttel, *Nature*, 2001, **414**, 353–358.

[6] A. W. C. van den Berg, C. O. Areán, *Chemical Communications*, 2008, **0**, 668–681.

[7] S. T. Yong, C. W. Ooi, S. P. Chai, X. S. Wu, *International Journal of Hydrogen Energy*, 2013, **38**, 9541–9552.

[8] J. Chi, H. Yu, *Chinese Journal of Catalysis*, 2018, **39**, 390–394.

[9] A. K. Hill, L. Torrente-Murciano, *Applied Catalysis B: Environmental*, 2015, **172**, 129–135.

[10] C. Smith, A. K. Hill, L. Torrente-Murciano, *Energy & Environmental Science*, 2020, **13**, 331–344.

[11] N. Edwards, S. R. Ellis, J. C. Frost, S. E. Golunski, A. N. J. van Keulen, N. G. Lindewald, J. G. Reinkingh, *Journal of Power Sources*, 1998, **71**, 123–128.

[12] D. R. Palo, R. A. Dagle, J. D. Holladay, *Chemical Reviews*, 2007, **107**, 3992–4021.

[13] S. K. Kamarudin, N. S. Shamsul, J. A. Ghani, S. K. Chia, H. S. Liew, A. S. Samsudin, *Bioresource Technology*, 2013, **129**, 463–468.

[14] P. Gautam, S. N. Upadhyay, S. Dubey, et al., *Fuel*, 2020, **273**, 117783.

[15] V. Menon, M. Rao, *Progress in Energy and Combustion Science*, 2012, **38**, 522–550.

[16] E. Malmgren, S. Brynolf, E. Fridell, M. Grahn, K. Andersson, *Sustainable Energy & Fuels*, 2021, **5**, 2753–2770.

[17] K. M. K. Yu, W. Tong, A. West, K. Cheung, T. Li, G. Smith, Y. Guo, S. C. E. Tsang, *Nature Communications*, 2012, **3**, 1–7.

[18] S. J. Peighambardoust, S. Rowshanzamir, M. Amjadi, *International journal of hydrogen energy*, 2010, **35**, 9349–9384.

[19] W. Kim, K. K. Mohaideen, D. J. Seo, W. L. Yoon, *International Journal of Hydrogen Energy*, 2017, **42**, 2081–2087.

[20] W. Tong, K. Cheung, A. West, K.-M. Yu, S. C. E. Tsang, *Physical Chemistry Chemical Physics*, 2013, **15**, 7240–7248.

[21] M. Turco, G. Bagnasco, U. Costantino, F. Marmottini, T. Montanari, G. Ramis, G. Busca, *Journal of Catalysis*, 2004, **228**, 56–65.

[22] J. K. Lee, J. B. Ko, D. H. Kim, *Applied Catalysis A: General*, 2004, **278**, 25–35.

[23] A. Burrows, J. Holman, A. Parsons, G. Pilling, G. Price in *Shriver and Atkins' Inorganic Chemistry 2nd ed.*, OUP, Oxford, 2013, pp. 673–674.

[24] P. Atkins, J. d. Paula in *Atkins' Physical Chemistry 9th ed.*, OUP, Oxford ; New York, 2009, pp. 799–808.

[25] A. Burrows, J. Holman, A. Parsons, G. Pilling, G. Price in *Shriver and Atkins' Inorganic Chemistry 2nd ed.*, OUP, Oxford, 2013, pp. 175–176.

[26] T. Helmenstine, *List of Electronegativity Values of the Elements*, 2015. `https://sciencenotes.org/list-of-electronegativity-values-of-the-elements/`.

[27] A. Burrows, J. Holman, A. Parsons, G. Pilling, G. Price in *Shriver and Atkins' Inorganic Chemistry 2nd ed.*, OUP, Oxford, 2013, p. 782.

[28] R. D. Shannon, R. X. Fischer, *American Mineralogist*, 2016, **101**, 2288–2300, Publisher: GeoScienceWorld.

[29] P. Atkins, T. Overton, J. Rourke, M. Weller, F. Armstrong in *Shriver and Atkins' Inorganic Chemistry 5th ed.*, OUP, Oxford ; New York, 2009, pp. 66–74.

[30] W. Li, J. Shi, K. H. Zhang, J. L. MacManus-Driscoll, *Materials Horizons*, 2020, **7**, 2832–2859.

[31] P. Atkins, J. d. Paula in *Atkins' Physical Chemistry 9th ed.*, OUP, Oxford ; New York, 2009, pp. 712–713.

[32] R. S. Treptow, *Journal of Chemical Education*, 1997, **74**, 919.

[33] P. Atkins, J. d. Paula in *Atkins' Physical Chemistry 9th ed.*, OUP, Oxford ; New York, 2009, pp. 697–698.

[34] E. Ameh, *The International Journal of Advanced Manufacturing Technology*, 2019, **105**, 3289–3302.

[35] D. Askeland, P. Fulay, W. Wright, *The Science and Engineering of Materials, SI Edition*, Cengage Learning, 2011.

[36] M. Wahab in *Numerical Problems in Crystallography*, Springer, 2021, pp. 137–178.

[37] A. Burrows, J. Holman, A. Parsons, G. Pilling, G. Price in *Shriver and Atkins' Inorganic Chemistry 2nd ed.*, OUP, Oxford, 2013, p. 627.

[38] A. Burrows, J. Holman, A. Parsons, G. Pilling, G. Price in *Shriver and Atkins' Inorganic Chemistry 2nd ed.*, OUP, Oxford, 2013, p. 26.

[39] P. Atkins, J. d. Paula in *Atkins' Physical Chemistry 9th ed.*, OUP, Oxford ; New York, 2009, pp. 884–902.

[40] P. Atkins, J. d. Paula in *Atkins' Physical Chemistry 9th ed.*, OUP, Oxford ; New York, 2009, p. 876.

[41] A. Burrows, J. Holman, A. Parsons, G. Pilling, G. Price in *Shriver and Atkins' Inorganic Chemistry 2nd ed.*, OUP, Oxford, 2013, pp. 56–58.

[42] K. G. Denbigh, *The Principles of Chemical Equilibrium: With Applications in Chemistry and Chemical Engineering 4th ed.*, Cambridge University Press, 1981.

[43] M. Spencer, *Catalysis letters*, 1995, **32**, 9–13.

[44] R. Burch, *Physical Chemistry Chemical Physics*, 2006, **8**, 5483–5500.

[45] E. B. Nauman, *Industrial & Engineering Chemistry Research*, 2008, **47**, 3752–3766.

[46] P. Atkins, T. Overton, J. Rourke, M. Weller, F. Armstrong in *Shriver and Atkins' Inorganic Chemistry 5th ed.*, OUP, Oxford ; New York, 2009, pp. 653–675.

[47] M. Abd Elmoula, E. Panaitescu, M. Phan, D. Yin, C. Richter, L. H. Lewis, L. Menon, *Journal of Materials Chemistry*, 2009, **19**, 4483–4487.

[48] A. Burrows, J. Holman, A. Parsons, G. Pilling, G. Price in *Shriver and Atkins' Inorganic Chemistry 2nd ed.*, OUP, Oxford, 2013, pp. 14–16.

[49] D. Vollath, F. D. Fischer, D. Holec, *Beilstein Journal of Nanotechnology*, 2018, **9**, 2265–2276.

[50] K. Oura, V. Lifshits, A. Saranin, A. Zotov, M. Katayama, *Surface science: an introduction*, Springer Science & Business Media, 2013.

[51] P. Atkins, J. d. Paula in *Atkins' Physical Chemistry 9th ed.*, OUP, Oxford ; New York, 2009, p. 720.

[52] P. Forzatti, L. Lietti, *Catalysis today*, 1999, **52**, 165–181.

[53] Y. Dai, P. Lu, Z. Cao, C. T. Campbell, Y. Xia, *Chemical Society Reviews*, 2018, **47**, 4314–4331.

[54] A. Cao, R. Lu, G. Veser, *Physical Chemistry Chemical Physics*, 2010, **12**, 13499–13510.

[55] C. Chen, J.-G. Lee, K. Arakawa, H. Mori, *Applied Physics Letters*, 2011, **99**, 013108.

[56] J. Zhu, Q. Fu, Y. Xue, Z. Cui, *Journal of Materials Science*, 2016, **51**, 4462–4469.

[57] H. H. Kart, H. Yildirim, S. O. Kart, T. Çağin, *Materials Chemistry and Physics*, 2014, **147**, 204–212.

[58] T. W. van Deelen, C. H. Mejía, K. P. de Jong, *Nature Catalysis*, 2019, **2**, 955–970.

[59] M. Sterrer, H.-J. Freund, *Catalysis Letters*, 2013, **143**, 375–385.

[60] E. D. Goodman, J. A. Schwalbe, M. Cargnello, *ACS Catalysis*, 2017, **7**, 7156–7173.

[61] C. T. Campbell, Z. Mao, *ACS Catalysis*, 2017, **7**, 8460–8466.

[62] B. Gates, *Journal of Molecular Catalysis A: Chemical*, 2000, **163**, 55–65.

[63] G. Marzun, C. Streich, S. Jendrzej, S. Barcikowski, P. Wagener, *Langmuir*, 2014, **30**, 11928–11936.

[64] C.-J. Pan, M.-C. Tsai, W.-N. Su, J. Rick, N. G. Akalework, A. K. Agegnehu, S.-Y. Cheng, B.-J. Hwang, *Journal of the Taiwan Institute of Chemical Engineers*, 2017, **74**, 154–186.

[65] K. Qian, H. Duan, Y. Li, W. Huang, *Chemistry–A European Journal*, 2020, **26**, 13538–13542.

[66] F. M. Pinto, V. Y. Suzuki, R. C. Silva, F. A. La Porta, *Frontiers in Materials*, 2019, **6**, Publisher: Frontiers.

[67] A. Ruiz Puigdollers, P. Schlexer, S. Tosoni, G. Pacchioni, *ACS Catalysis*, 2017, **7**, 6493–6513.

[68] A. Iulianelli, P. Ribeirinha, A. Mendes, A. Basile, *Renewable and Sustainable Energy Reviews*, 2014, **29**, 355–368.

[69] S. Xing, C. Zhao, S. Ban, Y. Liu, H. Wang, *International Journal of Hydrogen Energy*, 2020, **45**, 7015–7024.

[70] F. R. García-García, S. C. Tsang, K. Li, *Journal of Membrane Science*, 2014, **455**, 92–102.

[71] H. Song, Y. Kim, D. Yu, B. J. Kim, H. Ji, S. Yu, *Energies*, 2020, **13**, 4324.

[72] W. Tong, A. West, K. Cheung, K.-M. Yu, S. C. E. Tsang, *ACS Catalysis*, 2013, **3**, 1231–1244.

[73] P. Tijm, F. Waller, D. Brown, *Applied Catalysis A: General*, 2001, **221**, 275–282.

[74] I. Kasatkin, P. Kurr, B. Kniep, A. Trunschke, R. Schlögl, *Angewandte Chemie International Edition*, 2007, **46**, 7324–7327.

[75] S. Sá, H. Silva, L. Brandão, J. M. Sousa, A. Mendes, *Applied Catalysis B: Environmental*, 2010, **99**, 43–57.

[76] J. He, Z. Yang, L. Zhang, Y. Li, L. Pan, *International Journal of Hydrogen Energy*, 2017, **42**, 9930–9937.

[77] C. Mateos-Pedrero, C. Azenha, P. T. DA, J. Sousa, A. Mendes, *Applied Catalysis B: Environmental*, 2020, **277**, 119243.

[78] N. Iwasa, N. Takezawa, *Topics in Catalysis*, 2003, **22**, 215–224.

[79] N. Iwasa, T. Mayanagi, N. Ogawa, K. Sakata, N. Takezawa, *Catalysis Letters*, 1998, **54**, 119–123.

[80] N. Iwasa, S. Kudo, H. Takahashi, S. Masuda, N. Takezawa, *Catalysis Letters*, 1993, **19**, 211–216.

[81] C. Qi, J. C. Amphlett, B. A. Peppley, *Catalysis Letters*, 2005, **104**, 57–62.

[82] M. Khzouz, E. I. Gkanas, S. Du, J. Wood, *Fuel*, 2018, **232**, 672–683.

[83] X. Liu, Y. Men, J. Wang, R. He, Y. Wang, *Journal of Power Sources*, 2017, **364**, 341–350.

[84] J. Lin, C. Hu, X. Xu, M. Shao, Y. Hu, C. Ma, *Chemical Engineering & Technology*, 2021, **44**, 1121–1130.

[85] S.-q. Yang, J.-p. He, N. Zhang, X.-w. Sui, L. Zhang, Z.-x. Yang, *Journal of Fuel Chemistry and Technology*, 2018, **46**, 179–188.

[86] S. Kühl, M. Friedrich, M. Armbrüster, M. Behrens, *Journal of Materials Chemistry*, 2012, **22**, 9632–9638.

[87] M. V. Twigg, M. S. Spencer, *Topics in Catalysis*, 2003, **22**, 191–203.

[88] C. Qi, J. C. Amphlett, B. A. Peppley, *Catalysis Letters*, 2005, **104**, 57–62.

[89] M. Matsukata, T. Hayashi, M. Nishiyama, E. Kikuchi, Y. Morita, *Journal of The Japan Petroleum Institute*, 1987, **30**, 265–272.

[90] L. Oar-Arteta, A. Remiro, F. Epron, N. Bion, A. T. Aguayo, J. Bilbao, A. G. Gayubo, *Industrial & Engineering Chemistry Research*, 2016, **55**, 3546–3555.

[91] N. Iwasa, T. Mayanagi, W. Nomura, M. Arai, N. Takezawa, *Applied Catalysis A: General*, 2003, **248**, 153–160.

[92] J. A. Rodriguez, M. Kuhn, *The Journal of Physical Chemistry*, 1996, **100**, 381–389.

[93] J. Davis, M. Barteau, *Surface Science*, 1990, **235**, 235–248.

[94] R. W. McCabe, C. L. DiMaggio, R. J. Madix, *The Journal of Physical Chemistry*, 1985, **89**, 854–861.

[95] R. Madix, T. Yamada, S. Johnson, *Applications of Surface Science*, 1984, **19**, 43–58.

[96] B. Sexton, A. Hughes, N. Avery, *Surface Science*, 1985, **155**, 366–386.

[97] S. R. Segal, K. B. Anderson, K. A. Carrado, C. L. Marshall, *Applied Catalysis A: General*, 2002, **231**, 215–226.

[98] M. M. Günter, T. Ressler, R. E. Jentoft, B. Bems, *Journal of Catalysis*, 2001, **203**, 133–149.

[99] B. Lindström, L. J. Pettersson, P. G. Menon, *Applied Catalysis A: General*, 2002, **234**, 111–125.

[100] T. Fukunaga, N. Ryumon, N. Ichikuni, S. Shimazu, *Catalysis Communications*, 2009, **10**, 1800–1803.

[101] S. Patel, K. K. Pant, *Journal of Power Sources*, 2006, **159**, 139–143.

[102] Y. Chen, S. Li, S. Lv, Y. Huang, *Catalysis Communications*, 2021, **149**, 106215.

[103] Y. Mohtashami, M. Taghizadeh, *International Journal of Hydrogen Energy*, 2019, **44**, 5725–5738.

[104] Y. Liu, T. Hayakawa, T. Tsunoda, K. Suzuki, S. Hamakawa, K. Murata, R. Shiozaki, T. Ishii, M. Kumagai, *Topics in Catalysis*, 2003, **22**, 205–213.

[105] W. Qiao, S. Yang, L. Zhang, Y. Tian, H. Wang, C. Zhang, Z. Gao, *International Journal of Energy Research*, 2021, **45**, 12773–12783, https://onlinelibrary.wiley.com/doi/pdf/10.1002/er.6610.

[106] Y. Tang, Y. Liu, P. Zhu, Q. Xue, L. Chen, Y. Lu, *AIChE Journal*, 2009, **55**, 1217–1228.

[107] O. Jakdetchai, N. Takayama, T. Nakajima, *Kinetics and Catalysis*, 2005, **46**, 56–64.

[108] T. Shishido, Y. Yamamoto, H. Morioka, K. Takaki, K. Takehira, *Applied Catalysis A: General*, 2004, **263**, 249–253.

[109] T. Ressler, B. L. Kniep, I. Kasatkin, R. Schlögl, *Angewandte Chemie International Edition*, 2005, **44**, 4704–4707.

[110] S. G. Sanches, J. H. Flores, M. I. P. da Silva, *Molecular Catalysis*, 2018, **454**, 55–62.

[111] A. C. Fornari, J. L. C. W. Pimenta, O. A. A. dos Santos, L. M. de Matos Jorge, *Brazilian Journal of Chemical Engineering*, 2021, **38**, 523–548.

[112] P. Ribeirinha, C. Mateos-Pedrero, M. Boaventura, J. Sousa, A. Mendes, *Applied Catalysis B: Environmental*, 2018, **221**, 371–379.

[113] A. Y. Rozovskii, G. I. Lin, *Topics in Catalysis*, 2003, **22**, 137–150.

[114] I. E. Wachs, R. J. Madix, *Journal of Catalysis*, 1978, **53**, 208–227.

[115] G. Busca, *Journal of Molecular Catalysis*, 1987, **43**, 225–236.

[116] G. C. Chinchen, M. S. Spencer, K. C. Waugh, D. A. Whan, *Journal of the Chemical Society, Faraday Transactions 1: Physical Chemistry in Condensed Phases*, 1987, **83**, 2193–2212.

[117] D. K. Kim, E. Iglesia, *The Journal of Physical Chemistry C*, 2008, **112**, 17235–17243.

[118] S. Sakong, A. Gross, *The Journal of Physical Chemistry A*, 2007, **111**, 8814–8822.

[119] X.-K. Gu, W.-X. Li, *The Journal of Physical Chemistry C*, 2010, **114**, 21539–21547.

[120] B. A. Peppley, J. C. Amphlett, L. M. Kearns, R. F. Mann, *Applied Catalysis A: General*, 1999, **179**, 31–49.

[121] N. Takezawa, N. Iwasa, *Catalysis Today*, 1997, **36**, 45–56.

[122] P. Dilara, J. Vohs, *Surface Science*, 1994, **321**, 8–18.

[123] G. Busca, J. Lamotte, J. C. Lavalley, V. Lorenzelli, *Journal of the American Chemical Society*, 1987, **109**, 5197–5202.

[124] B. Frank, F. C. Jentoft, H. Soerijanto, J. Kröhnert, R. Schlögl, R. Schomäcker, *Journal of Catalysis*, 2007, **246**, 177–192.

[125] M. Manzoli, A. Chiorino, F. Boccuzzi, *Applied Catalysis B: Environmental*, 2005, **57**, 201–209.

[126] I. A. Fisher, A. T. Bell, *Journal of Catalysis*, 1999, **184**, 357–376.

[127] D. B. Clarke, D.-K. Lee, M. J. Sandoval, A. T. Bell, *Journal of Catalysis*, 1994, **150**, 81–93.

[128] J. Gomes, J. Gomes, *Surface Science*, 2001, **471**, 59–70.

[129] J. Gomes, J. Gomes, *Surface Science*, 2000, **446**, 283–293.

[130] Z.-J. Zuo, L. Wang, P.-D. Han, W. Huang, *International Journal of Hydrogen Energy*, 2014, **39**, 1664–1679.

[131] S. Yong, K. Hidajat, S. Kawi, *Catalysis Today*, 2008, **131**, 188–196.

[132] J.-Y. Bo, S. Zhang, K. H. Lim, *Catalysis Letters*, 2009, **129**, 444–448.

[133] P. G. Lustemberg, M. V. Bosco, A. Bonivardi, H. F. Busnengo, M. Ganduglia-Pirovano, *The Journal of Physical Chemistry C*, 2015, **119**, 21452–21464.

[134] S. Lin, D. Xie, H. Guo, *Journal of Molecular Catalysis A: Chemical*, 2012, **356**, 165–170.

[135] K. Geissler, E. Newson, F. Vogel, T.-B. Truong, P. Hottinger, A. Wokaun, *Physical Chemistry Chemical Physics*, 2001, **3**, 289–293.

[136] J. Agrell, H. Birgersson, M. Boutonnet, *Journal of Power Sources*, 2002, **106**, 249–257.

[137] B. A. Peppley, J. C. Amphlett, L. M. Kearns, R. F. Mann, *Applied Catalysis A: General*, 1999, **179**, 21–29.

[138] H. Xu, B. Wang, C. Shan, P. Xi, W. Liu, Y. Tang, *ACS Applied Materials & Interfaces*, 2018, **10**, 6336–6345.

[139] Y. Men, H. Gnaser, R. Zapf, V. Hessel, C. Ziegler, *Catalysis Communications*, 2004, **5**, 671–675.

[140] A. Mastalir, B. Frank, A. Szizybalski, H. Soerijanto, A. Deshpande, M. Niederberger, R. Schomäcker, R. Schlögl, T. Ressler, *Journal of Catalysis*, 2005, **230**, 464–475.

[141] J. K. Lee, J. B. Ko, D. H. Kim, *Applied Catalysis A: General*, 2004, **278**, 25–35.

[142] X. Wang, J. A. Rodriguez, J. C. Hanson, D. Gamarra, A. Martínez-Arias, M. Fernández-García, *The Journal of Physical Chemistry B*, 2006, **110**, 428–434.

[143] M. A. Henderson, *Surface Science Reports*, 2002, **46**, 1–308.

[144] X. Wang, J. A. Rodriguez, J. C. Hanson, D. Gamarra, A. Martínez-Arias, M. Fernández-García, *The Journal of Physical Chemistry B*, 2006, **110**, 428–434.

[145] K. Wong, Q. Zeng, A. Yu, *Chemical Engineering Journal*, 2011, **174**, 408–412.

[146] G. Raupp, J. Dumesic, *The Journal of Physical Chemistry*, 1985, **89**, 5240–5246.

[147] S. Wu, K.-Y. Tseng, R. Kato, T.-S. Wu, A. Large, Y.-K. Peng, W. Xiang, H. Fang, J. Mo, I. Wilkinson, et al., *Journal of the American Chemical Society*, 2021.

[148] X. Kang, A. Chatzitakis, T. Aarholt, X. Sun, C. Negri, T. Norby, *Journal of Materials Chemistry A*, 2022.

[149] J. Gao, Y. Meng, A. Benton, J. He, L. G. Jacobsohn, J. Tong, K. S. Brinkman, *ACS Applied Materials & Interfaces*, 2020, **12**, 38012–38018.

[150] S. J. Teichner, *Applied Catalysis*, 1990, **62**, 1–10.

[151] D. Rethwisch, J. Dumesic, *Applied Catalysis*, 1986, **21**, 97–109.

[152] C. Chen, C. Ruan, Y. Zhan, X. Lin, Q. Zheng, K. Wei, *International Journal of Hydrogen Energy*, 2014, **39**, 317–324.

[153] M. Ziemba, M. V. Ganduglia-Pirovano, C. Hess, *Faraday Discussions*, 2021, **229**, 232–250.

[154] H. Purnama, T. Ressler, R. E. Jentoft, H. Soerijanto, R. Schlögl, R. Schomäcker, *Applied Catalysis A: General*, 2004, **259**, 83–94.

[155] L. Gao, G. Sun, S. Kawi, *Journal of Solid State Chemistry*, 2008, **181**, 7–13.

[156] X. Huang, L. Ma, M. S. Wainwright, *Applied Catalysis A: General*, 2004, **257**, 235–243.

[157] T. Fujitani, T. Matsuda, Y. Kushida, S. Ogihara, T. Uchijima, J. Nakamura, *Catalysis Letters*, 1997, **49**, 175–179.

[158] G. Fierro, M. Lo Jacono, M. Inversi, P. Porta, F. Cioci, R. Lavecchia, *Applied Catalysis A: General*, 1996, **137**, 327–348.

[159] P. H. Matter, D. J. Braden, U. S. Ozkan, *Journal of Catalysis*, 2004, **223**, 340–351.

[160] R. Burch, S. E. Golunski, M. S. Spencer, *Journal of the Chemical Society, Faraday Transactions*, 1990, **86**, 2683–2691, Publisher: Royal Society of Chemistry.

[161] N.-Y. Topsøe, H. Topsøe, *Journal of Molecular Catalysis A: Chemical*, 1999, **141**, 95–105.

[162] C. N. R. Rao, G. U. Kulkarni, P. J. Thomas, P. P. Edwards, *Chemistry – A European Journal*, 2002, **8**, 28–35, https://chemistry-europe.onlinelibrary.wiley.com/doi/pdf/10.1002/1521-3765%2820020104%298%3A1%3C28%3A%3AAID-CHEM28%3E3.0.CO%3B2-B.

[163] M. Turco, G. Bagnasco, U. Costantino, F. Marmottini, T. Montanari, G. Ramis, G. Busca, *Journal of Catalysis*, 2004, **228**, 43–55.

[164] J. Frost, *Nature*, 1988, **334**, 577–580.

[165] I. Ritzkopf, S. Vukojević, C. Weidenthaler, J.-D. Grunwaldt, F. Schüth, *Applied Catalysis A: General*, 2006, **302**, 215–223.

[166] Z. Bian, W. Zhong, Y. Yu, B. Jiang, S. Kawi, *International Journal of Hydrogen Energy*, 2020, **45**, 27078–27088.

[167] J. Nakamura, T. Fujitani, S. Kuld, S. Helveg, I. Chorkendorff, J. Sehested, *Science*, 2017, **357**, eaan8074.

[168] P. L. Hansen, J. B. Wagner, S. Helveg, J. R. Rostrup-Nielsen, B. S. Clausen, H. Topsøe, *Science*, 2002, **295**, 2053–2055, Publisher: American Association for the Advancement of Science Section: Report.

[169] M. M.-J. Li, Z. Zeng, F. Liao, X. Hong, S. C. E. Tsang, *Journal of Catalysis*, 2016, **343**, 157–167.

[170] M. M.-J. Li, J. Zheng, J. Qu, F. Liao, E. Raine, W. C. H. Kuo, S. S. Su, P. Po, Y. Yuan, S. C. E. Tsang, *Scientific Reports*, 2016, **6**.

[171] F. Liao, B. T. Lo, D. Sexton, J. Qu, C. Ma, R. C.-T. Chan, Q. Lu, R. Che, W.-M. Kwok, H. He, et al., *ChemCatChem*, 2015, **7**, 230–235.

[172] J. Liu, S. T. Pantelides, *Physical Review Letters*, 2018, **120**, 207602.

[173] S. Kattel, P. J. Ramírez, J. G. Chen, J. A. Rodriguez, P. Liu, *Science*, 2017, **355**, 1296–1299.

[174] S. Kattel, P. J. Ramírez, J. G. Chen, J. A. Rodriguez, P. Liu, *Science*, 2017, **357**, eaan8210.

[175] H. Ter Veen, T. Kim, I. Wachs, H. Brongersma, *Catalysis Today*, 2009, **140**, 197–201.

[176] T. Lunkenbein, J. Schumann, M. Behrens, R. Schlögl, M. G. Willinger, *Angewandte Chemie International Edition*, 2015, **54**, 4544–4548.

[177] C. M. R. Wright, K. Ruengkajorn, A. F. R. Kilpatrick, J.-C. Buffet, D. O'Hare, *Inorganic Chemistry*, 2017, **56**, 7842–7850.

[178] Z. P. Xu, J. Zhang, M. O. Adebajo, H. Zhang, C. Zhou, *Applied Clay Science*, 2011, **53**, 139–150.

[179] G. Fan, F. Li, D. G. Evans, X. Duan, *Chemical Society Reviews*, 2014, **43**, 7040–7066.

[180] M. M.-J. Li, C. Chen, T. Ayvalı, H. Suo, J. Zheng, I. F. Teixeira, L. Ye, H. Zou, D. O'Hare, S. C. E. Tsang, *ACS Catalysis*, 2018, **8**, 4390–4401.

[181] C. Chen, M. Yang, Q. Wang, J.-C. Buffet, D. O'Hare, *Journal of Materials Chemistry A*, 2014, **2**, 15102–15110.

[182] V. Erastova, M. T. Degiacomi, D. O'Hare, H. Chris Greenwell, *RSC Advances*, 2017, **7**, 5076–5083.

[183] R. Sasai, H. Sato, M. Sugata, T. Fujimura, S. Ishihara, K. Deguchi, S. Ohki, M. Tansho, T. Shimizu, N. Oita, et al., *Inorganic Chemistry*, 2019, **58**, 10928–10935.

[184] N. Takeno, *Geological survey of Japan Open File Report*, 2005, **419**, 102.

[185] E. S. Zhitova, S. V. Krivovichev, I. Pekov, H. C. Greenwell, *Mineralogical Magazine*, 2019, **83**, 269–280.

[186] S. Radha, S. Prasanna, P. V. Kamath, *Crystal Growth & Design*, 2011, **11**, 2287–2293.

[187] P. Gao, L. Zhong, L. Zhang, H. Wang, N. Zhao, W. Wei, Y. Sun, *Catalysis Science & Technology*, 2015, **5**, 4365–4377.

[188] M. Szabados, C. Bús, M. Adok-Sipiczki, Z. Kónya, Á. Kukovecz, P. Sipos, I. Pálinkó, *Particuology*, 2016, **27**, 29–33.

[189] A. Ennadi, A. Legrouri, A. De Roy, J. Besse, *Journal of Solid State Chemistry*, 2000, **152**, 568–572.

[190] U. Costantino, F. Marmottini, M. Nocchetti, R. Vivani, *European Journal of Inorganic Chemistry*, 1998, **1998**, 1439–1446.

[191] S. J. Mills, P. S. Whitfield, A. R. Kampf, S. A. Wilson, G. M. Dipple, M. Raudsepp, G. Favreau, *Journal of Geosciences*, 2012, **57**, 273–279.

[192] 290927-ICSD, *National Institute of Standards and Technology Inorganic Crystal Structure Database, NIST Standard Reference Database Number 3, Gaithersburg MD, 20899*. 10.3190/jgeosci.127.

[193] 86655-ICSD, *National Institute of Standards and Technology Inorganic Crystal Structure Database, NIST Standard Reference Database Number 3, Gaithersburg MD, 20899*. 10.1002.

[194] S. P. Newman, W. Jones, P. O'Connor, D. N. Stamires, *Journal of Materials Chemistry*, 2002, **12**, 153–155.

[195] W. Budhysutanto, D. van Agterveld, E. Schomaker, A. Talma, H. Kramer, *Applied Clay Science*, 2010, **48**, 208–213.

[196] A. Faour, C. Mousty, V. Prevot, B. Devouard, A. De Roy, P. Bordet, E. Elkaim, C. Taviot-Gueho, *The Journal of Physical Chemistry C*, 2012, **116**, 15646–15659.

[197] S. Nagendran, P. V. Kamath, *European Journal of Inorganic Chemistry*, 2013, **2013**, 4686–4693.

[198] H.-M. Liu, X.-J. Zhao, Y.-Q. Zhu, H. Yan, *Physical Chemistry Chemical Physics*, 2020, **22**, 2521–2529.

[199] U. Müller, *Symmetry relationships between crystal structures: applications of crystallographic group theory in crystal chemistry*, *Vol. 18*, OUP, 2013.

[200] C. Hobbs, S. Jaskaniec, E. K. McCarthy, C. Downing, K. Opelt, K. Güth, A. Shmeliov, M. C. Mourad, K. Mandel, V. Nicolosi, *npj 2D Materials and Applications*, 2018, **2**, 1–10.

[201] L. Lin, W. Zhou, R. Gao, S. Yao, X. Zhang, W. Xu, S. Zheng, Z. Jiang, Q. Yu, Y.-W. Li, C. Shi, X.-D. Wen, D. Ma, *Nature*, 2017, **544**, 80–83.

[202] R. O. Idem, N. N. Bakhshi, *Chemical Engineering Science*, 1996, **51**, 3697–3708.

[203] M. Bukhtiyarova, *Journal of Solid State Chemistry*, 2019, **269**, 494–506.

[204] C. Suryanarayana, M. G. Norton in *X-Ray Diffraction*, Springer, 1998, pp. 125–152.

[205] C. Chen, A. Wangriya, J.-C. Buffet, D. O'Hare, *Dalton Transactions*, 2015, **44**, 16392–16398.

[206] C. Hobbs, S. Jaskaniec, E. K. McCarthy, C. Downing, K. Opelt, K. Güth, A. Shmeliov, M. C. D. Mourad, K. Mandel, V. Nicolosi, *npj 2D Materials and Applications*, 2018, **2**, 1–10, Number: 1 Publisher: Nature Publishing Group.

[207] B. Inkson in *Materials Characterization Using Nondestructive Evaluation (NDE) Methods*, Elsevier, 2016, pp. 17–43.

[208] P. Atkins, T. Overton, J. Rourke, M. Weller, F. Armstrong in *Shriver and Atkins' Inorganic Chemistry 5th ed.*, OUP, Oxford ; New York, 2009, p. 242.

[209] H. Seyama, M. Soma, B. Theng in *Handbook of Clay Science*, Vol. 5 of *Developments in Clay Science*, F. Bergaya, G. Lagaly (Eds.), Elsevier, 2013, pp. 161–176.

[210] P. Atkins, J. d. Paula in *Atkins' Physical Chemistry 9th ed.*, OUP, Oxford ; New York, 2009, pp. 353–363.

[211] D. Briggs, J. Grant, S. Limited, *Surface Analysis by Auger and X-ray Photoelectron Spectroscopy*, SurfaceSpectra, 2003.

[212] H. M. S. Al-Aani, E. Iro, P. Chirra, I. Fechete, M. Badea, C. Negrilă, I. Popescu, M. Olea, I.-C. Marcu, *Applied Catalysis A: General*, 2019, **586**, 117215.

[213] G. Kresse, D. Joubert, *Physical Review B*, 1999, **59**, 1758.

[214] J. P. Perdew, K. Burke, M. Ernzerhof, *Physical Review Letters*, 1996, **77**, 3865.

[215] S. Grimme, J. Antony, S. Ehrlich, H. Krieg, *The Journal of Chemical Physics*, 2010, **132**, 154104.

[216] A. Jain, S. P. Ong, G. Hautier, W. Chen, W. D. Richards, S. Dacek, S. Cholia, D. Gunter, D. Skinner, G. Ceder, et al., *APL Materials*, 2013, **1**, 011002.

[217] *Shanghai Metals Market Database - Zinc Price History*, (Accessed on: 25/03/2021). `https://www.metal.com/Zinc/201102250173`.

[218] *Shanghai Metals Market Database - Copper Price History*, (Accessed on: 25/03/2021). https://www.metal.com/Copper/201102250170.

[219] *Shanghai Metals Market Database - Magnesium Price History*, (Accessed on: 25/03/2021). https://www.metal.com/Other-Minor-Metals/202004280001.

[220] M. W. Gaultois, T. D. Sparks, C. K. H. Borg, R. Seshadri, W. D. Bonificio, D. R. Clarke, *Chemistry of Materials*, 2013, **25**, 2911–2920.

[221] *Shanghai Metals Market Database - Platinum Price History*, (Accessed on: 25/03/2021). https://www.metal.com/Other-precious-metals/201102250529.

[222] K. L. Luska, A. Bordet, S. Tricard, I. Sinev, W. Grünert, B. Chaudret, W. Leitner, *ACS Catalysis*, 2016, **6**, 3719–3726.

[223] A. Vizcaíno, P. Arena, G. Baronetti, A. Carrero, J. Calles, M. Laborde, N. Amadeo, *International Journal of Hydrogen Energy*, 2008, **33**, 3489–3492.

[224] A. Carrero, J. Calles, A. Vizcaíno, *Chemical Engineering Journal*, 2010, **163**, 395–402.

[225] T. Yang, G. Zhang, Q. Zhang, B. Liu, L. Zhang, *Catalysis Letters*, 2020, **150**, 2978–2990.

[226] A. Penkova, L. Bobadilla, S. Ivanova, M. Domínguez, F. Romero-Sarria, A.-C. Roger, M. Centeno, J. A. Odriozola, *Applied Catalysis A: General*, 2011, **392**, 184–191.

[227] X. Hou, S. Qing, Y. Liu, L. Li, Z. Gao, Y. Qin, *International Journal of Hydrogen Energy*, 2020, **45**, 477–489.

[228] X. Hou, S. Qing, Y. Liu, L. Zhang, C. Zhang, G. Feng, X. Wang, Z. Gao, Y. Qin, *Fuel*, 2021, **284**, 119041.

[229] D. Li, Y. Cai, Y. Ding, R. Li, M. Lu, L. Jiang, *International Journal of Hydrogen Energy*, 2015, **40**, 10016–10025.

[230] W. Haynes, *CRC Handbook of Chemistry and Physics, 92nd Edition*, Taylor & Francis, 2011.

[231] E. Cox, J. Cox, C. Unions, I. C. of Scientific Unions Committee on Data for Science, Technology, D. Wagman, V. Medvedev, D. Wagman, C. T. G. on Key Values for Thermodynamics, *CODATA Key Values for Thermodynamics*, of

CODATA series on thermodynamic properties, Hemisphere Publishing Corporation, 1989.

[232] S. S. Zumdahl, D. J. DeCoste, *Chemical Principles*, Nelson Education, 2012.

[233] V. Rabinovich, Z. Havin, *Brief chemical reference book*, L.: Himiya, 1977.

[234] R. K. Allada, E. Peltier, A. Navrotsky, W. H. Casey, C. A. Johnson, H. T. Berbeco, D. L. Sparks, *Clays and Clay Minerals*, 2006, **54**, 409–417.

[235] R. K. Allada, A. Navrotsky, J. Boerio-Goates, *American Mineralogist*, 2005, **90**, 329–335.

[236] J. Mullay, *Journal of the American Chemical Society*, 1984, **106**, 5842–5847.

[237] R. D. Shannon, *Acta Crystallographica Section A: Crystal Physics, Diffraction, Theoretical and General Crystallography*, 1976, **32**, 751–767, Number: 5 Publisher: International Union of Crystallography.

[238] R. Gao, D. Yan, *Nano Research*, 2018, **11**, 1883–1894.

[239] A. O. Sjåstad, N. H. Andersen, P. Vajeeston, J. Karthikeyan, B. Arstad, A. Karlsson, H. Fjellvåg, *European Journal of Inorganic Chemistry*, 2015, **2015**, 1775–1788.

[240] M. A. Aramendía, V. Borau, C. Jiménez, J. M. Marinas, F. J. Romero, J. R. Ruiz, *Journal of Solid State Chemistry*, 1998, **135**, 96–102.

[241] W. M. Haynes, *CRC Handbook of Chemistry and Physics, 95th Edition*, CRC Press LLC, Oakville, United Kingdom, 2014.

[242] M. Zabilskiy, V. L. Sushkevich, M. A. Newton, J. A. van Bokhoven, *ACS Catalysis*, 2020, **10**, 14240–14244.

[243] A. Borodziński, M. Bonarowska, *Langmuir*, 1997, **13**, 5613–5620.

[244] R. German, *Thermodynamics of Sintering*, Elsevier, 2010.

[245] J. Nakamura, J. M. Campbell, C. T. Campbell, *Journal of the Chemical Society, Faraday Transactions*, 1990, **86**, 2725–2734.

[246] O. Jakdetchai, T. Nakajima, *Journal of Molecular Structure: THEOCHEM*, 2002, **619**, 51–58.

[247] C. Mateos-Pedrero, C. Azenha, P. T. D.a., J. M. Sousa, A. Mendes, *Applied Catalysis B: Environmental*, 2020, **277**, 119243.

[248] *Shanghai Metals Market Database - Gallium Price History*, (Accessed on: 15/09/2021). https://www.metal.com/Indium-Germanium-Gallium/201102250326.

[249] *Shanghai Metals Market Database - Aluminium Price History*, (Accessed on: 15/09/2021). https://www.metal.com/Aluminum/201102250343.

[250] L. Alejo, R. Lago, M. Pena, J. Fierro, *Applied Catalysis A: General*, 1997, **162**, 281–297.

[251] C. Thurgood, J. Amphlett, R. Mann, B. Peppley, *Topics in Catalysis*, 2003, **22**, 253–259.

[252] J. Toyir, P. Ramírez de la Piscina, N. Homs, *International Journal of Hydrogen Energy*, 2015, **40**, 11261–11266.

[253] J. Schumann, M. Eichelbaum, T. Lunkenbein, N. Thomas, M. C. Alvarez Galvan, R. Schlögl, M. Behrens, *ACS Catalysis*, 2015, **5**, 3260–3270.

[254] F. Wong, R. Buchheit, *Progress in organic coatings*, 2004, **51**, 91–102.

[255] R. Santos, J. Tronto, V. Briois, C. Santilli, *Journal of Materials Chemistry A*, 2017, **5**, 9998–10009.

[256] Z. Yuan, S.-M. Bak, P. Li, Y. Jia, L. Zheng, Y. Zhou, L. Bai, E. Hu, X.-Q. Yang, Z. Cai, et al., *ACS Energy Letters*, 2019, **4**, 1412–1418.

[257] D. Lide, *CRC Handbook of Chemistry and Physics, 90th Edition*, Taylor & Francis, 2009.

[258] M. Salavati-Niasari, F. Davar, N. Mir, *Polyhedron*, 2008, **27**, 3514–3518.

[259] 230511-ICSD, *National Institute of Standards and Technology Inorganic Crystal Structure Database, NIST Standard Reference Database Number 3, Gaithersburg MD, 20899*. DOI: https://doi.org/10.18434/M32147.

[260] N. Koryabkina, A. Phatak, W. Ruettinger, R. Farrauto, F. Ribeiro, *Journal of Catalysis*, 2003, **217**, 233–239.

[261] M. Ginés, A. Marchi, C. Apesteguía, *Applied Catalysis A: General*, 1997, **154**, 155–171.

[262] *Shanghai Metals Market Database - Cerium Price History*, (Accessed on: 12/10/2021). https://www.metal.com/Rare-Earth-Metals/201102250153.

[263] M. Konsolakis, Z. Ioakeimidis, *Applied Surface Science*, 2014, **320**, 244–255.

[264] Y. Hu, W. Liu, K. Jiang, L. Xu, M. Guan, J. Bao, H. Ji, H. Li, *Inorganic Chemistry Frontiers*, 2020, **7**, 4461–4468, Publisher: Royal Society of Chemistry.

[265] M. Konsolakis, *Applied Catalysis B: Environmental*, 2016, **198**, 49–66.

[266] D. J. Stacchiola, *Accounts of Chemical Research*, 2015, **48**, 2151–2158.

[267] J. A. Rodriguez, J. Graciani, J. Evans, J. B. Park, F. Yang, D. Stacchiola, S. D. Senanayake, S. Ma, M. Pérez, P. Liu, et al., *Angewandte Chemie International Edition*, 2009, **48**, 8047–8050.

[268] Z. Lu, Z. Yang, B. He, C. Castleton, K. Hermansson, *Chemical Physics Letters*, 2011, **510**, 60–66.

[269] S. D. Senanayake, P. J. Ramírez, I. Waluyo, S. Kundu, K. Mudiyanselage, Z. Liu, Z. Liu, S. Axnanda, D. J. Stacchiola, J. Evans, et al., *The Journal of Physical Chemistry C*, 2016, **120**, 1778–1784.

[270] R. O. Idem, N. N. Bakhshi, *Industrial & Engineering Chemistry Research*, 1994, **33**, 2056–2065.

[271] P. Gao, F. Li, N. Zhao, F. Xiao, W. Wei, L. Zhong, Y. Sun, *Applied Catalysis A: General*, 2013, **468**, 442–452.

[272] C. Chen, C. Xu, L. Feng, Z. Li, J. Suo, F. Qiu, Y. Yang, *Advanced Synthesis & Catalysis*, 2005, **347**, 1848–1854.

[273] P. Gunawan, R. Xu, *The Journal of Physical Chemistry C*, 2009, **113**, 17206–17214.

[274] J. Das, D. Das, K. M. Parida, *Journal of Colloid and Interface Science*, 2006, **301**, 569–574.

[275] G. Carja, S. Dranca, G. Ciobanu, E. Husanu, I. Balasanian, *Materials Science-Poland*, 2009, **27**.

[276] T. Posati, F. Costantino, L. Latterini, M. Nocchetti, M. Paolantoni, L. Tarpani, *Inorganic Chemistry*, 2012, **51**, 13229–13236.

[277] Y. Fu, F. Ning, S. Xu, H. An, M. Shao, M. Wei, *Journal of Materials Chemistry A*, 2016, **4**, 3907–3913.

[278] P. Vicente, M. E. Pérez-Bernal, R. J. Ruano-Casero, D. Ananias, F. A. Almeida Paz, J. Rocha, V. Rives, *Microporous and Mesoporous Materials*, 2016, **226**, 209–220.

[279] M. Suárez-Quezada, G. Romero-Ortiz, V. Suárez, G. Morales-Mendoza, L. Lartundo-Rojas, E. Navarro-Cerón, F. Tzompantzi, S. Robles, R. Gómez, A. Mantilla, *Catalysis Today*, 2016, **271**, 213–219.

[280] T. Stumpf, H. Curtius, C. Walther, K. Dardenne, K. Ufer, T. Fanghänel, *Environmental Science & Technology*, 2007, **41**, 3186–3191.

[281] I. Gurrappa, L. Binder, *Science and Technology of Advanced Materials*, 2008.

[282] J. Moulder, J. Chastain, *Handbook of X-ray Photoelectron Spectroscopy: A Reference Book of Standard Spectra for Identification and Interpretation of XPS Data*, Physical Electronics Division, Perkin-Elmer Corporation, 1992.

[283] M. C. Biesinger, L. W. Lau, A. R. Gerson, R. S. C. Smart, *Applied Surface Science*, 2010, **257**, 887–898.

[284] N. X. ray Photoelectron Spectroscopy Database, *NIST Standard Reference Database Number 20, National Institute of Standards and Technology, Gaithersburg MD, 20899*. doi:10.18434/T4T88K.

[285] J. L. Bourque, M. C. Biesinger, K. M. Baines, *Dalton Transactions*, 2016, **45**, 7678–7696.

[286] M. C. Biesinger, L. W. Lau, A. R. Gerson, R. S. C. Smart, *Physical Chemistry Chemical Physics*, 2012, **14**, 2434–2442.

[287] F. de Groot, A. Kotani in *Core Level Spectroscopy of Solids*, CRC Press, 2008, p. 147.

[288] M. C. Biesinger, B. R. Hart, R. Polack, B. A. Kobe, R. S. C. Smart, *Minerals Engineering*, 2007, **20**, 152–162.

[289] P. Burroughs, A. Hamnett, A. F. Orchard, G. Thornton, *Journal of the Chemical Society, Dalton Transactions*, 1976, 1686–1698.

[290] A. Q. Wang, P. Punchaipetch, R. M. Wallace, T. D. Golden, *Journal of Vacuum Science & Technology B: Microelectronics and Nanometer Structures Processing, Measurement, and Phenomena*, 2003, **21**, 1169–1175.

[291] G. H. Jaffari, A. Imran, M. Bah, A. Ali, A. S. Bhatti, U. S. Qurashi, S. Ismat Shah, *Applied Surface Science*, 2017, **396**, 547–553.

[292] A. Kumar, R. Devanathan, V. Shutthanandan, S. V. Kuchibhatla, A. S. Karakoti, Y. Yong, S. Thevuthasan, S. Seal, *The Journal of Physical Chemistry C*, 2012, **116**, 361–366.

[293] A. Bianconi, A. Marcelli, H. Dexpert, R. Karnatak, A. Kotani, T. Jo, J. Petiau, *Physical Review B*, 1987, **35**, 806.

[294] V. Fernandes, I. Graff, J. Varalda, L. Amaral, P. Fichtner, D. Demaille, Y. Zheng, W. Schreiner, D. Mosca, *Journal of The Electrochemical Society*, 2011, **159**, K27.

[295] A. M. Shahin, F. Grandjean, G. J. Long, T. P. Schuman, *Chemistry of Materials*, 2005, **17**, 315–321.

[296] P. Glatzel, U. Bergmann, J. Yano, H. Visser, J. H. Robblee, W. Gu, F. M. de Groot, G. Christou, V. L. Pecoraro, S. P. Cramer, et al., *Journal of the American Chemical Society*, 2004, **126**, 9946–9959.

[297] G. Van der Laan, I. Kirkman, *Journal of Physics: Condensed Matter*, 1992, **4**, 4189.

[298] A. Soldatov, T. Ivanchenko, S. Della Longa, A. Kotani, Y. Iwamoto, A. Bianconi, *Physical Review B*, 1994, **50**, 5074.

[299] Y.-M. So, W.-H. Leung, *Coordination Chemistry Reviews*, 2017, **340**, 172–197.

[300] S. Sharif, I. U. Khan, O. Sahin, N. Jabeen, S. Ahmad, B. Khan, *Zeitschrift für Naturforschung B*, 2019, **74**, 255–260.

[301] 24887-ICSD, *National Institute of Standards and Technology Inorganic Crystal Structure Database, NIST Standard Reference Database Number 3, Gaithersburg MD, 20899*. DOI: 10.1002/aenm.202000783.

[302] H. Yang, C. Huang, A. Tang, X. Zhang, W. Yang, *Materials Research Bulletin*, 2005, **40**, 1690–1695.

[303] M. Khalfaoui, S. Knani, M. Hachicha, A. B. Lamine, *Journal of Colloid and Interface Science*, 2003, **263**, 350–356.

[304] K. S. Sing, *Pure and Applied Chemistry*, 1985, **57**, 603–619.

[305] K. S. Sing, R. T. Williams, *Adsorption Science & Technology*, 2004, **22**, 773–782.

[306] R. J. Hunter, *Foundations of colloid science*, Oxford university press, 2001.

[307] R. Bardestani, G. S. Patience, S. Kaliaguine, *The Canadian Journal of Chemical Engineering*, 2019, **97**, 2781–2791.

[308] Q. Wang, Y. Gao, J. Luo, Z. Zhong, A. Borgna, Z. Guo, D. O'Hare, *RSC Advances*, 2013, **3**, 3414–3420.

[309] Q. Wang, D. O'Hare, *Chemical Communications*, 2013, **49**, 6301–6303.

[310] J. Long, J. Zhang, X. Xu, F. Wang, *Materials Chemistry and Physics*, 2020, **254**, 123496.

[311] N. Seaton, *Chemical Engineering Science*, 1991, **46**, 1895–1909.

[312] F. Giordanino, E. Borfecchia, K. A. Lomachenko, A. Lazzarini, G. Agostini, E. Gallo, A. V. Soldatov, P. Beato, S. Bordiga, C. Lamberti, *The Journal of Physical Chemistry Letters*, 2014, **5**, 1552–1559.

[313] S. Natesakhawat, N. Means, B. Howard, M. Smith, V. Abdelsayed, J. Baltrus, Y. Cheng, J. Lekse, D. Link, B. Morreale, *Catalysis Science & Technology*, 2015, **5**, 5023–5036.

[314] M. A. Goula, N. D. Charisiou, K. N. Papageridis, A. Delimitis, E. Pachatouridou, E. F. Iliopoulou, *international journal of hydrogen energy*, 2015, **40**, 9183–9200.

[315] R. Klaewkla, M. Arend, W. F. Hoelderich, *A review of mass transfer controlling the reaction rate in heterogeneous catalytic systems*, *Vol. 5*, Intech Open Access Publisher London, 2011.

[316] H. Karadeniz, C. Karakaya, S. Tischer, O. Deutschmann, *Zeitschrift für Physikalische Chemie*, 2015, **229**, 709–737.

[317] M. P. Rosynek, *Catalysis Reviews Science and Engineering*, 1977, **16**, 111–154.

[318] H. Lee, S. Park, H. Kim, *Chemical Engineering Journal*, 2021, **414**, 128792.

[319] L.-Y. Sung, B.-J. Hwang, K.-L. Hsueh, W.-N. Su, C.-C. Yang, *Journal of power sources*, 2013, **242**, 264–272.

[320] T. Springer, T. Rockward, T. Zawodzinski, S. Gottesfeld, *Journal of the Electrochemical Society*, 2001, **148**, A11.

[321] C. Decarne, E. Abi-Aad, B. Kostyuk, V. Lunin, A. Aboukais, *Journal of Materials Science*, 2004, **39**, 2349–2356.

[322] F. Giordano, A. Trovarelli, C. de Leitenburg, M. Giona, *Journal of Catalysis*, 2000, **193**, 273–282.

[323] E. K. Plyler, *Journal of Research of the National Bureau of Standards*, 1952, **48**, 281–286.

[324] D. Ott, V. Kerr, T. Whaley, T. Benziger, R. Rohwer, *Journal of Labelled Compounds*, 1974, **10**, 315–324.

[325] J. Schumann, J. Kröhnert, E. Frei, R. Schlögl, A. Trunschke, *Topics in Catalysis*, 2017, **60**, 1735–1743.

[326] S. S. Sung, R. Hoffmann, *Journal of the American Chemical Society*, 1985, **107**, 578–584.

[327] M. Gajdoš, A. Eichler, J. Hafner, *Journal of Physics: Condensed Matter*, 2004, **16**, 1141.

[328] J.-S. Yu, S. Jin Kim, S. Bong Hong, L. Kevan, *Journal of the Chemical Society, Faraday Transactions*, 1996, **92**, 855–860.

[329] J. D. A. Bellido, E. M. Assaf, *Fuel*, 2009, **88**, 1673–1679.

[330] S. Velu, K. Suzuki, M. Okazaki, M. P. Kapoor, T. Osaki, F. Ohashi, *Journal of Catalysis*, 2000, **194**, 373–384.

[331] W.-P. Dow, Y.-P. Wang, T.-J. Huang, *Journal of Catalysis*, 1996, **160**, 155–170.

[332] P. Subramanian, E. Suresh, D. Srinivas, *Inorganic chemistry*, 2000, **39**, 2053–2060.

[333] C. Drouilly, J.-M. Krafft, F. Averseng, S. Casale, D. Bazer-Bachi, C. Chizallet, V. Lecocq, H. Vezin, H. Lauron-Pernot, G. Costentin, *The Journal of Physical Chemistry C*, 2012, **116**, 21297–21307.

[334] T. Su, Y. Yang, Y. Na, R. Fan, L. Li, L. Wei, B. Yang, W. Cao, *ACS Applied Materials & Interfaces*, 2015, **7**, 3754–3763.